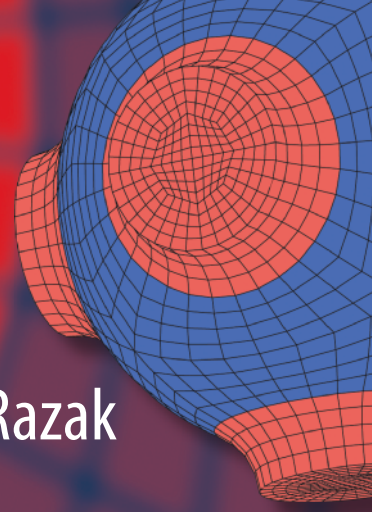


Advanced Structured Materials

Muhamad Husaini Abu Bakar  
Muhammad Al-Hapis Abdul Razak  
Andreas Öchsner *Editors*



# Progress in Engineering Technology IV

 Springer


# Advanced Structured Materials

Volume 169

## Series Editors

Andreas Öchsner, Faculty of Mechanical Engineering, Esslingen University of Applied Sciences, Esslingen, Germany

Lucas F. M. da Silva, Department of Mechanical Engineering, Faculty of Engineering, University of Porto, Porto, Portugal

Holm Altenbach , Faculty of Mechanical Engineering, Otto von Guericke University Magdeburg, Magdeburg, Sachsen-Anhalt, Germany

Common engineering materials reach in many applications their limits and new developments are required to fulfil increasing demands on engineering materials. The performance of materials can be increased by combining different materials to achieve better properties than a single constituent or by shaping the material or constituents in a specific structure. The interaction between material and structure may arise on different length scales, such as micro-, meso- or macroscale, and offers possible applications in quite diverse fields.

This book series addresses the fundamental relationship between materials and their structure on the overall properties (e.g. mechanical, thermal, chemical or magnetic etc.) and applications.

The topics of *Advanced Structured Materials* include but are not limited to

- classical fibre-reinforced composites (e.g. glass, carbon or Aramid reinforced plastics)
- metal matrix composites (MMCs)
- micro porous composites
- micro channel materials
- multilayered materials
- cellular materials (e.g., metallic or polymer foams, sponges, hollow sphere structures)
- porous materials
- truss structures
- nanocomposite materials
- biomaterials
- nanoporous metals
- concrete
- coated materials
- smart materials

Advanced Structured Materials is indexed in Google Scholar and Scopus.

More information about this series at <https://link.springer.com/bookseries/8611>

Muhamad Husaini Abu Bakar ·  
Muhammad Al-Hapis Abdul Razak ·  
Andreas Öchsner  
Editors

# Progress in Engineering Technology IV

 Springer



*Editors*

Muhamad Husaini Abu Bakar  
Malaysian Spanish Institute  
Universiti Kuala Lumpur  
Kulim, Kedah, Malaysia

Muhammad Al-Hapis Abdul Razak  
Malaysian Spanish Institute  
Universiti Kuala Lumpur  
Kulim, Kedah, Malaysia

Andreas Öchsner  
Faculty of Mechanical Engineering  
Esslingen University of Applied Sciences  
Esslingen am Neckar, Baden-Württemberg,  
Germany

ISSN 1869-8433

ISSN 1869-8441 (electronic)

Advanced Structured Materials

ISBN 978-3-030-93249-7

ISBN 978-3-030-93250-3 (eBook)

<https://doi.org/10.1007/978-3-030-93250-3>

© The Editor(s) (if applicable) and The Author(s), under exclusive license to Springer Nature Switzerland AG 2022

This work is subject to copyright. All rights are solely and exclusively licensed by the Publisher, whether the whole or part of the material is concerned, specifically the rights of translation, reprinting, reuse of illustrations, recitation, broadcasting, reproduction on microfilms or in any other physical way, and transmission or information storage and retrieval, electronic adaptation, computer software, or by similar or dissimilar methodology now known or hereafter developed.

The use of general descriptive names, registered names, trademarks, service marks, etc. in this publication does not imply, even in the absence of a specific statement, that such names are exempt from the relevant protective laws and regulations and therefore free for general use.

The publisher, the authors and the editors are safe to assume that the advice and information in this book are believed to be true and accurate at the date of publication. Neither the publisher nor the authors or the editors give a warranty, expressed or implied, with respect to the material contained herein or for any errors or omissions that may have been made. The publisher remains neutral with regard to jurisdictional claims in published maps and institutional affiliations.

This Springer imprint is published by the registered company Springer Nature Switzerland AG  
The registered company address is: Gewerbestrasse 11, 6330 Cham, Switzerland

# Preface

The volume contains a collection of peer-reviewed papers from the 2020 Conference on Multidisciplinary Engineering and Technology (COMET 2020), held via an online platform, which took place in Universiti Kuala Lumpur, Malaysian Spanish Institute (UniKL MSI), Kedah, Malaysia, on December 15–16, 2020. Progress in Engineering Technology IV contains twenty-five papers written by researchers participating in the conference. Topics covered in this volume including energy harvester, thermodynamics, vibration, dynamic of mechanics, manufacturing process, computer-aided manufacturing (CAM), CFD analysis, electronics, and microcontroller. Most of the topics are commonly encountered in industries and become an interest in the academic world. The learning of engineering technology curricular across universities are now essential topics covered in various higher learning institutions in Malaysia in general and in Universiti Kuala Lumpur (UniKL) specifically. It is hoped that this volume will serve as an excellent reference work for researchers and graduate students working with/on multidisciplinary engineering technology.

Kulim, Malaysia  
Kulim, Malaysia  
Esslingen am Neckar, Germany

Muhamad Husaini Abu Bakar  
Muhammad Al-Hapis Abdul Razak  
Andreas Öchsner

# Contents

<b>1</b>	<b>Brake Squeal Analysis and Optimization Using the Finite Element Method and Taguchi Techniques</b> .....	<b>1</b>
	Adib Kamarudin, Ahmad Razlee Ab Kadir, Zainal Nazri Mohd Yusuf, Muhammad Al'Hapis Abdul Razak, T. A. A. Razak, and M. N. Ahmad	
1.1	Introduction .....	2
1.2	Methodology .....	3
1.2.1	3D Design of the Brake Disc Model .....	4
1.2.2	Finite Element Analysis .....	5
1.2.3	Modal Analysis .....	5
1.3	Result and Discussion .....	6
1.3.1	Natural Frequency Using Mild Steel, Gray Cast Iron, and Carbon Ceramic .....	7
1.3.2	Comparison Natural Frequency Between All Three Design and Materials .....	8
1.3.3	Taguchi Method Using Minitab .....	11
1.4	Conclusion .....	13
	References .....	13
<b>2</b>	<b>Potential Experimental Analysis of Electrical Discharge Machine Process Parameters on Stainless Steel ANSI 304</b> .....	<b>15</b>
	Afnan Nizarif Ahmad Zamzuri, Muhammad Al'Hapis Abdul Razak, Aznizam Abdullah, Ahmad Razlee Ab Kadir, Ahmad Majdi Abdul-Rani, Farooq I. Azam, and Haizum Aimi Zaharin	
2.1	Introduction .....	16
2.2	Literature .....	16
2.2.1	Electrical Discharge Machining .....	16
2.2.2	Die-Sinking .....	17
2.2.3	Wire EDM Process .....	17
2.2.4	Dielectric Fluid .....	17

- 2.2.5 EDM Machine Components ..... 18
- 2.2.6 Material Removal Rate ..... 18
- 2.2.7 Surface Quality Analysis ..... 18
- 2.2.8 Taguchi Method ..... 19
- 2.3 Methodology ..... 20
  - 2.3.1 Research Structure ..... 20
  - 2.3.2 Experimental Setup ..... 20
  - 2.3.3 Selection of the Workpiece ..... 21
  - 2.3.4 Tool Design ..... 21
  - 2.3.5 Mechanism and Measurement of the MRR ..... 21
  - 2.3.6 Mechanism and Evaluation of Surface Roughness ..... 21
  - 2.3.7 Design of Experiments Analysis ..... 22
- 2.4 Conclusions ..... 22
- References ..... 22
- 3 Embedded System Using a PIC Microcontroller for Series Motor Four Quadrants Drive DC Chopper Controllers for the Application in Electrical Vehicles ..... 23**

Saharul Arof, Norramlee Mohamed Noor, Philip Mawby, Hamzah Arof, and Emilia Noorsal

  - 3.1 Introduction ..... 24
  - 3.2 Literature Review ..... 24
  - 3.3 Methodology ..... 26
    - 3.3.1 Embedded System of FQDC Controllers ..... 26
    - 3.3.2 Detailed Operation Function on Each of the Controllers ..... 28
    - 3.3.3 Simulation Software and Experimental Setup for Simulation and Experiment ..... 33
  - 3.4 Results ..... 34
  - 3.5 Conclusion ..... 35
  - References ..... 35
- 4 Pre-weld Heating Temperature Effect on the Welding Quality of a 100 T Truck Crack Frame—Case Study ..... 39**

Tumianto, Muhammad Al’Hapis Abdul Razak, Azmi Hassan, Iwan Susanto, Surya Atmadyaya, Mohd Riduan Ibrahim, and Asmawi Ismail

  - 4.1 Introduction ..... 40
  - 4.2 Methodologies ..... 40
    - 4.2.1 Data Collection Method ..... 41
    - 4.2.2 Data Analysis ..... 41
  - 4.3 Discussion ..... 42
    - 4.3.1 Taguchi Analysis ..... 42
  - 4.4 Conclusions ..... 44
  - References ..... 45

- 5 Features Extraction from a Second-Order Black Box Model Matched to the Veltink Model for a System Identification of Knee Extension for Control Law and Formulations of Close-Loop Controller Rehabilitation Using Functional Electrical Stimulation . . . . . 47**  
Saharul Arof, Emilia Noorsal, Saiful Zaimy Yahaya,  
Nor Haslina Ibrahim, and Hamzah Arof
  - 5.1 Introduction . . . . . 48
  - 5.2 Literature . . . . . 48
  - 5.3 Methodology . . . . . 49
    - 5.3.1 Second-Order Black Box Model System . . . . . 51
    - 5.3.2 Second-Order System Features Extraction . . . . . 53
    - 5.3.3 Simulation Model Using Matlab/Simulink Function . . . . . 55
  - 5.4 Result and Discussion . . . . . 55
  - 5.5 Conclusions . . . . . 62
  - References . . . . . 62
  
- 6 Analysis of an Adjustable Topside Mechanic’s Creeper for Automotive Repair and Maintenance Using Simulation Methods . . . . . 65**  
Siti Rohana Ahmad, Syasya Aqilah Mohamad Nadzri,  
and Muhammad Zunnurrin Ghazali
  - 6.1 Introduction . . . . . 66
  - 6.2 Literature . . . . . 66
  - 6.3 Methodology . . . . . 67
    - 6.3.1 Design Process . . . . . 67
    - 6.3.2 Design of Foldable Topside Mechanic’s Creeper . . . . . 68
    - 6.3.3 Simulation Analysis . . . . . 70
  - 6.4 Results and Discussion . . . . . 71
    - 6.4.1 Simulation Results and Discussion . . . . . 71
  - 6.5 Conclusions . . . . . 76
  - References . . . . . 76
  
- 7 Potential Use of a Vibration Energy Harvester in Vehicles Using a Linear Motion Electromagnetic Suspension System . . . . . 77**  
Fazidah Saad and Muhammad Najib Abdul Hamid
  - 7.1 Introduction . . . . . 77
  - 7.2 Linear Electromagnetic Energy Harvesting in the Vehicle Suspension System . . . . . 79
    - 7.2.1 Electromagnetic Regenerative Shock Absorber . . . . . 80
    - 7.2.2 Tubular Linear Electromagnetic Transducers . . . . . 82
    - 7.2.3 Electromagnetic Linear Vibration Energy Harvester with Ferrofluid as a Lubricant . . . . . 83
    - 7.2.4 Hybrid Regenerative Shock Absorber . . . . . 86
  - 7.3 Discussion . . . . . 87

7.4	Conclusion .....	88
	References .....	88
<b>8</b>	<b>Performance Analysis of a Coated Porous Medium Burner for Cogeneration .....</b>	<b>91</b>
	Ahmad Kamal Ismail, Mohd Zulkifly Abdullah, Nor Haslina Ibrahim, Khairul Akmal Shamsuddin, and Ayub Ahmed Janvekar	
8.1	Introduction .....	92
8.2	Literature .....	92
8.3	Methodology .....	93
8.4	Results and Discussion .....	94
8.5	Conclusions .....	97
	References .....	97
<b>9</b>	<b>Child Safety in Car Crashes: A Modeling Approach for Safety System Improvements .....</b>	<b>99</b>
	Shahrizan Yusoff, Nurul Syasya Fakhira, and Nor Haniza Bakhtiar Jemily	
9.1	Introduction .....	99
9.2	Literature .....	100
	9.2.1 Application of Child Booster Seat to Prevent Child Injuries .....	101
	9.2.2 Categorization of Child Car Seats .....	103
9.3	Methodology .....	103
9.4	Results and Discussion .....	104
9.5	Conclusion .....	107
	References .....	108
<b>10</b>	<b>Modelling of Air-Gap Magnetic Flux Density Distribution for Surface-Mounted Permanent Magnet Synchronous Motor Using the Analytical Sub-Domain Method .....</b>	<b>109</b>
	M. Rezal, D. Ishak, and M. S. Ahmad	
10.1	Introduction .....	109
10.2	Literature Review .....	110
	10.2.1 Sub-Domain Method .....	110
	10.2.2 Airgap Flux Density for Slotless PMSM .....	112
10.3	Methodology .....	113
	10.3.1 Motor Parameters and 2-D Design .....	113
	10.3.2 Airgap Flux Density for Slotless PMSM .....	113
10.4	Results and Discussion .....	115
10.5	Conclusion .....	116
	References .....	118

**11 Comparative Study on the Performance of Electrical Vehicles with DC Drive and Series Motor, DC Drive and Separately Excited DC Motor, and AC Drive and PMSM Motor. Part 1: Driving and Braking Operations** ..... 121  
 Saharul Arof, Mohamad Rosyidi Ahmad, Philip Mawby, Hamzah Arof, and Emilia Noorsal

11.1 Introduction ..... 122

    11.1.1 Review Stage ..... 122

    11.1.2 DC Series Motor and Four Quadrants DC Chopper Four Series Motor ..... 125

    11.1.3 DC Drive EV Four Quadrants DC Chopper for Series Motor ..... 125

    11.1.4 DC Separately Excited DC Motor and Four Quadrants DC Chopper ..... 126

    11.1.5 DC Drive EV Four Quadrants DC Chopper for Separately Excited DC Motor ..... 127

    11.1.6 Four Quadrants Drive DC Chopper Operation Modes ..... 128

    11.1.7 AC Drive EV with PMSM Motor ..... 128

    11.1.8 Permanent Magnet Synchronous Motor Drive System ..... 129

    11.1.9 AC Drive EV Inverter ..... 129

11.2 Methodology ..... 130

    11.2.1 Electric Car Motor ..... 130

    11.2.2 Vehicle Dynamics ..... 130

11.3 Conclusion ..... 136

References ..... 136

**12 Overall Heat Transfer Coefficient of Different Coolants and Frontal Air Velocity in Automotive Radiators** ..... 139  
 Ain Najwa Abdul Manan, Dzarisofea Anuar, Muhammad Latiff Abd Khalid, Ahmad Kamal Ismail, and Ishak Abdul Azid

12.1 Introduction ..... 139

12.2 Literature ..... 140

    12.2.1 Coolants ..... 140

    12.2.2 Air Flow ..... 141

12.3 Methodology ..... 141

    12.3.1 Experimental Setup ..... 141

    12.3.2 Data Analysis ..... 143

12.4 Results ..... 143

    12.4.1 Effect of Coolant in Real Engine and Educational Test Rig ..... 143

    12.4.2 Effect of Frontal Air Velocity in Real Engine at Different RPM ..... 144

12.5 Conclusions ..... 145

References ..... 145

**13 Magnetic Field Distribution for Single Coil Pulsed Linear Accelerator ..... 147**

M. Rezal, D. Ishak, and M. S. Ahmad

13.1 Introduction ..... 147

13.2 Literature Review ..... 148

13.3 Methodology ..... 148

13.4 Results and Discussion ..... 151

13.5 Conclusion ..... 152

References ..... 153

**14 Formulations After Features Extraction of Veltink to Second-Order Critical Damped Black Box Model for Observer Formation Representing Knee Extension ..... 155**

Saharul Arof, Norramlee Mohamed Noor, Emilia Noorsal, Saiful Zaimy, Zakaria Hussein, and Hamzah Arof

14.1 Introduction ..... 156

14.2 Methodology ..... 158

14.3 Result and Analysis ..... 159

14.4 Conclusion ..... 164

References ..... 164

**15 Optimization of Process Parameters in Electric Discharge Machining Wire-Cut of Magnesium Alloys Using the Taguchi’s Approach ..... 167**

Ariff Naquiddin Nazri, Muhammad Al’Hapis Abdul Razak, Mohd Rezal Mohamed, Mohamad Fadzli Haniff, Ahmad Razlee Ab Kadir, Sadaqat Ali, and Abdul’Azeez A. Aliyu

15.1 Introduction ..... 168

15.2 Literature ..... 168

    15.2.1 Magnesium Alloys ..... 169

    15.2.2 Electric Discharge Machine ..... 169

    15.2.3 Statistical Method ..... 170

15.3 Methodology ..... 171

15.4 Results and Discussion ..... 172

15.5 Conclusions ..... 173

References ..... 173

**16 Design of Micro Turbocharger Runners for Automotive Application ..... 175**

Khairul Shahril, Mohamad Wardi, Shahril Nizam, Muhammad Najib, and Ishak A. Azid

16.1 Introduction ..... 176

16.2 Literature Review ..... 176



- 16.2.1 Design of a New Improved Intake Manifold for F-SAE Car ..... 176
- 16.2.2 Simulation Analysis of Spark Ignition Engine Intake Manifold for Better Performance ..... 177
- 16.2.3 Air Flow Behaviour on Different Intake Manifold Angles for Small 4-Stroke PFI Retrofit Kit System .... 178
- 16.3 Methodologies/Experimental Set-Up/Model Set-Up ..... 179
  - 16.3.1 Methodology Process ..... 179
- 16.4 Results and Discussion ..... 181
- 16.5 Conclusion ..... 182
- References ..... 184
- 17 Study on Ripple Current, Ripple Torque in Parallel Mode of Series Motor Four Quadrants DC Chopper for Electric Vehicles ..... 185**

Saharul Arof, Mohamad Rosyidi Ahmad, Philip Mawby, Hamzah Arof, and Emilia Noorsal

  - 17.1 Introduction ..... 186
  - 17.2 Review Stage ..... 186
  - 17.3 Methodology ..... 188
  - 17.4 Results ..... 195
  - 17.5 Conclusion ..... 197
  - References ..... 198
- 18 Statistical Approach for Predictions of Motorcycle Engine Block Surface Roughness Property After CNC Machining ..... 201**

Shahrizan Yusoff, Sharifah Nur Anis Ajmal, Nur Nadhirah, and Baizura Zubir

  - 18.1 Introduction ..... 201
  - 18.2 Literature ..... 202
    - 18.2.1 Surface Roughness ..... 202
    - 18.2.2 CNC Milling ..... 203
    - 18.2.3 Cutting Speed ..... 203
    - 18.2.4 Feed ..... 204
    - 18.2.5 Depth of Cut ..... 204
    - 18.2.6 Cemented Carbide ..... 204
    - 18.2.7 Engine Cylinder Block ..... 205
    - 18.2.8 Response Surface Methodology ..... 205
  - 18.3 Methodology ..... 206
    - 18.3.1 Block Diagram of Surface Roughness ..... 206
    - 18.3.2 Block Diagram of CNC Milling Cutting ..... 208
  - 18.4 Results ..... 209
  - 18.5 Conclusion ..... 212
  - References ..... 212

**19 Contamination Control on Hydraulic Oil Excavator Using an Off-Board Filtering System—Case Study** ..... 213  
 Iwan Susanto, Muhammad Al-Hapis Abdul Razak, Azmi Hassan, Surya Atmadyaya, Tumianto, Mohd Shahrizan Yusoff, and Krishnan Subramaniam

19.1 Introduction ..... 214

19.2 Methodologies ..... 217

    19.2.1 Data Collection Method ..... 217

    19.2.2 Data Analysis ..... 217

19.3 Discussion ..... 218

    19.3.1 Taguchi Analysis of PC06 Response ..... 218

    19.3.2 Taguchi Analysis of PC14 Response ..... 221

    19.3.3 Taguchi Analysis of V100 Response ..... 223

19.4 Conclusions ..... 226

References ..... 226

**20 Hardware Development for Zero Crossing of a Multilevel Single Phase Rectifier Chopper for Plug-In Electric Car Battery Charger Using a PIC Microcontroller** ..... 227  
 Saharul Arof, Fathul H. Ahmad, Nurazlin M. Yaakop, Julaida A. Jalil, Philip Mawby, Hamzah Arof, and Emilia Noorsal

20.1 Introduction ..... 228

20.2 Review Stage ..... 228

    20.2.1 Literature on Zero Crossing ..... 230

20.3 Methodology ..... 230

    20.3.1 Hardware Application Circuit ..... 232

    20.3.2 Coding for Zero Crossing ..... 232

    20.3.3 Hardware Applications ..... 235

    20.3.4 Algorithm 2 ..... 236

    20.3.5 Simulation Applications ..... 237

    20.3.6 Hardware Development ..... 238

20.4 Conclusion ..... 239

References ..... 240

**21 Topology Optimization of an Engine Mounting Bracket Using Finite Elements** ..... 243  
 Akief Khan Ayob Khan, Ahmad Razlee Ab Kadir, Zainal Nazri, T. A. A. Razak, and M. N. Ahmad

21.1 Introduction ..... 243

    21.1.1 Based on Application Aspects of Mounts ..... 245

21.2 Methodology ..... 247

    21.2.1 Design Model 3D of Engine Mounting Bracket ..... 247

    21.2.2 Finite Element Analysis (FEA) ..... 247

    21.2.3 Modal Analysis ..... 248

    21.2.4 Topology Optimization ..... 250

21.3 Result and Discussion ..... 251

- 21.3.1 Comparison Result from FEA and EMA ..... 251
- 21.3.2 Optimized Design Engine Mounting Bracket ..... 251
- 21.4 Conclusions ..... 253
- References ..... 253
- 22 Air Conditioning System Comfort Level and Power Consumption Monitoring Device with RF-Based Wireless Sensor Modules and Android Mobile Application ..... 255**  
 Norzalina Othman, Mohamad Fadzli Haniff,  
 Hazlina Selamat, Tuan Muhammad Syahmi Tuan Saha' Arif,  
 Muhammad Al'Hapis Abdul Razak,  
 Mohd Usairy Syafiq Sama'in, and Julaida Abdul Jalil
- 22.1 Introduction ..... 256
- 22.2 Literature ..... 257
  - 22.2.1 Thermal Comfort ..... 257
  - 22.2.2 Mobile Applications ..... 258
- 22.3 Methodology ..... 260
  - 22.3.1 Project Planning ..... 260
  - 22.3.2 Fabrication ..... 264
  - 22.3.3 LCD Display Sample ..... 266
  - 22.3.4 Experimental Setup ..... 267
- 22.4 Results and Discussion ..... 268
- 22.5 Conclusions ..... 271
- References ..... 272
- 23 A Key Comparative Study Between a Self-Aspirated and an Air-Induced Porous Medium Burner ..... 273**  
 Ahmad Kamal Ismail, Chan Ping Yi, Mohd Zulkifly Abdullah,  
 Mazlan Mohamed, and Ayub Ahmed Janvekar
- 23.1 Introduction ..... 274
- 23.2 Literature ..... 274
- 23.3 Methodology ..... 274
- 23.4 Results and Discussion ..... 276
- 23.5 Conclusions ..... 280
- References ..... 280
- 24 Analysis of the Lower Control Arm in a Front Suspension System Using Finite Element Analysis and Analysis of Variance (ANOVA) Method ..... 283**  
 A. N. Ridzwan, A. R. A. Kadir, I. A. Azid, M. N. A. Hamid,  
 T. A. A. Razak, and M. N. Ahmad
- 24.1 Introduction ..... 284
- 24.2 Methodology ..... 286
  - 24.2.1 Three-Dimensional Design Model ..... 286
  - 24.2.2 Statics Structural Analysis of the Main Body Part ..... 286
  - 24.2.3 Load Impact Testing Experimental ..... 290

- 24.2.4 Modal Analysis Simulation ..... 291
- 24.2.5 Design Modifications ..... 293
- 24.2.6 Determining Factor of Analysis by Using ANOVA  
Method ..... 294
- 24.3 Result and Discussion ..... 294
  - 24.3.1 Modal Analysis with LMS Load Impact Testing  
Result ..... 294
  - 24.3.2 Statics Load Structural Analysis of Lower Control  
Arm ..... 295
  - 24.3.3 Statics Structural Analysis Result of the New  
Modified Result ..... 295
  - 24.3.4 Main Factor Analysis Result by using Analysis  
of Variance (ANOVA) ..... 297
  - 24.3.5 Comparison of Final Design and Existing Final  
Design Project ..... 298
- 24.4 Conclusions ..... 298
- References ..... 299
- 25 Model of Effectiveness Earned Value Management  
in the Malaysian Manufacturing Sector ..... 301**

Shahrizan Yusoff, Mohammad Hazim, Syed Ahmad Faiz,  
Sazali Said, and Huda Kassim

  - 25.1 Introduction ..... 301
  - 25.2 Literature ..... 302
    - 25.2.1 Implementation EVM in a Project ..... 302
    - 25.2.2 Problem Using Earn Value Management ..... 304
    - 25.2.3 Benefit of Using EVM ..... 304
  - 25.3 Methodology ..... 304
    - 25.3.1 Design of Conceptual Model ..... 305
    - 25.3.2 Conceptual Model of Effectiveness in EVM ..... 306
    - 25.3.3 Conceptual Model of Effect of Benefit in EVM ..... 307
    - 25.3.4 The Complete Conceptual Model ..... 308
  - 25.4 Results and Discussion ..... 308
    - 25.4.1 Outer Loading Based on the Model ..... 308
  - 25.5 Conclusions ..... 309
  - References ..... 310

# About the Editors

**Muhamad Husaini Abu Bakar** is a Director for System engineering and Energy Laboratory and at the Universiti Kuala Lumpur—Malaysian Spanish Institute, Malaysia. From 2017 till now, he also holds the position as Head of Research and Innovation Section at the same university. He has published over 50 scientific publications in Deep Learning, computational atomistic, and metal-air battery. His research activities were recognized by the innovation award of PECIPTA, IIDEX, I-COMPEX, I-ENVEX, and MARA due to his innovative invention in smart material and smart monitoring system.

**Muhammad Al-Hapis Abdul Razak** is a senior lecturer and Head of Industrial Linkages Section at Universiti Kuala Lumpur—Malaysian Spanish Institute, Malaysia. He obtained his Doctor of Philosophy (Ph.D.) in Mechanical Engineering from Universiti Teknologi Petronas, Malaysia. He is an active researcher and supervising post-graduate research students mainly in manufacturing industry and technology field. His works has been published in multiple reputable journals, books and conference proceedings and received awards from various innovation competition such as MARATex, ITEX, i-COMPEX, and MTE.

**Andreas Öchsner** is a Full Professor of Lightweight Design and Structural Simulation at Esslingen University of Applied Sciences, Germany. After completing his Dipl.-Ing. degree in Aeronautical Engineering at the University of Stuttgart (1997), he served as a research and teaching assistant at the University of Erlangen-Nuremberg from 1997 to 2003 while pursuing his Doctor of Engineering Sciences (Dr.-Ing.) degree. From 2003 to 2006, he was an Assistant Professor at the Department of Mechanical Engineering and Head of the Cellular Metals Group affiliated with the University of Aveiro, Portugal. He spent seven years (2007–2013) as a Full Professor at the Department of Applied Mechanics, Technical University of Malaysia, where he was also Head of the Advanced Materials and Structure Lab. From 2014 to 2017 he was a Full Professor at the School of Engineering, Griffith University, Australia and Leader of the Mechanical Engineering Program (Head of Discipline and Program Director).

# Chapter 1

## Brake Squeal Analysis and Optimization Using the Finite Element Method and Taguchi Techniques



**Adib Kamarudin, Ahmad Razlee Ab Kadir, Zainal Nazri Mohd Yusuf, Muhammad Al'Hapis Abdul Razak, T. A. A. Razak, and M. N. Ahmad**

**Abstract** It is well-known that automobile brakes generate several kinds of noises such as the squeal, groan, chatter, judder, moan, hum, and squeak. Squeal is the most prevalent, annoying, and can be reduced by variations in geometry, such as coefficient of friction and stiffness of a material. The brake squeal generally occurs in the range of 1–16 kHz. Furthermore, the development of methods to predict noise occurrence during the design of a brake system has been the target of many researchers in recent years. In order to withstand these vibrations and have a smooth ride, automotive engineers face the challenge of designing mechanisms. The design of the brake disc rotor is built in the CAD SolidWorks and was analyzed and simulated by using the finite element analyses.

**Keywords** Brake squeal · Brake disc rotor · SolidWorks · Finite elements analysis (FEA)

---

A. Kamarudin · A. R. Ab Kadir (✉) · Z. N. M. Yusuf · M. A. A. Razak · T. A. A. Razak · M. N. Ahmad  
Universiti Kuala Lumpur, Malaysian Spanish Institute, Kulim Hi-Tech Park, 09000 Kulim, Kedah, Malaysia  
e-mail: [ahmadrazlee@unikl.edu.my](mailto:ahmadrazlee@unikl.edu.my)

A. Kamarudin  
e-mail: [adib.kamarudin@unikl.edu.my](mailto:adib.kamarudin@unikl.edu.my)

Z. N. M. Yusuf  
e-mail: [zainalnazri@unikl.edu.my](mailto:zainalnazri@unikl.edu.my)

M. A. A. Razak  
e-mail: [alhapis@unikl.edu.my](mailto:alhapis@unikl.edu.my)

T. A. A. Razak  
e-mail: [tajuladli@unikl.edu.my](mailto:tajuladli@unikl.edu.my)

M. N. Ahmad  
e-mail: [mohdnizam@unikl.edu.my](mailto:mohdnizam@unikl.edu.my)

## 1.1 Introduction

A disc brake is a mechanical device that is used to decelerate a moving vehicle. The mechanism of braking works as one of the most basic safety-critical elements of industrial technology cars for tourists. The heat produced during the braking force can also be quickly dissipated as disc brakes are exposed to the environment, offering a much better output than the drum. Brake noise has been among the top vehicle quality warranty concerns in recent years. The most frequent of all brake sounds is brake squealing. This kind of noise emerges when a braking device displays elevated vibration levels, resulting in highly elevated sound waves. Most scientists and engineers accepted that squealing noise in the disc brake would cause instability due to friction forces, which would lead to self-excited vibrations. The disc, the pads, and the caliper in which they are mounted will vibrate under the right conditions.

In the last few decades, a considerable number of studies has been conducted by several experts around the world on the prospect of understanding the mechanisms of brake squeal noise in order to enhance the performance of car users' comfort and lower the required amount of ambient noise. Brake squeal investigations can be traced all the way back to the 1930s. To now, however, there is no technology and system available to fully reduce the brake squeal. Understanding the processes of generation of squeal is important for the creation of quiet brakes and the handling of noisy brakes. Key mechanisms would be set in order to clarify the phenomena of brake squeal—for example, stick-slip, sprag-slip, modal coupling, and hammering of the excitation mechanism.

The first mechanism explains that the brake squeal is the product of a stick-slip mechanism. As Kinkaid et al. [1] put it in his review article, Mills [2] believed that the brake squeal emerged because the dynamic friction coefficient decreased with increasing slippery velocity and contributed to steady-state sliding becoming unstable and caused friction-induced vibrations. A multi-degree finite element model was used to simulate a braking device and to analyze friction-velocity negative squealing effects [3]. It came to the conclusion that the squeal inclination improved as the friction level increased because there was no negative friction-speed curve. When an increase in friction level is present, it does not have any effect on squeal tendency and, in some brake systems, negative friction-speed inclination may have a superior effect on the tendency of the brake squeal. The Single Degree of Freedom (SDOF) system consists of a brake pad as a mass ( $m$ ) which rests on a rotating disc at constant speed ( $v$ ) and attaches to a linear spring at a fixed end, as shown in Fig. 1.1a. Mathematically, when the coefficient of friction  $\mu$  between the pad and the disc in Fig. 1.1b is considered to decrease linearly with the sliding velocity, for example,  $\mu = \mu_s - \alpha v$ , the motion equation of the pad will be as follows:

$$M\ddot{X} + C\dot{X} + KX = \mu F = F(\mu_s - \alpha(v - \dot{X})) \quad (1.1)$$

or

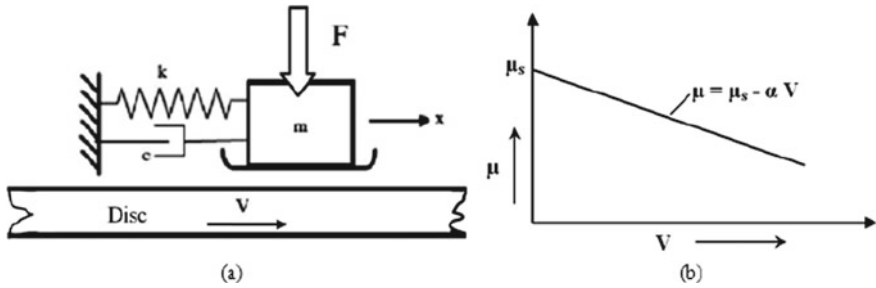


Fig. 1.1 Schematic diagram for stick-slip mechanism

$$M\ddot{X} + (c - \alpha F)\dot{X} + KX = F(\mu_s - \alpha v) \tag{1.2}$$

where  $K$  is the spring stiffness,  $m$  is the mass, and  $F$  is the friction force. The coordinate  $x$  is a measure of the displacement of the mass from the direction of the balance. The damping coefficient  $(c - \alpha F)$  can then be negative if  $(\alpha F > c)$  results in an oscillation of the pad with a greater amplitude which may lead to squealing rather than decreasing oscillations consistent with positive damping.

Squeal produced by the disc brake of the car was considered to be one of the major problems in the automobile industry due to repeated complaints that decrease customer satisfaction. Abendroth and Wernitz [4] noted that many friction material manufacturers have to spend up to 50% of their engineering budget on NVH problems. A variety of similar experiments have been performed on the action of disc brakes by modal analysis. Finite element model of the brake rotor disc was developed by the researcher to analyze the effect of the top hat configuration on the modality of the brake rotor disc. The result shows how the natural frequency of the configuration relates to the thickness of the disc and the structure of the hat. In 2009, Nouby et al. [5] found in their study a complex study of the value of the brake system, along with the configuration of the experiments, in order to determine the ideal nature of the brake system. They mentioned that by increasing Young’s back plate modulus and changing the form of the friction content by inserting chamfer and slots, the inclination of the brake squeal can be significantly reduced [6].

## 1.2 Methodology

The key concept behind this project is to create a 3D model of the vehicle’s brake disc to achieve vibration and deformation accuracy. In order to do this, the 3D model was constructed using SOLIDWORKS. The research was performed using the finite element method software. In the finite element method, the various properties of the materials would be used in the term to derive the result. The primary aim of the

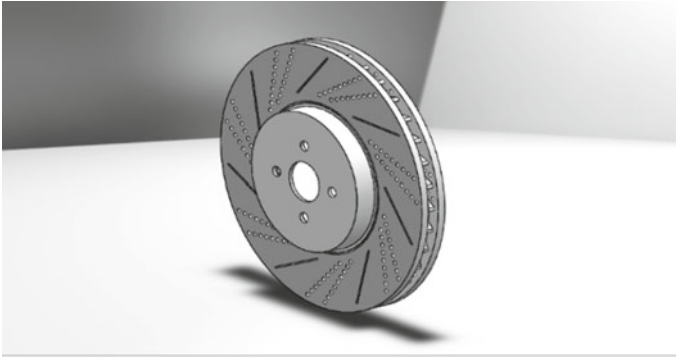


approach was to ensure that the project was properly planned in order to be effective in the study of the project.

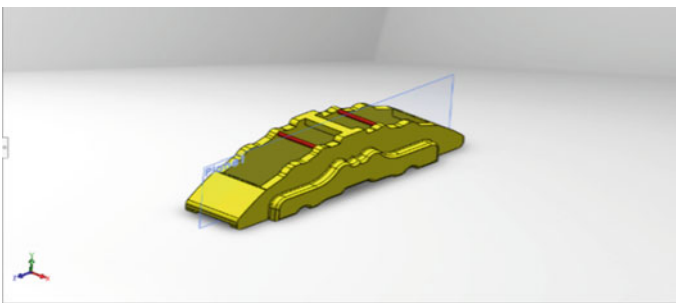
### ***1.2.1 3D Design of the Brake Disc Model***

#### **1.2.1.1 3D CAD Modeling**

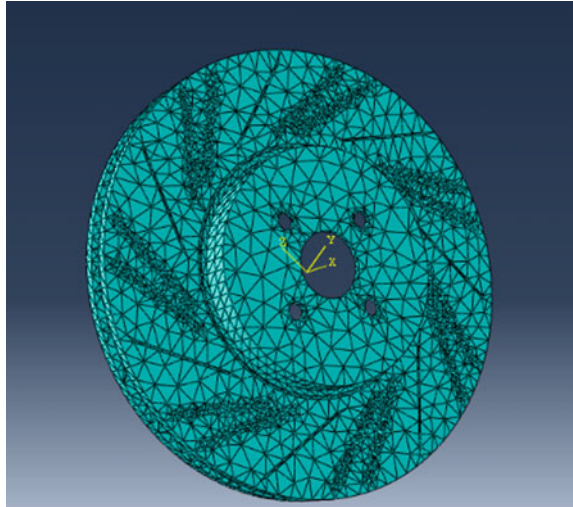
SOLIDWORKS is a modular parametric architecture that is simple to use and enables the user to edit design at any point. The brake disc rotor and caliper was modeled in the SOLIDWORKS 2019 software. The material of the brake disc rotor is gray cast iron. Figures 1.2 and 1.3 are 3D CAD model for the brake disc rotor design.



**Fig. 1.2** 3D model of brake rotor



**Fig. 1.3** 3D model of caliper

**Fig. 1.4** Mesh for the rotor

### ***1.2.2 Finite Element Analysis***

Simulia Abaqus CAE is the program used to do the finite element analysis (FEA) for the brake disc. Structural and machinery finite element analysis for solid (3D) modeling or surface (2D) development, object meshing, analysis setup, and post-processing solvers in a variety of other software applications including ANSYS, Autodesk simulation, and Marc. The benefit of using this app is an easier use as it allows the user to create/import geometry, to mesh the surface, to evaluate the input data, and to achieve animation and meaning in principle with any mode shape and frequency.

The physical model of the entire brake disc was modeled using the SOLIDWORKS simulation tools. The primary purpose of this research is to study and evaluate the disc brake disc rotor. The entire SOLIDWORKS assembly is stored as an initial graphics exchange specification (IGES) file that can be imported into the FEA program. This section has to be translated to an IGES file to convert a CAD model to a FEM model, so that it can run for review. Step manager is created to define the simulation in terms of natural frequency in linear perturbation. The next step is to create a finite element mesh for the solid using the tetrahedral mesh generator and to select all the disc rotor structure (Fig. 1.4).

### ***1.2.3 Modal Analysis***

The modal analysis was carried out in order to achieve the performance results using the impact test. The dynamic analysis of the brake disc rotor was studied using modal



**Fig. 1.5** Experiment setup

testing. The software used to conduct the analysis to extract modal properties is the LMS testing lab software. The disc rotor that implemented this ideal effect would get the right impulse that causes a limited duration and determines the constant amplitude of the frequency domain. A specific hammer is used to conduct this test which cell load was put in its tip to obtain the force of impact. This technique is also effective in terms of transducers and measuring methods, it is least efficient in terms of time because it requires a lot of time to shift the accelerometer. This approach is widely used in cases where space constraints make it possible to repair accelerometers when there is not enough space to use the impact hammer. In this project, the accelerometer used has a reasonable accuracy capability, with a sensitivity of 50.81 mV/g, the round accelerometer will deliver a frequency from 0.5 to 5000 Hz at a certain time. The accelerometer, laptop, NI Acoustic and Vibration Data Recorder, effect hammer, and frame structure are the equipment that was used (Fig. 1.5).

The drawing of the brake rotor structure has been created in LMS Test Lab software using the drawing tool according to the coordinate of the actual engine mounting bracket that has been measured. After finishing the drawing, there is the need to label the node points at the drawing (Figs. 1.6 and 1.7).

### 1.3 Result and Discussion

The results of the studies that have been performed will be discussed in this section. All variations in the outcomes will be explained in relation to the problem, whether during the experiment or the simulation procedures.

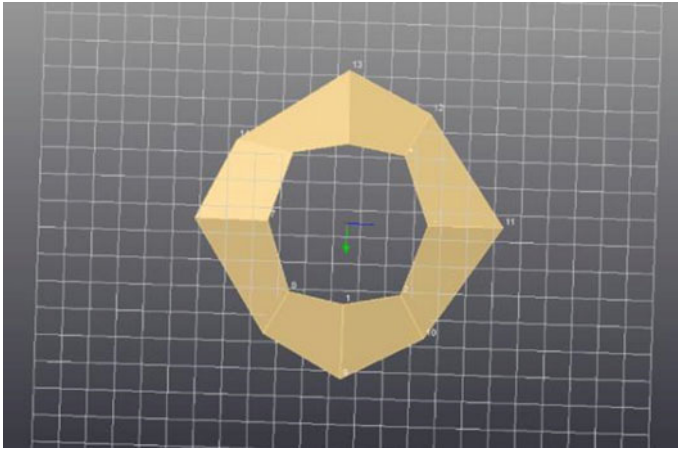


Fig. 1.6 The drawing of disc rotor in LMS software

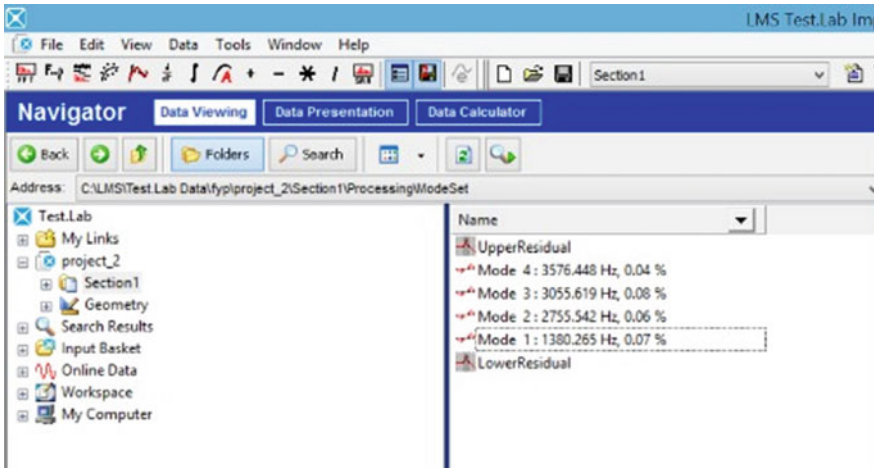


Fig. 1.7 Result obtained from EMA

### 1.3.1 Natural Frequency Using Mild Steel, Gray Cast Iron, and Carbon Ceramic

See Tables 1.1, 1.2 and 1.3.

**Table 1.1** Value of natural frequency for mild steel

Mode	Natural frequency (Hz)		
	Design 1	Design 2	Design 3
1	2039.0	1973.3	1827.8
2	2040.7	1974.3	1827.9
3	2648.8	2647.1	2640.9
4	4403.8	4398.1	4251.2
5	4408.9	4402.2	4521.6
6	4696.4	4546.7	4359.2
7	4698.3	4549.6	4379.2
8	4912.1	4734.9	4383.3

**Table 1.2** Value of natural frequency for gray cast iron

Mode	Natural frequency (Hz)		
	Design 1	Design 2	Design 3
1	1653.1	1599.8	1477.9
2	1654.5	1600.6	1478.6
3	2147.5	2146.1	2140.3
4	3570.3	3565.6	3434.9
5	3574.4	3569.0	3438.9
6	3807.5	3686.1	3526.8
7	3809.0	3688.5	3548.5
8	3982.3	3838.7	3550.4
9	4501.8	4412.8	4239.3
10	4513.1	4425.8	4252.6
11	4856.1	4714.5	4438.3
12	4860.8	4720.0	4447.4

### ***1.3.2 Comparison Natural Frequency Between All Three Design and Materials***

Table 1.4 compares design 1 simulation to mild steel, gray cast iron, and carbon ceramic. According to the results, carbon ceramic provides the best value of natural frequency. The carbon ceramic has an 8-mode frequency range of 1378.6–3321.2 Hz.

Table 1.5 compares it to mild steel, gray cast iron, and carbon ceramic for design 2 simulation. According to the results, carbon ceramic provides the best value of natural frequency. The carbon ceramic has an 8-mode frequency range of 1334.2–3201.4 Hz.

Table 1.6 compares design 3 simulation to mild steel, gray cast iron, and carbon ceramic. According to the results, carbon ceramic provides the best value of natural frequency.

**Table 1.3** Value of natural frequency for carbon ceramic

Mode	Natural frequency (Hz)		
	Design 1	Design 2	Design 3
1	1378.6	1334.2	1235.8
2	1379.8	1334.9	1235.9
3	1790.9	1789.8	1785.6
4	2977.5	2973.6	2874.4
5	2980.9	2976.4	2874.6
6	3175.3	3074.1	2947.4
7	3176.6	3076.1	2960.9
8	3321.2	3201.4	2963.6
9	3754.4	3680.2	3542.4
10	3763.8	3691.0	3552.3
11	4049.8	3931.8	3709.3
12	4053.8	3936.4	3720.0
13	4947.6	4939.2	4922.3
14	4956.1	4947.1	4927.8

**Table 1.4** Comparison natural frequency of design 1 with various material

Mode	Design: 1		
	Natural frequency (Hz)		
	Mild steel	Gray cast iron	Carbon ceramic
1	2039.0	1653.1	1378.6
2	2040.7	1654.5	1379.8
3	2648.8	2147.5	1790.9
4	4403.8	3570.3	2977.5
5	4408.9	3574.4	2980.9
6	4696.4	3807.5	3175.3
7	4698.3	3809.0	3176.6
8	4912.1	3982.3	3321.2

In comparison to all designs and materials, the value for natural frequency is smaller, and carbon ceramic with design 3 also delivers a smaller value than carbon ceramic with designs 1 and 2. The simulation results for all three designs and materials demonstrate that carbon ceramic has the lowest value when compared to other materials. Carbon ceramic has extraordinarily high and consistent coefficients of friction when compared with mild steel and gray cast iron, despite of surface moisture or temperature.

This implies that carbon ceramic brakes, on the other hand, counteract the so-called fading effect. Fading is the unwanted decline in braking impact that particularly because to longer braking and often successive braking movements, brakes

**Table 1.5** Comparison natural frequency of design 2 with various material

Mode	Design: 2		
	Natural frequency (Hz)		
	Mild steel	Gray cast iron	Carbon ceramic
1	1973.3	1599.8	1334.2
2	1974.3	1600.6	1334.9
3	2647.1	2146.1	1789.8
4	4398.1	3565.6	2973.6
5	4402.2	3569.0	2976.4
6	4546.7	3686.1	3074.1
7	4549.6	3688.5	3076.1
8	4734.9	3838.7	3201.4

**Table 1.6** Comparison natural frequency of design 3 with various material

Mode	Design: 3		
	Natural frequency (Hz)		
	Mild steel	Gray cast iron	Carbon ceramic
1	1827.8	1477.9	1235.8
2	1827.9	1478.6	1235.9
3	2640.9	2140.3	1785.6
4	4251.2	3434.9	2874.4
5	4521.6	3438.9	2874.6
6	4359.2	3526.8	2947.4
7	4379.2	3548.5	2960.9
8	4383.3	3550.4	2963.6

can get hot and the braking effect can be substantially diminished as a result of overheating. Carbon ceramic brake materials offer significant properties that help to minimize this so-called squeal. Carbon ceramic has a better toughness, lower density, extraordinarily high thermal shock resistance and breaking strength, and excellent conductivity. Indeed, design 3 will be the finest among the others in terms of design. It is because that the modification on design 3 is on the brake rotor which is the hole diameter. The hole is more compared to other designs while the hole also has a different diameter. It can be demonstrated that the value for 8 modes for design 3 with carbon ceramic is less than 3000 Hz.

**Fig. 1.8** Design summary of Taguchi method

## Design Summary

Taguchi Array L9(3<sup>3</sup>)

Factors: 3

Runs: 9

Columns of L9(3<sup>4</sup>) array: 1 2 3

### 1.3.3 Taguchi Method Using Minitab

The orthogonal arrays columns represent the factor while the rows of the orthogonal array represent the runs. A Taguchi design box appeared with 3-Level Design and Number of Factors = 3 (Fig. 1.8).

For the 3-Level Design, there are 3 different designs of brake disc had been selected and also there are 3 factors were chosen. The factors that were chosen are rotor diameter (mm), material density (kg/m<sup>3</sup>), and hole diameter (mm) (Tables 1.7; Figs. 1.9 and 1.10).

As a result from Table 1.8 and 1.9, the density of materials ranks first in terms of means. The density of material is likewise in the first rank, as is signal noise to ratios. Meanwhile, the rotor diameter and hole diameter came in the third spot, respectively. The phrase “smaller is better” was used to discover the optimal value of natural frequency. According to the graph, the optimal value for rotor diameter is 180 mm, density of material is 7840 kg/mm<sup>3</sup>, and hole diameter is 2.5 mm. Meanwhile, the optimal value for signal noise to ratios is 185 mm for rotor diameter, 2450 kg/mm<sup>3</sup> for material density, and 5.0 mm for hole diameter.

**Table 1.7** Taguchi orthogonal array design with complete data

Rotor diameter (mm)	Material (density kg/m <sup>3</sup> )	Hole diameter (mm)	Frequency (Hz)
175	2450	2.5	1378.6
175	7100	4	1523.4
175	7840	5	1572.3
180	2450	4	1290.7
180	7100	5	1505.6
180	7840	2.5	1953.7
185	2450	5	1235.8
185	7100	2.5	1354.9
185	7840	4	1736.6



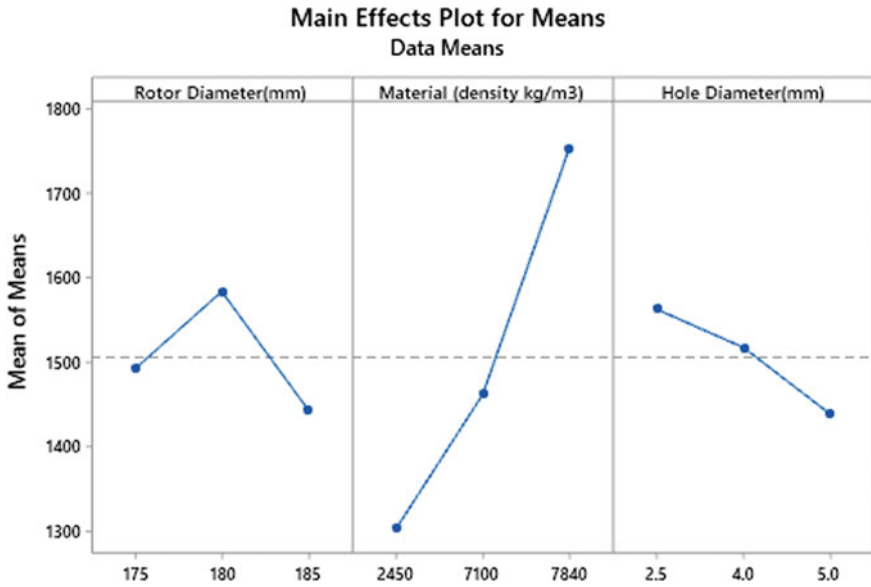
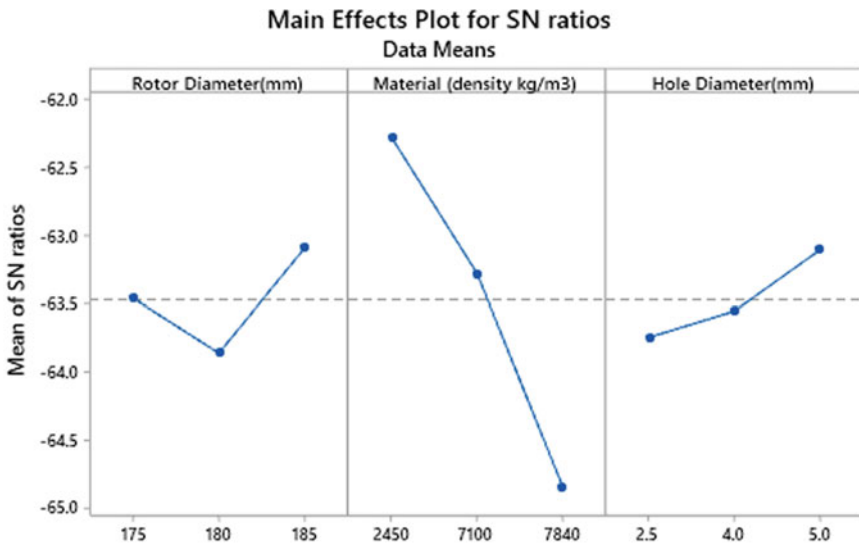


Fig. 1.9 Main effect plot for means



Signal-to-noise: Smaller is better

Fig. 1.10 Main effect plot for signal noise to ratios

**Table 1.8** Response table for means

Level	Rotor diameter (mm)	Material (density kg/m <sup>3</sup> )	Hole diameter (mm)
1	1419	1302	1562
2	1583	1461	1517
3	1442	1754	1438
Delta	141	453	125
Rank	2	1	3

**Table 1.9** Response for signal noise to ratios

Smaller is better			
Level	Rotor diameter (mm)	Material (density kg/m <sup>3</sup> )	Hole diameter(mm)
1	-63.46	-62.28	-63.75
2	-63.86	-63.28	-63.56
3	-63.09	-64.85	-63.11
Delta	0.77	2.57	0.64
Rank	2	1	3

### 1.4 Conclusion

The goal of this chapter is to verify the relation between the results of both FEA and EMA, as well as in the change of the brake disc. Furthermore, Minitab software was used to fulfill the objectives of Taguchi methods optimization. To maximize the optimal factor, the response and main effect for means and signal noise to ratios were determined. The simulation of 3D model of brake disc on three different designs was simulated by using FEA. It also analyzes the natural frequency on the brake disc from simulation in order to reduce the noisy squeal of the brake disc. It may be said that the lower the value of natural frequency, the less noise there will be during braking. By altering the design of the brake disc, it is able to attain a satisfactory result in terms of natural frequency in terms of vibration.

### References

1. Kinkaïd NM, O’ Reilly OM, Papadopoulos P (2003) Automotive disc brake squeal. *J Sound Vib* 267(1):105–166
2. Mills HR (1938) Brake squeal. The Institution of Automobile Engineers, Report No. 9162 B
3. Yuan Y (1995) A study of the effects of negative friction-speed slope on brake squeal. In: ASME design engineering technical conference, vol 3, Part A, DE-vol 84-1
4. Abendroth H, Wernitz B (2000) The integrated test concept dyno-vehicle; performance and noise. SAE technical paper 2000-01-2774

5. Nouby M, Mathivanan D, Srinivasan K (2009) A combined approach of complex eigenvalue analysis and design of experiments to study disc brake squeal. *Int J Eng Sci Technol* 1(1):254–271
6. Belhocine A, Gazaly NM (2016) Effect of Young's modulus on disc brake squeal using finite element analysis, *IIAV*

# Chapter 2

## Potential Experimental Analysis of Electrical Discharge Machine Process Parameters on Stainless Steel ANSI 304



**Afnan Nizarif Ahmad Zamzuri, Muhammad Al'Hapis Abdul Razak, Aznizam Abdullah, Ahmad Razlee Ab Kadir, Ahmad Majdi Abdul-Rani, Farooq I. Azam, and Haizum Aimi Zaharin**

**Abstract** In this research, the effect of electrical discharge machining (EDM) parameters such as pulse-on time (Ton), pulse-off time (Toff), voltage, (V), and current (I) on the material removal rate (MRR) in 304 stainless steel was studied. The experiments are carried out as per design of experiments approach using the L9 orthogonal array. From this study, it is found that different combinations of EDM process parameters are required to achieved higher MRR for 304. The contribution of each cutting parameters towards the MRR is also identified. The results from this study will be useful for manufacturing engineers to select appropriate EDM process parameters to machine stainless steel 304.

---

A. N. A. Zamzuri · M. A. A. Razak (✉) · A. Abdullah  
Manufacturing Section, Universiti Kuala Lumpur Malaysian Spanish Institute, Kulim Hi-Tech  
Park, 09000 Kulim, Kedah, Malaysia  
e-mail: [alhapis@unikl.edu.my](mailto:alhapis@unikl.edu.my)

A. N. A. Zamzuri  
e-mail: [afnan.zamzuri@s.unikl.edu.my](mailto:afnan.zamzuri@s.unikl.edu.my)

A. Abdullah  
e-mail: [aznizam@unikl.edu.my](mailto:aznizam@unikl.edu.my)

A. R. Ab Kadir  
Mechanical Section, Universiti Kuala Lumpur Malaysian Spanish Institute, Kulim Hi-Tech Park,  
09000 Kulim, Kedah, Malaysia  
e-mail: [ahmadrazlee@unikl.edu.my](mailto:ahmadrazlee@unikl.edu.my)

A. M. Abdul-Rani · F. I. Azam  
Mechanical Engineering Department, Universiti Teknologi PETRONAS, Bandar Seri Iskandar  
32610, Perak, Malaysia  
e-mail: [majdi@utp.edu.my](mailto:majdi@utp.edu.my)

F. I. Azam  
e-mail: [farooq.i\\_g03648@utp.edu.my](mailto:farooq.i_g03648@utp.edu.my)

H. A. Zaharin  
Faculty of Engineering and Built Environment, Universiti Kebangsaan Malaysia, Bangi, Selangor,  
Malaysia  
e-mail: [p100279@siswa.ukm.edu.my](mailto:p100279@siswa.ukm.edu.my)

**Keywords** Metal removal rate (MRR) · Taguchi method · 304 stainless steel

## 2.1 Introduction

Electric discharge machining (EDM) is an advanced manufacturing process. It is the removal of segments of electrically conductive metals by electrical pulses between two terminals (electrode and workpiece) within the dielectric. The electrical discharge melts and vapourizes workpiece. The main goals of EDM manufacturers and users are to achieve a machining stability and high productivity. With the increasing demands of higher surface finish and machining of complex shape geometries, conventional machining process are now being replaced by non-traditional machining processes. The major advantage of the process lies in its capability to easily machine any electrically conductive material regardless of its mechanical properties.

EDM is carried out by means of electric sparks that jump between two electrodes subjected to a voltage and submerged in a dielectric fluid. Thus, the voltage applied to them must be enough to create an electric field of higher intensity than the dielectric strength of the fluid used in the process.

In this process the material is removed from the workpiece due to erosion caused by rapidly recurring electrical spark discharge between the workpiece and the tool electrode. There is a small gap between the tool and the workpiece. The workpiece and the tool are submerged in dielectric fluid. The commonly used dielectric fluids are EDM oil, deionized water, and kerosene.

## 2.2 Literature

This section describes the review of the literature relevant to this project. Data collections are used as a reference by researchers to gather information about the study that has been carried out. The literature review analyses the information gathered by journal paper publications from other researchers and the information collected from the internet. This literature review can help to address the issues that have occurred during the study prior to the start of the creation of this project.

### 2.2.1 *Electrical Discharge Machining*

By way of electrical discharge operations, EDM is used to achieve the appropriate form. The phase of substance removal has ended due to the current discharge between two electrodes. Dielectric fluid and electrical voltage play a very significant role in this process. As we note, non-conventional machining methods include electrical discharge machining operations. It is mainly used for hard metal machining

operations and for complicated operations, which with obsolete methods are almost impossible to do [1].

### **2.2.2 Die-Sinking**

Two Russian scientists developed the die-sinking mechanism. In 1943, Lazarenko discovered means of avoiding tungsten electrical contact erosion due to electrical spark. They were unsuccessful in this task many times, but they discovered that if the electrodes were submerged in a dielectric solvent, the corrosion was more precisely regulated. This prompted them to create an EDM system that was used to deal with hard-to-machine materials like tungsten.

Two electrodes are mounted on the parts of the system, which are the work bench and the tool holder in this process. The electrodes both have to be electrically conductive. After that, with the assistance of the compressor, all electrodes are immersed in an insulating liquid dielectric. The EDM oil/kerosene/transformer oil is the dielectric. To get the appropriate shape and scale, set the machining parameters on the CNC controller for machining on the workpiece [1].

### **2.2.3 Wire EDM Process**

The wire-cut sort of machine was established during the 1960s to make instruments (kicks the bucket) from solidified steel. In this cycle the apparatus anode is a type of wire. To dodge the disintegration of material from the wire making it break, the wire is twisted between two spools with the goal that the dynamic portion of the wire is continually evolving.

The wire-cut EDM measure is additionally called the electric release wire cutting cycle. It is utilized for the delivering a few-dimensional complex shapes utilizing an electro warm instrument for disintegrating the material from a slim single abandoned by controlling a metal wire encompassed by deionized water which is utilized to the lead power [1].

### **2.2.4 Dielectric Fluid**

Dielectric fluid is used as a coolant, flushing medium, and a conductor of the catalyst as well. This plays a very significant role in the EDM process. The requirements are:

1. To act as insulation between tools and the workpiece, the dielectric should have compulsory and continuous dielectric strength before the breakdown voltage is reached.

2. Once the spark ejection has happened, it must de-ionize rapidly.
3. To have an efficient cooling mechanism and clear the swerve particles from the machining gap, it must require limited viscosity and a friendly moistening capacity.
4. During the spark, it should be flushed out of the element produced from the void. This is the dielectric fluid's most vital function. Insufficient flushing can cause arcing to reduce the electrode's life and increase the machining time.
5. Chemically, it should be neutral in order not to attack the instrument, function and the movable table or tank.
6. Its flash point should be high enough that no fire risks are present.
7. Any harmful vapours should not be released.
8. These properties should be preserved by temperature variations, degradation through operating residuals and decomposition materials.

It should be fundamentally economical and readily usable [1].

### ***2.2.5 EDM Machine Components***

The first part of EDM is the tool feeder that should be servo-driven in order to retain a driven distance. Regulated differences are an critical factor in the incidence of active discharges between the two electrodes. The second part is the power supply, which provides voltage and current in a particular ON/Off time in the form of pulses. The circulation unit is the third component; this unit extracts the dielectric from the debris, then flushes it back to the void. However, due to the variations in the method of spark erosion machining, the system part could be different [2].

### ***2.2.6 Material Removal Rate***

The MRR is the quantity of material extracted per unit of time, specifically aimed at efficiency improvement. This needs to be maximized in roughing operations and the processing of large batches. However, when it comes to completing operations, it is a consideration to be put on hold, forcing roughness and accuracy to the forefront. Both are often used for low roughness, usually low cutting speeds and feed per tooth, as MRR is usually very low for finishing.

### ***2.2.7 Surface Quality Analysis***

The surface is synonymous with different surface properties, such as the profile of microhardness, surface roughness, geometric residual tension, crack density, white

layer, and crack density. In order to meet the growing anxiety of complicated part efficiency, longevity, and reliability, the surface morphology of a machined surface is increasingly becoming more significant. It plays an important role in the inspection of product geometry, roughness, and dimensional precision in the industry and manufacturing industries. The measuring of the surface integrity factor is a time-consuming procedure using precious instruments such as microhardness testers, XRD, SEM, and roughness testers for the surface. A major consideration used to determine EDMed surface consistency is the surface roughness. In order to determine the effect of EDM parameters to account for SR in the specimen, the surface profile on the machined samples was calculated using various equipment, namely, surface roughness tester, atomic force microscopy (AFM), 3D profiler, etc. [3].

### 2.2.8 Taguchi Method

The Taguchi approach involves reducing the variance of a procedure through rigorous laboratory design. In order to coordinate the criteria influencing the method and the thresholds at which they should be varied, the experimental architecture suggested by Taguchi requires the use of orthogonal arrays; it enables the gathering of the required data to decide which variables impact product quality most with a minimal amount of experimentation, saving time and energy. The expression ‘signal’ in this system represents the desired value (mean) for the output characteristic and the word ‘noise’ represents the unfavourable value for the output characteristic, i.e., standard deviation (S.D). The S/N ratio is, thus, the ratio between the mean and the S.D. Determined by the shape of the features, various levels of S/N ratios are used for the Taguchi method—the lower-the-better, the higher-the-better, and the nominal-the-better. The main steps for designing experiments using the Taguchi method are as follows [4]:

- Description and evaluation of quality attributes and method parameters.
- Identification of the number of parameter levels and potential interactions with the parameters of the operation.
- Assignment of process parameters to the orthogonal array that is chosen.
- Conduction of orthogonal array-based experiments.
- Calculation of S/N ratio.
- Analyze the experimental results using the S/N ratio and ANOVA.
- Selection of the optimal levels of process parameters.
- Verifying the optimum parameters of the mechanism via the validation experiment.

The main step in the Taguchi system to achieve high efficiency without raising costs is the optimization of process parameters. The Taguchi system, however, was initially developed to optimize single output functions. The S/N ratio is the ratio of signal to noise according to the Taguchi equation, where the signal reflects the desired value and the unwanted value is expressed by noise. The Ra and Kf response is used to use the equation to measure the signal-to-noise ratio (S/N). Now, the experimental



effects are translated into a ratio of signal-to-noise (S/N). Since the minimum surface roughness and kerf width is required, the lower-the-better characteristic is used for calculating the S/N ratio. The best atmosphere would be the one that will reach the lowest S/N ratio [5].

## **2.3 Methodology**

The research effectively the methods used to complete and perform well this project. This experimental project was formulated prior to the implementation of the work. The method is used to achieve the objective of the project that will accomplish a perfect result. It consists of an L-27 orthogonal array using the Taguchi design, selection of workpiece, experimental setup, tool design, and calculation of material removal rate and surface roughness. A Gantt chart was developed which consists of activity duration estimation and the development of the project schedule.

### **2.3.1 Research Structure**

The problem needs to be understood so it can be solved. Next is about the objective of this research and how the goal can be achieved, and the scope of the study is the initial planning process. It typically involves drawing up a list of everything in this research in order to create the framework of the research.

### **2.3.2 Experimental Setup**

Using the electric discharge machine unit, the tests were carried out, the electrode polarity was set as positive while that of the workpiece was negative. EDM oil was the dielectric fluid that was used. The EDM consists of the following parts:

- i. Dielectric reservoir, pump, and circulation system.
- ii. Power generator and control unit.
- iii. Working tank with work holding device.
- iv. X–Y working table.
- v. The tool holder.
- vi. The servo system for feeding the tool.

### ***2.3.3 Selection of the Workpiece***

In every single mechanical application, AISI 304 stainless steel is one of the most widely used materials and records about 50% of the production and utilization of hardened steel worldwide. It has become the most favoured commodity over others as a result of its tasteful outlook in engineering, prevalent physical and mechanical properties, resistance to corrosion and plastic substances, weldability. Numerous standards and non-customary AISI 304 treated steel machining methods are available.

### ***2.3.4 Tool Design***

A variety of metals such as copper, metal, aluminium amalgams, silver blends, and so on will be the instrument material used in electro discharge machining. Copper is the content used in this experiment. The cathode of the instrument is a circular form with a 21 mm measurement.

### ***2.3.5 Mechanism and Measurement of the MRR***

MRR is the speed at which the workpiece is separated from the material. During the machining process, electric sparks are formed between the instrument and hence the workpiece. Each spark creates a tiny hole and hence induces material erosion. The MRR is defined by the ratio of the difference in weight between the material density and the machining time of the workpiece before and after machining:

$$\text{MRR} = \frac{W_i - W_f}{t(p)}$$

which is  $W_i$  = initial weight before the machining process

$W_f$  = final weight after the machining process

$t$  = machining time

$p$  is the density of AISI 304 SS.

### ***2.3.6 Mechanism and Evaluation of Surface Roughness***

Surface roughness is the indicator of surface which takes another expression here. It is classified in microns. The surface is rough if the value is high, and the surface is smooth if the value is low. The roughness values are denoted by Ra. For the final value, the arithmetic median of three readings is taken.

### 2.3.7 Design of Experiments Analysis

In order to increase the efficiency of producing products referred to as Taguchi techniques, Genichi Taguchi developed several statistical methods. This architecture offers a possible and practical way for multiple goods to be built that can work continuously over a good variety of conditions. Both static and dynamic response experiments are given by Minitab. In an orthogonal array, the arrangement of tests is used to find the most powerful combination of input variables. The input parameters considered in this experiment are current, Ton, and  $\text{Đ}$ . The design becomes a 3-level 3 factorial Taguchi design because three variables are picked. For the tests to be performed, the L27 orthogonal array was selected.

## 2.4 Conclusions

The use of stainless steel 304 to optimize the EDM multiple performance characteristics has been successfully reported in this paper. Optimization of multiple performance characteristics was simplified through this approach. The experimental result for the optimal setting shows that there is considerable improvement in the process. It is shown that the performance characteristics of the EDM process namely material removal rate, electrode wear ratio, and surface roughness are improved together by using this method.

## References

1. Jaiswal VK, Paul A, Yadav V, Singh V (2018) Literature review on electrical discharge machining (EDM). *Int J Sci Res Dev* 6(5):239–241
2. Ubaid AM, Dweiri FT, Aghdeab SH, Al-Juboori LA (2018) Optimization of electro discharge machining process parameters with fuzzy logic for stainless steel 304 (ASTM A240). *J Manuf Sci Eng Trans ASME* 140(1). <https://doi.org/10.1115/1.4038139>
3. Nahak B, Gupta A (2019) A review on optimization of machining performances and recent developments in electro discharge machining. *Manuf Rev* 6. <https://doi.org/10.1051/mfreview/2018015>.
4. Chandramouli S, Eswaraiah K (2017) Optimization of EDM process parameters in machining of 17-4 PH steel using Taguchi method. *Mater Today Proc* 4(2):2040–2047. <https://doi.org/10.1016/j.matpr.2017.02.049>
5. Durairaj M, Sudharsun D, Swamynathan N (2013) Analysis of process parameters in wire EDM with stainless steel using single objective Taguchi method and multi objective grey relational grade. *Procedia Eng* 64:868–877. <https://doi.org/10.1016/j.proeng.2013.09.163>

# Chapter 3

## Embedded System Using a PIC Microcontroller for Series Motor Four Quadrants Drive DC Chopper Controllers for the Application in Electrical Vehicles



**Saharul Arof, Norramlee Mohamed Noor, Philip Mawby, Hamzah Arof,  
and Emilia Noorsal**

**Abstract** The key success of an electric vehicle (EV) traction converter/inverter lies in the efficiency of its controller. In some complex systems such as an electric vehicle inverter/converter, the controller requires more than a single controller working together. The overall efficiency of such a controller much depends on its architecture and control strategy. This includes controller data distribution and communication between controllers. This paper describes a proposed four quadrants DC chopper (FQDC) controller architecture and a control strategy for controlling several modes of operation for EV applications. MATLAB/Simulink is used to establish the system under study and the results indicate that the proposed technique can be used.

**Keywords** DC drive · EV and HEV · Series motor · Four-quadrant chopper microcontroller · Embedded system

---

S. Arof (✉) · N. M. Noor

Universiti Kuala Lumpur, Malaysian Spanish Institute, Kulim Hi-Tech Park, 09000 Kulim, Kedah, Malaysia  
e-mail: [saharul@unikl.edu.my](mailto:saharul@unikl.edu.my)

N. M. Noor

e-mail: [noramlee@unikl.edu.my](mailto:noramlee@unikl.edu.my)

S. Arof · P. Mawby

University of Warwick School of Engineering, Coventry CV47AL, UK  
e-mail: [p.a.mawby@warwick.ac.uk](mailto:p.a.mawby@warwick.ac.uk)

H. Arof

Engineering Department, Universiti Malaya, Jalan Universiti, 50603 Kuala Lumpur, Malaysia  
e-mail: [ahamzah@um.edu.my](mailto:ahamzah@um.edu.my)

E. Noorsal

School of Electrical Engineering, College of Engineering, Universiti Teknologi MARA, Cawangan Pulau Pinang, Kampus Permatang Pauh, 13500 Pulau Pinang, Malaysia  
e-mail: [emilia.noorsal@uitm.edu.my](mailto:emilia.noorsal@uitm.edu.my)

### 3.1 Introduction

Using electric vehicles (EV) is one of the solutions to reduce global hydrocarbon emission. In future, the electric motor propulsion system (electric vehicle) will replace the internal combustion system (mechanical combustion engine). This is not only because of zero emission but it also has higher efficiency. Unfortunately, electric vehicles are not yet affordable for many people. Thus, there is a need for an efficient, compact drive system for EV and HEV that can reduce their cost and thus making them economical and affordable.

### 3.2 Literature Review

Oak Ridge National Laboratory (ORNL) [1], United States. In 2009, had succeeded in designing a DC brushed motor with high power output (55 kW), high efficiency (92%) that can operate in low operating voltages (13 V). This has started the interest to embark on research in DC Drive EC. Attempts to improve conventional H-Bridge chopper such as shown in Fig. 3.1, by increasing more operation or allowing motor reverse action have been continuously carried out such as driving, field weakening, parallel mode regenerative braking, and resistive braking [2–6]. Several other studies related to DC drive EV lead to research on EC battery charger [7], inclusive charging control algorithm [8] and state of charge estimator [9] and different types of DC drive motor that can be used for motor traction for DC EV such as separately excited [10] has been done. Detailed investigation on the chopper operation modes leads to the establishment of a simulation model to test the chopper operations for the application of Electric Car and Light Rail Transit (LRT) have been done [11]. This simulation model leads to further detailed investigation on Electric Car design requirements [12], for each of the chopper operations and on the specific pattern of motor voltage, current, torque, speed, of the series motor and FQDC running for DC drive EC application have been continuously carried out [13]. This includes details of circuit topology, mathematical modeling, and electrical circuits control strategies in several modes of operation. For DC series motor traction of EC application, the speed and torque control for the series motor in an attempt to reduce jerk and tire slip has been successfully done and implemented with direct current control technique [14]. For power regeneration, the FQDC offers generator mode with several techniques of starting the regenerated power and voltage control is studied and discussed in [15]. In order for the FQDC to be applied in the real world it needs controllers running control algorithms in the embedded system. The controller and its control algorithm are studied and tested using Processor in the Loop (PIL) technique [16]. To improve the new FQDC performance optimization tools such as Artificial Intelligence (AI) are introduced to control all of the chopper operations of the proposed FQDC chopper [17]. Among the three AI controllers ANFIS shows the best performance followed by neural network, self-tuning Fuzzy Logic Controller [18], and expert system [19]. Attempts of cruising test

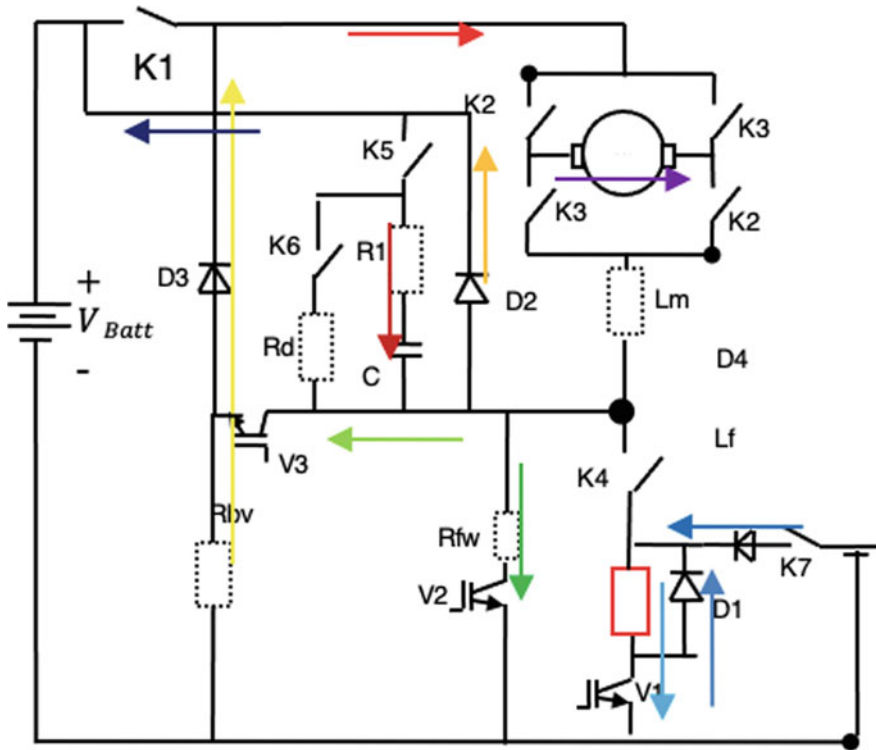


Fig. 3.1 Novel four quadrants DC chopper

with specific requirement of remaining distance traverse and battery State of charge using Fuzzy Logic [20] controller shows significance performance in controlling the EV operation.

Study on Neural Network controller to uncover proper method of tuning has been carried out such as using single controller with binary output [21]. On each specific FQDC chopper operation mode the performance can be further improved using AI optimization tool such as Genetics Algorithm [22] and gradient descend [23], to set up specific Look up table for field current. Pole placement [24] method used to tune Close loop PID controller to improve controller performance while Fuzzy Logic Controller is used to control motor current [25] is applied to improve the control performance and system stability. For fault diagnose and online system online tuning and optimization a Numerical representation using Taylor series [26] is studied and tried for driving mode. The cascade PID with ascend descend algorithm and after improvisation made associated to steering [27], vehicle movement control [28], and electrohydraulic brake control [29] be used for autonomous EV for automatic reverse parking.

To further investigate on this new series motor four quadrants DC chopper, the chopper operation controllers which are eventually running in an embedded system such as the PIC microcontroller are studied in this paper.

### 3.3 Methodology

#### 3.3.1 Embedded System of FQDC Controllers

The novel four quadrants chopper as shown in Fig. 3.1 has seven operations which are the driving, reverse, field weakening, parallel mode, regenerative braking, resistive braking, and generator. The FQDC controller requires controllers such as the one shown in Fig. 3.2. The controller must have electronics circuitry incorporated for the clock, voltage supply, analog to digital to read analog signals output generation such as PWM and have UART or SPI for data communication. The controllers which have a control algorithm running in it are purposely for control, selection, and passing data for communication via SPI and serial.

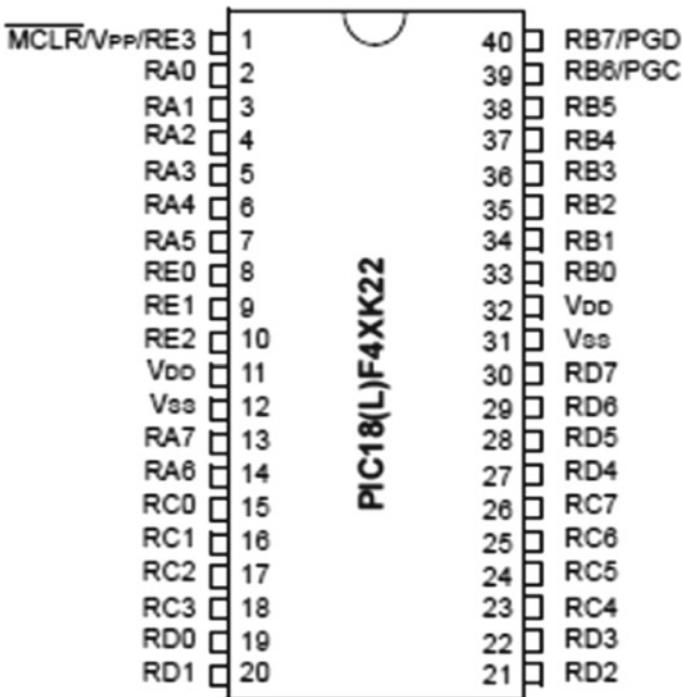


Fig. 3.2 PIC microcontroller

As the system has many operations, the chopper four quadrants controller contains four sub-controllers (PIC microcontrollers) which are for the data distribution, chopper operation, subsequent and delay, and finally IGBT firing controllers. The overall four quadrants chopper controllers are shown in Fig. 3.3.

The communication is needed between the controllers and in Fig. 3.4 a block diagram of flow of data communication is described.

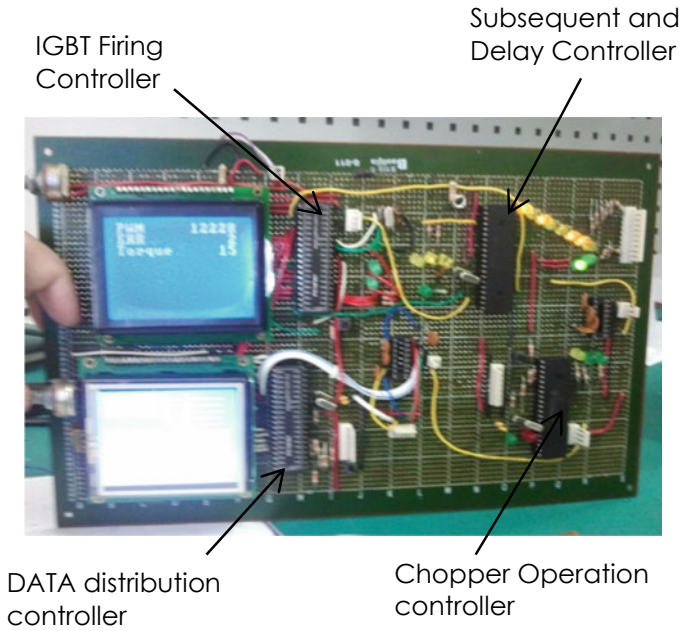
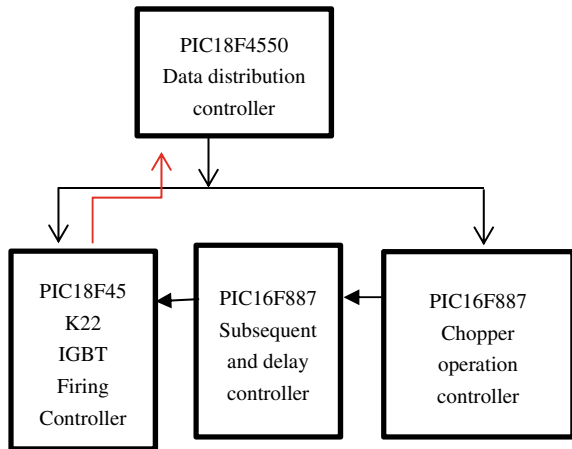


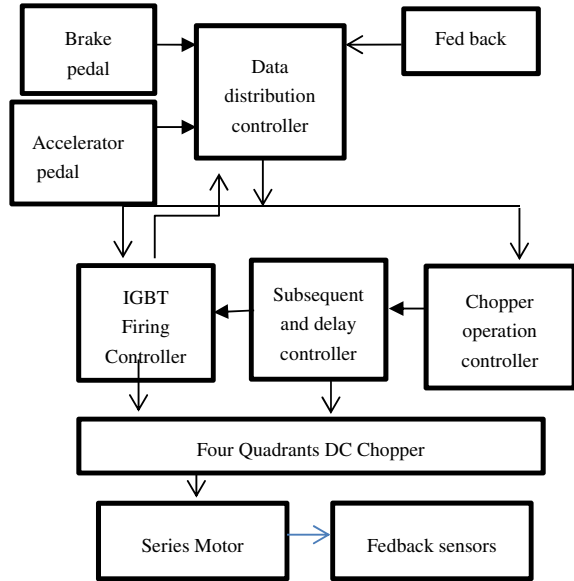
Fig. 3.3 Four quadrants chopper controllers

Fig. 3.4 Flow of data communication





**Fig. 3.5** Block diagram of data type for each controller



The details of data and what type of data being passed, i.e., whether it is analogue or digital or communication data for each controller, are as shown in the block diagram in Fig. 3.5.

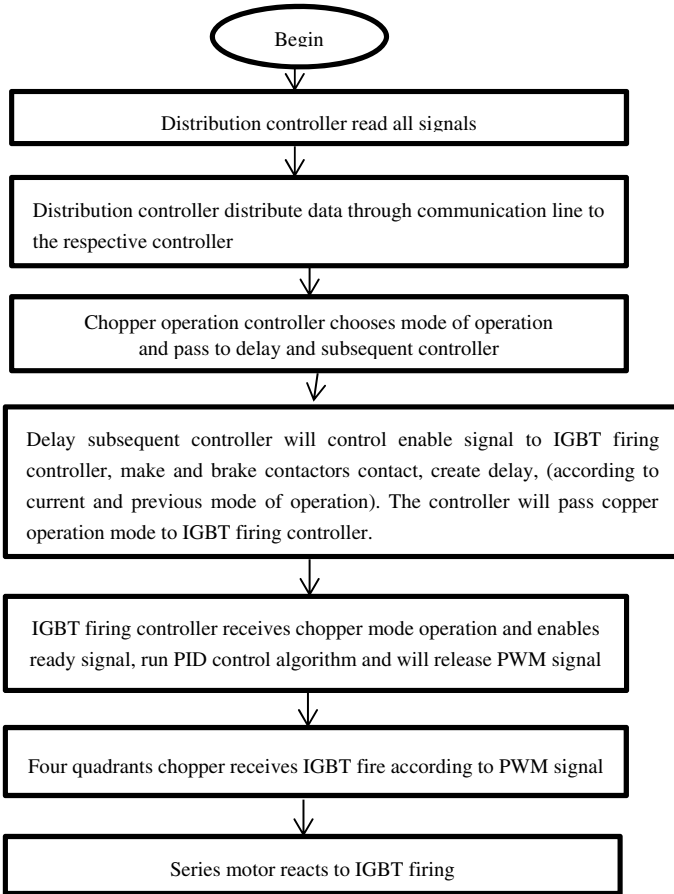
The overall operation of the four quadrants DC chopper controller is described as in the block diagram of Fig. 3.6.

### 3.3.2 Detailed Operation Function on Each of the Controllers

- i. **Data Distribution Controller.** The function of this controller is to read all the signals input and output and to segregate the data to respective controllers as shown in Fig. 3.7. A communication is established using serial communication and SPI. This controller also enables communication from the controller so that data can be read to MATLAB/LabVIEW software for data collection and processing.

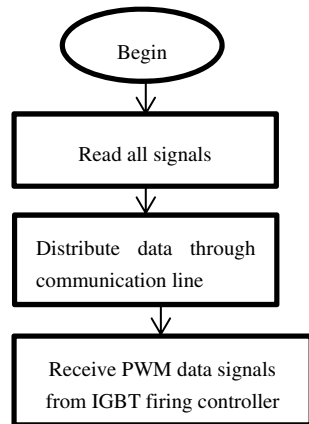
The controller will receive signals such as accelerator pedal, brake pedal, field current, armature current, armature voltage, battery voltage, motor speed, and vehicle speed.

- ii. **Chopper operation controller.** The chopper operation controller is a controller to choose what operation should be running at any particular moment when receiving data from the data distribution controller and output data of the chopper operation to subsequent and delay the controller. In order for this

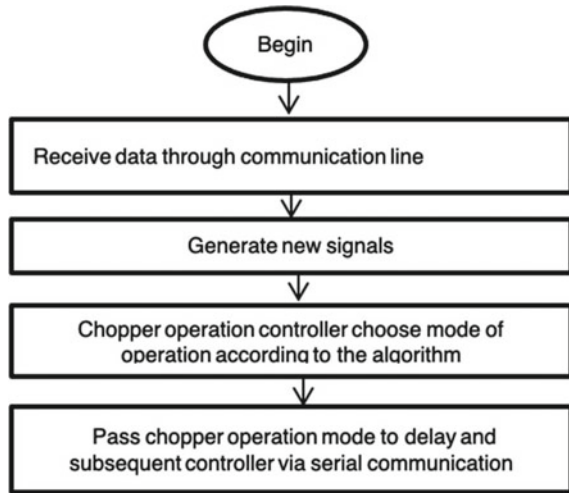


**Fig. 3.6** Overall chopper operation controller

**Fig. 3.7** Data distribution controller operation



**Fig. 3.8** Overall chopper controller operation



controller to choose the right operation, signals data should be further processed as described in Fig. 3.8.

The controller will receive several signals such as from the accelerator pedal, brake pedal, field current, armature current, armature voltage, battery voltage, and motor speed. From the received signals the controller will generate other signals such as the rate of speed. Several methods can be used to select the most appropriate chopper operation such as expert system (if than rules), fuzzy logic, neural network, self tuning fuzzy logic, and fuzzy neuro [9]. Table 3.1 summarizes the signals received and processed by the chopper operation controller. Table 3.2 contains general information on how the signals are processed to determine what chopper operation should be selected to drive the FQDC.

- iii. **Subsequent and Delay Controller.** The subsequent and delay controller has four functions. The first function is to make and break the contact of contactors according to the chopper operation as shown in Table 3.3.

**Table 3.1** Input signals table

	Zero	Low	Medium	High
Accelerator pedal	0–1 V	1–2.5 V	2.5–3.5 V	3.5–5.0 V
Brake pedal	0–1 V	1–2.5 V	2.5–3.5 V	3.5–5.0 V
Motor speed	0–50 rpm	50–500 rpm	500–1050 rpm	1050–2500 rpm
Error	0–50	50–250	250–500	500–1023
Armature voltage	0–1 V	1–2.5 V	2.5–3.5 V	3.5–5.0 V
Rate of speed	0–10	10–20	20–30	30–40

**Table 3.2** Chopper operation selection table

	Acc pedal	Brake signal	speed	Rate of speed	Armature voltage	Error
Driving	Bigger than zero	Zero	Zero to medium	NIL	NIL	NIL
Field weakening	Medium to high	Zero	Medium to high	NIL	NIL	NIL
Regen brake	NIL	Medium to high	Medium to high	Zero to negative	NIL	NIL
Rheostat brake	NIL	Low to high	Zero to High	Zero to negative	NIL	NIL
Generator	Low to medium	Zero	Medium to high	Zero to negative	NIL	NIL
Parallel	Medium to high	Zero	Medium to high	negative	NIL	Positive

**Table 3.3** Contactors operation table

	K1	K2	K3	K4	K5	K6	K7
Driving	1	1	0	1	0	1	0
Field weakening	1	1	0	1	0	1	0
Regen brake	0	0	1	1	1	0	0
Rheostat brake	0	0	1	1	1	0	0
Generator	0	0	1	0	1	0	1
Parallel	1	1	0	0	0	0	1
Reverse	1	0	1	1	0	1	0

This controller has the important function to allow the contactor to change the contactor operation is carried out in a zero voltage, zero current operation. It delays the transition of some chopper operations for example from driving to braking. The second function is to disallow immediate transition without delay from one chopper operation to the other chopper operation for example from driving to reverse. This is described in Table 3.4.

The third function of this controller is to send a ready signal to the IGBT firing controller. This signal is important since without the signal, the IGBT controller will not start functioning. The fourth and the last function of this controller is to pass the mode of operation to IGBT firing controller.

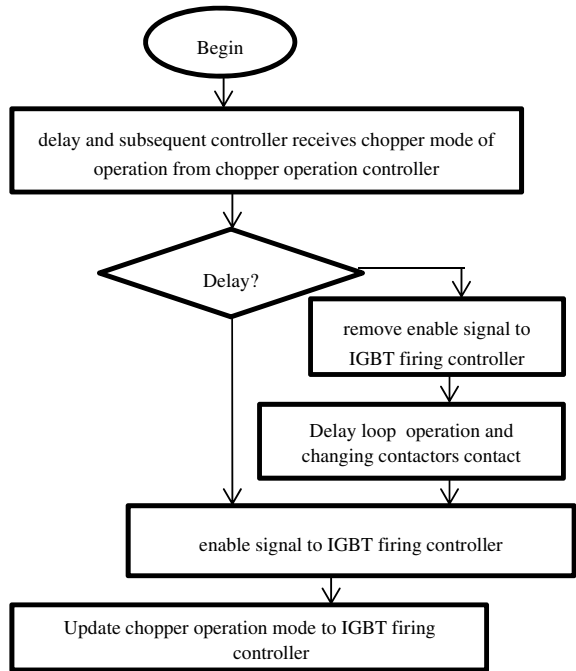
The delay in loop accessed is determined by comparing the current mode of operation with the previous mode. If the same operation happened no delay accessed is allowed. If different mode is chosen the delay mode accessed is granted. This is also described in the block diagram of Fig. 3.9.

- iv. **IGBT Firing Controller.** The IGBT firing controller receives three types of data signals which is data from the data distribution controller, and two types of

**Table 3.4** Delay mode operation table

Current mode	Previous mode	Delay mode
Driving	Driving	No
Field weakening	Driving	No
Regen brake	Field weakening	Yes
Rheostat brake	Regen brake	No
Generator	Field weakening	Yes
Parallel	Field weakening	Yes
Reverse	Driving	Yes

**Fig. 3.9** Delay subsequent controller block diagram operation



data from the subsequent and delay controller. First, it receives the input–output signal data, such as speed, field current, and armature voltages, from the data distribution controller. Second, it receives the chopper operation data which is from the delay and subsequent controller, and the data is being passed through the SPI communication. The third data is to enable the digital signal bit which is through the I/O pin from the subsequent and delay controller. There are two output signals of this controller where the first output is the IGBTs firing PWM to the four quadrants chopper. This PWM output is actually coming from a digital PID output control algorithm. The second output is all data related to the digital PID such as error and PWM output. When the controller has already

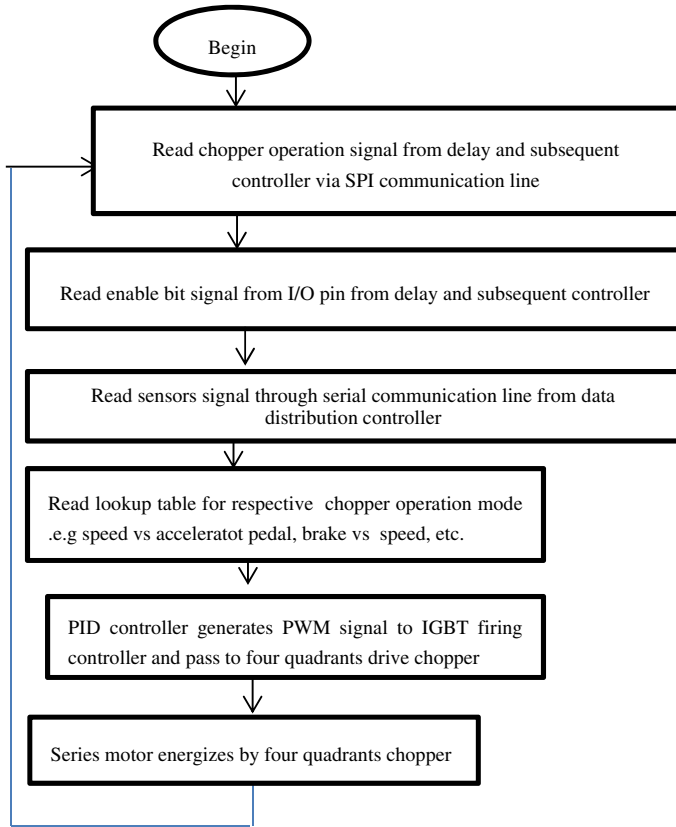


Fig. 3.10 IGBT firing controller operation block diagram

received these three input data signals, and according to the mode of operation that has been selected, the controller will first read the respective look up table and find the reference input (Fig. 3.10).

### 3.3.3 Simulation Software and Experimental Setup for Simulation and Experiment

The MATLAB/Simulink model is established and used for simulating and studying the chopper and controller behavior as shown in Fig. 3.11.

The experimental setup is shown in Fig. 3.12 where a 0.65 kW series motor is used to be driven using the proposed FQDC controller to perform the required six chopper operation.

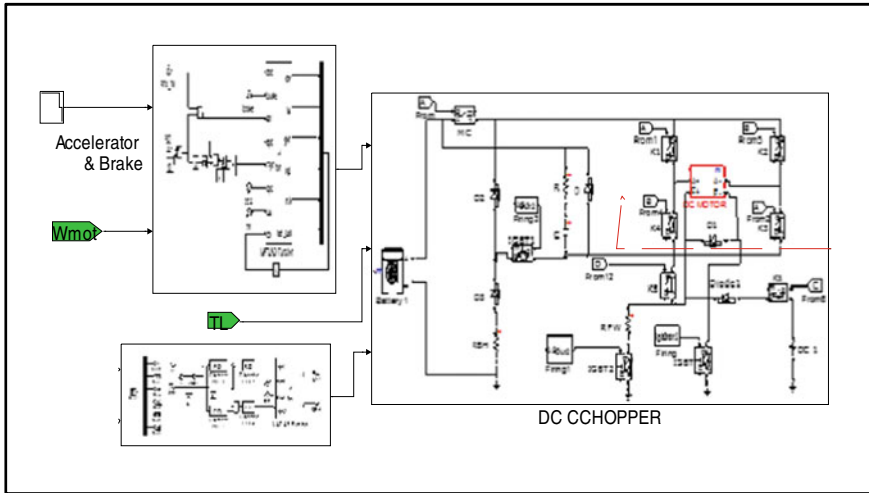


Fig. 3.11 MATLAB/Simulink model

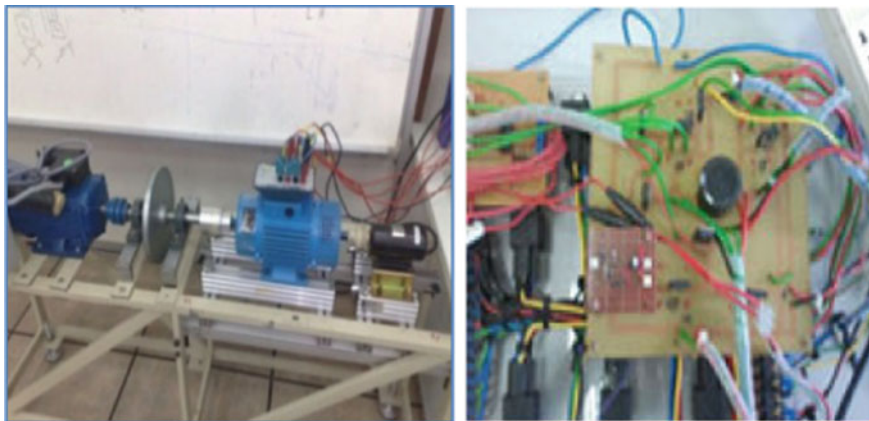


Fig. 3.12 Experimental setup

### 3.4 Results

The experimental and simulation results are plotted together and shown in Fig. 3.13. The speed of the motor, field, and armature current is plotted.

Six modes were tested and they are the driving, parallel, generator, field weakening, regenerative, and resistive braking modes and were tested one after another in continuous. First, in the driving mode the motor runs until it reaches the base speed. Then the motor is loaded to represent climbing a steep hill, the speed of the motor drops due to this load. When the parallel mode is activated the speed regains its speed

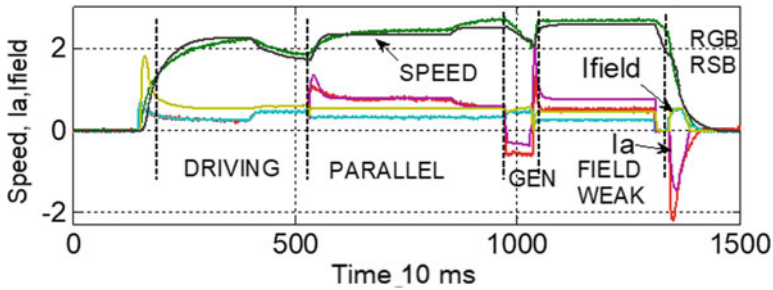


Fig. 3.13 Simulation and experiment of FQDC chopper

and when the load is removed the speed increases further. In the generator mode the speed decreases slightly due to generator torque and in the field weakening mode, the motor speed further increases due to the increase in armature current. During the regenerative and resistive mode the motor speed decreases at a faster rate due to the counter torque action.

### 3.5 Conclusion

The embedded system controller and FQDC are capable to perform as expected the operations to drive the operation to drive series motor and have a high potential to be utilized in EV. This is due to its simple design, low cost, and excellent controllability.

### References

1. Oak Ridge National Laboratory (2009) Advanced brush technology for DC motors. <http://peemrc.ornl.gov/projects/emdc3.jpg>
2. Arof S, Jalil JA, Yaakop NM, Mawby PA, Arof H (2014) Series motor four quadrants drive Dc chopper. Part1: Overall. In: IEEE International conference on power electronics
3. Arof S, Noorsal E, Mawby PA, Arof H (2020) Series motor four quadrants drive DC chopper for DC drive electric vehicle. Part 7: Resistive braking. In: International scientific forum (ISF2019), Melaka, Malaysia. eISBN: 978-967-10842-1-2
4. Arof S, Noorsal E, Mawby PA, Arof H (2020) Series motor four quadrants drive DC chopper for DC drive electric vehicle. Part 6: Regenerative braking. In: International scientific forum (ISF2019), Melaka, Malaysia. eISBN: 978-967-10842-1-2
5. Arof S, Diyanah NHN, Mawby PA, Arof H, Noorsal E (2021) Series motor four quadrants drive DC chopper. Part 3: Field weakening mode. IOP Conf Ser Mater Sci Eng 1127(1):012028. <https://doi.org/10.1088/1757-899X/1127/1/012028>
6. Arof S, Diyanah NHN, Mawby PA, Arof H, Noorsal E (2021) New series motor four quadrants drive DC chopper for economical EV, Part 5: Parallel mode. IOP Conf Ser Mater Sci Eng 1127(1):012025. <https://doi.org/10.1088/1757-899X/1127/1/012025>
7. Arof S, Diyanah NHN, Mawby P, Arof H, Yaakop NM (2019) Low harmonics plug-in home charging electric vehicle battery charger utilizing multi-level rectifier, zero crossing and buck



- chopper: Part 1: General overview. In: Progress in engineering technology, pp 103–108. [https://doi.org/10.1007/978-3-030-28505-0\\_9](https://doi.org/10.1007/978-3-030-28505-0_9)
8. Arof S, Ahmad MR, Yaakop NM, Mawby P, Arof H, Noorsal E, Bakar AA, Ali YM (2021) Low harmonics plug-in home charging electric vehicle battery charger utilizing multilevel rectifier, zero crossing, and buck chopper: state of charge estimator using current integration algorithm for embedded system. In: Progress in engineering technology III. [https://doi.org/10.1007/978-3-030-67750-3\\_19](https://doi.org/10.1007/978-3-030-67750-3_19)
  9. Arof S, Sazali MS, Noor NM, Nur Amirah J, Mawby P, Noorsal E, Bakar AA, Ali YM (2021) Low harmonics plug-in home charging electric vehicle battery charger utilizing multi-level rectifier, zero crossing, and buck chopper: BMS battery charging control algorithm. In: Progress in engineering technology III. [https://doi.org/10.1007/978-3-030-67750-3\\_18](https://doi.org/10.1007/978-3-030-67750-3_18)
  10. Arof S, Diyanah NHN, Noor NM, Jalil JA, Mawby PA, Arof H (2019) A new four quadrants drive chopper for separately excited DC motor in low cost electric vehicle. In: Progress in engineering, pp 119–138. [https://doi.org/10.1007/978-3-030-28505-0\\_10](https://doi.org/10.1007/978-3-030-28505-0_10)
  11. Arof S, Hassan H, Rosyidi M, Mawby PA, Arof H (2017) Implementation of series motor four quadrants Drive dc chopper for dc drive electric car and LRT via simulation model. *J Appl Environ Biol Sci* 7(3S):73–82
  12. Arof S, Noor NM, Nur Diyanah NH, Mawby P, Arof H, Noorsal E (2021) DC drive electric car utilizing series motor and four quadrants drive DC chopper parameter determination from general design requirements. In: Progress in engineering technology III. [https://doi.org/10.1007/978-3-030-67750-3\\_17](https://doi.org/10.1007/978-3-030-67750-3_17)
  13. Arof S, Noor NM, Elias F, Mawby PA, Arof H (2017) Investigation of chopper operation of series motor four quadrants DC chopper. *J Appl Environ Biol Sci* 7(3S)49–56
  14. Arof S, Jalil JA, Kamaruddin NH, Yaakop NM, Mawby PA, Arof H (2016) Series motor four quadrants drive Dc chopper. Part 2: Driving and reverse with direct current control. In: International conference on power electronics, pp 775–780. ISBN 978-1-5090-2547-3/16. <https://doi.org/10.1109/PECON2016.7951663>
  15. Arof S, Diyanah NHN, Noor NMN, Radzi Md, Jalil JA, Mawby PA, Arof H (2019) Series motor four quadrants drive DC chopper: Part 4: Generator mode. In: Progress in engineering, pp 155–167. [https://doi.org/10.1007/978-3-030-28505-0\\_12](https://doi.org/10.1007/978-3-030-28505-0_12)
  16. Arof S, Diyanah H, Yaakop MN, Mawby AP, Arof H (2019) Processor in the loop for testing series motor four quadrants drive direct current chopper for series motor driven electric car: Part1: Chopper operation modes testing. In: Advanced engineering for processes and technologies, pp 59–76. [https://doi.org/10.1007/978-3-030-05621-6\\_5](https://doi.org/10.1007/978-3-030-05621-6_5)
  17. Arof S, Zaman MK, Jalil JA, Mawby PA, Arof H (2015) Artificial intelligence controlling chopper operation of four quadrants drive DC chopper for low cost electric vehicle. *Int J Simul Syst Sci Technol*. <https://doi.org/10.5013/IJSSST.a.16.04.03.2015>
  18. Arof S, Khairulzaman MAK, Jalil JA, Arof H, Mawby PA (2015) Self tuning fuzzy logic controlling chopper operation of four quadrants drive DC chopper for low cost electric vehicle. In: 6th International conference on intelligent systems, modeling and simulation. IEEE Computer Society, pp 40–24
  19. Arof S, Faiz MR, Diyanah NHN, Yaakop NM, Mawby P, Arof H, Noorsal E (2021) Fault diagnose of DC drive EV utilizing a new series motor four quadrants DC chopper using an expert system and quadratic solver running in embedded: Part 1: During start up. In: Progress in engineering technology III. [https://doi.org/10.1007/978-3-030-67750-3\\_15](https://doi.org/10.1007/978-3-030-67750-3_15)
  20. Arof S, Diyanah NHN, Mawby PA, Arof H, Noorsal E (2020) DC drive electric car state of charge (SOC) and remaining distance traverse (RDT) optimized by fuzzy logic. In: International scientific forum (ISF2019), Melaka, Malaysia. eISBN: 978-967-10842-1-2
  21. Arof S, Diyanah NH, Mawby PA, Arof H (2019) Study on implementation of neural network controlling four quadrants direct current chopper: Part1: Using single neural network controller with binary data output. In: Advanced engineering for processes and technologies, pp 37–57
  22. Arof S, Diyanah NHN, Noor NM, Rosyidi M, Mawby PA, Arof H (2019) Genetics algorithm for setting up look up table for parallel mode of new series motor four quadrants dc chopper. In: Progress in engineering, pp 155–167. [https://doi.org/10.1007/978-3-030-28505-0\\_12](https://doi.org/10.1007/978-3-030-28505-0_12)

23. Arof S, Shauqee ARA, Rosyidi M, Diyanah NHN, Mawby P, Arof H, Noorsal E (2021) Gradient descend for setting up a look-up table of series motor four quadrants drive DC chopper in parallel mode. In: Progress in engineering technology III. [https://doi.org/10.1007/978-3-030-67750-3\\_16](https://doi.org/10.1007/978-3-030-67750-3_16)
24. Arof S, Noor NM, Alias MF, Noorsal E, Mawby P, Arof H (2020) Digital proportional integral derivative (PID) controller for closed-loop direct current control of an electric vehicle traction tuned using pole placement. In: Progress in engineering technology II. Advanced structured materials, vol 131. Springer, Cham. [https://doi.org/10.1007/978-3-030-46036-5\\_8](https://doi.org/10.1007/978-3-030-46036-5_8)
25. Arof S, Noor MN, Mohamad R, Noorsal E, Mawby PA, Arof H (2020) Close loop feedback direct current control in driving mode of a four quadrants drive direct current chopper for electric vehicle traction controlled using fuzzy logic. In: Progress in engineering technology II. Advanced structured materials, vol 131. Springer, Cham. [https://doi.org/10.1007/978-3-030-46036-5\\_7](https://doi.org/10.1007/978-3-030-46036-5_7)
26. Arof S, Sukiman ED, Diyanah NH, Noor NM, Noorsal E, Mawby PA, Arof H (2020) Discrete-time linear system of new series motor four-quadrant drive direct current chopper numerically represented by Taylor series. In: Progress in engineering technology II. Advanced structured materials, vol 131. Springer, Cham. [https://doi.org/10.1007/978-3-030-46036-5\\_10](https://doi.org/10.1007/978-3-030-46036-5_10)
27. Arof S, Said S, Diyanah NHN, Noor NM, Yaakop NM, Mawby P, Arof H, Noorsal E (2020) Series motor four-quadrant direct current chopper: reverse mode, steering position control with double-circle path tracking and control for autonomous reverse parking of direct current drive electric car. In: Progress in engineering technology II. Advanced structured materials, vol 131. Springer, Cham. [https://doi.org/10.1007/978-3-030-46036-5\\_12](https://doi.org/10.1007/978-3-030-46036-5_12)
28. Arof S, Said S, Diyanah NHN, Noor NM, Jalil JA, Mawby P, Arof H, Noorsal E (2020) Series motor four-quadrant DC chopper: reverse mode, direct current control, triple cascade PIDs, and ascend-descend algorithm with feedback optimization for automatic reverse parking. In: Progress in engineering technology II. Advanced structured materials, vol 131. Springer, Cham. [https://doi.org/10.1007/978-3-030-46036-5\\_13](https://doi.org/10.1007/978-3-030-46036-5_13)
29. Arof S, Sazali MS, Diyanah NHN, Mawby P, Arof H, Noorsal E (2021) Series motor four quadrants drive DC chopper: reverse mode with automatic reverse parking of DC drive electric car with constant brake motor control combine to the propulsion motor torque. In: Progress in engineering technology III. [https://doi.org/10.1007/978-3-030-67750-3\\_20](https://doi.org/10.1007/978-3-030-67750-3_20)

# Chapter 4

## Pre-weld Heating Temperature Effect on the Welding Quality of a 100 T Truck Crack Frame—Case Study



**Tumianto, Muhammad Al'Hapis Abdul Razak, Azmi Hassan, Iwan Susanto, Surya Atmadyaya, Mohd Riduan Ibrahim, and Asmawi Ismail**

**Abstract** The heat generated during the welding process tends not to be evenly distributed between the weld metal, base metal, and heat affected zone and produces residual stresses. To obtain the desired result from the welding process it needs to be subjected to a heat treatment for removing residual stress through pre-weld and post-weld heat-treatment procedures. This research aims to determine the effect of the pre-weld heat-treatment process on the results of the FCAW welding of a 100-ton truck crack frame with temperature variations between 120 and 150 °C with a hold time of 15–30 min which is heated at the and cooled in free air. The combination of temperature and time that can optimize the welding quality in regard to crack failure of the truck frame is 100 °C temperature and 15 min. Temperature factor has an effect of 54.4% and the time. The time factor has an impact of 24.2%. The temperature interaction factor and time have an impact of 0.004% on pre-weld heating. The prediction of the meant time between stoppage (MTBS) of the truck from pre-weld heating on truck frame cracking failure if the optimal design is used, i.e., 100 °C

---

Tumianto · M. A. A. Razak (✉) · I. Susanto · S. Atmadyaya · M. R. Ibrahim  
Manufacturing Section, Universiti Kuala Lumpur Malaysian Spanish Institute, Kulim Hi-Tech  
Park, 09000 Kulim, Kedah, Malaysia  
e-mail: [alhapis@unikl.edu.my](mailto:alhapis@unikl.edu.my)

I. Susanto  
e-mail: [iwan.susanto@s.unikl.edu.my](mailto:iwan.susanto@s.unikl.edu.my)

S. Atmadyaya  
e-mail: [atmadyaya.surya@s.unikl.edu.my](mailto:atmadyaya.surya@s.unikl.edu.my)

M. R. Ibrahim  
e-mail: [mohdriduan@unikl.edu.my](mailto:mohdriduan@unikl.edu.my)

A. Hassan  
Electrical, Electronics and Automation Section, Universiti Kuala Lumpur Malaysian Spanish  
Institute, Kulim Hi-Tech Park, 09000 Kulim, Kedah, Malaysia  
e-mail: [azmi.hassan@unikl.edu.my](mailto:azmi.hassan@unikl.edu.my)

A. Ismail  
Maritime Engineering Technology, Universiti Kuala Lumpur Malaysian Institute of Marine  
Engineering Technology, 32200 Lumut, Perak, Malaysia  
e-mail: [asmawiis@unikl.edu.my](mailto:asmawiis@unikl.edu.my)

preheat for 15 min is 603 days. The type of research conducted is an experimental investigation.

**Keywords** Temperature · Preheat · Welding · Crack · Frame · Truck · Mining · Coal

## 4.1 Introduction

Because welding is a joining process using energy heat, the metal around the weld experiences a fast thermal cycle which causes complex metallurgical changes, deformations and thermal stresses. This is very closely related to toughness, weld defects, cracks, etc., which generally have a fatal effect on safety of weld construction [1]. Metals will experience a heating effect due to welding and experiencing changes in the microstructure around the weld area. The shape of the microstructure depends on the highest temperature reached welding speed and cooling rate of the weld area.

Welding consists of three parts:

1. Weld metal is a part of the metal at that time the welding melts and then solidifies.
2. Base metal, the base metal where heat and temperature welding does not cause structural changes and nature.
3. The area of heat influence is called the heat affected zone (HAZ). This is base adjacent to the weld metal during welding and is subjected to a fast heating and cooling process.

Apart from these three main divisions, there is still one special region which limits between the weld metal and the area of heat influence, which is called the weld boundary (fusion line) [2].

For a weld construction to be done correctly and successfully so that it is safe against the work done, then every welding job must start with the proper selection. Welding electrode, the welding process, and other important variables such as the form of the connection to be worked on, both in fabrication and in the field, as well as the treatment to be carried out at the start and completion of welding, preheat, and PWHT post-weld heat treatment (PWHT) [3].

Preheat or preheating before welding is done for slowing down the cooling rate and prevents weld cracking. Preheat is sometimes also needed to relieve the residual stress to increase the toughness, and to control the metallurgical properties in the HAZ.

## 4.2 Methodologies

Methodologies on the research will be described as follow:

### 4.2.1 Data Collection Method

The truck for the experiment, which has some cracking failure on the frame because of operation in coal mining environment, has been selected. Difference pre-weld heating treatments were done and recorded. The data used on this research is taken from the mean Time between Stoppages (MTBS) [4] of those selected 100 T truck when the second (indication) cracking failure was identified based on regular inspection.

### 4.2.2 Data Analysis

The variables used in the analysis consisted of two types of variables, namely, the response variable and the independent variable. The response variable used is a variable that indicates the quality of the pre-weld heating. In this case the truck MTBS is used to determine the durability of preheating:

- a. Mean Time Between Stoppages (MTBS). The signal to the noise ratio (SNR) of truck MTBS variables will be measured as

$$\text{Larger is the better characteristic SNR: } -10 \log \frac{1}{n} \left( \sum \frac{1}{y^2} \right) \quad (4.1)$$

$n$  is the sample observed

$y_1, y_2, \dots$  is the data results.

While the independent variables in this analysis are the variables used to optimize the quality welding, and each has two levels, namely,

- b. Temperature, which consists of the level 100 and 150 °C.
- c. Time, which consists of levels 15 (in minute duration) and 30 min.

The following Table 4.1 presents a summary of the factors and levels used.

Based on the available data, this analysis uses four data for each combination of factor levels Temperature and Time Interval The data are taken is data from the truck release after failure until it identifies crack at the around same area. Data are presented in the Tables 4.2 and 4.3 below.

**Table 4.1** Pre-weld heating level and factor

Level	Temperature (°C)	Time (minutes)
1	100	15
2	150	30

**Table 4.2** Historical data captured on trial 1

Truck ID	Temperature (°C)	Time (minutes)	MTBS (days)
TR1	100	15	533
TR2	100	30	427
TR3	150	15	492
TR4	150	30	229

**Table 4.3** Historical data captured on trial 2

Truck ID	Temperature (°C)	Time (minutes)	MTBS (days)
TR5	100	15	672
TR6	100	30	512
TR7	150	15	312
TR8	150	30	302

### 4.3 Discussion

Results of the experimental investigation on the effect of pre-weld heating on the crack frame failure are discussed in the following.

#### 4.3.1 Taguchi Analysis

##### 4.3.1.1 Orthogonal Array on Pre-weld heating

The analysis used two factors that are thought to influence the response, namely, temperature (X1) and time (X2), where each factor has two levels [5]. This analysis used an orthogonal array of 2 experiments with four repetitions for each experiment (a combination of factors on each level). The orthogonal arrangement design is as follows:

$$\begin{aligned}
 x &= \text{experiment} = 2 \\
 n &= \text{sample observed} = 2 \\
 a &= \text{factor level X1} = 2 \\
 b &= \text{factor level X2} = 2.
 \end{aligned}$$

##### 4.3.1.2 Signal to Noise Ratio (SNR)

SNR measures the level of performance and also the obscurity of the output quality characteristics. The higher the performance as measured by the higher SNR is the same as, the smaller the loss (Table 4.4).

**Table 4.4** SNR on pre-weld heating

No.	Temperature (°C)	Time (minutes)	Y bar	S/R ratio for pre-weld heating
	(X1)	(X2)		
1	100	15	602.500	55.425
2	100	30	469.500	53.326
3	150	15	402.000	51.425
4	150	30	265.500	48.34
Average			434.875	52.103

**Table 4.5** ANOVA on pre-weld heating

CF	DOF	SS	V	F ratio	F (0.95; dof1; dof2)	P value	%C
X1	1	81,810.125	81,810.125	10.183	7.709	0.033	54.442
X2	1	36,315.125	36,315.125	4.520	7.709	0.101	24.167
X1 * X2	1	6.125	6.125	0.001	7.709	0.979	0.004
Error	4	32,137.500	8034.375				
Total	7	150,268.875					

**4.3.1.3 ANOVA on Response**

The results of the ANOVA analysis can be explained as shown in Table 4.5.

**4.3.1.4 Large Factor Contributions**

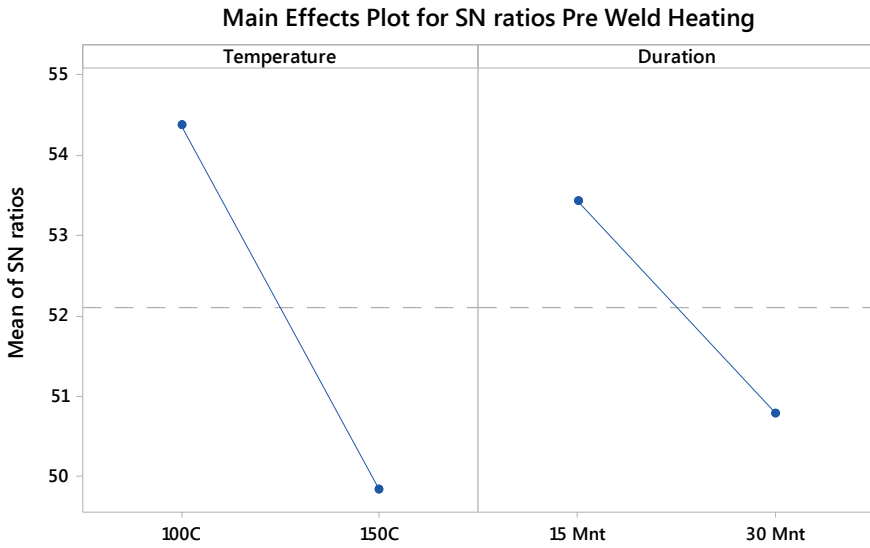
The proportion of each factor’s contribution to the response: Temperature factor has an effect of 54.442%. The time factor has an impact of 24.167%. The temperature interaction factor and time have an impact of 0.004% on the pre-weld heating.

**4.3.1.5 Response SNR Pre-weld Heating**

The effect is shown in Table 4.6 by Calculating the SNR average value at each level of each corresponding factor.

**Table 4.6** Response pre-weld heating

Level	X1	X2
1	54,376	53,425
2	49,830	50,780
Delta	4,546	2,645
Optimal	1	2
Rank	1	2



*Signal-to-noise: Larger is better*

**Fig. 4.1** Average SNR pre-weld heating

The design that produces the best SNR value is the design with a temperature of 100 °C and 15 min.

It is clearly shown if the design that produces the best SNR value is the design with temperatures 100 °C and 15 min (Fig. 4.1).

**4.3.1.6 SNR Predictions**

The prediction of the value from pre-weld heating on the truck frame cracking failure if the optimal design is used, i.e., preheating at 100 °C for 15 min. The prediction results are as follows:

$$\hat{y} = \overline{X1}_{100} + \overline{X2}_{15} - \bar{y}_{..} = 603$$

The average truck MTBS will be 603 h.

**4.4 Conclusions**

The combination of temperature and time that can optimize the welding quality on the crack failure of the truck frame is 100 °C temperature and 15 min.



Temperature factor has an effect of 54.442%. The time factor has an impact of 24.167%. The temperature interaction factor and time have an impact of 0.004% on pre-weld heating.

The prediction of the meant time between stoppage of the truck from pre-weld heating on truck frame cracking failure if the optimal design is used, i.e., preheating at 100 °C for 15 min is 603 h.

## References

1. Jeffus L (2020) *Welding: principles and applications*. Cengage Learning
2. Rodrigues LAS et al (2019) Welding procedures influence analysis on the residual stress distribution and distortion of stiffened panels welded via robotized FCAW. *Thin-Walled Struct* 141:175–183
3. Jiang J et al (2018) Effect of welding and heat treatment on strength of high-strength steel columns. *J Constr Steel Res* 151:238–252
4. Mostafa S, Dumrak J, Soltan H (2015) Lean maintenance roadmap. *Procedia Manuf* 2:434–444. <https://doi.org/10.1016/j.promfg.2015.07.076>
5. Stephanie Fraley MO, Terrien B, Zalewski J (2020) Design of experiments via Taguchi methods—orthogonal arrays

# Chapter 5

## Features Extraction from a Second-Order Black Box Model Matched to the Veltink Model for a System Identification of Knee Extension for Control Law and Formulations of Close-Loop Controller Rehabilitation Using Functional Electrical Stimulation



Saharul Arof, Emilia Noorsal, Saiful Zaimy Yahaya, Nor Haslina Ibrahim,  
and Hamzah Arof

**Abstract** Real-world functional electrical stimulation (FES) encounters nonlinear effects of fatigue and time delay that cause the FES controller to under-perform or sometimes fail. Nonlinearities cause the system to change, but it is not possible to re-tune the controller once its parameters are set. System representation using an observer can allow the patient's knee extension to be represented in a numerical computation algorithm and can exist, run, or be executed in an embedded system. This enables the closed-loop controller to be tuned to the system being imitated. The second-order black box model can be matched to the Veltink model to represent the knee extension in which the model is transformed into a linear differential equation, and then into a physical-based model. The numerical computation using

---

S. Arof (✉)

School of Electrical Engineering, College of Engineering, Universiti Teknologi MARA,  
Cawangan Pulau Pinang, Kampus Permatang Pauh, 13500 Perai, Pulau Pinang, Malaysia  
e-mail: [saharul@unikl.edu.my](mailto:saharul@unikl.edu.my)

S. Arof · E. Noorsal · S. Z. Yahaya · N. H. Ibrahim

Universiti Kuala Lumpur, Malaysian Spanish Institute, Kulim Hi-Tech Park, Kulim, Kedah,  
Malaysia  
e-mail: [emilia.noorsal@uitm.edu.my](mailto:emilia.noorsal@uitm.edu.my)

S. Z. Yahaya

e-mail: [saiful053@uitm.edu.my](mailto:saiful053@uitm.edu.my)

N. H. Ibrahim

e-mail: [norhaslina@unikl.edu.my](mailto:norhaslina@unikl.edu.my)

H. Arof

Engineering Department, Universiti Malaya, Jalan Universiti, 50603 Kuala Lumpur, Malaysia  
e-mail: [ahamzah@um.edu.my](mailto:ahamzah@um.edu.my)

Taylor series is then used to convert the physics-based model using a computational algorithm that represents the knee extension system in a discrete-time linear system. Prior to the conversion of the numerical model, certain parameters need to be extracted from the actual system response of the patient knee angle trajectory upon receiving an open-loop signal from FES. This paper focuses on the control algorithm technique for extracting the second-order black box model parameters matched the actual knee extension system response. MATLAB/Simulink is used to test the parameter extraction algorithms. The results indicate that the extraction algorithms succeeded in extracting the actual system parameters that are similar to the ones obtained by extracting the parameters representing the knee extension model.

**Keywords** Rehabilitation · FES · Observer · Features extraction · FIR filter · Finite state machine · Black box

## 5.1 Introduction

In recent decades, functional electrical stimulation (FES) has been widely used for neuromuscular applications to restore function to paralyzed muscles and limbs. The major challenge of muscle contraction induced by FES is early muscle fatigue which greatly limits activities such as FES-assisted standing and walking [1]. The cause of early muscle fatigue is due to the inefficiency of the stimulation waveform and strategy inherent from the FES device [2]. The conventional stimulation technique of the existing FES device, which employs the single open-loop stimulation channel, delivers a fixed stimulation pattern on the same motor unit and synchronously has resulted the motor unit to be overworked and fatigue easily [3]. The main objective of this research work is to establish algorithms to extract parameters from the actual knee trajectory response to form an observer that represents a knee extension system of the person under treatment using a computational algorithm [4] whereby it can be run, simulated, and tuned in an embedded system such as a microcontroller. The expected outcome of this research work is to produce an efficient features extraction computation algorithm to improve the close-loop controller performance.

## 5.2 Literature

Closed-loop control algorithms can theoretically improve the performance of open-loop control algorithms for FES applications. However, the actual performance of closed-loop controllers of FES is still inadequate and it must be greatly improved before they can be implemented effectively. It seems that the feedback controllers exhibit significantly degraded performance when real-world nonlinear effects (that is, fatigue and spasticity) are taken into consideration [5]. Moreover, the functioning

of the feedback controllers is dependent on the parameters of the muscle recruitment function, which change during real-world FES use [6].

For a smooth feedback control operation, an accurate muscle model [7, 8] of the system (patient to be treated) is needed. However, it is difficult to include the nonlinear aspects of the human muscle of a user such as fatigue [9] and spasticity into the model used by the closed-loop controller. Furthermore, the FES devices in the market do not have the feature to incorporate personalized muscle parameters of a user into the feedback controller to influence its operation as the patient to be treated is unknown a priori. In this case, the knee and muscle of the user may experience degrading performance as a result of fatigue and spasticity [10–12], since it is impossible to tune the closed-loop feedback controllers to suit the patient's leg and knee [13]. Unlike FES devices in the laboratory that can be set up to suit several pre-determined persons, the FES devices in the market have to cater for variations in the weight, damping, etc. of different people who are unknown [14]. These unknown parameters could prevent the system from running at its highest performance, or could sometimes cause it to fail, and cause injuries to the patient [15]. An accurate model requires the identification process to be established and this is considered as impractical in a clinic setting due to time constraints and fast-changing dynamics [16]. Nonlinear effects require system changes but updating the system or retuning the controller are not possible.

### 5.3 Methodology

System representations [4] using an observer can allow that the patient knee extension is represented in a numerical computation algorithm and can exist, run, or being executed in an embedded system. This allows close-loop controller tuning to the imitate system using optimization tool such as genetics algorithm [17] or gradient descend [18]. The second-order system can be used to represent knee extension models [11–14] in a black box model. For observer formation, the model is transformed into a linear differential equation [4], and then into a physical-based model. The numerical computation using Taylor series is then used to convert the physics-based model to a computational algorithm [4] that represents the knee extension system. This computational algorithm allows the model to stand as an independent system and to operate in an embedded system such as the microcontroller such as shown in Fig. 5.1. Prior to the conversion to a numerical model, certain parameters need to be extracted from the actual system response of the knee extension system. The knee response is recorded and stored in the memory for future analysis and extraction of the system parameters. This paper focuses on the control algorithm technique for extracting the second-order black box model parameters from the actual knee extension system response.

The knee extension model can be represented by a body part and joint dynamic equation and an electrically stimulated muscle model as depicted in Fig. 5.2. Veltink et al. [19], in a controlled study of the ankle joint movement, used a second-order

Fig. 5.1 PIC microcontroller

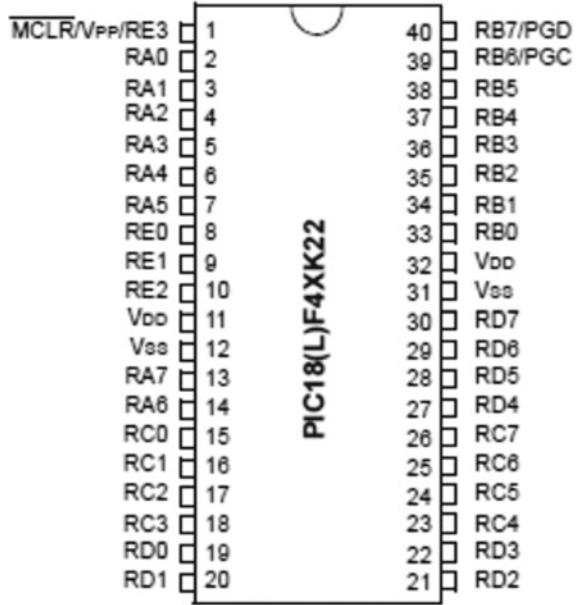
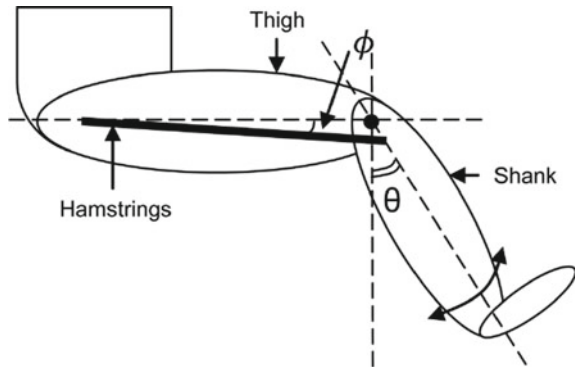


Fig. 5.2 Knee extension



linear system to determine the relation between torque and angle, see Eq. (5.1). They proposed the following equation to relate the two parameters

$$M = I\ddot{\theta} + B\dot{\theta} + \frac{\theta - \theta_{nom}}{C} \tag{5.1}$$

where  $M$  is the joint torque,  $\theta$  is joint angle, and  $\theta_{nom}$  is the angle at which the steady-state torque equals zero,  $I$  is the inertia,  $B$  is the damping, and  $C$  is the compliance of the load.

The overall knee extension represented in a system can be matched, categorized, and simplified by a second-order system.

### 5.3.1 Second-Order Black Box Model System

A black box is a device, system, or object which can be viewed in terms of its inputs and outputs, without any knowledge of its internal workings. The Veltink model can be equated to the black box second-order system. The second-order system as depicted in Fig. 5.3 can fall into four categories, which are under-damped, critical damped, damped and over-damped. Natural frequency ( $\omega_n$ ), damping ratio ( $\zeta$ ), system gain, and time constants are important parameters that determine the categories.

The second-order transfer function form is provided in Eq. (5.2).

$$\frac{C(s)}{R(s)} = \frac{\omega_n^2}{s^2 + 2\zeta\omega_n s + \omega_n^2} \tag{5.2}$$

where  $\omega_n^2$  is the natural frequency, and  $\zeta$  is the damping.

A linear differential equation of the Veltink and second-order in linear differential Equation (LDE) can be represented as given in Eqs. (5.3) and (5.4)

$$I\ddot{\theta} + B\dot{\theta} + \frac{\theta - \theta_{nom}}{C} = M \tag{5.3}$$

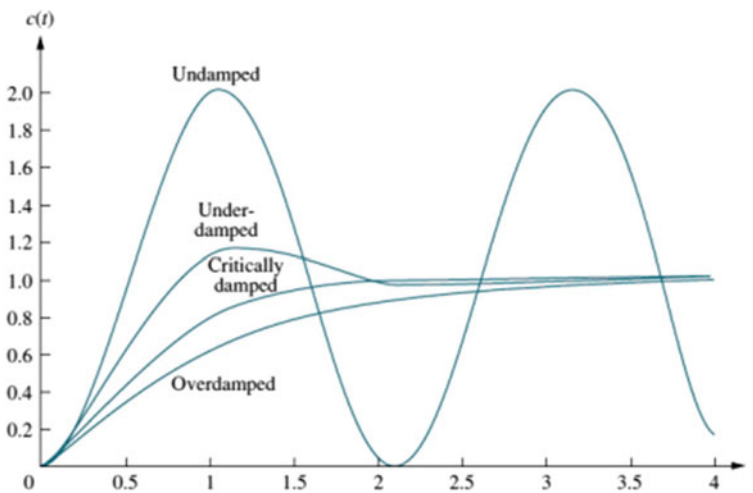


Fig. 5.3 Second-order black box

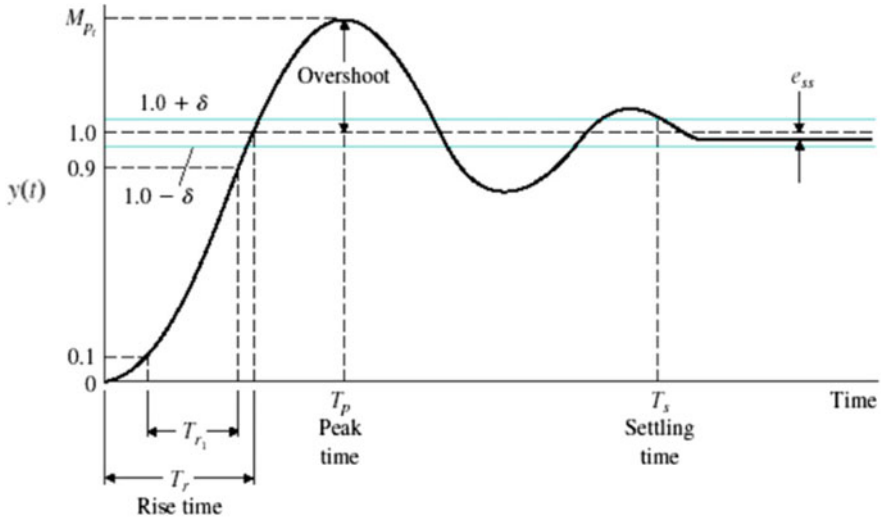


Fig. 5.4 Second-order dynamic behavior

Second-order using  $\zeta$  and  $w_n$

$$Ax'' + \zeta x' + w_n x = y \tag{5.4}$$

For a second-order system, by knowing the natural frequency  $w_n$  damping ratio ( $Z$ ), system gain, and time constants the black box system can be represented.  $Z$  influences the damping effect, natural frequency, and system gain influence the steady-state output, and the time constant influences the time response. The general equations for the establishment of the second-order black box model as in Fig. 5.4 are described in Eqs. (5.5)–(5.9).

$$\text{Overshoot Ratio} = \frac{\text{Peak}}{\text{Steady state output}} \tag{5.5}$$

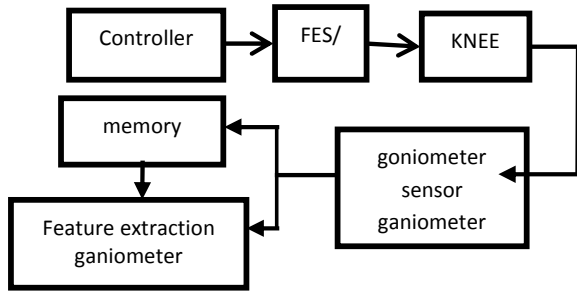
$$W_n = \frac{\text{Steady state output}}{\text{Step input}} \tag{5.6}$$

$$\zeta = \sqrt{\frac{\ln(0.5)^2}{\pi^2 + \ln(0.5)^2}} \tag{5.7}$$

$$\text{Rise Time } (T_r) = \frac{T_s}{\sqrt{1 - z^2}} (\pi - \cos^{-1} z) \tag{5.8}$$

$$\text{Settling time } T_s = \frac{\sqrt{1 - z^2}}{2\pi} P \tag{5.9}$$

**Fig. 5.5** Block diagram of feature extraction during open-loop test



These parameters need to be extracted to find the  $\zeta$  (damping),  $w_n$  (natural frequency), and  $K$  (system gain) and time constant (i.e., steady-state time, steady-state value, input value, overshoot, etc.). These parameters are determined during open-loop FES test as shown in Fig. 5.5.

Once the input start signal is received, the controller will output the pre-determined pulse width and frequency to the FES device. The actual knee extension response is processed and is also stored in the memory for further comparison, data extraction, and signal processing use. The memory is needed to store the actual system response for finding parameters such as the final steady-state output.

### 5.3.2 Second-Order System Features Extraction

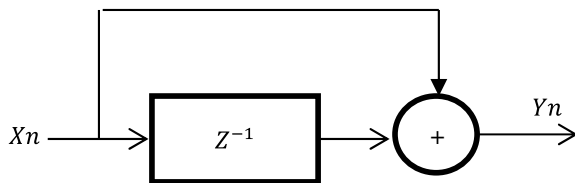
To extract the feature of steady-state value required digital signal processing order filter. The simplest Digital/Discrete order filter is given by the following difference equation:

$$y(n) = x(n) + x(n - 1) \tag{5.10}$$

where  $x(n)$  is the filter input amplitude at time (or sample),  $y(n)$  is the output amplitude at  $n$ . The  $x(n - 1)$  is the previous sample. The signal flow graph (or simulation diagram) for this little filter is given in Fig. 5.6.

The symbol ' $Z^{-1}$ ' means a delay of one sample, i.e.,  $Z^{-1} x(n) = x(n - 1)$ .

**Fig. 5.6** System diagram for the filter





The algorithms needed to perform the features extraction is by using the time domain technique by having three points separated with specific time interval that works as the order filter as shown in Fig. 5.7. At each point, it is connected to the controller preset with the finite state machine if-then rules control law.

The time to reach the steady-state value is also recorded and used to determine the system time constant. An incremental counter is set up with pre-determined step-up time, to record the total time until the actual knee trajectory response reaches steady state. At each sampling time, the first output value as stated as point 1 (P1) is recorded and stored in the memory. In the second time interval, the output value is updated as the new point 1 (P1) and the previous point 1 (P1) value which was stored in the memory is transferred and recognized as the second point or point 2 (P2). At third time interval, the new output value is updated as point 1, the previous point 1 value is updated as point 2 and the previous point 2 value has become point 3 and the process continues. If the three points have significantly different values, this means that the steady state is not yet reached. However, if the three points have almost the same values, the system is at steady state. The value is divided with the input value and the result is the natural frequency. This natural frequency value reflects the system gain.

To obtain the overshoot value, the memory needs to be used. An algorithm to find the system's maximum value or overshoot value is by comparing each point of the knee trajectory response to one value preset in the memory. If the response has a higher value than the one in the memory, it is stored in the memory, and this ends up as the highest value collected in the memory. This value is used to find damping/zheta. To determine the overshoot time called the peak time ( $T_p$ ), the three points technique and another incremental counter that is running are used. If the first point (P1) is lower than point 2 (P2), and point 3 (P3) is lower than point 2 (P2) and point 1(P1), the maximum point is reached. The time to reach the maximum/overshoot value is then recorded.

Once those values have been obtained, the data in the memory is re-run/recalled and is compared to find the rise time  $T_r$  and  $T_p$  of the system. An incremental counter is run to locate the count when the values of  $T_r$  and  $T_p$  are reached.  $T_r$  is the value at 50% earlier determined of the steady-state value and is then compared to the memory value and finally determined. The time constant  $T_r$  value is at 50% of the steady-state value and the other  $T_p$  is at 100% of the steady-state value. Two incremental counters

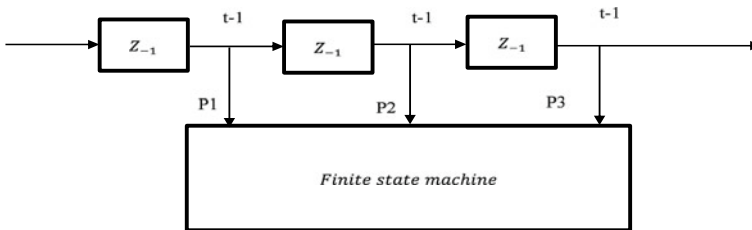
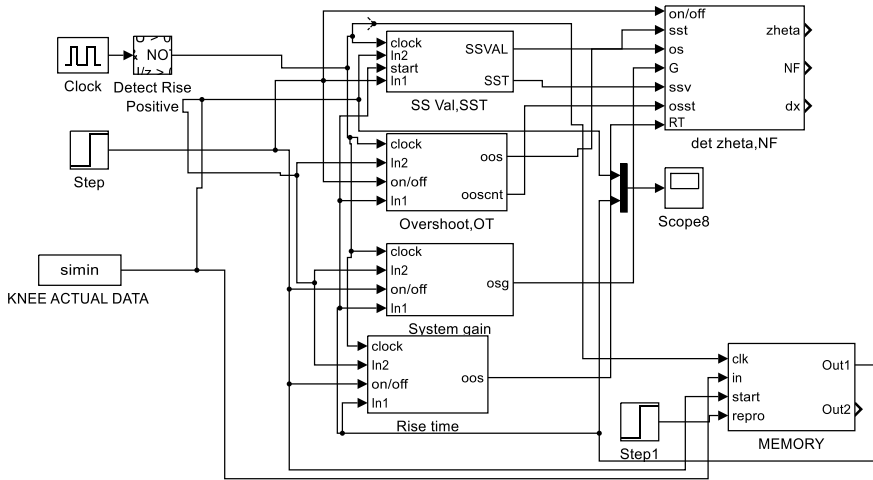


Fig. 5.7 Three points and finite state machine system diagram



**Fig. 5.8** Simulation model of features extraction for second-order model

value is used to find the values. The system gain can be determined by dividing the steady-state value to the input value.

### 5.3.3 Simulation Model Using Matlab/Simulink Function

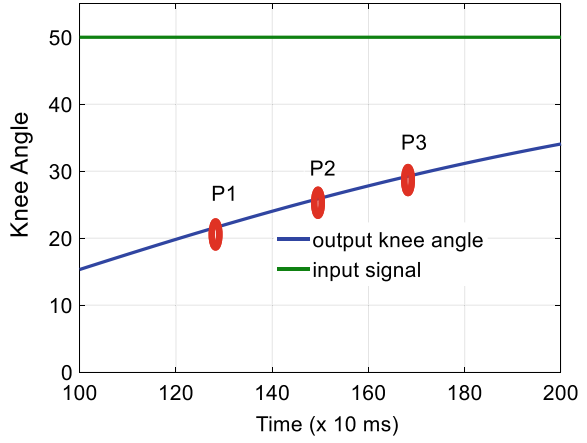
A MATLAB/Simulink simulation model is used to represent the controller and memory of the embedded system that holds the control algorithms. Figure 5.8 exhibits the MATLAB/Simulink simulation model for the second-order system. The knee extension trajectory that was previously simulated and recorded is included and simulated together with the embedded system controller to test the control algorithms.

Figures 5.9, 5.10 and 5.11 are some of the results of the three points technique.

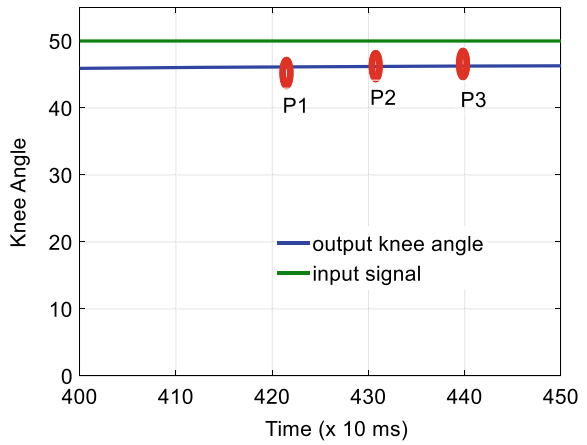
## 5.4 Result and Discussion

The simulation results are shown in Figs. 5.12, 5.13, 5.14, 5.15, 5.16, 5.17, 5.18 and 5.19. Table 5.1 is the conclusion of the expected parameters extraction results. In Fig. 5.12, the overshoot value is determined using the algorithm. In Fig. 5.13, the counter value to count time constant ( $T_c$ ) from the steady-state time is shown. The steady-state value is shown in Fig. 5.14. In Fig. 5.15, the counter value to count the steady-state time for the second-order system is shown. The counter value to obtain the  $T_r$  and  $T_p$  values is shown in Fig. 5.16. Figures 5.17 and 5.18 show the use of memory to find the  $T_r$  and  $T_p$  values. Figure 5.19 is the final result after the

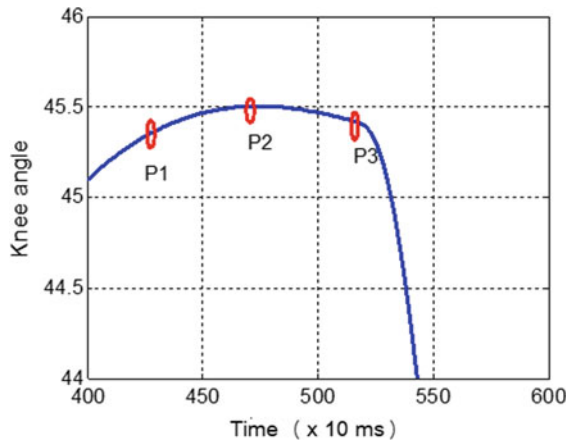
**Fig. 5.9** The three points during transient response



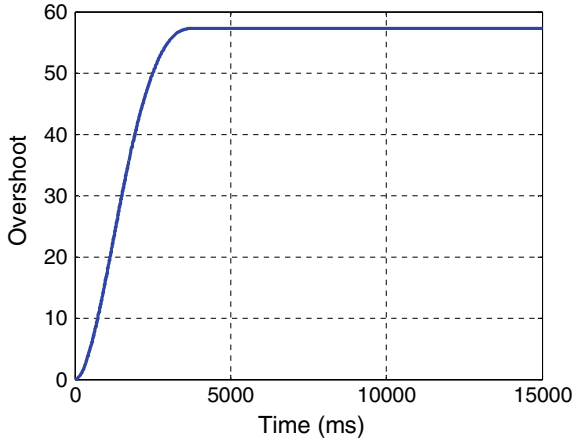
**Fig. 5.10** Three points reach steady-state value



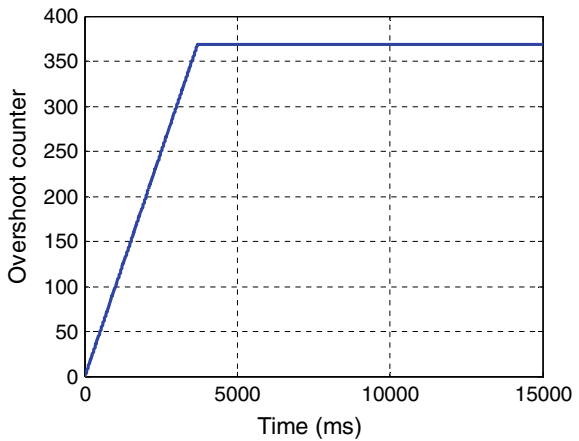
**Fig. 5.11** Three points found maximum point



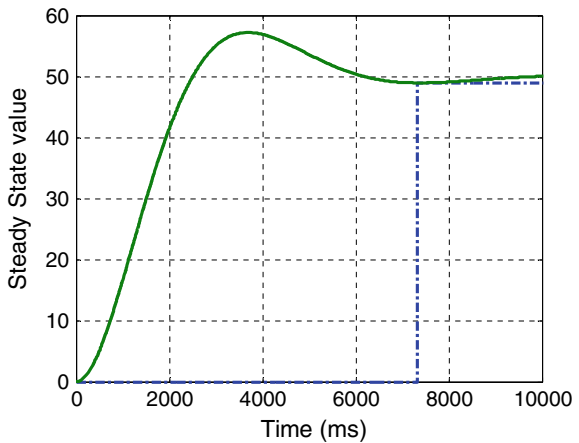
**Fig. 5.12** Second-order overshoot value



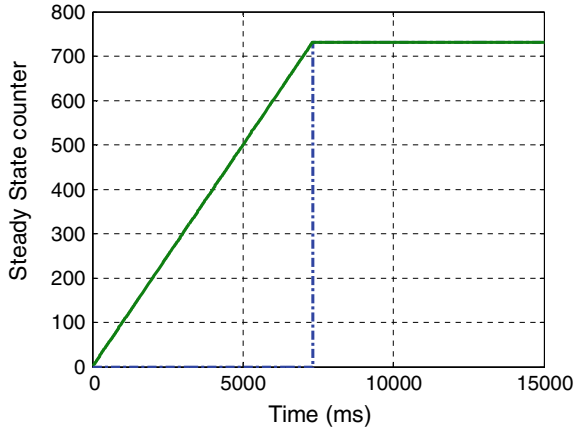
**Fig. 5.13** Overshoot time counter



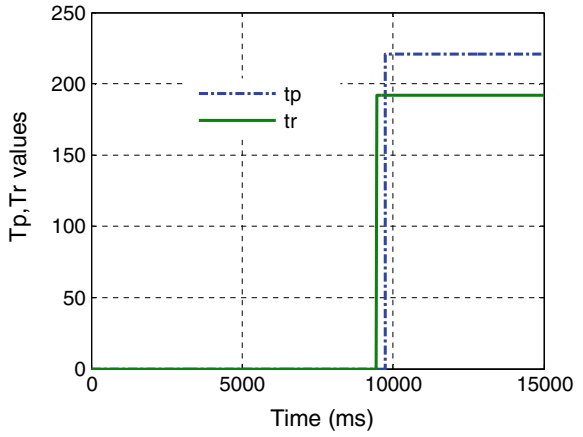
**Fig. 5.14** Finding of steady-state value



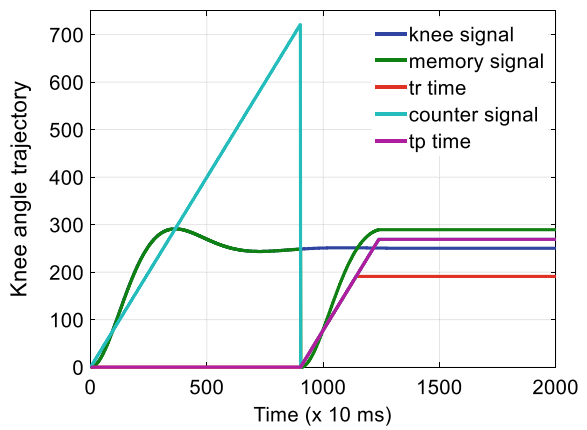
**Fig. 5.15** Results of second-order steady-state time



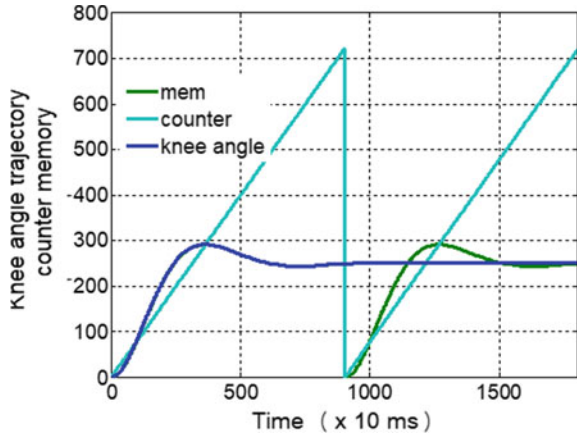
**Fig. 5.16** Results to determine  $T_r$  and  $T_p$



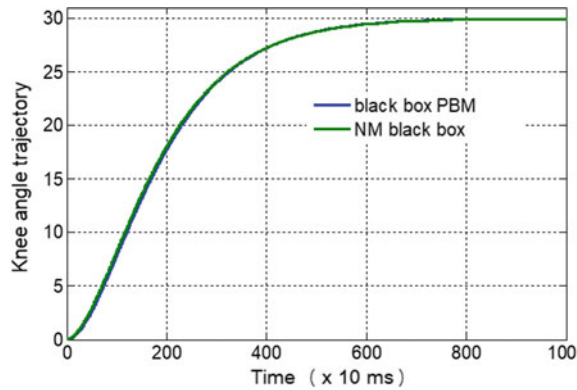
**Fig. 5.17** Used of memory



**Fig. 5.18** Counter find time constant



**Fig. 5.19** Numerical observer



**Table 5.1** Features values

$T_p$	$T_r$	Os	Ost	Freq	ssv	sst
185	100	57	365	1000	49	700

extracted parameters have been transformed to  $\zeta$ ,  $w_n$  and time constant and finally used to re-form the system. The simulated system is compared to the actual system for comparison.

Table 5.1 collates all the extracted parameters for further processing and transformation to determine zeta, natural frequency  $w_n$ , and system gain. The data time interval or frequency for data storing is also important and is included in the table.

$\zeta$ , natural frequency  $w_n$  and system gain are computed using the equations below:

$$\zeta = ((\text{Overshoot-steady-state value})/\text{steady-state value}) \quad (5.12)$$

$$w_n^2 = \text{Normalize Steady-state value}/\text{normalize input signal} \tag{5.13}$$

$$Dx = \text{steady-state counter value} * \text{controller frequency} \tag{5.14}$$

By knowing the damping ratio, system gain, and time constants, the second-order system  $\zeta$  and natural frequency can be determined. This black box model is then converted into the linear differential equation model and solved by numerical methods.

MATLAB/Simulink software with MATLAB function is used in the MATLAB function.

**Output of the Simulation Model Using MATLAB/Simulink Function**

A MATLAB/Simulink model using MATLAB function is used to represent the embedded system. Figures 5.20, 5.21 and 5.22 exhibit the transfer function, physical-based model, and MATLAB/Simulink simulation model using Taylor series.

Figure 5.23 shows the MATLAB/Simulink simulation result of the Taylor series representing the knee extension.

From the graph in Fig. 5.23, the pattern of each type of simulation is considered acceptable but not equal. Further improvement can be done by controlling the time step and different values of h.

Once the system parameters have been determined, the linear differential equation can be established. Then the equation is converted to the physics-based model before constructing the numerical method representation. The Taylor series method is used for the numerical representation of the knee extension because its calculation is much easier. Details of the conversion process are not in the scope of this paper but will

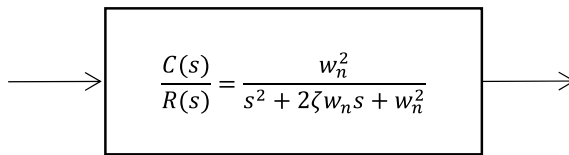


Fig. 5.20 Transfer function model

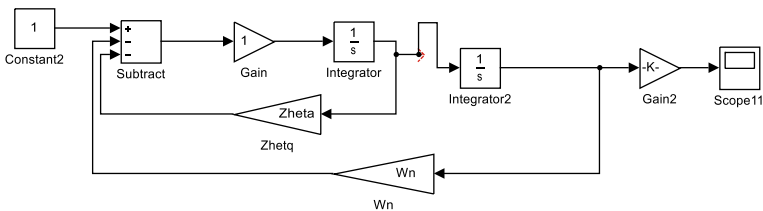
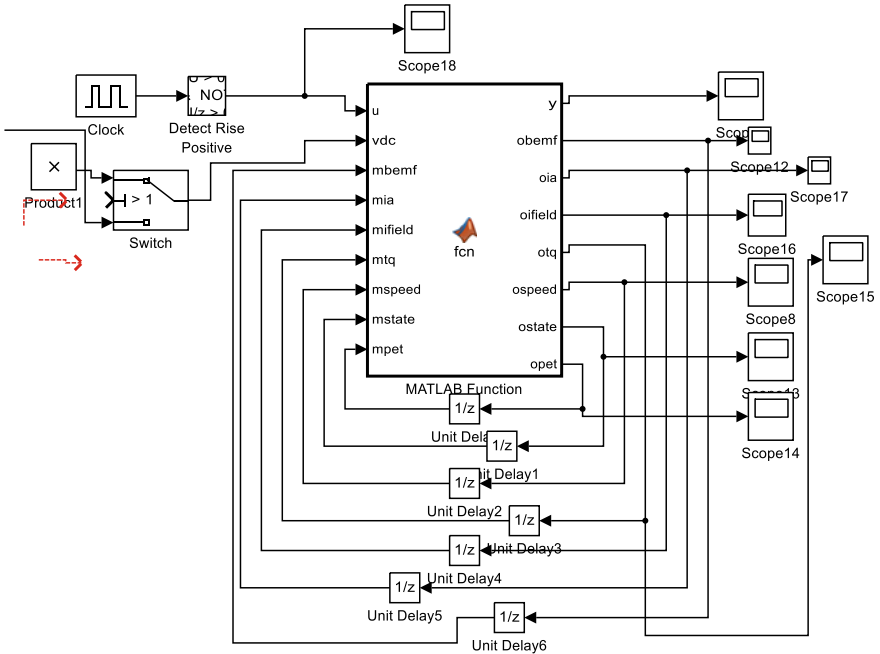
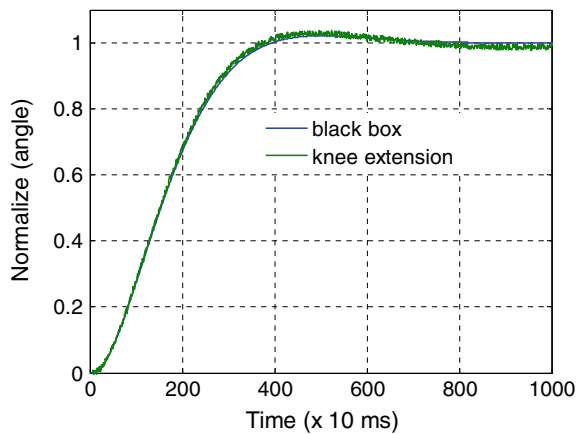


Fig. 5.21 Physical-based model



**Fig. 5.22** Simulation model of embedded system running Taylor series using MATLAB/Simulink function

**Fig. 5.23** Simulation result of Taylor series expansion representing knee extension



be covered in a separate paper. The final result is shown in Fig. 5.23. The numerical model can be used along close loop feedback controller such as Fuzzy Logic [20], PID, Sliding mode for controller tuning purposes using gradient descend, genetics algorithm or particle swarm optimization.



**Table 5.2** Influence parameters

Parameters	Accuracy
1. Analog to digital conversion resolution	Higher resolution results in better accuracy
2. Range tolerance of FIR order Filter	The smaller ranges tolerance result in better accuracy
3. Separation point	Closer will produce better result

The accuracy of the result is measured based on point-to-point comparison. At a lower accuracy, the graph line of the original and the one which is stored in the memory cannot be distinguished, while at a higher accuracy, two separate lines can be observed. The three parameters that influence the performance of the system are provided in Table 5.2.

## 5.5 Conclusions

The technique of features extraction using memory and digital signal processing with order filter have successfully been implemented and utilized to extract useful parameters in representing the second-order system representing the knee extension system. In summary, the performance of a features extraction method in extracting the second-order system compared to the actual knee extension is good and suitable to be used for system conversion to a linear differential equation, physical-based model, and finally to numerical computation utilizing the Taylor series algorithm for observer formation.

## References

1. Abbas JJ, Gillette JC (2001) Using electrical stimulation to control standing posture. *IEEE Control Syst Mag* 21(4):80–90
2. Thrasher T, Flett H, Popovic M (2006) Gait training regimen for incomplete spinal cord injury using functional electrical stimulation. *Spinal Cord* 44(6):357–361
3. Kralj A, Bajd T, Turk R (1988) Enhancement of gait restoration in spinal injured patients by functional electrical stimulation. *Clin Orthopaed Relat Res* 233:34–43
4. Arof S, Sukiman E, Diyanah N, Noor N, Noorsal E, Mawby P, Arof H (2020) Discrete-time linear system of New series motor four-quadrant drive direct current chopper numerically represented by Taylor series. *Progress in engineering technology*, II edn. Springer, pp 101–112
5. Lynch CL, Popovic MR (2012) A comparison of closed-loop control algorithms for regulating electrically stimulated knee movements in individuals with spinal cord injury. *IEEE Trans Neural Syst Rehabil Eng* 20(4):539–548
6. Lynch CL, Popovic MR (2008) Functional electrical stimulation. *IEEE Control Syst Mag* 28(2):40–50

7. Previdi F, Carpanzano E (2003) Design of a gain scheduling controller for knee-joint angle control by using functional electrical stimulation. *IEEE Trans Control Syst Technol* 11(3):310–324
8. Jezernik S, Wassink RG, Keller T (2004) Sliding mode closed-loop control of FES controlling the shank movement. *IEEE Trans Biomed Eng* 51(2):263–272
9. Noorsal E, Yahaya SZ, Hussain Z, Boudville R, Ibrahim MN, Ali YM (2020) Analytical study of flexible stimulation waveforms in muscle fatigue reduction. *Inter J Electr Comput Eng (IJECE)* 10(1):690. <https://doi.org/10.11591/ijece.v10i1.pp690-703>
10. Tu Y, Matthews GI, Lee S-Y, Fang Q (2015) A closed-loop micro-stimulator controlled by muscle fatigue status and function impairment level for upper limb rehabilitation. Paper presented at the 2015 international symposium on bioelectronics and bioinformatics (ISBB)
11. Alouane MA, Rifai H, Amirat Y, Mohammed S (2018) Cooperative control for knee joint flexion-extension movement restoration. Paper presented at the 2018 IEEE/RSJ international conference on intelligent robots and systems (IROS)
12. Benahmed S, Tadjine M, Kermia O (2017) Adaptive super twisting controller: In search of a universal controller for the paraplegic knee movement using FES. Paper presented at the 2017 5th international conference on electrical engineering-Boumerdes (ICEE-B).
13. Alibeji N, Kirsch N, Sharma N (2015) Dynamic surface control of neuromuscular electrical stimulation of a musculoskeletal system with activation dynamics and an input delay. Paper presented at the 2015 American control conference (ACC)
14. Lynch CL, Sayenko D, Popovic MR (2012) Co-contraction of antagonist muscles during knee extension against gravity: insights for functional electrical stimulation control design. Paper presented at the 2012 annual international conference of the IEEE engineering in medicine and biology society
15. Abdulla SC, Tokhi MO (2014) Comparative assessment of two fuzzy logic based control approaches for a flywheel and electrical clutch assist mechanism in FES cycling. Paper presented at the 2014 19th international conference on methods and models in automation and robotics (MMAR)
16. Kawai H, Bellman MJ, Downey RJ, Dixon WE (2017) Closed-loop position and cadence tracking control for FES-cycling exploiting pedal force direction with antagonistic biarticular muscles. *IEEE Trans Control Syst Technol* 27(2):730–742
17. Arof S, Diyanah NHN, Noor NM, Rosyidi M, Mawby PA, Arof H (2019) Genetics algorithm for setting up Look Up Table for parallel mode of new series motor four quadrants DC chopper. *Progress in engineering*, pp 155–167. [https://doi.org/10.1007/978-3-030-28505-0\\_12](https://doi.org/10.1007/978-3-030-28505-0_12)
18. Arof S, Shauqee ARA, Rosyidi M, Diyanah NHN, Mawby P, Arof H, Noorsal E (2021) Gradient descend for setting up a look-up table of series motor four quadrants drive DC chopper in parallel mode. *Progress in engineering technology*, III edn. [https://doi.org/10.1007/978-3-030-67750-3\\_16](https://doi.org/10.1007/978-3-030-67750-3_16)
19. Veltink PH, Chizeck HJ, Crago PE, El-Bialy A (1992) Nonlinear joint angle control for artificially stimulated muscle. *IEEE Trans Biomed Eng* 39(4):368–380
20. Noorsal E, Arof S, Yahaya SZ, Hussain Z, Kho D, Mohd Ali Y (2021) Design of an FPGA-based fuzzy feedback controller for closed-loop FES in Knee Joint Model. *Micromachines* 12(8):968. <https://doi.org/10.3390/mi12080968>

# Chapter 6

## Analysis of an Adjustable Topside Mechanic's Creeper for Automotive Repair and Maintenance Using Simulation Methods



Siti Rohana Ahmad, Syasya Aqilah Mohamad Nadzri,  
and Muhammad Zunnurrin Ghazali

**Abstract** A mechanic's creeper is synonym in automotive industry especially during maintenance or repair of a vehicle. A topside creeper is the easiest way and more ergonomic to carry on with repair or service work without feeling tired or injuring the body. The application of mechanic's creepers is also expected to increase the quality of service. Currently, the price of creepers is expensive, and the current structure has several problems due to its heavy weight material (heavy-duty steel frame). Furthermore, it is difficult to handle the creeper (assembly and dissemble after usage), and it is hard to store the creeper. Some of products have had many different sizes, heights, weight and are less ergonomic in terms of the design for Asian's mechanics, especially in Malaysia. In this paper, the design and analysis of an ergonomic and adjustable height of topside mechanic's creeper structure was carried out using the SOLIDWORKS 2016 software. The 70, 100, and 130 kg of load were used by referring to some typical weights of Asian's mechanics. Two types of aluminum (Al) profiles were used (40 mm × 40 mm and 60 mm × 60 mm). The larger Al diameters of mechanic's creeper structure indicates ~60% higher strength and a ~55% lower strain compared to the small Al profile diameters. Therefore, the design of the mechanic's creeper structure is expected to be the less expensive and more convenient for automotive mechanics in maintenance and/or repair works.

**Keywords** Mechanic's creeper · Structure · Automotive · SOLIDWORKS

---

S. R. Ahmad (✉) · S. A. M. Nadzri  
Universiti Kuala Lumpur, Malaysian Spanish Institute, Kulim Hi-Tech Park, Kulim, Kedah,  
Malaysia  
e-mail: [sitirohana@unikl.edu.my](mailto:sitirohana@unikl.edu.my)

S. R. Ahmad · M. Z. Ghazali  
R&Z Auto, Car Repair and Service Centre, 470, Jalan Kota Kenari 3, Taman Kenari, 09000  
Kulim, Kedah, Malaysia

## 6.1 Introduction

Automotive mechanics or technician duties have a great deal to do with fixing the vehicle. Automotive mechanics spend a lot of their workdays under cars or hovering over an engine. They are exposed to a variety of work stresses such as a hot noisy environment, strenuous posture, improperly designed tools and machinery, and poor psycho-social environment that can affect their safety and health. The mechanic who works in an automotive repair shop often requires a device that supports more physical support, as it leans over the engine compartment of an automobile to inspect and/or to repair its components.

A mechanic's creeper is a synonym in automotive industry especially during maintenance or repair work of the vehicle. There are two types of mechanic's creeper used, one for the underside of a vehicle and the other one is used to overhead the engine vehicle to perform maintenance or inspection. A topside creeper is the easiest way and more ergonomic to carry on with repair or service work without feeling tired or injuring the body [1–3].

There are a few overhead creepers with many unique features but providing the same functionality to provide additional support for vehicle maintenance or repair. By using a creeper, not only improves the comfort to the mechanic while working but also increases the productivity [4].

There are several issues of the current mechanic's creepers. One of them is that the product's price is too expensive. It is slightly a burden for mechanics to purchase the product. Besides, the current structure has several problems due to its heavy weight material (heavy-duty steel frame), it is difficult to handle the creeper (assembly and disassemble after used), and it is hard to store the creeper. The latest products have many different sizes, heights, and weights and are less ergonomic in terms of design for Asian's mechanics, especially in Malaysia.

In this project, an ergonomic foldable topside automotive mechanic's structure was designed and analyzed based on previous outcomes of researchers. The design and simulation of the creeper structure were done using the SOLIDWORKS software.

## 6.2 Literature

*Work-related back discomfort and associated factors among automotive maintenance mechanic.*

Back pain has been identified as a common cause of the disability within the working population. Automotive mechanics usually use an uncomfortable back posture during their manual operation and therefore may be at risk for back pain associated with work.

Abaraogu and co-workers stated that musculoskeletal disorders, including low back pain, are known for the occupations involving manual handling and physical workload. Maintenance mechanics for automotive use work mostly standing,

**Table 6.1** Associated factors among automotive maintenance mechanics [5]

The associated factor among automotive maintenance mechanics	Problem
Association with daily working hours	Longer daily working hours more than 5 h in automotive mechanic maintenance tend to lead to a rise in the currency of back pain. Workers who had worked for lengthy periods were at a higher risk than those who worked for shorter durations may increase the risk of injury
Association with age	The back pain among the participants increased significantly with advancing age up to the 50–59 years old. This may suggest that these age groups are critical to back pain incidence among automotive mechanics workers

kneeling, or half kneeling, in forward flexion and on a hard floor. Individuals who follow these positions consistently would be more likely to experience back pain [1].

In this research, they discuss the associated factors that happen among automotive maintenance mechanics, which is association with age, association with daily working hours, association with weight status, and perceived workplace stressors responsible for back pain. Only two factors are related to this project. Two associated factors with problem are stated in Table 6.1.

The back pain among automobile mechanics is higher, and the majority of these workers do not seek consultation with a medical doctor or a physiotherapist even when the majority of pain is severe and limits the activity. These researchers suggest that the health education programmers and measures directed toward prevention of occupational diseases would help to improve the health of automotive maintenance mechanics, particularly in decreasing the back pain. Specifically, seminars and workshops should be aggressively pursued; and clinicians should include ergonomic education as a core component of interventions during back pain management [3, 5].

## 6.3 Methodology

### 6.3.1 Design Process

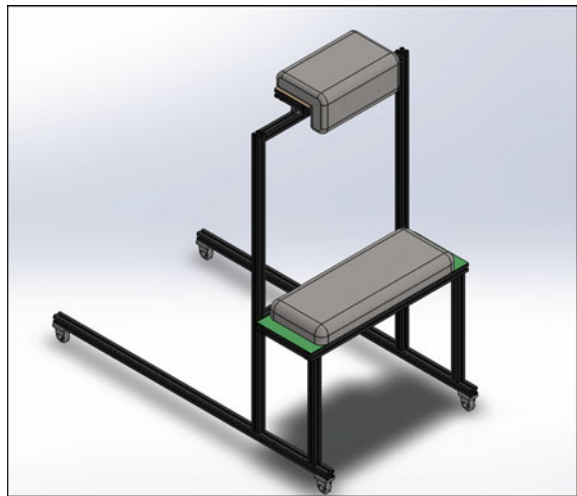
All designs were sketched on paper first before drawing them in SOLIDWORKS. There were six designs created with two different dimensions of aluminum profiles [5]. The first 3 design concepts used an aluminum alloy with dimensions of 40 mm × 40 mm of the profile and another 3 designs used an aluminum profile with dimensions of 60 mm × 60 mm. The purpose to use two different dimensions of aluminum profile is to test the strength of every design in terms of stress and strain analysis by using the integrated simulation tool in SOLIDWORKS.

### 6.3.2 Design of Foldable Topside Mechanic's Creeper

The design 1 consists of the structure, chest cushion, kneel cushion, four wheels with the lock, and a plate as shown in Fig. 6.1. This design is the first idea that was carried out from the market survey [6, 7]. Table 6.2 shows the material parameters used for all structures made of aluminum profiles with dimensions of 40 mm × 40 mm and 60 mm × 60mm. The density of the aluminum profiles is lower than the commonly used metal density, and it is light but strong. It is suitable to use and can solve the problem of the current product because the material of the current product is a heavy-duty material. Based on the design 1, it can flip the kneel and with adjustable chest cushion that helps the user for comfortable position while working at the engine compartment.

Each part of design 2 in Fig. 6.2 is almost similar to the specification of design 1.

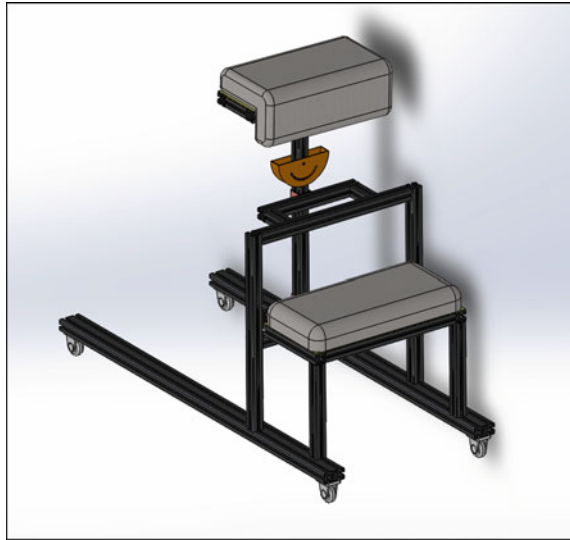
**Fig. 6.1** Isometric view of design 1



**Table 6.2** Specification of design 1

Specification	Dimension
1. Adjustable kneel cushion	1. Design 1 used aluminum profile
2. Adjustable cushion	40 mm × 40 mm
3. Padded chests move (upward and downward)	Overall dimension: 1600 mm × 880 mm × 1766 mm
4. Fixed height	
5. Fixed angle	2. Design 1 used aluminum profile
6. 4 wheels with lock	60 mm × 60 mm
	Overall dimension: 1600 mm × 880 mm × 1766 mm

**Fig. 6.2** Isometric view of design 2



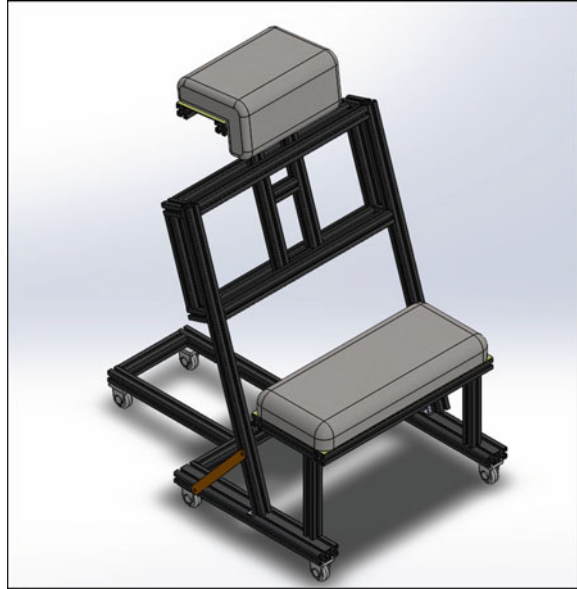
The main differences of the design are the movement of the padded chest support on the right-hand and left-hand side. The second functionality is that it also can adjust the height of structure for the exact mechanic's height depending on their comfort (see Table 6.3).

The design 3 in Fig. 6.3 slightly looks different compared to the two previous designs. Table 6.4 indicates that this design has more feature, i.e., a storage box for tools, adjustable angle and it can move the structure cushion to the left- and right-hand side. The functionality is still the same as previous design, but a different type of mechanism structure is used for easier movement and to maintain the stability of the user while working at the vehicle engine compartment.

**Table 6.3** Specification of design 2

Specification	Dimension
1. Adjustable height	1. Design 2 used aluminum profile
2. Adjustable cushion	40 mm × 40 mm
3. Adjustable padded chest (move left and right side)	Overall dimension: 1500 mm × 680 mm × 1263 mm
4. Fixed angle	2. Design 2 used aluminum profile
5. 4 wheels with lock	60 mm × 60 mm
	Overall dimension: 1500 mm × 680 mm × 1263 mm

**Fig. 6.3** Isometric view of design 3



**Table 6.4** Specification of design 3

Specification	Dimension
1. Adjustable height	1. Design 3 used aluminum profile
2. Adjustable padded chest (downward and upward)	40 mm × 40 mm
3. Adjustable angle	Overall dimension: 110 mm × 788 mm × 1379 mm
4. 4 wheels with lock	2. Design 3 used aluminum profile 60 mm × 60 mm
	Overall dimension: 110 mm × 788 mm × 1379 mm

**6.3.3 Simulation Analysis**

The SOLIDWORKS software is used to simulate the foldable topside mechanic’s creeper structure. This software has been chosen for this simulation due to its simplicity to assign the materials. There were three phases to complete the analysis: first phase, pre-processing (mechanical components and assemblies). The second phase is the post-processing (analysis, meshing, and boundary conditions), and the last phase is the solution and the evaluation of the results: stress and strain. The steps involved in the SOLIDWORKS simulation are as follows. Note that Fig. 6.4 shows the example for design 3. The method used was similar to all designs.



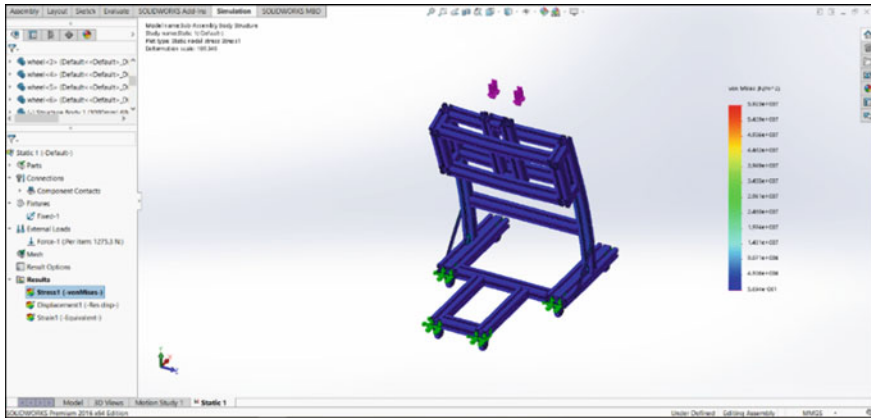


Fig. 6.4 Design 3 in simulation view

## 6.4 Results and Discussion

The design of the foldable topside mechanic's creeper focused on three different weights that were tested at the padded chest in design structure, which is 700, 1000, and 1300 N with two different sizes and dimensions of aluminum (Al) profiles 40 mm × 40 mm and 60 mm × 60 mm that were used in the product design. Three designs were managed to be constructed. Each design has a different operation and function.

### 6.4.1 Simulation Results and Discussion

After the simulation step, the mechanic creeper structure is discussed in terms of maximum stress and strain values. The maximum and value of stress and strain is generated in simulation analysis. These results are shown in Tables 6.5 and 6.6. These tables show the effect of different mechanic weights on the design 1, 2, and 3.

Figures 6.5, 6.6, 6.7, 6.8, 6.9 and 6.10 show the comparison of the three designs in terms of their stress and strain. The result based on the three different loading, 700, 1000, and 1300 N. The result of stress and strain will help to choose which is the best design according to the objective of this project.

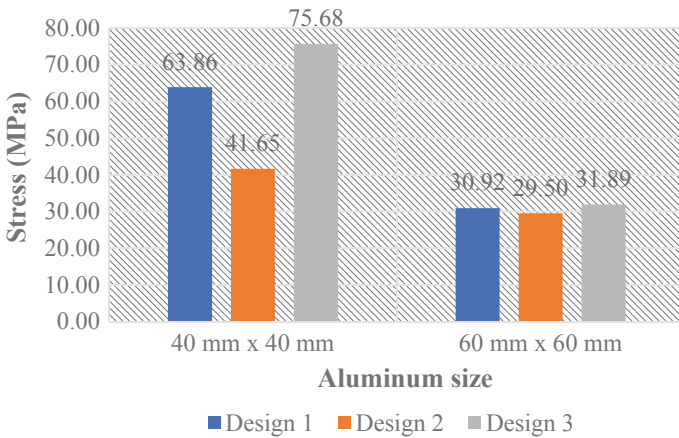
Figures 6.5, 6.6, and 6.7 show the stress versus the aluminum sizes for three designs with a load of 700, 1000, and 1300 N, respectively. For the dimension of 40 mm × 40 mm, the maximum value of stress is 75.68 MPa for design 3 as shown in Fig. 6.5. Meanwhile, the minimum value of stress is 41.65 MPa for design 2. Design 3 increased by around 16% compared to design 1. For the dimension 60 mm × 60 mm, the maximum value is for design 3 (31.89 MPa) and the minimum value is for design 2 (29.50 MPa). The difference between design 2 and design 3 is only a 9%.

**Table 6.5** Stress and strain of the design 1, 2, and 3 for 40 mm × 40 mm of Al sizes

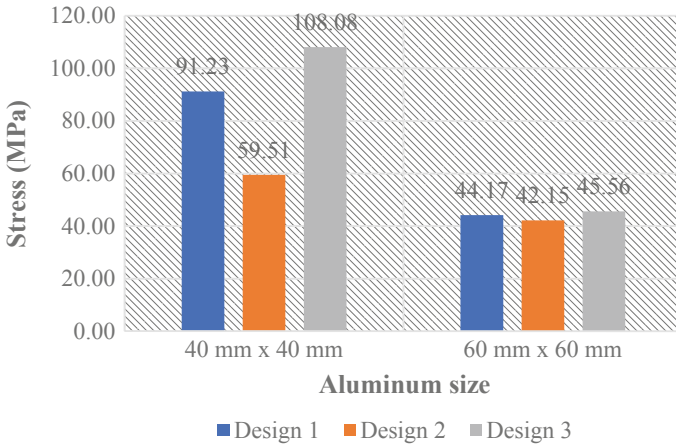
Design	Load (N)	Stress (MPa)	Strain (%)
1	700	63.861	0.000548
	1000	91.231	0.007830
	1300	118.601	0.001020
2	700	41.65	0.00031
	1000	59.51	0.00044
	1300	77.36	0.00057
3	700	75.68	0.00033
	1000	108.08	0.00047
	1300	140.58	0.00061

**Table 6.6** Stress and strain of design 1, 2, and 3 for 60 mm × 60 mm of Al sizes

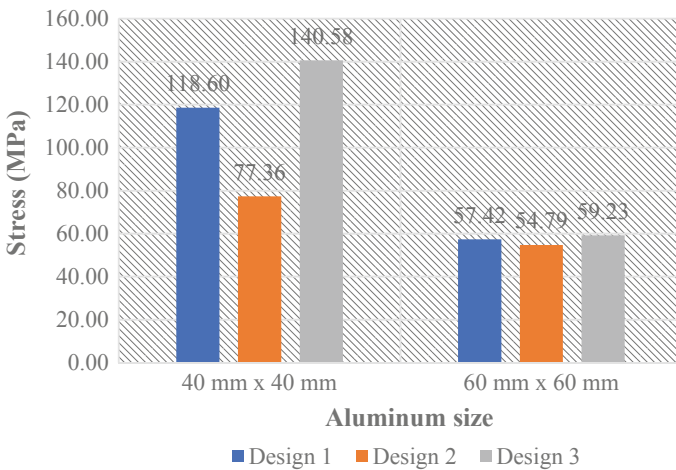
Design	Load (N)	Stress (MPa)	Strain (%)
1	700	30.920	0.00027
	1000	44.170	0.00039
	1300	57.410	0.00051
2	700	29.50	0.00016
	1000	42.15	0.00023
	1300	54.79	0.00031
3	700	31.89	0.00014
	1000	45.56	0.00020
	1300	59.23	0.00026



**Fig. 6.5** Stress analysis; comparison of the three designs at 700 N of load for 40 mm × 40 mm and 60 mm × 60 mm size of aluminum profile



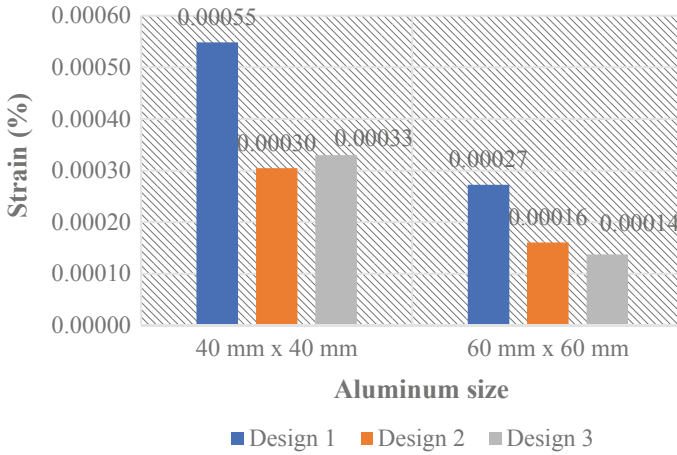
**Fig. 6.6** Stress analysis; comparison of the three designs at 1000 N of load for 40 mm × 40 mm and 60 mm × 60 mm size of aluminum profile



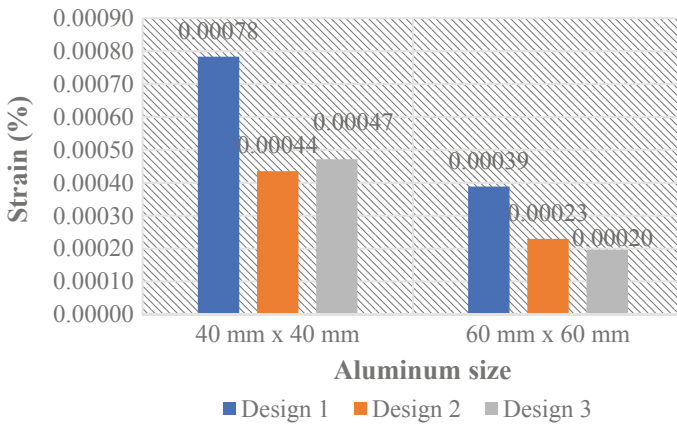
**Fig. 6.7** Stress analysis; comparison of the three designs at 1300 N of load for 40 mm × 40 mm and 60 mm × 60 mm size of aluminum profile

In Fig. 6.6, the design 3 indicates that the highest stress is 108.08 MPa for the 40 mm × 40 mm size of aluminum at 1000 N of load. However, the lowest stress is 59.51 MPa. There are slightly small differences between the stress values for the 60 mm × 60 mm size of aluminum. The maximum and minimum stresses are 45.56 MPa for design 3 and 42.15 MPa for design 2, respectively. The stress value for the 40 mm × 40 mm is higher compared to 60 mm × 60 mm size of aluminum.

The stress versus the size of aluminum profile for design 1, 2, and 3 is shown in Fig. 6.7 for 1300 N of load. For 40 mm × 40 mm, the maximum value of stress is



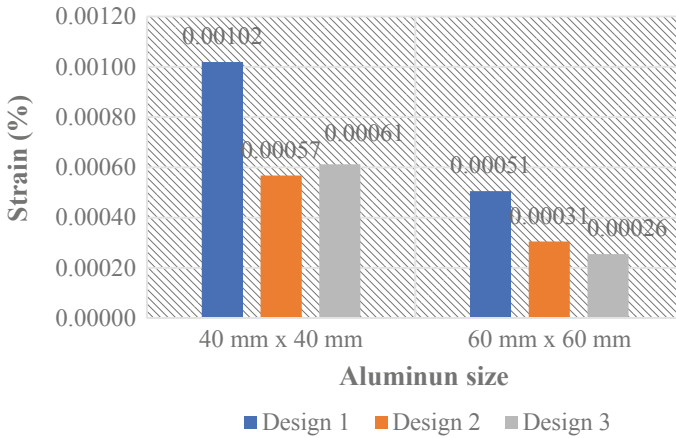
**Fig. 6.8** Strain analysis; comparison of the three designs at 700 N of load for 40 mm × 40 mm and 60 mm × 60 mm size of aluminum profile



**Fig. 6.9** Strain analysis; comparison of the three designs at 1000 N of load for 40 mm × 40 mm and 60 mm × 60 mm size of aluminum profile

140.58 MPa for design 3. The design 2 indicates that the minimum value of stress is 77.36 MPa. In comparison, the stress value dramatically increased about 80% compared to design 2. This figure also indicates small differences in stress value which is the maximum value is 59.23 MPa for design 3 and the minimum value is 54.79 MPa for design 2 for 60 mm × 60 mm of aluminum size.

The strain against the aluminum size for design 1, 2, and 3 with a load 700 N is shown in Fig. 6.8. For the dimension 40 mm × 40 mm, the maximum value of strain is 0.00055% for design 1. However, the minimum value of strain is 0.00030% for design 2. For 60 mm × 60 mm aluminum sizes, the strain decreased as 40 mm ×



**Fig. 6.10** Strain analysis; comparison of the three designs at 1300 N of load for 40 mm × 40 mm and 60 mm × 60 mm size of aluminum profile

40 mm. The maximum strain for design 1 is 0.00027%, and the minimum strain for design 2 is 0.00014%. The percentage of design 3 decreased significantly by 15% compared to design 2.

The strain versus the dimension of aluminum size for design 1, 2, and 3 for 1000 N load is shown in Fig. 6.9. Design 1 indicates that the maximum strain is 0.00078%, and design 2 shows that the minimum strain is about 0.00044% for the 40 mm × 40 mm aluminum size. The minimum and maximum stress for the 60 mm x60mm are 0.00020 for design 3 and 0.00039% for design 1, respectively.

Figure 6.10 shows the strain against the dimension of aluminum profile for design 1, 2, and 3 for 1300 N. The average strain is 0.00073 and 0.00036% for the 40 mm × 40 mm and 60 mm × 60 mm of aluminum sizes, respectively.

Each design has its own considerations over others. For design 1, the design structure is much simpler than the other designs in terms of the design, operation, and function. Designs 1 and 3 have the same movement direction of padded chest. It can move upward and downward. But, for design 2, it can move right- and left-hand side direction. Based on the design structure, the structure of design 3 is much complex than other design for any upcoming fabrication.

The most suitable dimension design of 40 mm × 40 mm to be considered is for design 2 due to its lowest stress and strain value which is at 700 and 1300 N. These values are much lower compared to the other designs. For 60 mm × 60 mm, design 3 is the most suitable to be chosen as the strain value remains to a lower value even though it manages to hold a heavier load as design 2 in dimension 40 mm × 40 mm.

Based on the two-dimensions stated (40 mm × 40 mm and 60 mm × 60 mm), the most appropriate dimension to be used for the aluminum profile based on the analysis is 60 mm × 60 mm. This benefits from lower stress and strain values compared to higher values when using 40 mm × 40 mm dimension. Here, for future development of a real product, the 60 mm × 60 mm aluminum profile dimension in design 3 is

also the most applicable when undergoing a fabrication process. However, further study of safety factor must be done to determine the appropriate aluminum size to fabricate the product. If the design is more than 1 of the safety factors, that means the size is over-designed.

## 6.5 Conclusions

Based on the theory of foldable topside mechanic's creeper and reference of previous designs, three design outputs with two different dimensions were generated. This project focused on the study of strength of a foldable topside mechanic's creeper. For design 1, the design has a fixed height and fixed angle. Design 2 utilizes a similar function as design 3 with the upward and downward movement of the chest support (padded chest). Simulation of strength of the foldable topside mechanic's creeper has been carried out for design 1, design 2, and design 3. Each design has three different load and has been tested with two different dimensions of Al profiles. The stress and strain have been obtained from SOLIDWORKS. The larger Al profile diameters of mechanic's creeper structure indicates ~60% higher strength and a ~55% lower strain compared to the small diameter Al profile diameters.

## References

1. Abaraogu UO, Ezema CI, Igwe SE, Egwuonwu AV, Okafor UC (2016) Work-related back discomfort and associated factors among automotive maintenance mechanics in Eastern Nigeria: a cross sectional study. *Work* 53(4):813–823. <https://doi.org/10.3233/WOR-162247>
2. Moradi M, Poursadeghiyan M, Khammar A, Hami M, Darsnj A, Yarmohammadi H (2017) REBA method for the ergonomic risk assessment of auto mechanics postural stress caused by working conditions in Kermanshah (Iran). *Ann Trop Med Public Health* 10:3
3. Syed Mohamed MS, Basiri MNH (2015) Working posture assessment in a small and medium industry (SMI): automotive repair facility. *Appl Mech Mater* 761:664–667. <https://doi.org/10.4028/www.scientific.net/amm.761.664>
4. Kant I, Noterman JHV, Borm PJA (1990) Observations of working postures in garages using the ovako working posture analysing system (OVVAS) and consequent workload reduction recommendations. *Ergonomics* 33(2):209–220
5. Vyas H, Das S, Mehta S (2011) Occupational injuries in automobile repair workers. *Ind Health* 1108050094–1108050094
6. Creeper Topside mechanic ladder for Garage Workshop Padded Deck Swivel Castors *Buy Creepers* - 890407. (n.d.). <https://www.mydeal.com.au/creeper-topside-mechanic-ladder-for-garage-workshop-padded-deck-swivel-castors-890407>. Accessed 4 Mar 2020
7. Menon B (2017) A study on consumer behaviour of passenger car segments through logistic regression modelling. *Metamorphosis J Manag Res* 16(1):20–32. <https://doi.org/10.1177/0972622517706876>

# Chapter 7

## Potential Use of a Vibration Energy Harvester in Vehicles Using a Linear Motion Electromagnetic Suspension System



Fazidah Saad and Muhammad Najib Abdul Hamid

**Abstract** Vibration energy is one type of abundant energy that can be harvested from a vehicle. The vehicle vibrates due to many reasons such as worn-out parts and joints, or it will vibrate due to engine and transmission vibration. In recent years, several new methods of energy intake have been proposed for vehicle suspensions such as to use the linear electromagnetic energy vibrations. The kinetic energy of the linear motion of a harvest suspension system is converted into electrical energy by a magnetic generator, which generally consists of a set of magnets and coils. The current in the coil is created by the relative movement between the magnets and the coils. Therefore, maximizing the magnetic flux density through the coils is a key element to obtain good regeneration of electrical energy. This article presents the different types of vibration linear electromagnetic energy harvesters used in vehicle suspension systems and the potential use of them. The design and working principle of the linear energy harvesters are explained and discussed. It is concluded that the hybrid linear electromagnetic energy harvester is the most viable when applied to vehicle suspensions because of the higher power generated if compared to other energy harvesters.

**Keywords** Energy harvester · Vibration · Suspension · Linear electromagnetic energy harvesting

### 7.1 Introduction

In recent years, people are paying more attention to the energy intake of the vehicle suspension and its impact on fuel storage. Several studies show that an average

---

F. Saad (✉) · M. N. A. Hamid  
Engineering Section, Universiti Kuala Lumpur, Malaysian Spanish Institute, Kulim Hi-Tech Park,  
09000 Kulim, Kedah, Malaysia  
e-mail: [fazidah@unikl.edu.my](mailto:fazidah@unikl.edu.my)

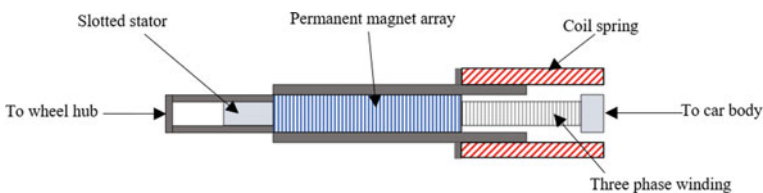
M. N. A. Hamid  
e-mail: [mnajib@unikl.edu.my](mailto:mnajib@unikl.edu.my)

passenger car can produce between 100 and 400 W of power moving at average roads with the average speed was about 97/km/h [1]. Subsequently, the fuel efficiency improvement also can be achieved when there is electrical energy generated [2] and this will directly improve the fuel-saving in vehicles [3].

There is numerous researches in energy harvesting from the vehicle suspension system to recover the dissipated vibration energy in a vehicle suspension, and it has been suggested that there are many types of energy harvesting mechanisms for the suspension system. The research to date has tended to characterize three of the most established transducers methods of energy harvesting from a vehicle suspension that is electrostatic, piezoelectric, and electromagnetic [4].

The electrostatic transducers can extract current flow from the movement of the overlapping two electrodes of a polarized capacitor change when the suspension is vibrating. The overlapping movement causes the voltage inside the capacitor to change so that the current flow will rise from an external circuit. The piezoelectric transducer operates by using the vibrations from the suspension to distort a piezoelectric material such as ceramic to raise the voltage in the capacitor and to directly generate electric power. Among the various methods of collecting vibration energy, electromagnetic collectors are the most popular in vehicle suspension systems due to their high energy conversion capacity, quick response, strong control, and energy recovery capabilities [5–7]. The electromagnetic transducers utilize the relative vibration motion between a magnet and a coil to change the magnetic flux in the system, and this will generate an alternating current and voltage across the coil.

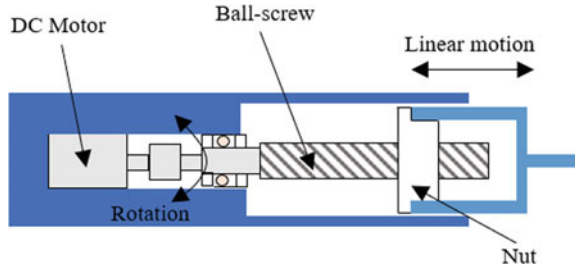
The main purpose of the electromagnetic generator is to convert the kinetic energy of the vibration into electricity. The electromagnetic energy harvester at vehicle suspension uses the linear vibration motion of the suspension to drive an electromagnetic generator which can be linear or rotational. Therefore, there are mainly two types of electromagnetic energy harvester that is depending on the motion mechanism of the electromagnetic generator, whether it is linear motion or rotational motion. The linear electromagnetic collector converts the vertical oscillating energy capacity directly into electricity based on the medium structure's electromagnetic induction [8] as shown in Fig. 7.1, whereas the rotational motion of the electromagnetic generator uses mechanism such as ball screw, rack-pinion, and hydraulic motor to convert linear vibration into rotational motion [6]. Figure 7.2 shows the ball screw energy harvester, and Fig. 7.3 shows the rack-pinion energy harvester. Although there are two types of electromagnetic energy harvester for the vehicle suspension system,



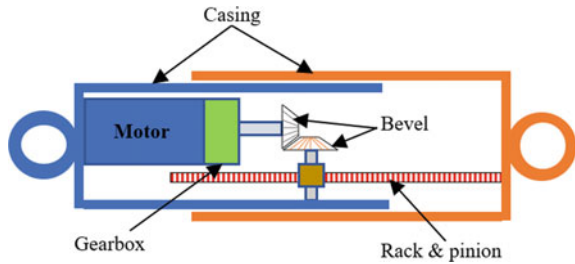
**Fig. 7.1** Linear electromagnetic energy harvester [9]



**Fig. 7.2** Ball screw electromagnetic energy harvester [4]



**Fig. 7.3** Rack-pinion electromagnetic energy harvester [4]



this paper aims to study only the linear type of electromagnetic energy harvester in the vehicle suspension system.

## 7.2 Linear Electromagnetic Energy Harvesting in the Vehicle Suspension System

Linear electromagnetic energy harvesting is a simple structural system that converts vertical oscillating kinetic energy into electrical energy by electromagnetic induction. The relative oscillation movement of the oscillation propagates to the magnetic translation movement with respect to the coil and causes a change in the magnetic flux within the induced voltage coil. The induced voltage here is according to Faraday’s law as in Eq. (7.1).

$$\varepsilon_v = -\frac{d\varnothing_B}{dt}, \tag{7.1}$$

where  $\varepsilon_v$  is the induced voltage and  $\varnothing_B$  is the magnetic flux.

If compared to a rotary electromagnetic energy harvester, the linear harvester offers a high capacity of regenerated power because there is no power loss due to transmission of the rotary generator mechanism. There are many types of linear electromagnetic energy harvesters for vehicle suspensions, and the most common types are discussed in this paper.

### 7.2.1 Electromagnetic Regenerative Shock Absorber

Regenerative electromagnetic dampers are popular with all types of regenerative dampers due to their small design and modest production. By manipulating the magnet and coil design to change the design, the output power generated can be increased.

#### 7.2.1.1 Magnetic Array System Design

To increase the strength of the magnetic field at high output power, different magnetic methods are recommended. One of the easiest methods is to double the number of magnets, producing more lines of magnetic flux that can get trapped between two layers of magnets. The coil is connected between two magnetic layers, thus increasing the output voltage [10]. Many researchers have tried this way in their designs as it is efficient and simple to produce [11–13]. Although this method is efficient to boost the output voltage, it will create the problem of extra weight and this is not appropriate as the main objective of the regenerative shock absorber is to save fuel consumption. Figure 7.4 shows an example of the design of the electromagnetic damper with two layers of magnets [11].

In Fig. 7.4, the magnets are separated by spacers. Separation is important for magnetic flux cancellation because no separation occurs due to short-distance magnetic force, so the behavior is a combination of two isolated individual magnets. As the distance between the magnets increases, when the distance between the thicknesses is equal to that of the magnet, the cancellation of the magnetic flux becomes clearer, and the captured energy reaches the maximum value [10].

Besides arranging the magnets with spacer, the magnetic arrangement pattern of the Halbach array had proven to successfully generate more output voltage. Figure 7.5 illustrates by rotating the direction of the magnetic pole each time to make a Halbach arrangement, and the magnetic flux line merges on the side of the Halbach line closest

Fig. 7.4 Design with two layers of magnets of the electromagnetic damper [11]

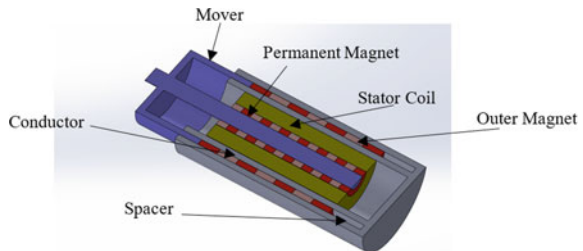
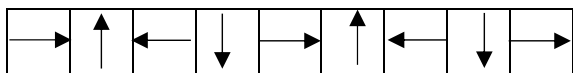
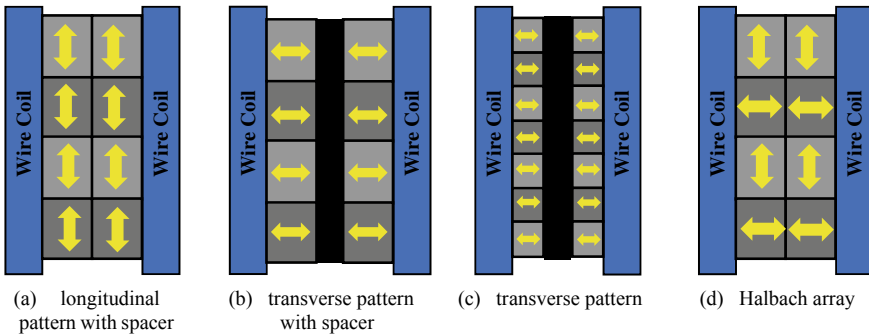


Fig. 7.5 Halbach array magnet stack [15]





**Fig. 7.6** Different magnetic flux plots [14]

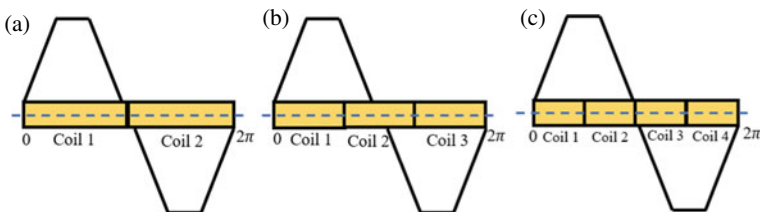
to the coil, while maintaining zero magnetic field intensity on the other side of the magnetic field [14].

By using the Halbach array, with or without a spacer, the magnetic flux density obtained is higher than that of conventional longitudinal and transverse magnetic polarization systems. Figure 7.6 demonstrates the different magnetic flux plots in different magnet arrangements.

### 7.2.1.2 Coil Design

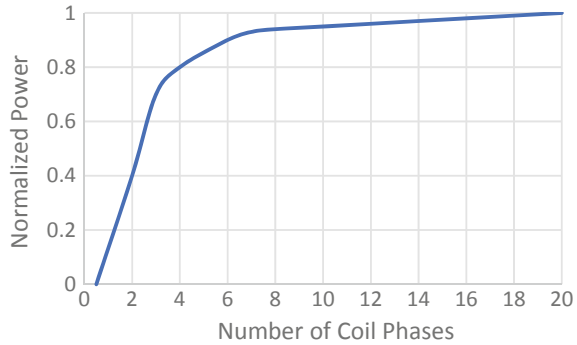
There are studies proposed in designing the coil based on the magnet arrangement to get more energy generated [16]. The results show that the number of coil layers, coil resistance, and wire strips affect producing more energy with more coil layers. Although the use of lower specification numbers does not produce a higher voltage, it requires less space and can be installed properly in the harvester parking lot.

Figure 7.7 demonstrates the results of using different phase coil in one magnetic cycle, and Fig. 7.8 indicates the relationship between the numbers of coil phases with the normalized power. It is proven that with a higher coil phase number, it will produce higher normalized power [13].



**Fig. 7.7** Different coil design [13]: **a** Two-phase coil. **b** Three-phase coil. **c** Four-phase coil

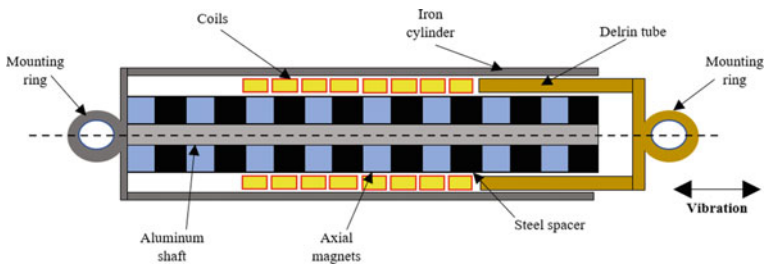
**Fig. 7.8** Normalized power and number of coils phases [13]



### 7.2.2 Tubular Linear Electromagnetic Transducers

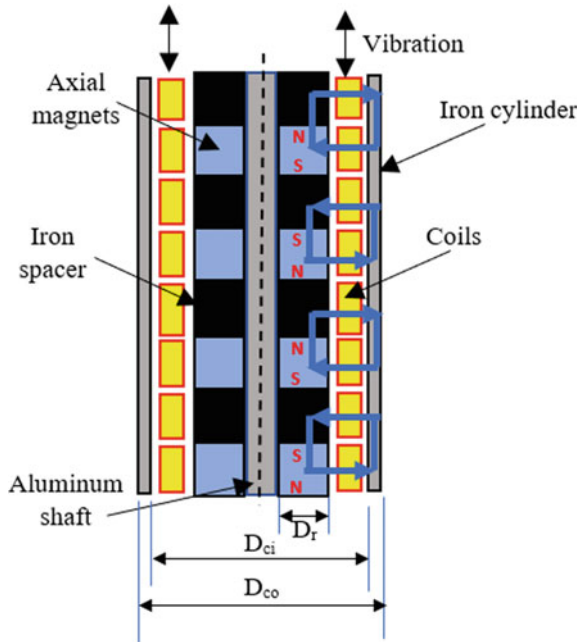
Same as other linear electromagnetic energy harvesters, the tubular linear electromagnetic transducer is comprised of coil assemblies and a magnet. It converts the vibration energy at the suspension into electricity when operating simultaneously. There are four types of tube linear electromagnetic transformers, according to different magnetic configurations. They are steel spacers and single layer axial magnets, double layer shaft magnets and steel spacers, single layer axial and radial magnets, and two-layer axial and radial magnets. Figure 7.9 shows the single-layer tubular linear electromagnetic transducer with axial magnets.

The tubular linear electromagnetic transducer has a magnet assembly that is made of ring-shaped NdFeB permanent magnets and ring-shaped high magnetically permeable steel spacers that are stacked on a high reluctance material rod such as aluminum and covered in a tubular steel casing [13]. The magnets are arranged such that adjacent magnetic poles face each other to deflect the magnetic flux radially. A concentric outer cylinder made of material with high magnetic permeability (such as steel) is used to reduce the magnetic resistance of the magnetic ring and increases the density of the magnetic flux in the coil. The coil assembly consists of several copper coils in a tube.



**Fig. 7.9** Single-layer tubular linear electromagnetic transducer with axial magnets [13]

**Fig. 7.10** Tubular linear electromagnetic energy harvester dimensions and parameters [13]



During the vibration at the suspension, the coil casing moves relatively in the energy harvester and this creates the magnetic flux when it moves on the permanent magnet. This is clearly shown in Fig. 7.10.

The result obtained from energy harvesting is that when RMS suspension velocity is at 0.025–0.5 m/s, the prototype was able to harvest 16–64 W of energy [17].

### 7.2.3 Electromagnetic Linear Vibration Energy Harvester with Ferrofluid as a Lubricant

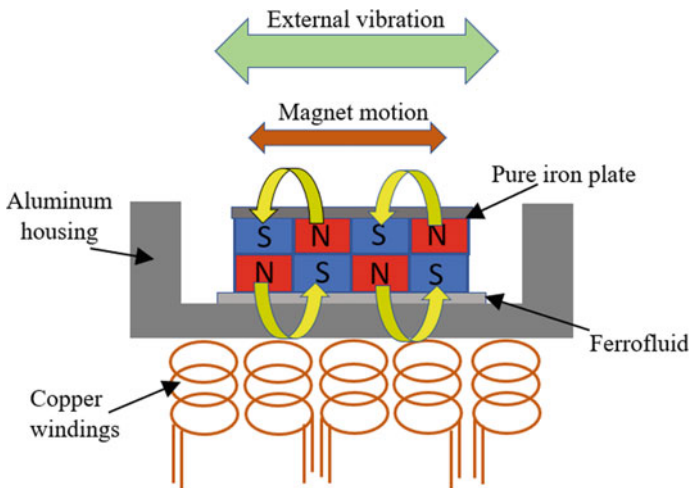
This section introduces the electromagnetic linear vibration energy harvester, which uses a rectangular permanent magnetic arrangement to complete the test without springs and ferromagnetic fluids as lubricants. A ferrofluid is a pulp suspension made of ferrofluid particles suspended in carrier liquids such as organic solvents or water. The magnetic properties of the dispersion of each particle are described by the Langevin theory of paramagnetism. There are two types of these energy harvesters which are by using a springless proof mass and using a sliding permanent magnet array but both of them are using the ferrofluid as the lubricant.

### 7.2.3.1 Using Springless Proof Mass

A linear electromagnetic collector with a spring-free mass must maintain a constant motion between the permanent magnet and the coil while maintaining a short gap and a magnetic direction [18]. Many types of magnets can be utilized as permanent magnets such as rectangular magnets, rolling magnets [19], ball bearing [20], and cylindrical magnet [21] but the simplest assembly is the rectangular magnets. A schematic diagram of the linear rectangular magnet energy harvester using a ferrofluid is shown in Fig. 7.11.

In response to low-frequency external vibrations in the suspension, a multi-pole magnetic field's lateral motion produces a voltage across the set of copper coils formed under the aluminum housing. When the suspension vibrates laterally, the multi-pole magnet vibrates horizontally and is caused by a voltage across the series copper coil. Ferro-fluids reduce friction between the magnetic surface and the aluminum housing.

The results for this harvester proved that when it is applied with sinusoidal vibration ranging from 7 to 20 Hz, the maximum voltage of 0.47 V was obtained when the test did not use the ferrofluid while there was a slight increment when using the ferrofluid that the maximum generated voltage was 13 Hz [18].

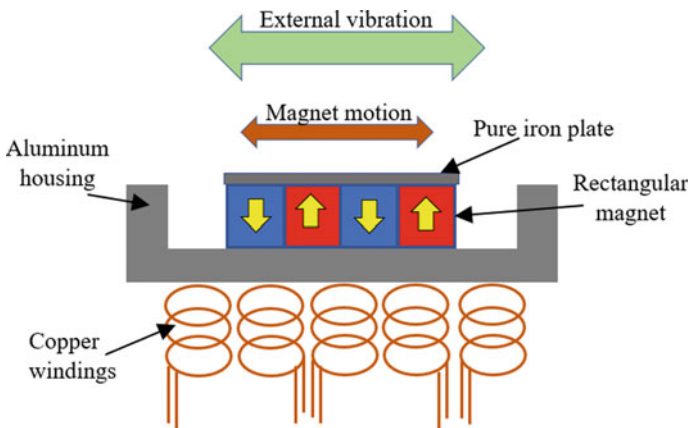


**Fig. 7.11** Schematic of linear energy harvester using springless multi-pole planar magnets with ferrofluid lubrication [18]

### 7.2.3.2 Using Sliding Permanent Magnet Array

As the suspension vibrates and the harvester moves sideways, the magnetic assembly slides backwards onto the housing, thus reducing wear caused by friction and ferro-magnetic fluids, which greatly increases the long-term reliability of the device. The multi-polar magnetic arrangement with four bar magnets and polar shoes is used as a test mass, which moves inside the housing due to the suspension vibration. Same as the previous design, an array of copper windings is fixed at five coil bobbins and connected in series. As the magnets are not supported by a spring element, they can make constant impacts with the sidewall of the aluminum housing when dealing with vibration motion [22]. By having the ferrofluid inside the housing, the magnets can move freely inside the housing with the aid of the ferrofluid as the lubricant. The ferrofluid has large magnetic permeability and forms a very thin layer under the magnet array. Thus, when ferrofluid droplets are distributed on the surface of the magnetic field, a high density of magnetic flux is formed at the edges of the magnet, and when the magnetic field is placed on the housing, it is squeezed into a thin layer. The magnetic channels float in a thin layer of ferrofluid and sliding, reducing friction and responding to external vibrations [22]. When the suspension vibrates, the magnet motion induces the variation of magnetic flux through the copper coil winding, which will immediately generate electric power. Figure 7.12 shows the top and bottom view of linear energy harvester using a sliding permanent magnet array with ferrofluid lubrication.

Harvesting is tested with different input frequencies and accelerations. For equipment using ferrofluid for lubrication, the maximum output power produced is 493 W, which is 4.37% higher than without ferrofluid [22].

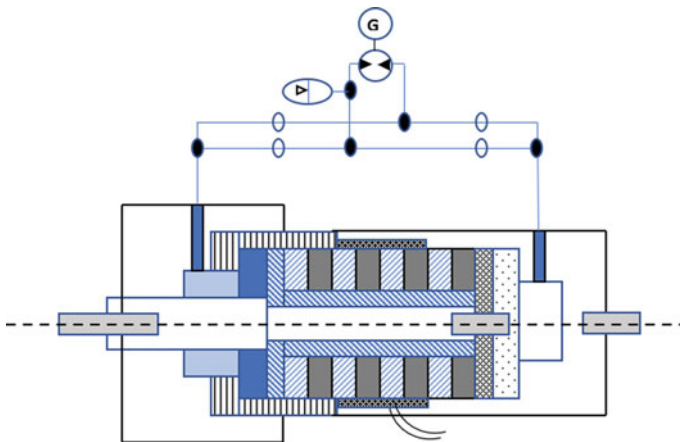


**Fig. 7.12** Schematic diagram of linear energy harvester using sliding permanent magnet array with ferrofluid lubrication [22]

### 7.2.4 Hybrid Regenerative Shock Absorber

Previously, only the single element transducer which is an electromagnetic transducer was discussed. This section examines hybrid power intake, which is integrated with piezoelectric and electromagnetic transformers. In addition to piezoelectric and electromagnetic, there are also energy harvesting prototypes, in which the coil and piezoelectric are cantilever beams and their mass are not tungsten alloy magnets [23]. Besides, there was another prototype that was similar to the previous energy harvester but used a silicon wafer as the cantilever beam [24]. The harvester can generate more power within its size range. Hybrid units that use both powers without increasing their size have a power harvest that combines piezoelectric and electromagnetic transformers. Hybrid energy harvesters that mix piezoelectric and electromagnetic sensors can produce strong magnetic fields on stationary coils [25]. This is because when the crop is excited by external vibrations, both piezoelectric and electromagnetic produce electricity or energy.

In addition to the hybrid regenerative shock absorber list, there is the hydraulic and linear electromagnetic generator. Figure 7.13 shows the cross-sections of hybrid energy-saving shock absorbers. The two-cylinder system, in which the master cylinder is used as a shock absorber, reduces vibration through vehicle suspension and provides accelerated acceleration to the secondary cylinder. If the additional cylinder fails, the main cylinder will continue to operate as a passive exhaust. It can generate large amounts of energy without affecting travel comfort and road handling performance [26]. In addition, hydraulic regenerative shock absorbers are also being developed, which eliminate the movement of hydraulic oils and vibrating body energy. The energy generated by hydraulic piston generators and linear generators can be used to charge energy-saving devices [27].



**Fig. 7.13** The cross-section of the hybrid regenerative shock absorber [27]



The hydraulic piston with linear electromagnetic generator [25] succeeded to generate 15 W of output during 35 km/h of vehicle speed while the combined linear electromagnetic generator and hydraulic rotary generator produce 6 V of voltage output and 0.003 W at 0.005 m/s vehicle speed. All these results had shown that by efficiently integrating the hybrid transducer, more power could be generated as compared to a single transducer.

### 7.3 Discussion

In this paper, a linear electromagnetic energy harvester for automotive applications is studied. Today the use of energy harvester suspension devices is necessary for vehicle construction to increase not only the driving comfort but also safety and performance. The main purpose of the optimization of the linear energy harvester is aiming at harvesting the vibration energy dissipated in the traditional suspension system and directly reduce fuel consumption and pollutants. Commonly designed systems for the linear electromagnetic energy harvester are depending on their working principle, which is electromagnetic regenerative shock absorber, tubular linear electromagnetic transducers, electromagnetic linear vibration energy harvester with ferrofluid as a lubricant, and hybrid regenerative shock absorber. The characteristics of some studies carried out in this direction are given in Table 7.1.

**Table 7.1** Studies on energy harvesting suspension systems and their characteristics

Reference	Energy harvesting system	Method	Approach	Power output
Gupta [12]	Electromagnetic regenerative shock absorber	Experimental	Frequency range of 0–100 Hz	7.4–88.8 W
Tang [13]	Tubular linear electromagnetic transducers	Experimental	0.11 m/s	2.8 W
Zuo [17]		Experimental	0.025–0.5 m/s	16–64 W
Chae [18]	Electromagnetic linear vibration energy harvester with ferrofluid as lubricant	Experimental	7–20 Hz	0.47 V
Chae [22]		Experimental	7–20 Hz	0.493 $\mu$ W
Singh [26]	Hybrid regenerative shock absorber	Simulation	35 km/h	15 W
Demetgul [27]		Analytical	0.05 m/s	6 V, 0.03 W

## 7.4 Conclusion

There have been several studies in the methods of vibration energy harvesting from the vehicle suspension and a few of them are focusing on the linear motion electromagnetic type because of the simplicity of the design yet achieving high generated energy. The feasibility and potential of the vibration linear motion electromagnetic energy harvesters at the suspension in converting the vibration energy into electrical energy is very providential. This paper presented some common linear electromagnetic energy harvester used in vehicle suspensions with a view of understanding the method of energy harvesting and its compatibility of being used at the vehicle suspension. It was found that there is potential in generating high electrical energy from vibration energy harvester using the linear motion electromagnetic suspension system. This is proven by Gupta [12] who used a linear tubular electromagnetic energy harvester and able to generate up to 88.8 W of output power during testing on an ATV traverse over a  $4 \times 4$  beam.

In summary, the current study unveils just the tip of the iceberg of the linear electromagnetic energy harvester. Each type of linear energy harvester has its own advantageous and disadvantageous, but from all types of linear energy harvesters presented in the paper, the hybrid regenerative energy suspension has more potential in generating more energy as they gained power from not only one method of energy harvester, and this is the most opportune matter to achieve the main purpose of the energy harvester.

Despite the fact that the potential use of linear electromagnetic energy harvester is very promising, there are still rooms to improve in terms of the mechanical and electrical circuit design, system efficiency, vehicle handling and comfort, and many more issues as the optimum use of high energy permanent magnets requires sturdy basis design.

## References

1. Zuo L, Zhang PS (2013) Energy harvesting, ride comfort, and road handling of regenerative vehicle suspensions. *J Vib Acoust Trans ASME* 135(1):1–8. <https://doi.org/10.1115/1.4007562>
2. Fairbanks J (2011) Vehicular thermoelectrics: a new green technology. In: Proceedings of the 2nd thermoelectrics applications
3. Anderson Z (2009) Levant Power A ground-breaking active suspension system
4. Eriksson J, Piroti S (2016) Review of methods for energy harvesting from a vehicle suspension system.
5. Cassidy IL, Scruggs JT, Behrens S, Gavin HP (2011) Design and experimental characterization of an electromagnetic transducer for large-scale vibratory energy harvesting applications. *J Intell Mater Syst Struct* 22(17):2009–2024. <https://doi.org/10.1177/1045389X11421824>
6. Li P, Zuo L (2014) Electromagnetic re-generative suspension system for ground vehicles. *IEEE Int Conf Syst Man Cybern* 2513–2518. <https://doi.org/10.1109/SMC.2014.6974304>
7. Li Z, Zuo L, Kuang J, Luhrs G (2013) Energy-harvesting shock absorber with a mechanical motion rectifier. *Smart Mater Struct* 22(2). <https://doi.org/10.1088/0964-1726/22/2/025008>

8. Abdelkareem MAA, Xu L, Ali MKA, Elagouz A, Mi J, Guo S et al (2018) Vibration energy harvesting in automotive suspension system: a detailed review. *Appl Energy* 229:672–699. <https://doi.org/10.1016/j.apenergy.2018.08.030>
9. Gysen BLJ, Van Der Sande TPJ, Paulides JJH, Lomonova EA (2011) Efficiency of a regenerative direct-drive electromagnetic active suspension. *IEEE Trans Veh Technol* 60(4):1384–1393. <https://doi.org/10.1109/TVT.2011.2131160>
10. Zhang R, Wang X, John S (2018) A comprehensive review of the techniques on regenerative shock absorber systems. *Energies* 11(5). <https://doi.org/10.3390/en11051167>
11. Ebrahimi B, Bolandhemmat H, Khamesee MB, Golnaraghi F (2011) A hybrid electromagnetic shock absorber for active vehicle suspension systems. *Veh Syst Dyn* 49(1–2):311–332. <https://doi.org/10.1080/00423111003602400>
12. Gupta A, Jendrzejczyk JA, Mulcahy TM, Hull JR (2006) Design of electromagnetic shock absorbers. *Int J Mech Mater Des* 3(3):285–291. <https://doi.org/10.1007/s10999-007-9031-5>
13. Tang X, Lin T, Zuo L (2014) Design and optimization of a tubular linear electromagnetic vibration energy harvester. *IEEE/ASME Trans Mechatron* 19(2):615–622. <https://doi.org/10.1109/TMECH.2013.2249666>
14. Zhang PS (2010) Design of electromagnetic shock absorber for energy harvesting from vehicle suspensions. Thesis of Master of Science degree
15. Jang SM, Choi JY, Lee SH, Cho HW, Jang WB (2004) Analysis and experimental verification of moving-magnet linear actuator with cylindrical Halbach array. *IEEE Trans Magn* 40(4 II):2068–2070. <https://doi.org/10.1109/TMAG.2004.832157>
16. Elvin NG, Elvin AA (2011) An experimentally validated electromagnetic energy harvester. *J Sound Vib*. <https://doi.org/10.1016/j.jsv.2010.11.024>
17. Scully B, Zuo L, Shestani J, Zhou Y, Scully B, Shestani J, Zhou Y (2010) Design and characterization of an electromagnetic energy harvester for vehicle suspensions. In: ASME international mechanical engineering congress and exposition, proceedings, vol 10(PART B), pp 1007–1016. <https://doi.org/10.1115/IMECE2009-12091>
18. Chae SH, Ju S, Choi Y, Jun S, Park SM, Lee S, et al (2013) Electromagnetic vibration energy harvester using springless proof mass and ferrofluid as a lubricant. *J Phys Conf Ser* 476(1). <https://doi.org/10.1088/1742-6596/476/1/012013>
19. Bowers BJ, Arnold DP (2009) Spherical, rolling magnet generators for passive energy harvesting from human motion. *J Micromech Microeng* 19(9). <https://doi.org/10.1088/0960-1317/19/9/094008>
20. Hergert RJ, Hanrahan B, Ghodssi R, Holmes AS (2013) Performance of integrated retainer rings in silicon micro-turbines with thrust style micro-ball bearings. *J Micromech Microeng* 23(6). <https://doi.org/10.1088/0960-1317/23/6/065033>
21. Pillatsch P, Yeatman EM, Holmes AS (2012) A scalable piezoelectric impulse-excited energy harvester for human body excitation. *Smart Mater Struct* 21(11). <https://doi.org/10.1088/0964-1726/21/11/115018>
22. Chae SH, Ju S, Choi Y, Chi YE, Ji CH (2017) Electromagnetic linear vibration energy harvester using sliding permanent magnet array and ferrofluid as a lubricant. *Micromachines* 8(10). <https://doi.org/10.3390/mi8100288>
23. Roundy S, Wright PK, Rabaey J (2003) A study of low level vibrations as a power source for wireless sensor nodes. *Comput Commun* 26(11):1131–1144. [https://doi.org/10.1016/S0140-3664\(02\)00248-7](https://doi.org/10.1016/S0140-3664(02)00248-7)
24. Beeby SP, Torah RN, Tudor MJ, Glynne-Jones P, O'Donnell T, Saha CR, Roy S (2007) A micro electromagnetic generator for vibration energy harvesting. *J Micromech Microeng* 17(7):1257–1265. <https://doi.org/10.1088/0960-1317/17/7/007>
25. Ab Rahman MF, Kok SL, Ali NM, Hamzah RA, Aziz KAA (2013) Hybrid vibration energy harvester based on piezoelectric and electromagnetic transduction mechanism. In: CEAT 2013—2013 IEEE conference on clean energy and technology, pp 243–247. <https://doi.org/10.1109/CEAT.2013.6775634>
26. Singh S, Satpute NV (2015) Design and analysis of energy-harvesting shock absorber with electromagnetic and fluid damping. *J Mech Sci Technol* 29(4):1591–1605. <https://doi.org/10.1007/s12206-015-0331-7>

27. Demetgul M, Guney I (2017) Design of the hybrid regenerative shock absorber and energy harvesting from linear movement. *J Clean Energy Technol* 5(1):81–84. <https://doi.org/10.18178/jocet.2017.5.1.349>

# Chapter 8

## Performance Analysis of a Coated Porous Medium Burner for Cogeneration



**Ahmad Kamal Ismail, Mohd Zulkify Abdullah, Nor Haslina Ibrahim, Khairul Akmal Shamsuddin, and Ayub Ahmed Janvekar**

**Abstract** The cogeneration concept can be applied to various heat producing generating systems, one of the popular choices is the burner. The popular way in which heat energy can be converted into electrical energy is by adopting thermoelectric (TE) cells. TE cells can perform better if a porous media burner can be involved instead of conventional burners. The present work took butane as source of fuel, and the equivalence ratio was varied to the best possible extend. The range to get a stable flame was found from 0.16 lpm to 0.25 lpm. The unit to measure the flow rate of both butane and air was kept at lpm (liter per minute). The burner was more of portable in nature, and the maximum amount of power it can produce was upto 0.5 W. In addition, coating of the porous media was on the factors which was used to enhance the conversion efficiency by 0.45%, while thermal efficiency was noted about 57%. With this data it was made acceptable that coating can be a good way to improve the burner performance.

**Keywords** Combustion · Burner · Porous media combustion · Porous media burner · Cogeneration

---

A. K. Ismail (✉) · N. H. Ibrahim · K. A. Shamsuddin  
Universiti Kuala Lumpur, Malaysian Spanish Institute Kulim Hi-Tech Park, 09000 Kedah, Malaysia  
e-mail: [ahmadkamal@unikl.edu.my](mailto:ahmadkamal@unikl.edu.my)

N. H. Ibrahim  
e-mail: [norhaslina@unikl.edu.my](mailto:norhaslina@unikl.edu.my)

K. A. Shamsuddin  
e-mail: [khairulakmal@unikl.edu.my](mailto:khairulakmal@unikl.edu.my)

A. K. Ismail · M. Z. Abdullah  
Universiti Sains Malaysia, Engineering Campus, 14300 Penang, Malaysia  
e-mail: [mezul@usm.my](mailto:mezul@usm.my)

A. A. Janvekar  
School of Mechanical Engineering, VIT University, Chennai, TN 600127, India

## 8.1 Introduction

Nowadays the authorities impose strict conditions on air pollution caused by hazardous gases released from industrial and domestic combustion devices, due to its effect on global warming. It is rather impossible to avoid carbon footprint from combustion products such as carbon dioxide as long as hydrocarbon fuels are consumed on a daily basis. A better combustion and thermal efficiency produced by a burner is the indicator of better emission released. A new technique in combustion has demonstrated an improvement in combustion which is the porous medium combustion technique. Another main concern of researchers is that the heat generated is not fully utilized, and the majority of the heat is dissipated to the environment. Therefore, recent studies focused on the so-called cogeneration system which utilizes the heat provided by the burner and convert it into other forms of energy. Thermoelectric (TE) generators operate by utilizing the Seebeck effect which produces electricity when subjected to a temperature gradient across two dissimilar metals joined together.

## 8.2 Literature

There exist various ways in which conversion of heat energy can be converted into electric energy, one of the optimum ways can be used by utilizing thermoelectric (TE) cells. The basic phenomenon which runs in the background of TE cells is the Seebeck effect, where the cell diodes present in TE cells help in converting the heat energy into electric power. The intension is always to get more power from TE cells, which can be improved by enhancing the temperature differences across hot and cold regions of cells. Different types of semiconductors are available in the commercial market, but the selection should be done based on the working temperature of the burner. Generally, n- or p-type semiconductor components are popular due to their high performance capacity [19]. There are numerous investigation reported on TE cells in combination with burners and still today are trending due to its demand [3, 4, 13, 14, 16, 18, 20]. Qiu and Hayden [17] focused on an experimental work with a burner involving a power generation system with TE cells. The objective of the work was to get more power output, and furthermore it can be produced in large scale for household applications. Addition of porous media in burners has more application in household stoves rather than industrial applications [2]. The other applications of porous media burners can be used by considering a submerge flame [7–9]. While, Posthill [16] took a challenge on focusing on the portability issue with burners. The intension of the team is to make a more portable burner by reducing the shape and size of the important components of the burner system. To make the system more effective, they replaced the conventional LPG by butane as the main fuel input. Next, Mueller [15] avoided the ball porous media and adopted foam as the main type of material. The team considered a SiC porous medium in the reaction zone and generated power to best possible extent. Furthermore, another unique and novel

porous media burner can be seen in literature [1, 10–12]. To enhance the porous media performance in combustion, coating is the best technique which has attracted many researchers [6]. Furthermore, burners with higher thermal efficiency can also be noted [5]. Now, restricting toward only indoor/outdoor applications, the presented burner was developed to get more electric power. It focused only on the heat generated on the wall of the burner.

### 8.3 Methodology

The actual setup of the burner system with the cogeneration unit can be seen in Fig. 8.1. The system involves all the commonly used components, namely the burner housing, TE cells, ducts for the supply of butane and air, premix units, and the stand to hold the unit. Thermocouples were used to get temperature profiles, while combustion gas analyses was performed using a commercially available gas detector. To get the accurate equivalence ratio the air alone was changed, since the flue input

**Fig. 8.1** Burner setup



Fig. 8.2 TE cells

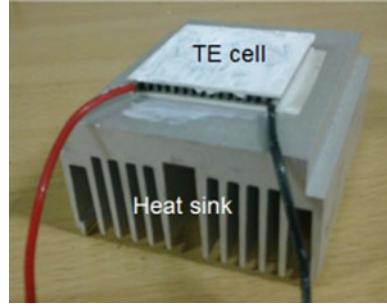
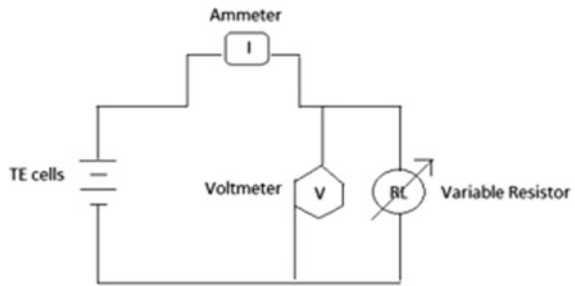


Fig. 8.3 Circuit diagram



was kept constant. Furthermore, the effect of coating was also considered across various equivalence ratios. Figure 8.2 indicates the TE cells used. In addition, with the line diagram the actual connection of electric circuit is highlighted (Fig. 8.3).

Collocation of thermal efficiency is the critical aspect in case of a porous media burner, one of the ways is considering the law of conservation of energy. Wherein a simple concept of energy flowing inside the system and energy coming out of the system is considered. To represent in mathematical form, Eq. (8.1) is written as below to get the thermal efficiency.

$$\eta_{th} = \frac{Q_{heating}}{Q_{in}} \times 100. \tag{8.1}$$

### 8.4 Results and Discussion

The resistance in a circuit plays a vital role to get the maximum voltage and current in the circuit. In the present used circuit the resistance was maintained at 100 Ω. For the considered resistance, voltage and current were noted at optimum equivalent ratio. The best equivalence ratios are 0.8 and 1.3, which are under lean and rich conditions, respectively. The graphs are plotted as indicated in Figs. 8.4 and 8.5. Since a base reaction zone was established with the uncoated alumina, the performance of the



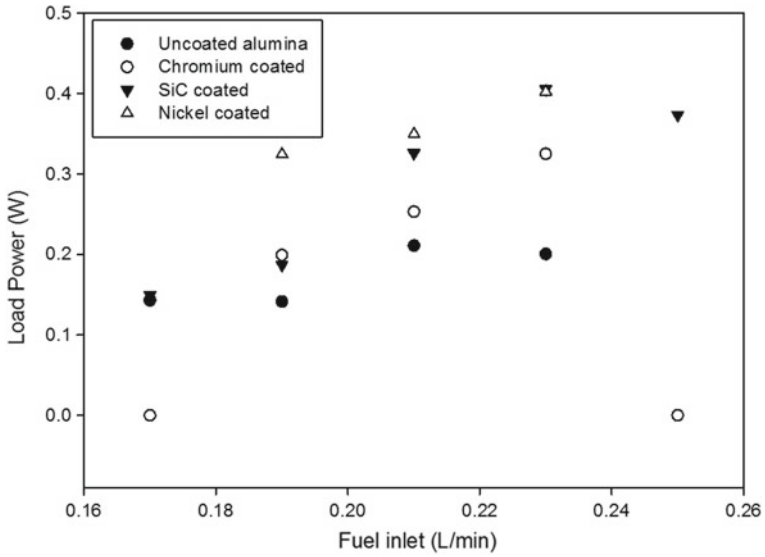


Fig. 8.4 Variation of electric load with various fuel input at equivalence ratio 0.8

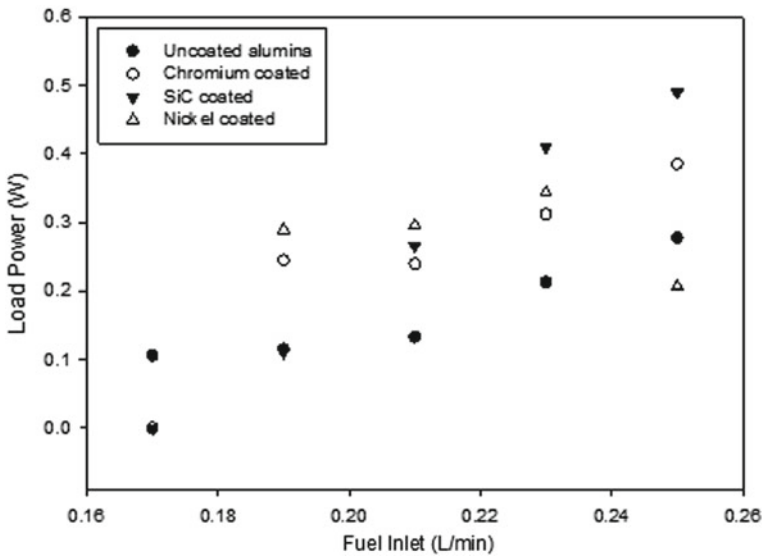
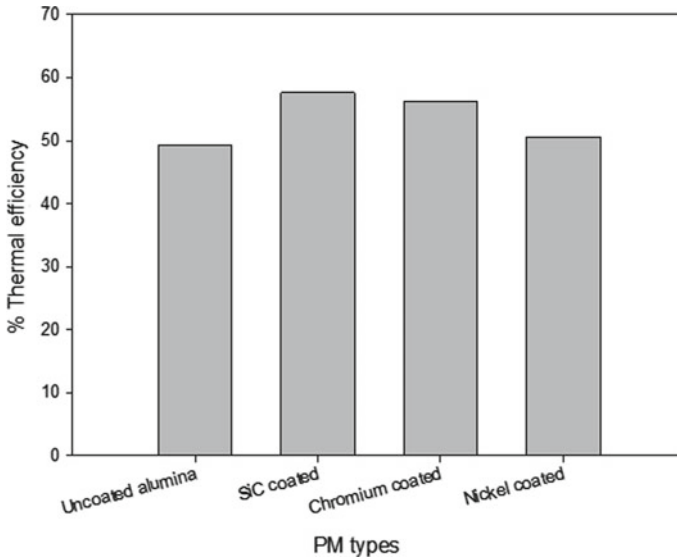


Fig. 8.5 Variation in electric load with various fuel inputs at equivalence ratio 1.3



**Fig. 8.6** Variation in  $\eta_{th}$  and reaction zone

burner was decreased. To enhance further the performance, a Ni coating was given thereby the electric performance was enhanced from 0.15 W to nearly 0.4 W. Now, with SiC coating the value moved from 0.15 W to 0.41 W. The range of fuel was kept between 0.16 lpm to 0.25 lpm.

On the other hand, with an equivalence ratio of 1.3 which comes under the category of rich combustion, the performance was slightly better as shown in Fig. 8.5.

In addition, the thermal efficiency was also noted for various configurations and with the help of Fig. 8.6 a better overview can be generated. It is clear that the maximum thermal efficiency was noticed for the coating with SiC.

On the other hand, the study also intended to consider the conversion efficiency. To get better overall view Fig. 8.7 is plotted, from which maximum cogeneration efficiency notices by adopting silicon carbide coating. Which was then lined up by chromium and nickel coating. On commenting with actual percentage of conversion efficiency, it can be noticed that for 6 cell connection conversion efficiency for thermometric cells was rounded up to 0.073% as compared to a total of 0.438%. While, the conversion efficiency with SiC coating was found out to be 0.44%. Thus, it can be noted that coating adds value in overall performance of the burner.

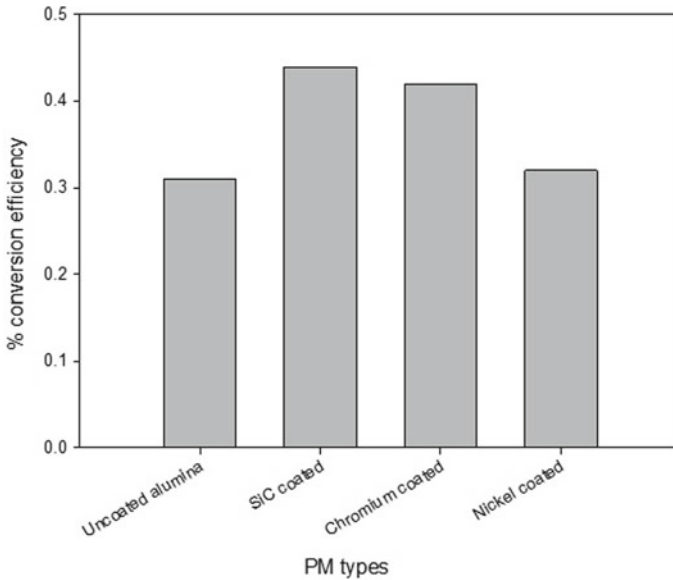


Fig. 8.7 Variation in % conversion efficiency and reaction zone

## 8.5 Conclusions

Adopting the porous media inside the burner is an advantageous procedure. The porous media burner promotes better the thermal and conversion efficiency. In addition, involvement of coating technique further enhances the overall performance of the burner. A comparative study was made by adopting various coating materials: SiC, Ni, and Cr. The coating methods boost both the cogeneration and conversion efficiency. By the technique of dual output, the power and heat generation was integrated in the PMB. The developed PMB can be made more effective by integrating the setup with better physical design and an effective thermal management system. The developed system can be of commercial value and can be a good alternating option in the domestic market. With the ready to use option of power output it finds application in outdoor activities.

## References

1. Janvekar AA, Abdullah MZ et al (2018) Experimental and numerical studies of porous media combustion in micro burner. *J Adv Res Fluid Mech Therm Sci* 43(1):112–120
2. Champier D, Bedecarrats J-P et al (2010) Thermoelectric power generation from biomass cook stoves. *Energy* 35(2):935–942
3. Chen W-H, Liao C-Y et al (2012) Experimental study on thermoelectric modules for power generation at various operating conditions. *Energy* 45(1):874–881

4. Gou X, Xiao H et al (2010) Modeling, experimental study and optimization on low-temperature waste heat thermoelectric generator system. *Appl Energy* 87(10):3131–3136
5. Ibrahim N, Zubair M et al. (2018) A practical approach in porous medium combustion for domestic application: a review
6. Ismail AK, Abdullah MZ et al (2016) Effect of ceramic coating in combustion and cogeneration performance of  $\text{Al}_2\text{O}_3$  porous medium. *J Energy Inst* 89(1):81–93
7. Janvekar AA, Abdullah M et al. (2017) Assessment of porous media burner for surface/submerged flame during porous media combustion. In: AIP conference proceedings. AIP Publishing LLC
8. Janvekar AA, Abdullah M et al. (2018) Investigation of micro burner performance during porous media combustion for surface and submerged flames. In: IOP conference series: materials science and engineering
9. Janvekar AA, Abdullah M et al. (2018) Experiential study on temperature and emission performance of micro burner during porous media combustion. In: IOP conference series: materials science and engineering
10. Janvekar AA, Abdullah M et al (2018) Assessment of porous media combustion with foam porous media for surface/submerged flame. *Mater Today: Proc* 5(10):20865–20873
11. Janvekar AA, Abdullah M et al. (2019) Influence of reaction layer thickness on surface/submerged flame during porous media combustion of micro burner. In: IOP conference series: materials science and engineering. IOP Publishing
12. Janvekar AA, Abdullah M et al. (2019) Development of foam porous media to undergo surface and submerged flame during premixed combustion. In: IOP conference series: materials science and engineering. IOP Publishing
13. Krishnan S, Karri NK et al (2012) Progress towards an optimization methodology for combustion-driven portable thermoelectric power generation systems. *J Electron Mater* 41(6):1622–1631
14. Martínez A, Astrain D et al (2011) Experimental and analytical study on thermoelectric self cooling of devices. *Energy* 36(8):5250–5260
15. Mueller KT, Waters O et al (2013) Super-adiabatic combustion in  $\text{Al}_2\text{O}_3$  and SiC coated porous media for thermoelectric power conversion. *Energy* 56:108–116
16. Posthill J, Reddy A et al. (2005) Portable power sources using combustion of butane and thermoelectrics. ICT 2005. In: 24th international conference on thermoelectrics. IEEE
17. Qiu K, Hayden A (2003) Performance of low bandgap thermophotovoltaic cells in a small cogeneration system. *Sol Energy* 74(6):489–495
18. Qiu K, Hayden A (2009) A natural-gas-fired thermoelectric power generation system. *J Electron Mater* 38(7):1315–1319
19. Riffat SB, Ma X (2003) Thermoelectrics: a review of present and potential applications. *Appl Therm Eng* 23(8):913–935
20. Weinberg F, Rowe D et al (2002) On thermoelectric power conversion from heat recirculating combustion systems. *Proc Combust Inst* 29(1):941–947

# Chapter 9

## Child Safety in Car Crashes: A Modeling Approach for Safety System Improvements



Shahrizan Yusoff, Nurul Syasya Fakhira, and Nor Haniza Bakhtiar Jemily

**Abstract** Traffic-related trauma is the most common cause of fatality and severe injury to children in developed countries. Injury epidemiology has shown that special attention is needed for the 3-year-olds in boosters and the 12-year-olds in seat belts only. The aim of this paper is to study the frontal and side-impact models and to use them to investigate and define the beneficial characteristics of restraint systems and other crash-related car parameters. Qualitative approaches using two load cases were analyzed and validated via video. The validations from the frontal impact type and near-side impact showed that the child had high potential to mitigate injuries resulting from a frontal impact. The upper belt anchor point should be positioned so that the belt is routed near the mid-shoulder (slightly toward the neck) and encloses the shoulder (tight fit). These findings are significant contributions to the continuous work of mitigating traffic accident induced injuries and fatalities to children.

**Keywords** Child safety · Side impact · Frontal impact · Near-side · Rear seat · Evaluations · Finite elements · Rigid body · Reconstructions · Child seat · Belt positioning booster

### 9.1 Introduction

Unintentional injury remains the leading cause of death and disability for children older than 1 year. Most of the related trauma to children occurs when they are passengers in cars in frontal or side impacts, which account for about 50% and 25%

---

S. Yusoff (✉) · N. S. Fakhira · N. H. B. Jemily  
Universiti Kuala Lumpur, Malaysian Spanish Institute Kulim Hi-Tech Park, 09000 Kulim, Kedah, Malaysia

e-mail: [mshahrizan@unikl.edu.my](mailto:mshahrizan@unikl.edu.my)

N. S. Fakhira

e-mail: [syasya.anis@s.unikl.edu.my](mailto:syasya.anis@s.unikl.edu.my)

N. H. B. Jemily

e-mail: [norhaniza@unikl.edu.my](mailto:norhaniza@unikl.edu.my)

of the crashes, respectively [1]. At particular risk for injury in moving vehicle crash (MVC) are children aged 4–12 years. Children aged 4–12 years who were injured in MVCs were more likely to experience significant abdominal injuries as a result of the premature transition to seat belts. These injuries, known as “seat belt syndrome”, include abdominal bruising, intra-abdominal injury, and spine injuries [2]. Facial injuries are also often present. These publications have shown that the head is the most frequently injured body region, regardless of the type of restraint or type of impact. Physicians indicate that head injuries are complicated to treat and for some injury types there are no known treatments. These injuries are caused by both impacts and non-impacts. Therefore, injury mitigation should be directed to both reducing the likelihood of impacts and reducing the accelerations that the children are exposed to in a crash.

Another study by [3] shows that the chest is the second most commonly injured body region. Chest trauma in children is caused by high-energy blows, due in general to traffic accidents that involve several other body regions. They occur mainly in the first decade of life and can be penetrating but are more often non-penetrating. Rib fractures and lung contusions, sometimes associated with pneumothorax or haemothorax, are the more usual injuries, but tracheobronchial rupture, cardiac, oesophageal, or diaphragmatic injuries may also occur. These injuries are treated with supportive respiratory and haemodynamic measures, drainage of air or blood from the pleural space and, at times, surgical repair of the injured organ(s). Ruptures of the airway may be difficult to treat and occasionally require suture, anastomosis, or resection. Oesophageal injuries can be treated conservatively with antibiotics, drainage, and parenteral nutrition. Diaphragmatic tears should be repaired operatively. Overall mortality ranges from 6 to 20%. Mortality is high but this is mainly due to the associated presence of extra-thoracic trauma and particularly to head injuries. Furthermore, inside impacts, the thorax is the most frequently injured body region among children older than 12 years and adults. It can be concluded that the head is the most important body region to concentrate on for children up to 12 years, while for older children and adults, the thorax is equally important, especially in side impacts.

## 9.2 Literature

A study by the Malaysian Institute of Road Safety Research (MIROS) shows that 58% of child and infant deaths in the country are due to road accidents and lack of child safety systems are serious contributing factors to deaths. Using car seats for children and installing them properly can reduce the risk of fatal injuries by up to 70%. This fact clearly shows the importance of awareness of all parents to start emphasizing the use of infant and child seats in the car to ensure their safety.

The use of child safety seats is important to ensure that small passengers are safe during the driving period. This chair also serves to protect children from suffering serious injuries in the event of a road accident. Director-General of the Road Safety Department (JKJR), Mohd Nasri Ishak [4], said based on statistics from the Malaysian

Road Safety Research Institute, a total of 1,559 deaths were recorded involving children at the age of 10 during the 10 years starting 2007 [5]. Reports equivalent to losing one life for every 84 min due to road accidents, the situation is more critical as these young children face the risk of accidental death. Thus, the child restraint system (CSR) or child safety seat protects them from serious injury. This facility protects children in the vehicle in the event of a violation. The use of CRS in developed countries has successfully reduced the impact of violations, thereby preventing serious injuries and deaths.

Existing provisions through the Motor Car (Seat Belt) Rules (Amendment 2008) in accordance with the Road Transport Act 1987, the government enforced the rules on the use of seat belts for rear seats since 1 January 2009 [6]. Previously, the government gave three years (1 January–31 December 2011) to vehicles registered on and after 1 January 1995 to install seat belts on the rear seats. From January 2020, the use of child safety seats is mandatory. MIROS sets the CRS position to be placed front and back according to the type of seat as well as the group category, children aged 0–18 months are categorized in Group 0/0+, the CSR seats installed should face backward. For this group, children weigh at least nine kilograms (kg) but are encouraged up to 13 kg at a height of 83 cm (cm).

The CRS should not be placed on the front passenger seat which has an active airbag because the bag cannot be switched off using the switch. However, conditions are allowed if no airbag is active or the switch can be turned off. These chairs must use three- or five-point harness seat belts. For front-mounted CSR, this safety seat is for groups of one to three aged 15 months to four years and above with a weight of nine to 18 kg children and a height of 71 cm. For Group two, children aged four to seven years with an estimated weight of 15–25 kg and a height of 100 cm, the installation should be on a seat that has a support (booster). Meanwhile, group three involving children aged six years and above is recommended to weigh around 25–36 kg, height 135 cm, and need a seat with support (booster). Its installation is recommended on the rear passenger seat, if placed on the front passenger seat, it should be adjusted to the rear, i.e., position away from the airbag. The chair should use a five-point harness (seat belts).

### ***9.2.1 Application of Child Booster Seat to Prevent Child Injuries***

The discrepancies in injury rates by age may be in part explained by lower observed rates of restraint use in 4-year to 7-year-olds (46% in booster seats and another 20% in car seats for a total of 66%) compared with the high observed rates of restraint use for younger children (98% in children age <1 year and 95% in children age 1–3 years), demonstrating a significant reduction inappropriate restraint use as a child age [7]. Child booster seats are part of a suite of regulated safety products targeted at reducing MVC related morbidity and mortality. While seat belts were designed to

accommodate motor vehicle passengers over four foot nine inches in height, booster seats refer to a heterogeneous group of products whose intent is to elevate children and youth to improve seat belt fit.

Three main configurations of booster seats are on the market: backless booster seats (specialized cushion with armrests that serve to guide the lap belt to an appropriate position); belt-positioning boosters (like a backless booster, but with back and head support and a built-in shoulder belt guide); and combination boosters (a child safety seat with seat belt guides so once the five-point harness is removed the child is restrained using the vehicle's seat belt) [8]. While booster seats are mandatory across much of the country, each jurisdiction establishes its regulations for use, with specific combinations of height, weight, and age restrictions. Booster seat laws are consistent in their criteria for transitioning from a child safety seat to a booster seat, and generally, recommend commencing use when the child reaches 40 pounds. Laws differ, however, regarding the criteria for when a child can transition out of a booster seat to a seat belt alone, with varying weight (40–81.5 lbs) and height (25" seated height or 57 in.) minimums.

Parents are generally recommended to begin booster seat use between the ages of four and six, and graduate children to seatbelts between the ages of six and ten. Considerable energy has been directed toward encouraging the use of booster seats, supported by systematic reviews of promotion strategies to improve booster seat uptake. Booster seats continue to be evaluated through laboratory and simulation studies, before and aftermarket use, to evaluate their efficacy, and to improve their structure to most benefit child safety. At the same time, evidence of booster seat effectiveness in reducing injury in motor vehicle crashes is inconsistent. Research studies have reported reduced injuries and death for children five years of age and under, and six to eight years of age when using a booster seat with a seat belt compared to a seat belt alone; however, mixed findings have also been reported.

Several factors account for low rates of booster seat use or early transition to vehicle seat belts. These include lack of knowledge about the safety benefits of booster seats, low perception of risk to child passengers, and lack of perceived threat of being ticketed for restraint violations. In addition to previously stated factors, child passenger safety initiatives such as hospital-based child passenger safety programs generally place greater emphasis on car seat inspections for infants and toddlers than car seat inspections for older children. Vehicle and restraint safety devices have largely been optimized through laboratory-based or computational test programs using anthropomorphic test devices (ATDs) intended to mimic the human occupant. Most of the test protocols evaluate restraint performance with ATDs placed in ideal positions (e.g., ATD against the seatback, perfectly upright) and under these conditions, the majority of restraints perform very well [9]. Recent real-world evidence has suggested, however, that the ideal test conditions do not always reflect actual conditions and despite being seated in the correct restraint system for their age and size, an unacceptable number of children die or are seriously injured in real-world crashes. For example, previous research has demonstrated the mechanisms of injury for children who died as a result of interaction with frontal passenger airbag deployments. Rather than being seated ideally, these children were in the path of the airbag when



**Table 9.1** The data which categorize child car seats

Category	Height	Weight	Age	Type of seat
Group 0/0+	Below 83 cm	Below 9 kg	0–18 months	Rear-facing infant car seat
Group 1	Minimum 71 cm	Between 9 and 18 kg	15 months–4 years	Forward-facing child car seat
Group 2	Minimum 100 cm	Between 15 and 25 kg	4–7 years	Child booster seat with a harness
Group 3	Up to 135 cm	Between 22 and 36 kg	6–12 years	Child booster seat (car seat belt as the harness)

it deployed and the energy associated with the airbag deployment was transferred to the occupant, resulting in serious injuries or death [10].

### 9.2.2 Categorization of Child Car Seats

A child safety seat (CRS) should be chosen according to the weight and height of the child. The MIROS guidelines break these down into four groups (based on guidelines) divided along these lines. Age is not necessarily a factor in which seat to use as children of the same age can differ greatly in terms of size. Table 9.1 shows data which categorize child car seats into four different types depending on the height and weight of a child. Every child with height under 135 cm is required to use either a child car seat or a booster seat.

## 9.3 Methodology

Exploratory research is defined as research used to investigate a problem that is not clearly defined. It is conducted to have a better understanding of the existing problem. For such research, a researcher starts with a general idea and uses this research as a medium to identify issues that can be the focus for future research.

In this study, videos were observed and recorded. This type of data is collected through methods of observations from the accident video. The study found from the videos that there are two accidents situations that occur to children using the child safety seat. The first accident was a collision from the front, and the second accident was a collision from the side. The data collected are the effects that occur on children who have used this CRS.

In the event of a collision from the front collision, the child may be injured due to a loose-fitting safety belt. And in the event of a collision from the side, the child



**Fig. 9.1** Collision from front

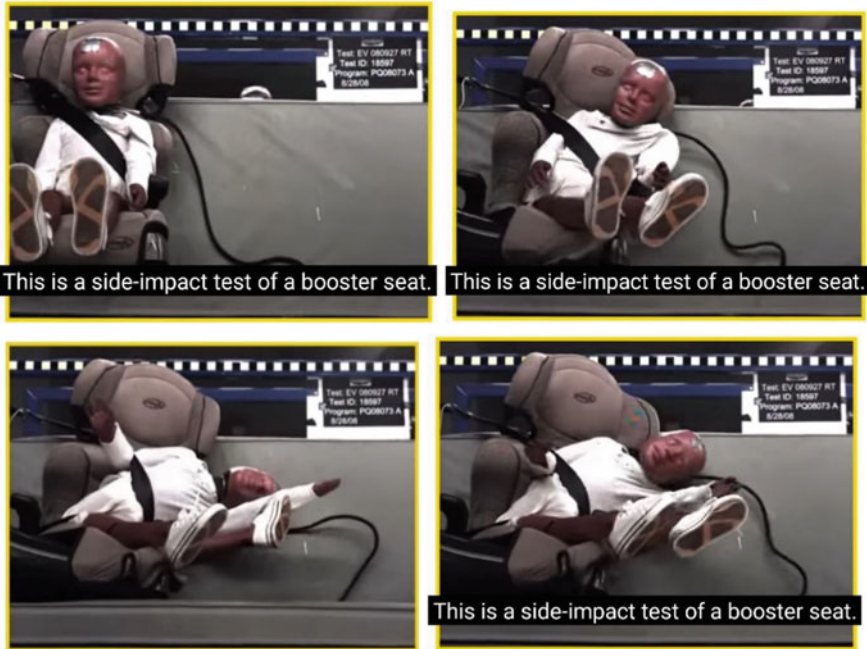
in the CRS is injured due to the CRS designed on the relatively short waist-to-back area as per Figs. 9.1 and 9.2, while Table 9.2 shows the impact of the collision.

## 9.4 Results and Discussion

These four child safety seats will suffer almost the same damage because, when a strong impact occurs, the same pressure will occur on the child. The rear-facing seat offers the best protection, as the seat keeps the child's head, neck, and spine aligned during the collision. In the event of a collision, the car seat facing backward will embrace the child and absorb the force of the accident. The front-facing seat helps to slow down a child in an accident but does not support their head, neck, and spine. This means that while their torso is slowing down with car seats, their head, neck, and spine are still moving forward with incredible strength. For children whose spine is still developing, this can result in serious spinal cord injuries.

Therefore, each child safety seat needs to be modified for the safety of the child who uses it. This is to ensure that children who use the child safety seat do not suffer serious injuries in the event of an unwanted accident. First of all, the seat belt needs to be tightened slightly to fit the child's body so that when there is a hit on the front and side of the child in the child safety seat does not inflate strongly. Injuries to the chest and abdomen can also be avoided if the safety belt is used properly and meets the comfort of the child using it.

In addition, the position of the waist-to-back area should be taken into consideration. Because if there is an impact on the side and front, it is likely that children who use this child safety seat will experience cracks or fractures in the thighs. Therefore,



**Fig. 9.2** Collision from side

**Table 9.2** Impact of collision

Collision from front	Collision from side
<p><b>Head:</b> There will be concussions in the brain</p>	<p><b>Head/neck:</b> Children drift to the side causing serious injuries to the spine in the neck or called “cervical”. Concussions in the brain will also occur if it involves the neck</p>
<p><b>Neck:</b> Neck and head to snap forward forcefully, resulting in an excessive touch of the chin-to-chest</p>	<p><b>Shoulder:</b> The collarbone or shoulder bone can crack or break due to strong bounce and movement that exceeds the seat belt used on the child’s body. The same thing happens with the thighs, due to the strong pressure</p>
<p><b>Stomach:</b> Children will soar forward and may cause injuries to the abdomen</p>	<p><b>Stomach/kidney:</b> Injury to the abdomen or side of the kidney due to relatively strong pressure on one side</p>

this part needs to be modified by extending it slightly to pass the waist level so that such incidents do not happen to children. Besides, it can save the lives of children who use the Child Safety Seat. Parents do not have to worry about using the Child Safety Seat on their children anymore (Figs. 9.3, 9.4, 9.5, 9.6).

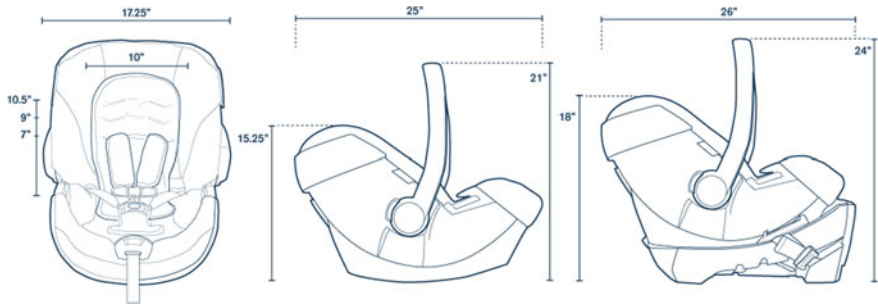


Fig. 9.3 Infant car seat

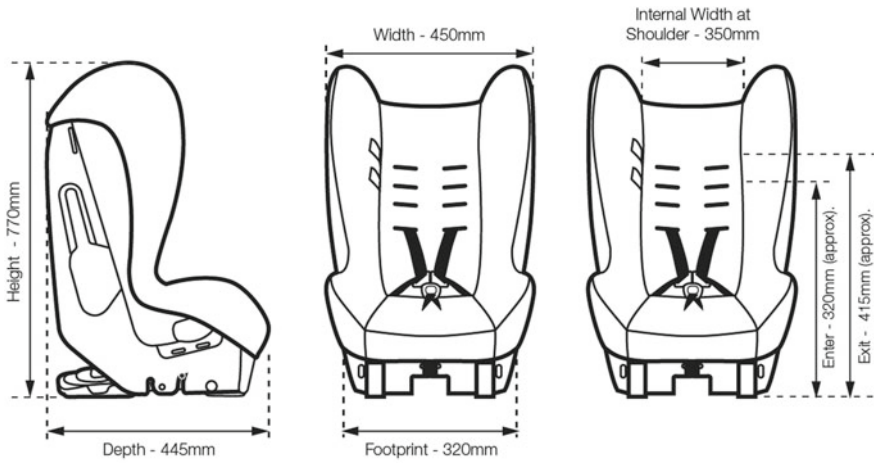


Fig. 9.4 Convertible car seat

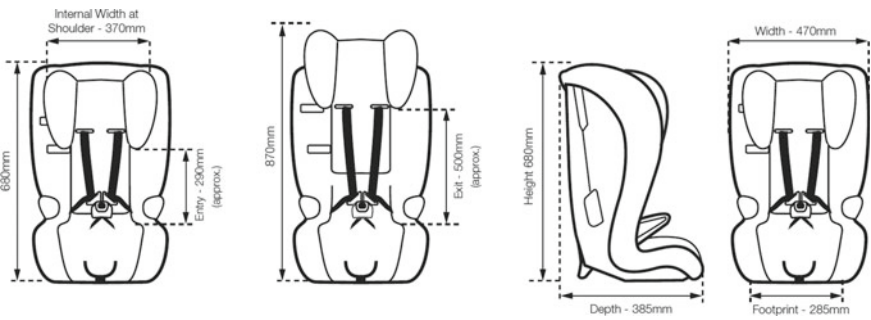
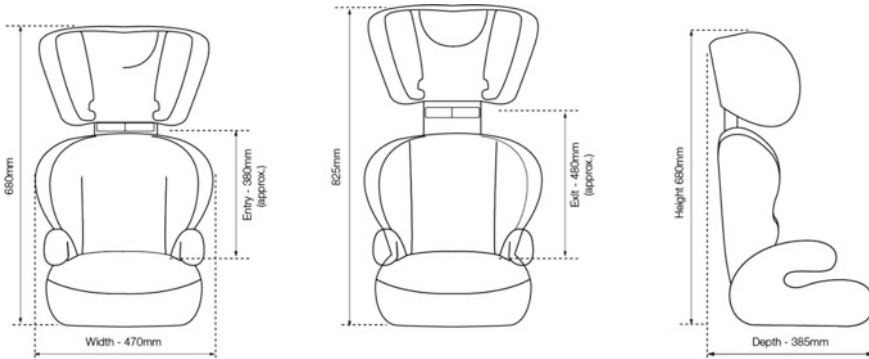


Fig. 9.5 Harnessed car seat



**Fig. 9.6** Booster seat

Based on the four examples of child safety seats above, then the sketch for the proposed new design can be illustrated by referring to the dimensional examples given. For new CRS design suggestions, just focus on the waist-to-back. Therefore, the researchers only added dimensions and design to the waist-to-back section. The purpose is to protect the child in the event of a collision from the side, so as not to suffer some injuries such as fractures in the thighs, and fractures of the waist and spine.

### 9.5 Conclusion

The design of the child safety seat (CRS) has been completed by finding some information that is the dimensions for the CRS parts that need to be modified. Apart from that, road accident statistics in Malaysia also show a bad record as the number of accidents is increasing every day. Children are also involved in this situation, this is due to the negligence of parents who do not use CRS for children, and thus the risk of injury and death of children will occur. However, some parents are concerned about using CRS for their child, but injuries and deaths still occur, and this is because the CRS designed does not fully protect the safety of the child. Loose-fitting seat belts for children in CRS are also the cause of injuries to children during collisions from the front and side. Therefore, parents are advised to be careful when installing CRS for children. On the waist-to-back of the CRS, it has been proposed to be designed by extending the part so that when there is a collision from the side, the child in the CRS is not thrown and suffers a series of injuries. It is hoped that with the advent of this new CRS design, child safety will be more secure when using it.

## References

1. Arbogast KB, Kim J, Loeb H, Kuo J, Koppel S, Bohman K, Charlton JL (2016) Naturalistic driving study of rear seat child occupants: Quantification of head position using a Kinect™ sensor. *Traffic Injury Prevent*. <https://doi.org/10.1080/15389588.2016.1194981>
2. Asbridge M, Ogilvie R, Wilson M, Hayden J (2018) The impact of booster seat use on child injury and mortality: Systematic review and meta-analysis of observational studies of booster seat effectiveness. *Accid Anal Prev*. <https://doi.org/10.1016/j.aap.2018.07.004>
3. Høyve A (2016) How would increasing seat belt use affect the number of killed or seriously injured light vehicle occupants? *Accid Anal Prev*. <https://doi.org/10.1016/j.aap.2015.12.022>
4. Jermakian JS, Weast RA (2018) Passenger use of and attitudes toward rear seat belts. *J Safety Res*. <https://doi.org/10.1016/j.jsr.2017.12.006>
5. JKJR (2019) Road safety statistics book. In: Road safety department of Malaysia
6. Kroeker AM, Teddy AJ, Macy ML (2015) Car seat inspection among children older than 3 years: using data to drive practice in child passenger safety. *J Trauma Acute Care Surg*. <https://doi.org/10.1097/TA.0000000000000674>
7. Sivak M, Schoettle B (2015) Road safety with self-driving vehicles: general limitations and road sharing with conventional vehicles. *Transp Res Inst. UMTRI-2015-2*
8. Tovar JA, Vazquez JJ (2013) Management of chest trauma in children. *Paediatric Respiratory Rev*. <https://doi.org/10.1016/j.prrv.2013.02.011>
9. Tylko S, Bohman K, Bussières A (2015) Responses of the Q6/Q6s ATD positioned in booster seats in the far-side seat location of side impact passenger car and sled tests. *SAE Tech Papers*. <https://doi.org/10.4271/2015-22-0012>
10. Visvikis C, Thurn C, Müller T (2019) Effect of the Q10 dummy upgrade kit in UN Regulation No. 129 front and side impact tests. *Traffic Injury Prevent*. <https://doi.org/10.1080/15389588.2019.1662264>

# Chapter 10

## Modelling of Air-Gap Magnetic Flux Density Distribution for Surface-Mounted Permanent Magnet Synchronous Motor Using the Analytical Sub-Domain Method



M. Rezal, D. Ishak, and M. S. Ahmad

**Abstract** This paper discusses an analytical modelling for a slotless surface-mounted permanent magnet synchronous motor (PMSM) at airgap region using the sub-domain method. The slotless PMSM has no cogging effect compared to a slotted PMSM. The radial magnetization of the magnetic flux is applied in the motor design with 6-slot/4-pole configuration. The analytical model of magnetic flux density distributions shows a good agreement with the numerical results from finite element analysis.

**Keywords** Sub-domain · Permanent magnet · Synchronous motor · Magnetic flux

### 10.1 Introduction

As we know, the permanent magnet synchronous motor (PMSM) has good performance characteristics compared to other types of electrical machines (EM). PMSM has high torque density, wide speed range of power capability, which is most suitable in automotive and mechatronics area [1]. But PMSM still has a few disadvantages such as the cogging torque and eddy current loss [2]. In this research, the modelling of a surface-mounted PMSM using the analytical subdomain method is presented. The finite element analysis has longer computational time which leads to longer EM

---

M. Rezal (✉)

Universiti Kuala Lumpur, Malaysian Spanish Institute, Kulim, Kedah, Malaysia

e-mail: [mrezal@unikl.edu.my](mailto:mrezal@unikl.edu.my)

D. Ishak

School of Electrical and Electronic Engineering, Universiti Sains Malaysia, Penang, Malaysia

e-mail: [dahaman@usm.my](mailto:dahaman@usm.my)

M. S. Ahmad

School of Electrical System Engineering, Universiti Malaysia Perlis, Arau, Perlis, Malaysia

e-mail: [saufiahmad@unimap.edu.my](mailto:saufiahmad@unimap.edu.my)

© The Author(s), under exclusive license to Springer Nature Switzerland AG 2022

M. H. Abu Bakar et al. (eds.), *Progress in Engineering Technology IV*,

Advanced Structured Materials 169,

[https://doi.org/10.1007/978-3-030-93250-3\\_10](https://doi.org/10.1007/978-3-030-93250-3_10)

design stage. Due to that problem, the analytical sub-domain is often selected and preferred due to its faster computational time.

## 10.2 Literature Review

In general, PMSM can be simulated using three modelling techniques i.e. finite element (FE) model, magnetic equivalent circuit (ME) model, and analytical sub-domain (ASD) model [3]. The ASD model has the shortest computational time compared to the ME and FE models, whereas ME has computational time shorter than FE model [4]. The FE model has the longest computational time, torque accuracy and magnetic loss limitation, but it has better design flexibility [5]. Despite the advantage of computational effort, the analytical model has few disadvantages such as less accuracy, less flexible compared to FE, and no 3-D effect capability. It is suitable to analyse a 2-D design with less complexity in the design [4].

### 10.2.1 Sub-Domain Method

The separation of variable technique is applied for the analytical sub-domain (ASD) model. The air-gap and slot opening regions can be determined using the 2-D Laplace's equation, while magnet and winding slot regions using the 2-D Poisson's equation [6]. The ASD model also can determine the slot mutual and armature reaction [6]. The PMSM parameters during on-load and open circuit can also be determined using ASD model [7, 8]. Air-gap, magnet, winding slot, and slot opening are the four regions involved in this ASD model [6–9]. The ASD model also can estimate the electromagnetic torque, phase back-emf, winding inductance, and magnetic field distribution for the PMSM [6–10]. The magnetic vector potential is the common formulae for the ASD model. The magnet  $A_{z1}$ , air-gap  $A_{z2}$ , winding slots  $A_{z3i}$ , and slot-openings  $A_{z4i}$  in 2-D polar coordinates are shown in Eqs. (10.1)–(10.4) [12].  $M_r$  and  $M_\alpha$  are the radial and circumferential components of the magnet magnetization. The current density is  $J$ , while  $\mu_0$  is the relative permeability of the free space.

$$\frac{\partial^2 A_{z1}}{\partial r^2} + \frac{1}{r} \frac{\partial A_{z1}}{\partial r} + \frac{1}{r^2} \frac{\partial^2 A_{z1}}{\partial \alpha^2} = -\frac{\mu_0}{r} \left( M_\alpha - \frac{\partial M_r}{\partial \alpha} \right), \quad (10.1)$$

$$\frac{\partial^2 A_{z2}}{\partial r^2} + \frac{1}{r} \frac{\partial A_{z2}}{\partial r} + \frac{1}{r^2} \frac{\partial^2 A_{z2}}{\partial \alpha^2} = 0, \quad (10.2)$$

$$\frac{\partial^2 A_{z3i}}{\partial r^2} + \frac{1}{r} \frac{\partial A_{z3i}}{\partial r} + \frac{1}{r^2} \frac{\partial^2 A_{z3i}}{\partial \alpha^2} = -\mu_0 J, \quad (10.3)$$



$$\frac{\partial^2 A_{z4i}}{\partial r^2} + \frac{1}{r} \frac{\partial A_{z4i}}{\partial r} + \frac{1}{r^2} \frac{\partial^2 A_{z4i}}{\partial \alpha^2} = 0. \tag{10.4}$$

The PMSM is divided into four sub-domains i.e. the magnet, air-gap, slot opening, and winding slot regions [11]. In order to reduce the modelling complexity, the rotor and stator cores have an infinite permeability and zero conductivity. Due to that, there is no eddy current loss. The slot has a spoke shaped teeth, no end-effect, and the magnet have linear properties. Sub-domain modelling can be divided into two types, i.e. the semi sub-domain and full sub-domain. The semi sub-domain can be a combination between two regions such as the magnet region with the air-gap region or the air-gap region with the slot-opening region, whereas full sub-domain consists of four regions, i.e. the air-gap magnet, winding slot, and slot-opening. The internal rotor surface-mounted PMSM with radial magnetization configuration is shown in Fig. 10.1, while the radial component for radial magnetization is shown in Fig. 10.2. There is no tangential component for radial magnetization.

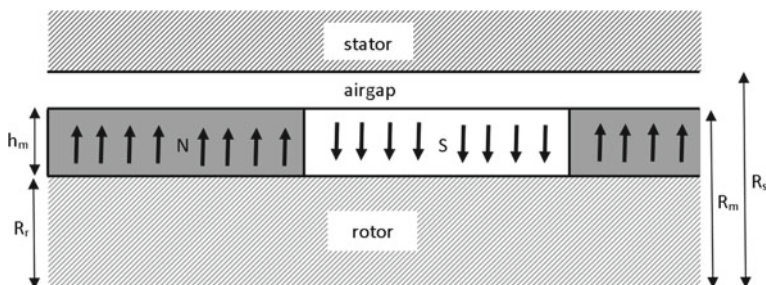
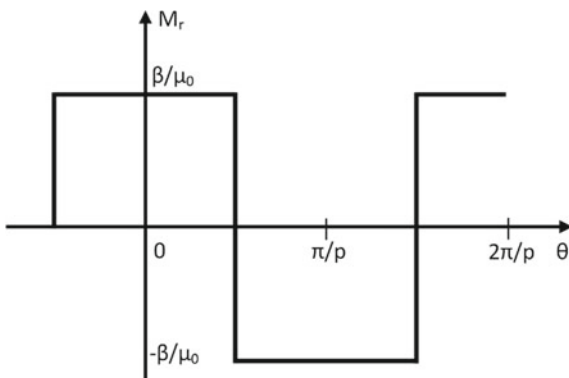


Fig. 10.1 Internal rotor SPMSM with radial magnetization

Fig. 10.2 Radial component for radial magnetization internal rotor surface-mounted PMSM



### 10.2.2 Airgap Flux Density for Slotless PMSM

The magnetic flux density in the airgap region for slotless PMSM consists of radial and tangential components in polar coordinate is shown as per Eqs. (10.5) and (10.6), respectively [12].

$$B_{rI}(r, \theta) = \sum_{n=1,3,5,\dots}^{\infty} K_B(n) \cdot f_{B_r}(r) \cdot \cos(np\theta), \quad (10.5)$$

$$B_{\theta I}(r, \theta) = \sum_{n=1,3,5,\dots}^{\infty} K_B(n) \cdot f_{B_{\theta}}(r) \cdot \sin(np\theta). \quad (10.6)$$

When the number of slot per pole is  $np = 1$ , then

$$K_B(n) = \frac{\mu_o M_n}{2\mu_r} \cdot \left\{ \frac{A_{3n} \left(\frac{R_m}{R_s}\right)^2 - A_{3n} \left(\frac{R_r}{R_s}\right)^2 + \left(\frac{R_r}{R_s}\right)^2 \ln \left(\frac{R_m}{R_r}\right)^2}{\frac{\mu_r + 1}{\mu_r} \left[1 - \left(\frac{R_r}{R_s}\right)^2\right] - \frac{\mu_r - 1}{\mu_r} \left[\left(\frac{R_m}{R_s}\right)^2 - \left(\frac{R_r}{R_m}\right)^2\right]} \right\}, \quad (10.7)$$

$$f_{B_r}(r) = 1 + \left(\frac{R_s}{r}\right)^2, \quad (10.8)$$

$$f_{B_{\theta}}(r) = -1 + \left(\frac{R_s}{r}\right)^2. \quad (10.9)$$

For radial magnetization,

$$A_{3n} = np. \quad (10.10)$$

However, when  $np \neq 1$ , for the case of radial magnetization,

$$A_{3n} = 1. \quad (10.11)$$

For internal rotor motor,  $R_s > R_m > R_r$ ,

$$K_B(n) = \frac{\mu_o M_n}{2\mu_r} \cdot \frac{np}{(np)^2 - 1} \cdot \left(\frac{B_{ir}}{C_{ir}}\right), \quad (10.12)$$

$$B_{ir} = (A_{3n} - 1) + 2\left(\frac{R_r}{R_m}\right)^{np+1} - (A_{3n} + 1)\left(\frac{R_r}{R_m}\right)^{2np}, \quad (10.13)$$

$$C_{ir} = \frac{\mu_r + 1}{\mu_r} \left[1 - \left(\frac{R_r}{R_s}\right)^{2np}\right] - \frac{\mu_r - 1}{\mu_r} \left[\left(\frac{R_m}{R_s}\right)^{2np} - \left(\frac{R_r}{R_m}\right)^{2np}\right], \quad (10.14)$$

$$f_{B_r}(r) = \left(\frac{r}{R_s}\right)^{np-1} \left(\frac{R_m}{R_s}\right)^{np+1} + \left(\frac{R_m}{r}\right)^{np+1}, \quad (10.15)$$

$$f_{B_\theta}(r) = -\left(\frac{r}{R_s}\right)^{np-1} \left(\frac{R_m}{R_s}\right)^{np+1} + \left(\frac{R_m}{r}\right)^{np+1}. \quad (10.16)$$

### 10.3 Methodology

The research starts with defining the PMSM parameters. Then an ASD model is applied to determine the magnetic flux density in the air-gap region i.e. the radial and tangential components. Next, a 2-D finite element (FE) method is used to design the PMSM and validate the outputs. The PMSM parameters need to be adjusted if there is a difference of results between the ASD and FE model. The methodology to design the PMSM is shown in Fig. 10.3.

#### 10.3.1 Motor Parameters and 2-D Design

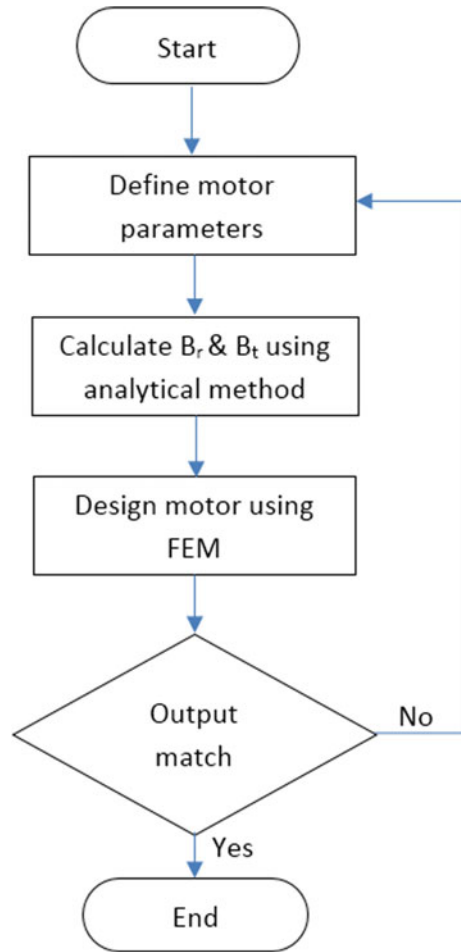
In this research, a radial magnetization, internal rotor type, 6-slot/4-pole, three-phase, PMSM was selected. The detail of the PMSM parameters is shown in Table 10.1. The 2-D design of 6-slot/4-pole slotless PMSM is shown in Fig. 10.4. A static analysis in FEM is used to compute the magnetic flux distributions of the internal rotor 6-slot/4-pole slotless PMSM using a commercial finite element software package, i.e. Opera2D.

#### 10.3.2 Airgap Flux Density for Slotless PMSM

Applying Eqs. (10.5)–(10.16), the radial  $B_{rI}$  and tangential  $B_{\theta I}$  of the air-gap magnetic flux density for internal rotor radial magnetization surface-mounted PMSM can be obtained using Eqs. (10.17) and (10.18), respectively.

$$B_{rI}(r, \theta) = \sum_{n=1,3,5,\dots}^{\infty} \frac{\mu_o M_n}{2\mu_r} \cdot \frac{np}{(np)^2 - 1} \cdot \left( \frac{2 \left[ \left(\frac{R_r}{R_m}\right)^{np+1} - \left(\frac{R_r}{R_m}\right)^{2np} \right]}{\frac{\mu_r+1}{\mu_r} \left[ 1 - \left(\frac{R_r}{R_s}\right)^{2np} \right] - \frac{\mu_r-1}{\mu_r} \left[ \left(\frac{R_m}{R_s}\right)^{2np} - \left(\frac{R_r}{R_m}\right)^{2np} \right]} \right)$$

**Fig. 10.3** PMSM design flowchart



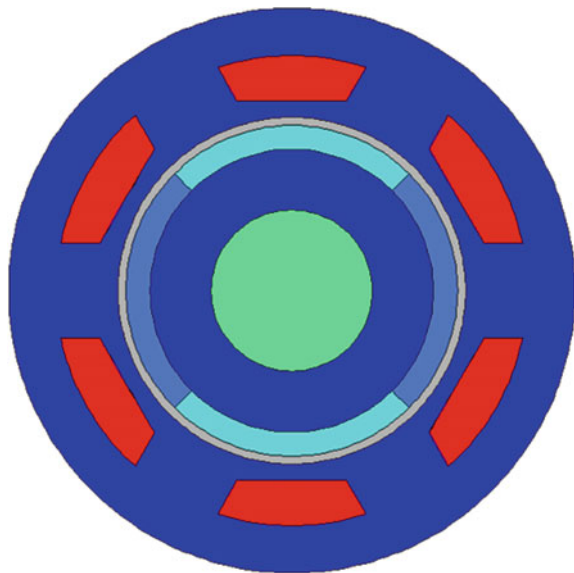
$$\cdot \left[ \left( \frac{r}{R_s} \right)^{np-1} \left( \frac{R_m}{R_s} \right)^{np+1} + \left( \frac{R_m}{r} \right)^{np+1} \right] \cdot \cos(np\theta), \quad (10.17)$$

$$B_{\theta I}(r, \theta) = \sum_{n=1,3,5,\dots}^{\infty} \frac{\mu_o M_n}{2\mu_r} \cdot \frac{np}{(np)^2 - 1} \cdot \left( \frac{\frac{\mu_r+1}{\mu_r} \left[ 1 - \left( \frac{R_r}{R_s} \right)^{2np} \right] - \frac{\mu_r-1}{\mu_r} \left[ \left( \frac{R_m}{R_s} \right)^{2np} - \left( \frac{R_r}{R_m} \right)^{2np} \right]}{2 \left[ \left( \frac{R_r}{R_m} \right)^{np+1} - \left( \frac{R_r}{R_m} \right)^{2np} \right]} \right) \cdot \left[ - \left( \frac{r}{R_s} \right)^{np-1} \left( \frac{R_m}{R_s} \right)^{np+1} + \left( \frac{R_m}{r} \right)^{np+1} \right] \cdot \sin(np\theta). \quad (10.18)$$

**Table 10.1** PMSM Parameters

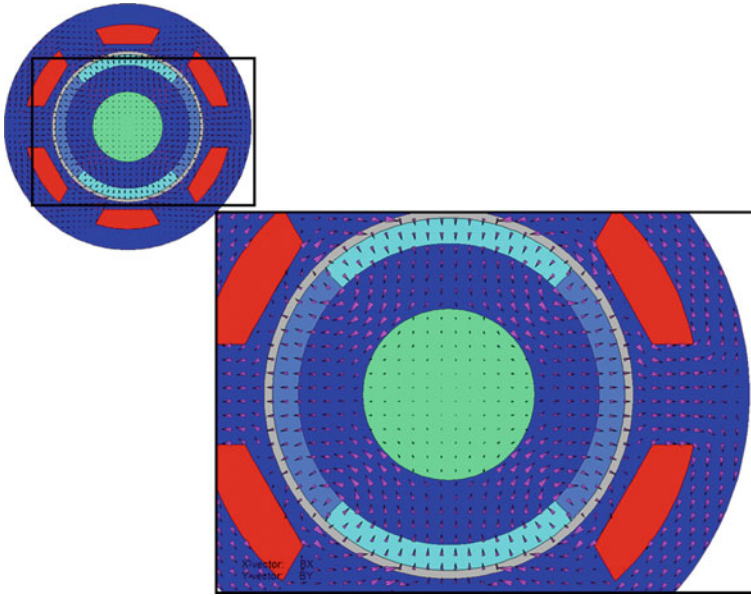
Parameter	Symbol	Value	Unit
Pole-pairs number	$p$	2	–
Stator slot number	$Q_s$	6	–
Magnet arc-pole pitch ratio	$\alpha_p$	1	–
Air gap length	$g$	1.0	mm
Magnet radial thickness	$h_m$	3.0	mm
Rotor surface radius	$R_r$	17.5	mm
Magnet surface radius	$R_m$	20.5	mm
Stator inner bore radius	$R_s$	21.5	mm
Stack length	$l$	50.0	mm
Magnet remanence	$B_r$	1.12	T
Relative recoil permeability	$\mu_r$	1.05	–
Motor speed	$\omega_{rm}$	1500	rpm
Field solution in air gap	$R_g$	21.0	mm

**Fig. 10.4** 2-D design of 6-slot/4-pole slotless PMSM



### 10.4 Results and Discussion

The magnetic flux vectors across the motor sectional area due to the radial magnetization in the magnets during open-circuit condition for 6-slot/4-pole slotless PMSM is illustrated in Fig. 10.5. The magnetic flux flows equally throughout the magnets and goes into the stator teeth from the north-pole to the south-pole of the magnets. The magnetic flux lines distribute equally along the four regions as represented in

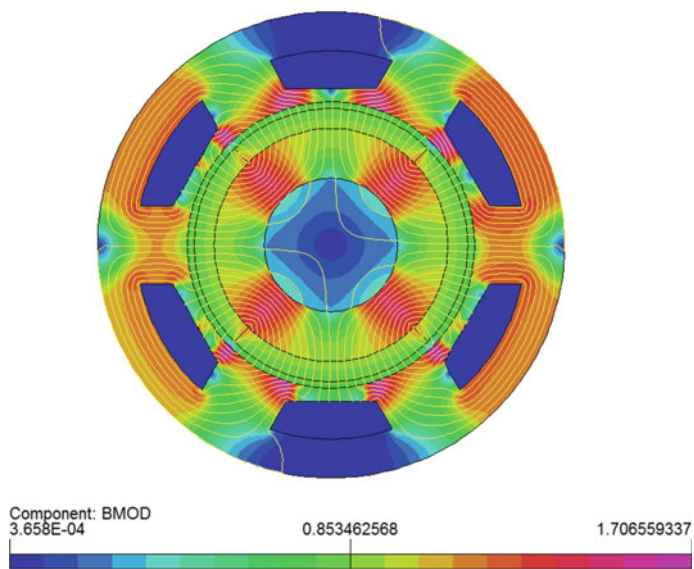


**Fig. 10.5** Magnetic vector field contour in 6-slot/4-pole slotless PMSM

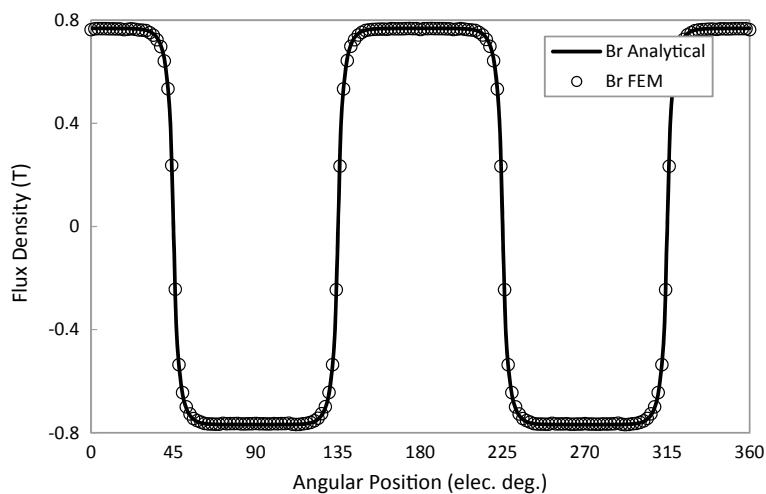
Fig. 10.6. The magnetic field density is less than the saturated value which is less than 1.7 T. A good design should have a maximum magnetic field density near to 1.7 T during open-circuit condition. This can be done by adjusting the stator dimensions. A few locations at stator shoe had high magnetic field density which can be improved by adjusting the stator shoe dimensions. The radial and tangential components of the magnetic flux density are represented in Figs. 10.7 and 10.8, respectively. It shows that the analytical calculation has a good match with the FE model. The magnetic flux density for the radial component has a smooth line due to slotless effect at the stator part. At tangential component there is little fluctuation due to the north–south magnet effect. The analysis can be extended more by rotating the rotor and observing the magnetic flux density at different rotor angular positions. This result can be applied to do analyses for slotted PMSM by introducing the slot opening at the stator part.

## 10.5 Conclusion

This paper has presented an analytical modelling of a slotless surface-mounted PMSM having 6-slot/4-pole configuration and radially magnetized magnets. Applying the Laplacian's and Poisson's equations, the derivations of the magnetic vector potential  $A_z$  can be formulated which later can be used to analytically predict the radial and tangential components of magnetic flux density in the air-gap region. A

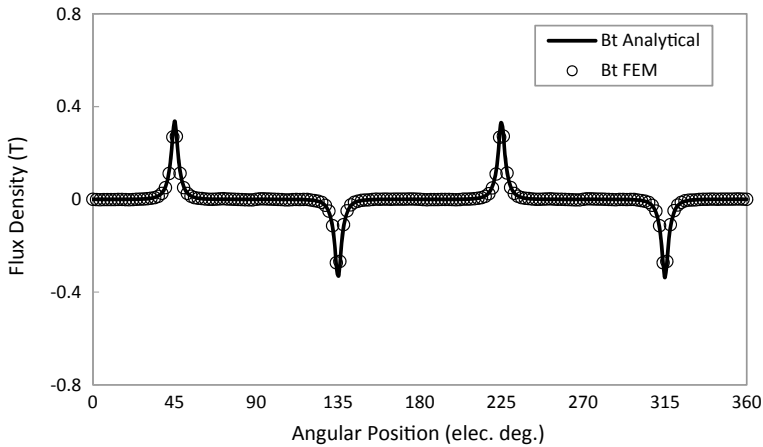


**Fig. 10.6** Magnetic flux lines and density contour for 6-slot/4-pole slotless PMSM



**Fig. 10.7** Air-gap magnetic flux density distribution (radial component)

good agreement has been achieved when results from the ASD model are compared with the 2-D FE model.



**Fig. 10.8** Air-gap magnetic flux density distribution (tangential component)

## References

1. Zhu ZQ, Chan CC (2008) Electrical machine topologies and technologies for electric, hybrid, and fuel cell vehicles. IEEE Vehicle Power and Propulsion Conference, 2008 (VPPC '08), Harbin, pp 1–6
2. EL-Refaie AM (2010) Fractional-slot concentrated-windings synchronous permanent magnet machines: opportunities and challenges. IEEE Trans Indus Electron 57(1):107–121
3. Duan Y, Ionel DM (2013) A review of recent developments in electrical machine design optimization methods with a permanent-magnet synchronous motor benchmark study. IEEE Trans Ind Appl 49(3):1268–1275
4. Yilmaz M, Krein PT (2008) Capabilities of finite element analysis and magnetic equivalent circuits for electrical machine analysis and design. In: IEEE power electronics specialists conference, 2008 (PESC 2008), Rhodes, pp 4027–4033
5. Sizov GY, Ionel DM, Demerdash NA (2011) A review of efficient FE modeling techniques with applications to PM AC machines. In: IEEE power and energy society general meeting, 2011, San Diego, CA, pp 1–6
6. Lubin T, Mezani S, Rezzoug A (2011) 2-D exact analytical model for surface-mounted permanent-magnet motors with semi-closed slots. IEEE Trans Magn 47(2):479–492
7. Wu LJ, Zhu ZQ, Staton D, Popescu M, Hawkins D (2010) Comparison of analytical models for predicting electromagnetic performance in surface-mounted permanent magnet machines. In: IEEE vehicle power and propulsion conference (VPPC), 2010, Lille, pp 1–6
8. Wu LJ, Zhu ZQ, Staton D, Popescu M, Hawkins D (2011) An improved subdomain model for predicting magnetic of surface-mounted permanent magnet machines accounting for tooth-tips. IEEE Trans Magn 47(6):1693–1704
9. Zhu ZQ, Wu LJ, Xia ZP (2010) An accurate subdomain model for magnetic field computation in slotted surface-mounted permanent-magnet machines. IEEE Trans Magn 46(4):1100–1115
10. Gilson A, Tavernier S, Dubas F, Depernet D, Espanet C (2015) 2-D analytical subdomain model for high-speed permanent-magnet machines. In: 18th international conference on electrical machines and systems (ICEMS), 2015, Pattaya, pp 1508–1514



11. Tiang TL, Ishak D, Lim CP, Jamil MKM (2015) A comprehensive analytical subdomain model and its field solutions for surface-mounted permanent magnet machines. *IEEE Trans Magn* 51(4):1–14
12. Zhu ZQ, Howe D, Chan CC (2002) Improved analytical model for predicting the magnetic field distribution in brushless permanent-magnet machines. *IEEE Trans Magnet* 38(1):229–238

# Chapter 11

## Comparative Study on the Performance of Electrical Vehicles with DC Drive and Series Motor, DC Drive and Separately Excited DC Motor, and AC Drive and PMSM Motor. Part 1: Driving and Braking Operations



**Saharul Arof, Mohamad Rosyidi Ahmad, Philip Mawby, Hamzah Arof, and Emilia Noorsal**

**Abstract** Conventional vehicles emit carbon monoxide and nitro oxide during the engine combustion. These two gases are two major contributors toward pollution to the environment. Electric vehicles (EVs) and hybrid electric vehicles (HEVs) offer an alternative solution to the above mentioned scenarios. However the prices of AC drive EVs and HEVs vehicle are unaffordable to people in some developed countries and of course to people in developing and third world countries. DC drives which consists of DC motor and DC converter or chopper offer good controllability and cheaper in price. Nevertheless, AC drives claim AC drive claims for less maintenance and good motor performance. The research aim is to compare the performance of AC drives EVs powered by PMSM AC motors, DC Drive EVs with series motors and DC drive EVs with separately excited DC motors.

---

S. Arof (✉) · M. R. Ahmad  
Universiti Kuala Lumpur, Malaysian Spanish Institute Kulim Hi-Tech Park, 09000 Kulim, Kedah, Malaysia  
e-mail: [saharul@unikl.edu.my](mailto:saharul@unikl.edu.my)

M. R. Ahmad  
e-mail: [mrosyidi@unikl.edu.my](mailto:mrosyidi@unikl.edu.my)

S. Arof · P. Mawby  
University of Warwick School of Engineering, Coventry CV47AL, UK  
e-mail: [p.a.mawby@warwick.ac.uk](mailto:p.a.mawby@warwick.ac.uk)

H. Arof  
Engineering Department, Universiti Malaya, Jalan Universiti, 50603 Kuala Lumpur, Malaysia  
e-mail: [ahamzah@um.edu.my](mailto:ahamzah@um.edu.my)

E. Noorsal  
School of Electrical Engineering, College of Engineering, Universiti Teknologi MARA, Cawangan Pulau Pinang, Kampus Permatang Pauh, 13500 Pulau Pinang, Malaysia  
e-mail: [emilia.noorsal@uitm.edu.my](mailto:emilia.noorsal@uitm.edu.my)

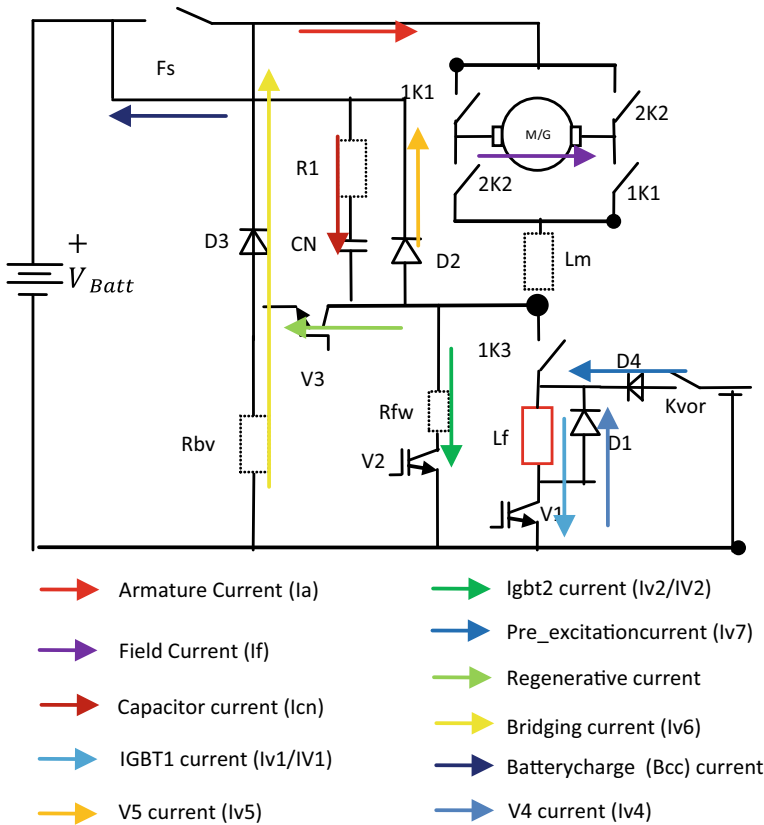
**Keywords** DC drive · FQDC · Design requirement · EV · Mathematical model chopper · NEDC · Series motor · Four quadrants chopper

## 11.1 Introduction

Using electric vehicles is one of the solutions to reduce global hydrocarbon emission [1]. The electric motor propulsion system (electric vehicle) will replace the internal combustion system (mechanical combustion engine not only because of zero-emission but it also due to higher efficiency).

### 11.1.1 Review Stage

Oak Research National Laboratory (ORNL) [1], United States in 2009, successfully designed a DC brushed motor with high power output (55 kW), high efficiency (92%) that can operate in low operating voltages (13 V) and this has initiated the interest in DC drive electric vehicles. Attempts to improve the conventional bridge chopper by increasing the operations or allowing the motor reverse action have been continuously carried out but ever since the development of the new motor by the ORNL, a new series motor four quadrants DC chopper such as shown in Fig. 11.1, was designed and the proposed chopper has multiple operations [2]. Different types of DC drive motors that can be used for motor traction for DC EVs such as the separately excited [3] has been developed. As part of EV design requirement [4] which need details investigations on the chopper operation modes led to the establishment of a simulation model to test the chopper operations for the application of electric car and light rail transit (LRT) [5]. This simulation model used to investigate each of the chopper operations of motor voltage, current, torque, speed, and FQDC for DC drive EC application [6] inclusive for system trouble shooting and fault diagnose [7]. This covers several modes of operation such as driving, field weakening [8], parallel mode [9], regenerative braking [10], and resistive braking [11]. For DC series motor traction of EC application, the speed and torque control for the series motor, in an attempt to reduce jerk and tire slip, has been implemented using direct current control technique [12]. For power regeneration, the FQDC offers the generator mode with several techniques of starting the regenerated power and voltage control is studied and discussed in [13]. In order for the FQDC to be applied in the real world it needs controllers running the control algorithm in the embedded system. The controller and its control algorithm are studied and tested using the processor in the loop (PIL) technique [14]. To improve the performance, artificial intelligence (AI) is introduced to control all of the chopper operations of the proposed FQDC chopper [15, 16]. Among the four AI controllers ANFIS shows the best performance, followed by neural network, the self-tuning Fuzzy logic controller and expert system [7]. An attempt cruising test with a specific requirement of remaining the traverse distance and battery state of charge using the



**Fig. 11.1** Novel DC chopper circuit with current flows indicated

Fuzzy logic [17] controller shows significance performance in controlling the EV operation. A study on a neural network controller to uncover the proper tuning method has been carried out based on using single controller with binary output [18]. On each specific FQDC chopper operation mode the performance can be further improved using an AI optimization tool such genetics algorithm [19] and gradient descend [20] to set up specific look up table of field current. The pole placement method [21] was used to tune the close controller to improve the controller performance while a Fuzzy logic controller is used to control the motor current [22] and to improve the control performance and system stability. For system fault diagnose and online system tuning and optimization, a numerical representation using Taylor series [23] is studied and tried for driving mode. The cascade PID with an ascend descend algorithm and after improvisation was associated to steering [24], brake [25], and vehicle movement control [26] to be used for autonomous EV for automatic reverse parking. Several other studies related to DC drive EV led to research on EC battery chargers [27], charging control algorithm [28], and the SOC estimator [29]. This charger circuit

mainly consists of the multi-level rectifier, buck chopper, and zero crossing circuit. This paper continues on the study on the EV performance to compare dc series, separately excited and AC PMSM motors.

A DC drive system offers lower cost due to its simple circuit, controller design, and control strategy [30–32]. The system is easy to control, maintain and trouble-shoot. The total cost of a drive system (AC or DC) depends on several factors such as the number of gate drive circuits, power electronics devices used, its cooling system, heat sinks, motor, and auxiliary devices. Normally, in a DC drive chopper, there are less power electronic devices used compared to an AC drive equipped with a frequency inverter. As a result, the number of gate drives is less. Thus, for a 4-quadrant drive application on motors with rated power bigger than 15 kW, a DC drive is always much cheaper than an AC drive system [33, 34]. Every time a power electronics device switches (on and off), it dissipates heat due to power loss [2]. In fact, power loss is bigger during turn off compared to turn on. The heat dissipated is absorbed by the heat sink and gets dissipated. Since the heat sink should have sufficient surface area for effective heat dissipation, the drive system with a smaller number of power electronics devices would incur lower switching power loss and has smaller size and weight. In a DC drive, no extra circuit is required to utilize the regenerative power to charge the battery but in an AC drive, a three-phase controlled bridge rectifier is necessary to convert the generated AC voltage to DC voltage before the battery or ultra capacitor can be charged [29]. This rectifier circuit complicates the design and control technique, generates conversion loss and requires more power for electronics devices and space which increases weight and cost.

With the latest technology, DC motor manufacturers have developed better DC motors suitable for EV/HEV applications. Such motors possess high power output, higher efficiency, smaller size, less weight, long lasting carbon brush and commutator, low operating voltage (less than 50 V), and modular concept (easy to replace parts like carbon brush, etc.) [24–32]. The advanced brush technology for DC motors allows the motor to be used at low voltages [1, 2] which results in lower losses that guarantees longer travel distance. The lifespan of the carbon brush and commutator of a DC motor is longer than the lifespan of the rotor bearing of an AC induction motor. The brush can last until 30,000 km, while the commutator can last until 250,000 km before it flushes over. The latest technology with a soft-commutated DC motor which has a high reliability of 88–90% and spark reduction system can further extend the brush life. The optimization of the design and control technique yield a DC motor drive which is comparable in performance to the AC drive but cheaper in price [1, 2].

An AC drive is expensive due to its complexity in the motor system, inverter system, bidirectional buck-boost converter system, and complex control strategy. The AC drive system uses more power electronic devices compared to a DC drive, because not only the inverter uses more power electronics than a chopper but it also needs more power electronic switching devices in the bidirectional buck-boost converter. The fact that the inverter is operated at high frequency and the AC drive uses lots of power electronic switching devices, AC drive needs a larger heat sink to remove heat as a result of the power switching losses. The total efficiency of an AC drive is lower compared to the efficiency of the PMSM motor itself, due to the need

of power conversion from battery power to buck-boost chopper, from buck-boost chopper to inverter and from inverter to the PMSM motor. A DC drive only requires conversion from the battery to the dc chopper and from DC chopper to the DC motor. The field weakening effect in an AC drive is only 1.5 of the base speed compared to the DC drive which is 5 times the base speed. The regenerative and resistive braking to brake and charging battery in an AC drive is more complex because the permanent magnet produces a constant magnetic flux and this is not controllable. Thus, the permanent magnet could generate an AC voltage could result the permanent magnet generates an AC voltage which could be too high or too low.

### ***11.1.2 DC Series Motor and Four Quadrants DC Chopper Four Series Motor***

A DC series motor is commonly used for electric vehicle traction. The DC brush series motor has the highest starting torque if compared to the same rated power to other types of electrical motors, inclusive separately excited DC motor. This special characteristic is very suitable for the traction of vehicles. The highest torque is only required to move the vehicle from standstill. Once the vehicle has already made a movement, it has already inertia, and due to this inertia, lower torque is required to propel the vehicle. Due to the fact that the series motor has a high starting torque, a lower kilowatt power of DC series motor can be used to propel the same weight of vehicle, compared to the other types of electrical motors inclusive separately excited DC motor. DC series motor is cheaper, is smaller in size, and is much lighter if the same rated power of DC series motor is compared to a separately excited DC motor. This is because separately excited dc motor has more winding turns in the armature and field winding to balance the starting current and back emf. A separately excited DC motor also requires two set of power supplies, and each is meant for armature and the field circuit. There are three IGBTs in the proposed chopper as shown in Figs. 11.3 and 11.4, and they are the main, the field weakening, and bridging IGBTs.  $L_M$  is the inductance of the motor and is connected in series with the armature windings to smoothen the armature current of the motor and  $R_{BV}$  is the brake series resistor.

### ***11.1.3 DC Drive EV Four Quadrants DC Chopper for Series Motor***

The four quadrants DC chopper is designed to overcome the limitations of common H-bridge chopper for controlling field wound DC series motor. A common H-bridge can perform driving and regenerative braking but is incapable of performing generator, resistive braking, and field weakening operations. Although the H-bridge is able to perform regenerative braking, but it depends on the remanence of the magnetic

field and not very effective because it only lies on the second quadrants of chopper operations which is when the speed of the rotor is higher than the base speed or when the voltage terminal is lower than the generated back emf. The novel design of the chopper has five main operations which is driving, field weakening, regenerative braking, resistive braking, and generator mode. The chopper circuits are designed by aligning and connecting power semiconductors such as IGBTs, diodes, resistors, inductors, and capacitors. The keys or two most important things for the novel chopper to perform such required operations are by controlling the direction of the current path/flows and controlling the number of current flows. The change of current direction flow causes changes in chopper operations. The advantage of the novel chopper is not just on extra operations that it can perform but the novel chopper has a lower number of power semiconductors compared to the common H-bridge chopper. This is to ensure lower cost and lower losses. Unlike the regenerative braking operations that a common H-bridge can perform, this novel chopper offers better regenerative braking power by the ability of separating, combining, and controlling the field inductor from the armature inductor motor to result in more braking power and more regenerative power produced. The result of reduction the field current is a reduction in back emf voltage. Even though the decreasing field current will cause the torque to decrease according to the theoretical equations, but the armature current will rise thus increasing the torque. The resistive braking action is done by creating a loop path for generated voltage to flow through a resistor called resistive braking or bridging resistor. The chopper switching frequency is determined by simulating the chopper driving operation. The chopper is tested at the minimum of IGBTs switching duty ratio. The best frequency is when the current has the lowest ripple. The lower the ripple current, the lower the ripple torque.

#### ***11.1.4 DC Separately Excited DC Motor and Four Quadrants DC Chopper***

It is well known that separately excited DC motors are easier to control and more stable in any mode of operation than series and shunt DC motors. To date, separately excited DC motors have been used in many prototypes or products for EV and HEV such as in the Peugeot 106, Citroen Saxo, GM EV and Lada [9, 10]. Research also has shown that separately excited DC motors offer EV with longer distance traversed for a lower price [9]. However, the last generation DC motors had disadvantages in their size, weight, performance, and reliability. The separately excited DC motors can provide sufficient high starting torque and constant torque during operation. In the working region above base speed/nominal speed, DC motors still have higher torque compared to that of AC motors [11–14]. The motor can supply almost constant torque during their operation which is good for climbing a steep hill so that speed will not drop drastically. The motors also feature high electrical braking power due to less power loss [15, 16] and a very good speed and controllability for regenerative power.

### 11.1.5 DC Drive EV Four Quadrants DC Chopper for Separately Excited DC Motor

A new four quadrant drive DC chopper (FQDC) design shown in Fig. 11.2 is proposed to work with a separately excited DC motor. The system has resistive braking mode to achieve higher efficiency during braking. While the common H-bridge [2–6] shown in Fig. 11.2 utilizes at least two semiconductors at a time, the proposed FQDC uses only one semiconductor with the same operation. The proposed chopper design helps to improve power as well as to reduce ripple.

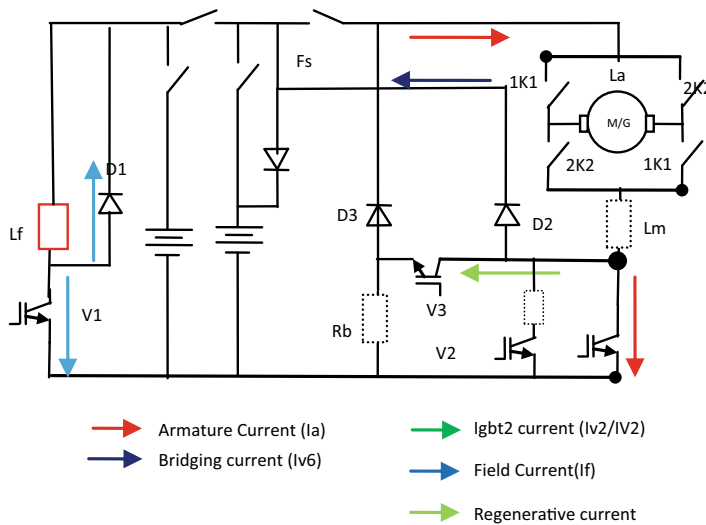


Fig. 11.2 Proposed FQDC topology

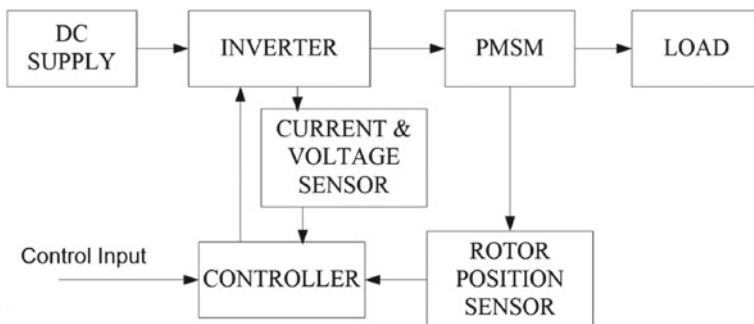
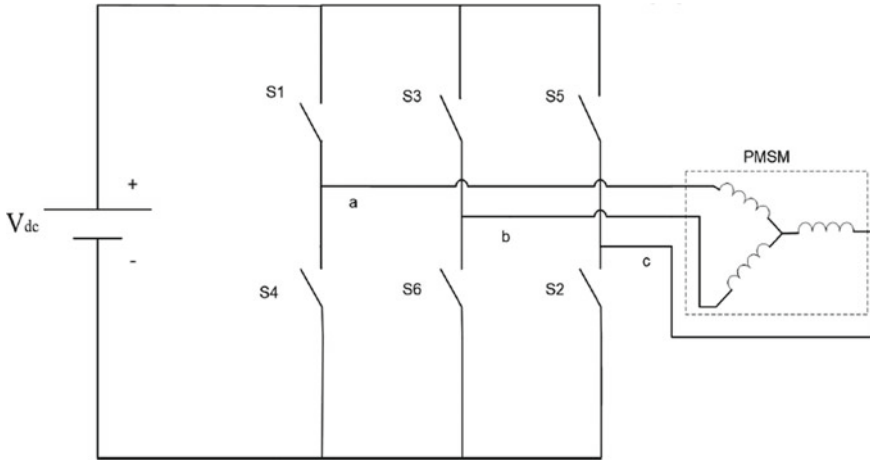


Fig. 11.3 Components permanent magnet synchronous motor drive





**Fig. 11.4** Voltage source inverter with DC supply and load (PMSM)

### ***11.1.6 Four Quadrants Drive DC Chopper Operation Modes***

The proposed FQDC is designed to work in five modes of operation: driving, field weakening, generator, regenerative braking, and resistive braking. These modes of operation can be controlled by an AI controller such as expert system, fuzzy logic, self-tuning fuzzy [2–4, 8], neural network as well as ANFIS. However, this paper focused only on the circuit operation of each mode of the proposed topology.

### ***11.1.7 AC Drive EV with PMSM Motor***

PM synchronous motors are very popular in a wide application area. The PMSM lacks a commutator and is therefore more reliable than the DC motor. The PM synchronous motor also has advantages when compared to an AC induction motor. Because a PMSM achieves higher efficiency by generating the rotor magnetic flux with rotor magnets, a PMSM is used in high-end white goods (such as refrigerators, washing machines, dishwashers); high-end pumps; fans; and in other appliances which require high reliability and efficiency. This application creates a speed closed-loop PM synchronous drive using a vector control technique. The PMSM consists of conventional three phase windings in the stator and permanent magnets in the rotor. The purpose of the field windings in the conventional synchronous machine is done by permanent magnets in PMSM. The conventional synchronous machine requires AC and DC supply, whereas the PMSM requires only AC supply for its operation. One of the greatest advantages of PMSM over its counterpart is the removal of DC supply for field excitation. The development of PMSM has happened due to the invention of

novel magnetic materials and rare earth materials. PMSM give numerous advantages in scheming recent motion management systems. Energy efficient PMSM is designed due to the availability of permanent magnet materials of high magnetic flux density. In synchronous motors the rotor rotates at the speed of stator revolving field.

The speed of the revolving stator field is called as synchronous speed. The synchronous speed can be found by the frequency of the stator input supply ( $f_s$ ) and the number of stator pole pairs. The stator of a three-phase synchronous motor consists of distributed sine three phase winding, whereas the rotor consists of the same number of p-pole pairs as stator, excited by permanent magnets. Both (typically) have a permanent-magnet rotor, and a wound stator BLDC (brushless DC) motor is a permanent-magnet brushless motor with trapezoidal back EMF PMSM (Permanent-magnet synchronous motor) and is a permanent-magnet brushless motor with sinusoidal back EMF.

### ***11.1.8 Permanent Magnet Synchronous Motor Drive System***

The motor drive essentially consists of four main components such as the PMSM, the inverter, the main control unit, and the position sensor. Interconnections of the components are shown in Fig. 11.3.

### ***11.1.9 AC Drive EV Inverter***

For variable frequency and magnitude, voltage source inverters are devices which convert the constant DC voltage level to variable AC voltage. As specified in the function, these inverters are commonly used in adjustable speed drives. The vector control strategy is far more complicated than the control of a DC motor requiring use of multiple control loops.

Figure 11.4 shows a voltage source inverter with a supply voltage VDC and with six switches. The frequency of the AC voltage can be variable or constant based on the applications [31–33].

Three phase inverters consist of a DC voltage source and six power ON/OFF switches connected to the PMSM as shown in Fig. 11.4. Selection of the inverter switches must be carefully done based on the necessities of operation, ratings, and the application. There are several devices available in the market, and these are thyristors, bipolar junction transistors (BJTs), MOS field effect transistors (MOSFETs), insulated gate bipolar transistors (IGBTs), and gate turn off thyristors (GTOs). It has been inferred that MOSFETs and IGBTs are preferred in the industry because of their advantages that the MOS gating permits high power gain and control advantages. MOSFET is considered to be a universal power ON/OFF device for low power and low voltage applications, whereas IGBT has wide acceptance in the motor drive applications and other application in the low and medium power range.

The power devices when used in motor drives applications require an inductive motor current path provided by antiparallel diodes when the switch is turned off.

## 11.2 Methodology

### 11.2.1 Electric Car Motor

The same kilowatt power of series motor, separately excited motor, and AC permanent magnet synchronous motor are used to be tested for EV propulsion and performance comparisons.

### 11.2.2 Vehicle Dynamics

The MATLAB/Simulink simulation models of the vehicle dynamics for the DC drive with series and separately excited and AC drive with PMSM motor are prepared for the test. The vehicle dynamics simulation model is shown in Fig. 11.5 and is derived using mathematical equations with some parameters set as follows:

$m = 1350$  kg, (full load)  $C_D = 0.2$ ,  $A_F = 2$  m<sup>2</sup>,  $C_O = 0.009$ ,  $C_1 = 0$ ,  $\rho = 1.1614$  kg/m<sup>3</sup>, and  $g = 9.81$  m/s<sup>2</sup>,  $r_{wh}$  = radius of wheel 0.28 m = 11 in., gear ratio = 4.2.

The complete MATLAB/Simulink simulation results of EV with separately excited DC motor, AC permanent magnet synchronous motor (AC PMSM), and

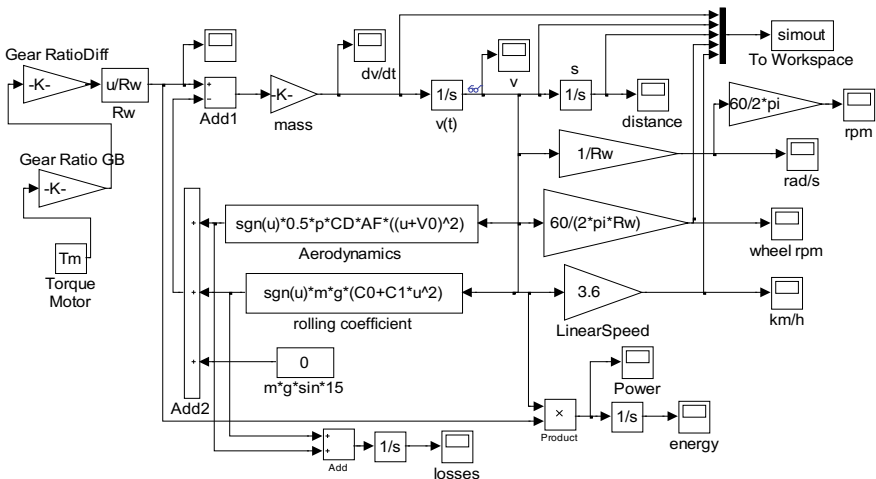


Fig. 11.5 Simulation of vehicle

DC series motor are tested using the same vehicle dynamic EV model for comparison. A 35 kW of series motor and separately excited DC motor operated at the maximum power of 22 kW are used for the test for DC Drive electric car. A 22 kW of AC synchronous motor is also tested for AC drive system to drive a car with a weight of 1325 kg (Figs. 11.6, 11.7, 11.8).

The simulation model results of the three motor drives systems are shown in Figs. 11.9, 11.10, 11.11, 11.12, 11.13, 11.14, 11.15, 11.16, 11.17, 11.18, 11.19.

### Results During Driving Operation

In Fig. 11.9, energy usage comparison are made. Dc series uses almost the same amount energy compared to the other two motors.

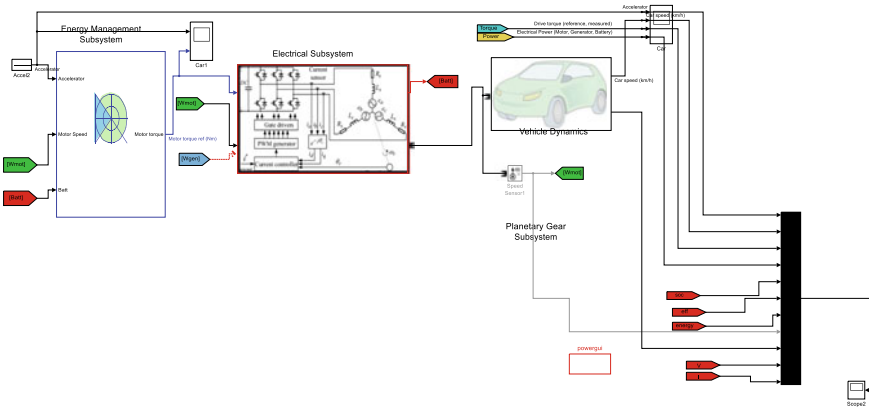


Fig. 11.6 Simulation of vehicle with DC drive series motor and FQDC chopper

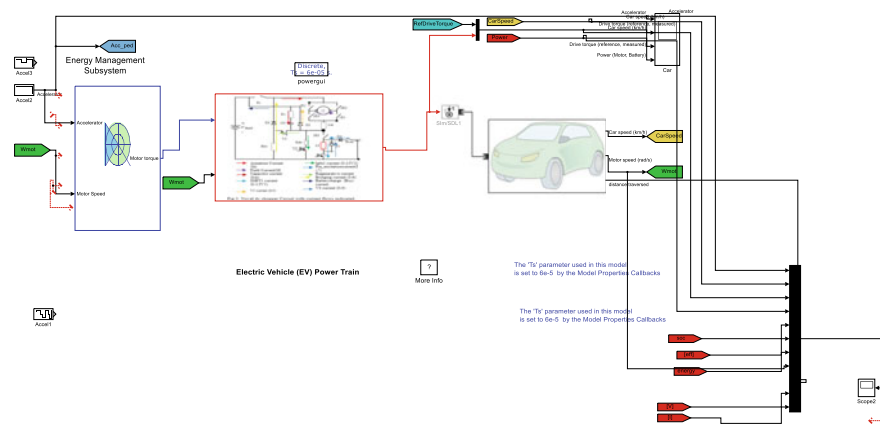


Fig. 11.7 Simulation of vehicle with AC PMSM motor and inverter

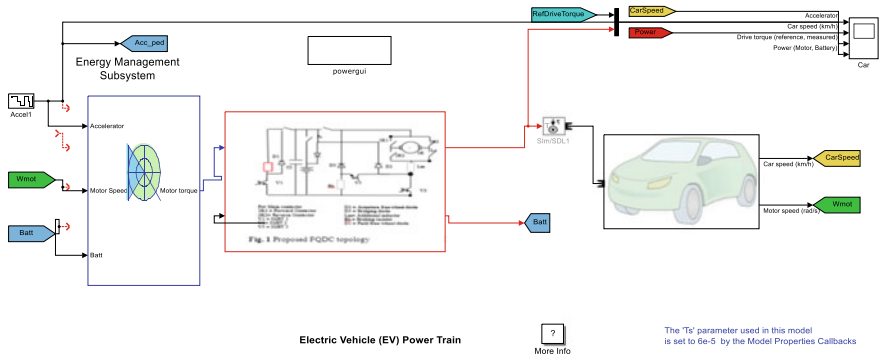


Fig. 11.8 Simulation of vehicle with DC drive separately excited dc motor and FQDC chopper

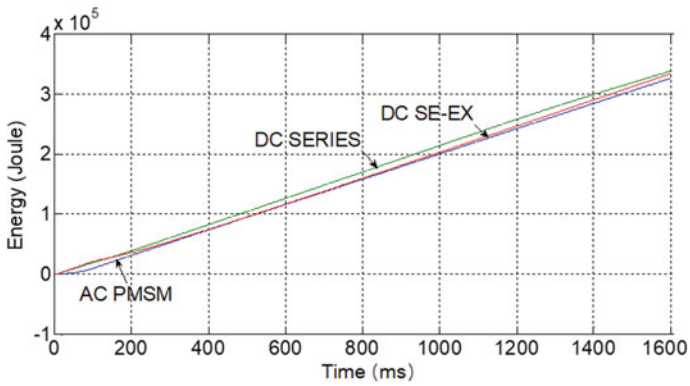


Fig. 11.9 Energy usage comparison

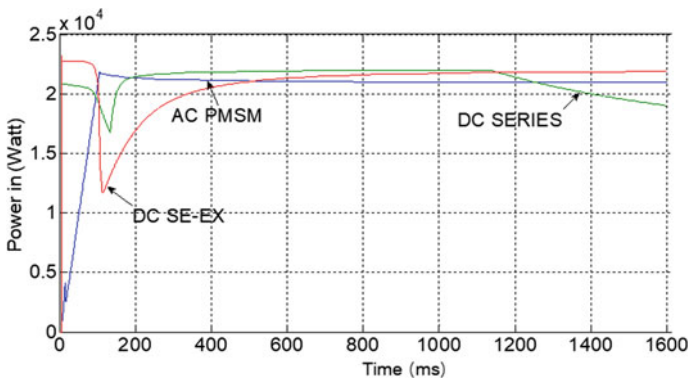


Fig. 11.10 Motor power at the starting before back emf effect drops it

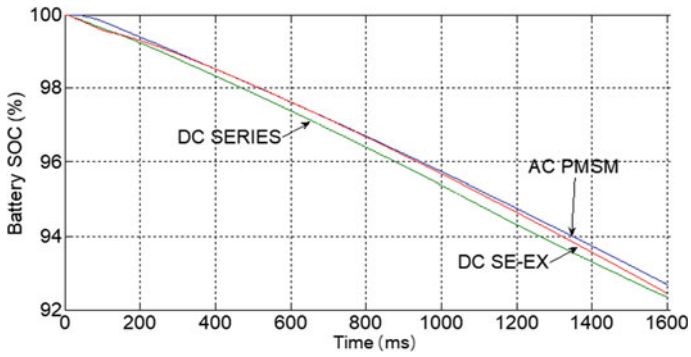


Fig. 11.11 Energy used at the starting point

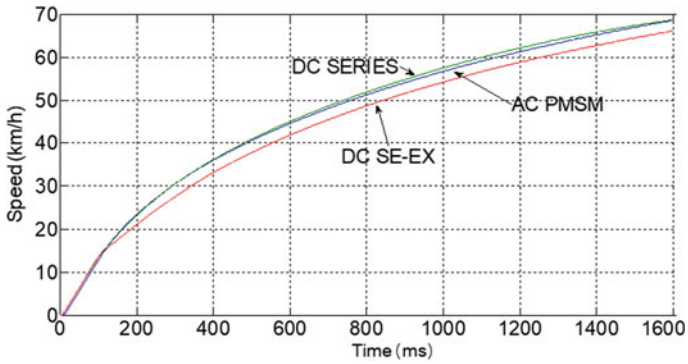


Fig. 11.12 EV speed from standstill

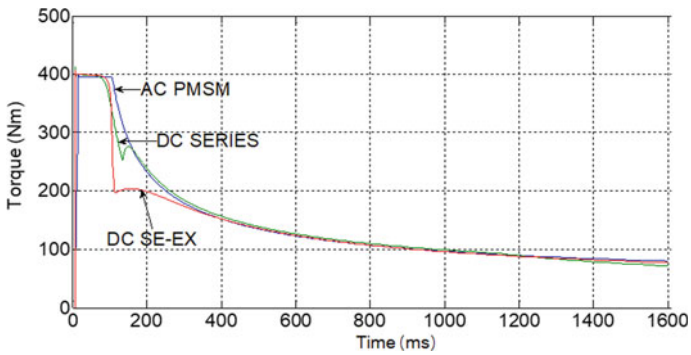


Fig. 11.13 Start losing the motor torque due to back emf

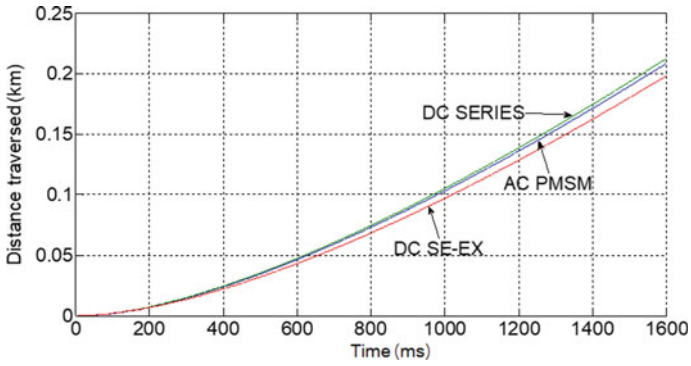


Fig. 11.14 Distance traverse comparison

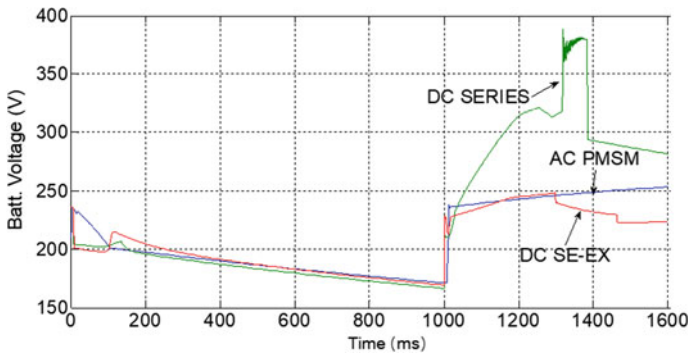


Fig. 11.15 Voltage generated during braking operation

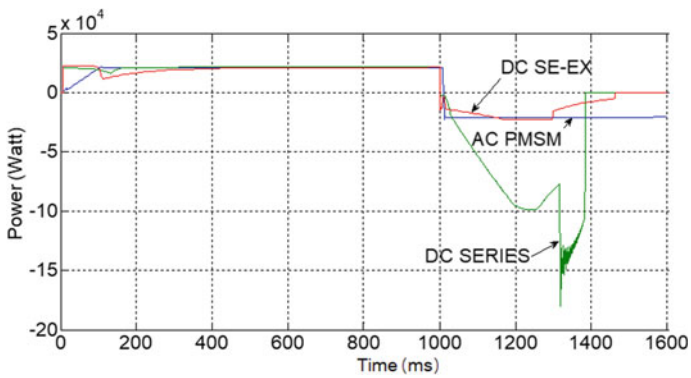


Fig. 11.16 Regenerative braking power comparison

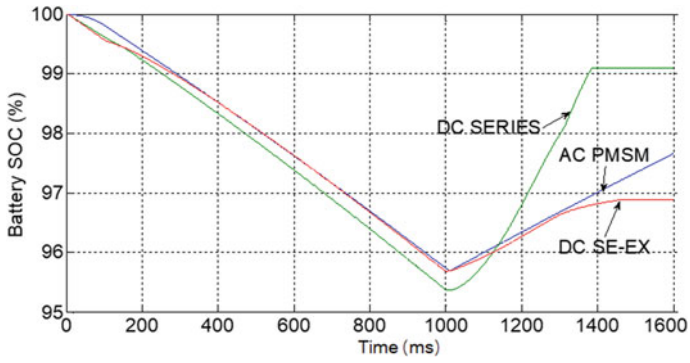


Fig. 11.17 Regenerative power to charge battery

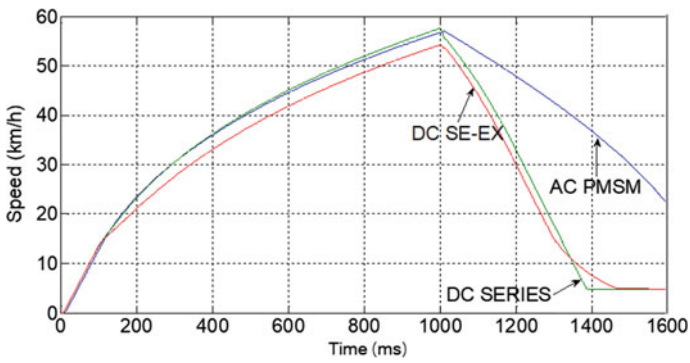


Fig. 11.18 Longer braking power for vehicle deceleration

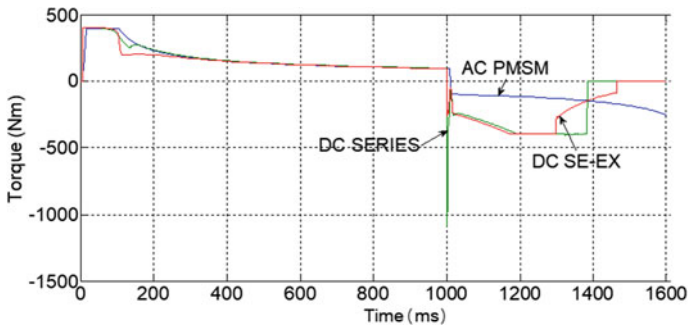


Fig. 11.19 Longest hold braking torque before depleted



In Fig. 11.10, separately excited motor exhibits good performance in which it can maintain motor power longer at the starting before drops due to back emf effect drops it.

In Fig. 11.11, DC series uses lesser energy compared to the other motors, and this is as a result of higher starting torque of the motor.

In Fig. 11.12, the EV speed of DC series and AC PMSM are close due to high starting torque.

In Fig. 11.13, EV with separately excited Dc motor is the first losing motor torque due to back emf.

In Fig. 11.14, EV using Dc series motor reach faster the distance traverse compared to the other two motors due to high starting torque.

### Braking Operation

In Fig. 11.15, DC series can generate high voltage due to special characteristics provide by FQDC during voltage built-up during generator mode.

In Fig. 11.16, regenerative braking power is high with dc series motor due to the FQDC design. While the AC PMSM is limited by permanent magnet. The Se-ex motor limited by field and armature current resistance and inductance.

In Fig. 11.17, regenerative power used to charge battery is the highest with dc series motor due to special FQDC architecture.

In Fig. 11.18, DC series produce the longer braking power for vehicle deceleration.

In Fig. 11.19, DC series has the longest hold braking torque before depleted due to FQDC design.

## 11.3 Conclusion

DC drive EV is suitable to be used as propulsion motor. With the FQDC chopper the performance is enhanced to the maximum and is comparable to AC drive motor and AC drive EV. The FQDC can improve the performance of the DC motor to be used as motor propulsion for DC drive EV.

## References

1. Oak Ridge National Laboratory (2009) Advanced brush technology for DC motors. Available: <http://peemrc.ornl.gov/projects/emdc3.jpg>
2. Arof S, Jalil JA, Yaakop NM, Mawby PA, Arof H (2014) Series motor four quadrants drive dc chopper part1: overall. Int Conf Power Electron
3. Arof S, Diyanah NHN, Noor NM, Jalil JA, Mawby PA, Arof H (2019) A new four quadrants drive chopper for separately excited DC motor in low cost electric vehicle. Progress Eng 119–138
4. Arof S, Noor NM, Nur Diyanah NH, Mawby P, Arof H, Noorsal E (2021) DC drive electric car utilizing series motor and four quadrants drive DC chopper parameter determination

- from general design requirements. *Progress Eng Technol* 3. [https://doi.org/10.1007/978-3-030-67750-3\\_17](https://doi.org/10.1007/978-3-030-67750-3_17)
5. Arof S, Hassan H, Rosyidi M, Mawby PA, Arof H (2017) Implementation of series motor four quadrants drive DC chopper for DC drive electric car and LRT via simulation model. *J Appl Environ Biol Sci* 7(3S):73–82
  6. Arof S, Noor NM, Elias F, Mawby PA, Arof H (2017) Investigation of chopper operation of series Motor Four Quadrants DC Chopper. *J Appl Environ Biol Sci* 7(3S):49–56
  7. Arof S, Faiz MR, Diyanah NHN, Yaakop NM, Mawby P, Arof H, Noorsal E (2021) Fault diagnose of DC drive EV utilizing a new series motor four quadrants DC chopper using an expert system and quadratic solver running in embedded: part 1: during start up. *Progress Eng Technol* 3. [https://doi.org/10.1007/978-3-030-67750-3\\_15](https://doi.org/10.1007/978-3-030-67750-3_15)
  8. Arof S, Diyanah NHN, Mawby PA, Arof Emilia Noorsal H (2021) Series motor four quadrants drive DC chopper part3: field weakening mode. *IOP Conf Series Mater Sci Eng* 1127(1):012028. <https://doi.org/10.1088/1757-899X/1127/1/012028>
  9. Arof S, Diyanah NHN, Mawby PA, Arof Emilia Noorsal H (2021) New series motor four quadrants drive DC chopper for economical EV, part5: parallel mode. *IOP Conf Series Mater Sci Eng* 1127(1):012025. <https://doi.org/10.1088/1757-899X/1127/1/012025>
  10. Arof Emilia Noorsal S, Mawby PA, Arof H (2020) Series motor four quadrants drive DC chopper for DC drive electric vehicle part6: regenerative braking. *International Scientific Forum (ISF2019)*, Melaka, Malaysia, eISBN: 978-967-10842-1-2
  11. Arof S, Noorsal E, Mawby PA, Arof H (2020) Series motor four quadrants drive DC chopper for DC drive electric vehicle part 7: resistive braking. *Int Sci Forum (ISF2019)*, Melaka, Malaysia, eISBN: 978-967-10842-1-2
  12. Arof S, Jalil JA, Kamaruddin NH, Yaakop NM, Mawby PA, Arof H (2016) Series motor four quadrants drive dc chopper part 2: driving and reverse with direct current control. *Int Conf Power Electron* 775–780. <https://doi.org/10.1109/PECON2016.7951663>
  13. Arof S, Diyanah NHN, Noor NMN, Radzi M, Jalil JA, Mawby PA, Arof H (2019) Series motor four quadrants drive DC chopper: part 4: generator mode. *Progress Eng* 155–167. [https://doi.org/10.1007/978-3-030-28505-0\\_12](https://doi.org/10.1007/978-3-030-28505-0_12)
  14. Arof S, Diyanah H, Yaakop NM, Mawby PA, Arof H (2019) Processor in the loop for testing series motor four quadrants drive direct current chopper for series motor driven electric car: part1: chopper
  15. Arof S, Muhd Khairulzaman AK, Jalil JA, Arof H, Mawby PA (2015) Self tuning fuzzy logic controlling chopper operation of four quadrants drive DC chopper for low cost electric vehicle. In: 6th international conference on intelligent systems, modeling and simulation. *IEEE computer Society*, pp 40–44
  16. Arof S, Zaman MK, Jalil JA, Mawby PA, Arof H (2015) Artificial intelligence controlling chopper operation of four quadrants drive DC chopper for low cost electric vehicle. *Int J Simul Syst Sci Technol*. <https://doi.org/10.5013/IJSSST.a.16.04.03>
  17. Arof S, Diyanah NHN, Mawby PA, Arof Emilia Noorsal H (2020) DC drive electric car state of charge (SOC) and remaining distance traverse (RDT) optimized by fuzzy logic. *International Scientific Forum (ISF2019)*, Melaka, Malaysia, eISBN: 978-967-10842-1-2
  18. Arof S, Diyanah NH, Mawby PA, Arof H (2019) Study on implementation of neural network controlling four quadrants direct current chopper: part1: using single neural network controller with binary data output. *Adv Eng Process Technol* 37–57
  19. Arof S, Diyanah NHN, Noor NM, Rosyidi M, Mawby PA, Arof H (2019) Genetics algorithm for setting up look up table for parallel mode of new series motor four quadrants dc chopper. *Progress Eng* 155–167. [https://doi.org/10.1007/978-3-030-28505-0\\_12](https://doi.org/10.1007/978-3-030-28505-0_12)
  20. Arof S, Shauqee ARA, Rosyidi M, Diyanah NHN, Mawby P, Arof H, Noorsal E (2021) Gradient descend for setting up a look-up table of series motor four quadrants drive DC chopper in parallel mode. *Progress Eng Technol* 3. [https://doi.org/10.1007/978-3-030-67750-3\\_16](https://doi.org/10.1007/978-3-030-67750-3_16)
  21. Arof S, Noor NM, Alias MF, Noorsal E, Mawby P, Arof H (2020) Digital proportional integral derivative (PID) controller for closed-loop direct current control of an electric vehicle traction tuned using pole placement. *Progress Eng Technol II Adv Struct Mater* 131. Springer, Cham. [https://doi.org/10.1007/978-3-030-46036-5\\_8](https://doi.org/10.1007/978-3-030-46036-5_8)

22. Arof S, Noor NM, Mohamad R, Noorsal E, Mawby PA, Arof H (2020) Close loop feedback direct current control in driving mode of a four quadrants drive direct current chopper for electric vehicle traction controlled using fuzzy logic. *Progress Eng Technol II Adv Struct Mater* 131. Springer, Cham. [https://doi.org/10.1007/978-3-030-46036-5\\_7](https://doi.org/10.1007/978-3-030-46036-5_7)
23. Arof S, Sukiman ED, Diyanah NH, Noor NM, Emilia Noorsal, Mawby PA, Arof H (2020) Discrete-time linear system of new series motor four-quadrant drive direct current chopper numerically represented by Taylor Series. *Progress Eng Technol II Adv Struct Mater* 131. Springer, Cham. [https://doi.org/10.1007/978-3-030-46036-5\\_10](https://doi.org/10.1007/978-3-030-46036-5_10)
24. Arof S, Said S, Diyanah NHN, Noor NM, Yaakop NM, Mawby P, Arof H, Noorsal E (2020) Series motor four-quadrant direct current chopper: reverse mode, steering position control with double-circle path tracking and control for autonomous reverse parking of direct current drive electric car. *Progress Eng Technol II Adv Struct Mater* 131. Springer, Cham. [https://doi.org/10.1007/978-3-030-46036-5\\_12](https://doi.org/10.1007/978-3-030-46036-5_12)
25. Arof S, Sazali MS, Diyanah NHN, Mawby P, Arof H, Noorsal E (2021) Series motor four quadrants drive DC chopper: reverse mode with automatic reverse parking of DC drive electric car with constant brake motor control combine to the propulsion motor torque. *Progress Eng Technol III*. [https://doi.org/10.1007/978-3-030-67750-3\\_20](https://doi.org/10.1007/978-3-030-67750-3_20)
26. Arof S, Said S, Diyanah NHN, Noor NM, Jalil JA, Mawby P, Arof H, Noorsal E (2020) Series motor four-quadrant DC chopper: reverse mode, direct current control, triple cascade PIDs, and ascend-descend algorithm with feedback optimization for automatic reverse parking. *Progress Eng Technol II Adv Struct Mater* 131. Springer, Cham. [https://doi.org/10.1007/978-3-030-46036-5\\_13](https://doi.org/10.1007/978-3-030-46036-5_13)
27. Arof S, Diyanah NHN, Mawby P, Arof H, Mohd Yaakop N (2019) Low harmonics plug-in home charging electric vehicle battery charger utilizing multi-level rectifier, zero crossing and buck chopper: part 1: general overview. *Progress Eng* 103–108. [https://doi.org/10.1007/978-3-030-28505-0\\_9](https://doi.org/10.1007/978-3-030-28505-0_9)
28. Arof S, Ahmad MR, Yaakop NM, Mawby P, Arof H, Noorsal E, Bakar AA, Mohd Ali Y (2021) Low harmonics plug-in home charging electric vehicle battery charger utilizing multilevel rectifier, zero crossing, and buck chopper: state of charge estimator using current integration algorithm for embedded system. *Progress Eng Technol* 3. [https://doi.org/10.1007/978-3-030-67750-3\\_19](https://doi.org/10.1007/978-3-030-67750-3_19)
29. Arof S, Sazali MS, Mohamed Noor N, Nur Amirah J, Mawby P, Noorsal E, Abu Bakar A, Mohd Ali Y (2021) Low harmonics plug-in home charging electric vehicle battery charger utilizing multi-level rectifier, zero crossing, and buck chopper: BMS battery charging control algorithm. *Progress Eng Technol III*. [https://doi.org/10.1007/978-3-030-67750-3\\_18](https://doi.org/10.1007/978-3-030-67750-3_18)
30. Gao Y, Ehsani M (2010) Design and control methodology of plug-in hybrid electric vehicles. *IEEE Trans Ind Electron* 57(2):633–640
31. Westbrook MH (2001) The electric and hybrid electric vehicle. SAE
32. Husain I (2003) Electric and hybrid electric vehicles, design fundamentals. CRC Press
33. Bansal RC (2005) Birla institute of technology and science, Pilani, India. electric vehicle. Handbook of automotive power electronics and motor drives. Taylor & Francise group CRC Press
34. Rashid MH (2004) Power electronics, circuits, devices and applications, 3rd edn. Prentice Hall

# Chapter 12

## Overall Heat Transfer Coefficient of Different Coolants and Frontal Air Velocity in Automotive Radiators



Ain Najwa Abdul Manan, Dzarisofea Anuar,  
Muhammad Latiff Abd Khalid, Ahmad Kamal Ismail,  
and Ishak Abdul Azid

**Abstract** An educational experimental test rig was designed to evaluate the performance of an automotive radiator. The effect of liquid coolants and frontal air velocity on the radiator performance based on the overall heat transfer coefficient were investigated by using the test rig. The experimental setup consisted of a real engine and an educational test rig. A set of experiments was conducted with three different coolants while parameters including inlet and outlet temperatures were recorded at constant flow rate. In order to study the effect of frontal air velocity, the engine was taken to be in motion by giving an external air flow to the radiator. An air tunnel was designed to be mounted at the frontal area of the radiator. In this experiment, the temperature of the radiator was also measured at different engine speeds and frontal air velocities. Analysis of engine cooling parameters such as flow rate, inlet, and outlet temperature, surrounding and radiator temperature, surface area, and rate of heat dissipation was performed using the log mean temperature different (LMTD) method and finally the overall heat transfer coefficient (OHTC) was determined. The results showed that the radiator performance for both real engine and educational test rig increased when a coolant is used. In addition, increasing the speed of fan at the frontal area improved the heat dissipation of the radiator.

**Keywords** Educational test rig · Overall heat transfer coefficient · Coolants

### 12.1 Introduction

An automotive radiator is a heat exchanger that cools the internal combustion engine and helps to prevent from heat seizure due to thermal expansion. The combustion

---

A. N. A. Manan · D. Anuar · M. L. A. Khalid · A. K. Ismail (✉) · I. A. Azid  
Universiti Kuala Lumpur, Malaysian Spanish Institute Kulim Hi-Tech Park, 09000 Kulim, Kedah, Malaysia  
e-mail: [ahmadkamal@unikl.edu.my](mailto:ahmadkamal@unikl.edu.my)

I. A. Azid  
e-mail: [ishak.abdulazid@unikl.edu.my](mailto:ishak.abdulazid@unikl.edu.my)

processes that convert thermal energy into mechanical work have to remove some of the heat energy into the surrounding through exhaust gases and also absorbed by the engine block [5]. A pump circulates cooling liquids between the radiator and the engine block water jacket so that the engine temperature can be maintained at a suitable operating temperature. The cooling liquid pump commonly known as water pump is connected to the engine belting and radiator fan. This connection ensures that the pump and fan speed are controlled by the engine power. In the radiator, the cooling liquids have to pass through tubes where the outside of the tubes is surrounded with fins. Since the radiator itself is normally made from high thermal conductivity materials such as copper or brass, the heat inside the cooling liquids will be easily dissipated to the outside of the tubes. Due to this phenomena, the cooling liquids must be very efficient to collect heat from the engine and remove it from the radiator. High efficiency engines with better cooling system are the challenges faced by the automotive manufacturers nowadays for better fuel consumption and less emission [1]. A high performance engine is also based on the cooling system for endurance and durability. A compact radiator may reduce the vehicle weight. By optimizing design and size of a radiator, it reduces the materials and the cost of the manufacturer [6]. In order to evaluate the performance of an automotive radiator, the educational test rig was designed and fabricated to be located in the laboratory. The radiators are installed into the test setup and the data from the educational test rig is be compared with data from the real engines. The experimental rig was designed with flexibility where different types of car radiators can be installed and the flow rate of water with different coolants can be applied. This work presented preliminary results of different coolants applied to the Perodua Kelisa radiator with different frontal air velocities.

## 12.2 Literature

### 12.2.1 Coolants

Performance evaluation on the various parameters by using a different coolant has been done in previous literatures [3, 7, 8]. The works focused on comparative studies between coolants such as water and other mixtures such as water in propylene glycol. Ethylene glycol such as (IUPAC name: ethane-1, 2-diol) can be categorized as an organic compound normally used as an automotive antifreeze and a precursor to polymers. The coolants performance nowadays have been investigated by many researchers in order to improve the performance as well as to extend their lifetime. It has been done by introducing  $\text{Al}_2\text{O}_3$ /water-mono as nanofluids and tested experimentally as a coolant for automotive radiators [2, 7]. The mixture between water and coolant varies and is usually tested in laboratories. Some used 50:50 proportions by volume. For the nanofluids used as coolant, it can be observed that the heat transfer performance of radiator is increased compared to conventional coolants.

### **12.2.2 Air Flow**

The air flow from outside or the frontal area of the car plays an important role to ensure the radiator works efficiently. Therefore, this area requires a proper design [4, 9]. By referring to Pang et al. [6], the ram air and radiator fan are the two main sources of energy which contribute to the cooling air flow through the under hood or frontal area of the vehicle. During vehicle acceleration at high speed, the cooling air flow is dominated by ram air and when the vehicles decelerate, the main source of cooling from air comes from the radiator fan. Ram air is produced from the movement of the vehicles normally at high speed that affect the static pressure gradient between the vehicle frontal opening inlets and underbody. The interfaces of interaction between air and the radiator are the frontal opening and the underside of the engine bay [2]. The study by Zhang et al. stated that the proper under hood airflow behavior of vehicles has two main goals. The first target is to ensure the required cooling performance of the heat exchangers. Next, the goal is to minimize the cooling drag component of the total vehicle drag. This emphasizes the important design of the frontal area for vehicles. At constant normal velocity such as at the rate of highway speeds, the volumetric flow rate and flow pattern observed over the radiator surface act as the major causes that influence the radiator performance. In contrast, if a vehicle travels at low speeds or idling, a different phenomenon will occur that may reduce the system performance. This phenomenon is known as under hood hot air recirculation. In designing the frontal area of the vehicle to improve the air circulation around the radiator, the drag effect must be taken into account as it will reduce the performance of the car and fuel efficiency.

## **12.3 Methodology**

### **12.3.1 Experimental Setup**

An experimental setup has been designed and fabricated in our laboratory. The various components of the experimental setup are described below. As shown in Figs. 12.1 and 12.2, the important components of the system are; engine, radiator, radiator hose, water tank and heating element, water pump, piping and fitting, flow meter and a thermocouple. The three types of coolants used were Proton coolant, Toyota coolant, and Nissan coolant. The flow rate was set at 18 L/min for the educational test rig. In this study, a test facility for a real engine has been developed by using a 4-stroke engine, 4 cylinders with 1499 cc. A set of thermocouples (K-type) were used to monitor the temperature distribution at the radiator core and water tank. The thermocouples were connected to the data acquisition having  $\pm 0.1$  °C accuracy.

**Fig. 12.1** Educational test rig



**Fig. 12.2** Real engine with frontal air induced



### 12.3.2 Data Analysis

The log mean temperature difference (LMTD) method was used to calculate the OHTC and to obtain the required outlet temperatures. The general formula as shown in Eq. (12.1) for cross-flow heat exchangers has been done by using the LMTD method. The inlet and outlet temperature data obtained from the experiment were used in this equation. The equation is given by

$$Q = UAF \Delta T \text{ log-mean} \tag{12.1}$$

where Q is the overall heat transfer rate of the radiator, U is the overall heat transfer coefficient (OHTC), A is the surface area measured from the design of tubes and fins, F is the correction factor, and  $\Delta T_{\text{log-mean}}$  is the log mean temperature difference of the two fluids.

## 12.4 Results

### 12.4.1 Effect of Coolant in Real Engine and Educational Test Rig

Graphs in Figs. 12.3 and 12.4 show the results of the overall heat transfer coefficient (OHTC) obtained from the real engine and educational test rig. Both results indicated that OHTC for the radiator with Nissan, Toyota, and Proton coolant manufacturer

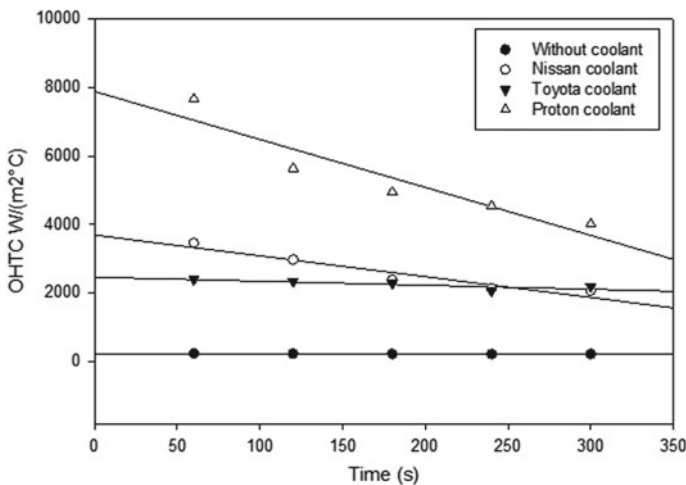
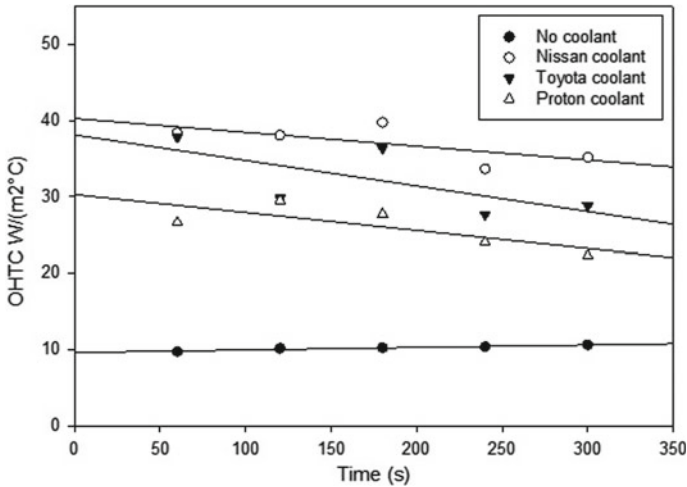


Fig. 12.3 OHTC of different coolants in the real engine





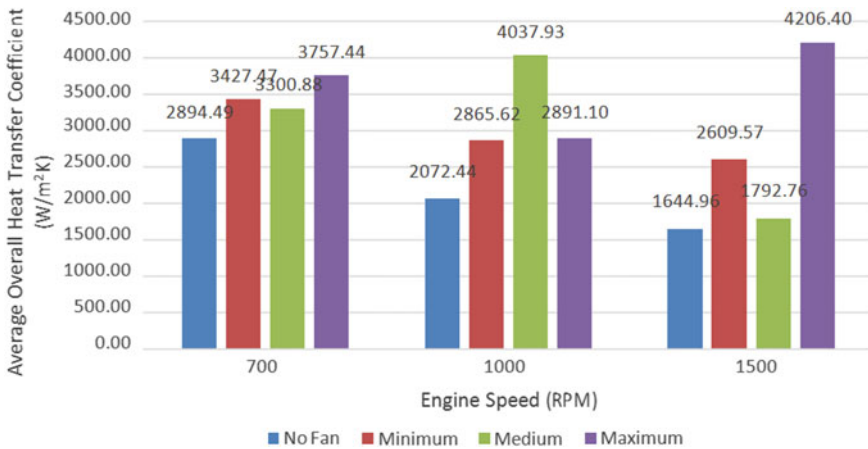
**Fig. 12.4** OHTC of different coolants in the educational test rig

applied as cooling fluids mixture have better performance than without coolant (only distilled water). The trend for OHTC with different coolants was the same for both the educational test rig and the real engine. It means that the educational test rig can be used to replace the real engine in investigating the performance of different coolants such as nanofluid in the future.

### 12.4.2 Effect of Frontal Air Velocity in Real Engine at Different RPM

Figure 12.5 shows the result of average overall heat transfer coefficient against engine speed. Based on the results as shown, at 1500 RPM, at maximum fan speed, the average overall heat transfer was the highest. At medium and minimum fan speed, the average overall heat transfer coefficient decreased. Without air flow (no fan), the average overall heat transfer coefficient was small. At 1500 RPM, the maximum fan speed shows the highest value compared to others.

There are many factors that affect the overall heat transfer coefficient of the radiator such as the temperature difference, specific heat capacity, and flow velocity. The temperature difference depends on the inlet and outlet of the radiator. The higher the temperature difference, the higher the overall heat transfer coefficient. Increased value of the heat transfer coefficient means that the performance of the radiator improved. The specific heat capacity depends on the average of the inlet and outlet temperature of the radiator while the flow velocity depends on the air flow. However, at 700 RPM, the overall heat transfer coefficient was not constant due to the engine RPM that increased from time to time. At 1000 RPM, the overall heat transfer



**Fig. 12.5** Overall heat transfer coefficient against engine speed

coefficient at medium fan speed improved while at 1500 RPM, the maximum fan speed showed the highest improvement. At 1000 and 1500 RPM, the overall heat transfer coefficient of the radiator without fan decreased while at 700 RPM, the value increased. It can be concluded that the overall heat transfer coefficient can be improved by giving external air flow.

## 12.5 Conclusions

A test facility has been successfully developed in the study on the fluid cooling system for automotive as shown in this work. It has been validated with the real engine cooling system with radiator. The results trend has shown some similarities. The value of overall heat transfer coefficient, OHTC using coolants have better performance than without coolant for both real engine and educational test rig. The performance of the radiator induced with frontal air was successfully analysed by taking the temperature of the radiator at the inlet and outlet. It can also be concluded that the design of the automotive frontal area may also increase the velocity of air which also increases the OHTC.

## References

1. Amrutkar PS, Patil SR (2013) Automotive radiator performance–review. *Int J Eng Adv Technol* 2(3):563–565
2. Bhogare RA, Kothawale B (2014) Performance investigation of automobile radiator operated with Al<sub>2</sub>O<sub>3</sub> based nanofluid. *IOSR J Mech Civ Eng* 11(3):23–30

3. Jha BK, Khandelwal N et al (2015) Analysis of automobile radiator test rig using different coolants. *Int J Adv Technol Eng Sci* 3:420–421
4. Kishanrao CD (2016) Thermal optimization of fan assisted heat exchanger radiator by design improvements
5. Mukkamala Y (2017) Contemporary trends in thermo-hydraulic testing and modeling of automotive radiators deploying nano-coolants and aerodynamically efficient air-side fins. *Renew Sustain Energy Rev* 76:1208–1229
6. Pang S, Kalam M et al (2012) A review on air flow and coolant flow circuit in vehicles' cooling system. *Int J Heat Mass Transf* 55(23–24):6295–6306
7. Subhedar DG, Ramani BM et al (2018) Experimental investigation of heat transfer potential of Al<sub>2</sub>O<sub>3</sub>/Water-Mono Ethylene Glycol nanofluids as a car radiator coolant. *Case Stud Therm Eng* 11:26–34
8. Vashist D, Bhatia S et al (2014) Some studies on the performance of automotive radiator at higher coolant temperature. *J Basic Appl Eng Res* 1(3):41–46
9. Zhang C, Uddin M et al (2018) Full vehicle CFD investigations on the influence of front-end configuration on radiator performance and cooling drag. *Appl Therm Eng* 130:1328–1340

# Chapter 13

## Magnetic Field Distribution for Single Coil Pulsed Linear Accelerator



M. Rezal, D. Ishak, and M. S. Ahmad

**Abstract** This paper presents the magnetic field distribution for a single coil pulsed linear accelerator. The design of the pulsed linear accelerator is implemented using a coil and capacitor bank. A Hall-effect sensor is applied to measure the magnetic field inside the coil. Basically, this project focuses on the magnetic field distribution for different Hall-effect positions inside the coil with different settings of capacitor banks. The capacitor bank is operated as a pulse current generator for the coil. The result obtained is compared for different magnetic field distributions with different Hall-effect positions inside the coil. The result is tabulated and analyzed using a graphical method. The purposes of the research are to analyze the magnetic field distribution for a single coil pulsed linear accelerator using a Hall-effect sensor and to obtain the highest magnetic field for a specific Hall-effect sensor position inside the coil. The result showing that the 200 V, 1120  $\mu\text{F}$  capacitor bank with Hall-effect sensor position of 7 mm and magnetic field of 12.2 mT.

**Keywords** Magnetic field · Coil · Pulsed · Accelerator

### 13.1 Introduction

A linear pulsed accelerator is a device to accelerate particles in a straight line by electric fields which is mostly used within industry, radiotherapy, and others. Nowadays, electromagnetism plays an important role. This project presents the real application for electromagnetism which is used to move the particle of the linear accelerator.

---

M. Rezal (✉)

Universiti Kuala Lumpur, Malaysian Spanish Institute, Kulim, Kedah, Malaysia  
e-mail: [mrezal@unikl.edu.my](mailto:mrezal@unikl.edu.my)

D. Ishak

School of Electrical and Electronic Engineering, Universiti Sains Malaysia, Penang, Malaysia  
e-mail: [dahaman@usm.my](mailto:dahaman@usm.my)

M. S. Ahmad

School of Electrical System Engineering, Universiti Malaysia Perlis, Arau, Perlis, Malaysia  
e-mail: [saufiahmad@unimap.edu.my](mailto:saufiahmad@unimap.edu.my)

Basically this project focuses on how to find the magnetic field characteristic that is produced from the coil when the Hall-effect sensor is moved from one position to another inside the coil. This project focuses on the electromagnetic characteristic for a single coil pulsed linear accelerator. Apart from that, the coil is developed using a copper wire winding through the cylindrical casing. At the same time the magnetic field of the coil is measured using a Hall-effect sensor for different Hall-effect sensor positions inside the coil. An electrolyte capacitor is used to supply the pulse current that flows into the coil. Since the Hall-effect sensor position is moved, then results are produced and displayed at the output of the digital oscilloscope. The result will be computed and plotted to find the best magnetic field at the best position of the Hall-effect sensor inside the coil.

## 13.2 Literature Review

For the past few years, two ideas were investigated to get the source for a particle accelerator, i.e. the Wideroe's ray-transformer and the Ising's linear accelerator [1]. The Ising's linear accelerator used a RC circuit as source and spark gap as the switch element [2]. A series of linear accelerators is applied in order to increase the electron velocity in the tube. Earlier in 1945, a better result was obtained when particle beams collided compared to bombarding stationary targets. Betatron is applied to the circulating accelerator because it has no accelerating cavities and was the first circular machine to have a rising field that had to keep up with the rising energy of the accelerated electrons. The Wideroe's ray transformer is an upgrade version of Betatron [3]. An experiment to find the magnetic field was developed by using a single turns coil beyond 100 T toward the state-of-the-art equipment [4]. A non-shielded solenoid is equipped with other coils in order to reduce its electromagnetic interference near to other radio frequency equipment [5]. A Cryo module is developed to measure the passive magnetic field inside the solenoid. The magnetization of the solenoid can be canceled by controlling the hysteresis cycling of the solenoid. In 1909, the Mica dielectric capacitor was invented for radio transmission [6]. Silver mica is reliable because it has excellent dielectric properties with outstanding discharge resistance [7]. Magnetic fields can be measured using a Hall-effect device [8]. In recent years, the most important one in electromagnetic area is the RLC circuit which consists of a resistor, an inductor, and a capacitor [9].

## 13.3 Methodology

The research starts with defining the pulsed linear accelerator parameters. The coil has a 60 mm length,  $l_a$ . The outer and inner diameter of the coil is 60 mm and 9 mm, respectively. Table 13.1 shows the developed coil's parameters. Next, the capacitor bank is set with different values of voltage, i.e. 100 and 200 V and capacitance, i.e.

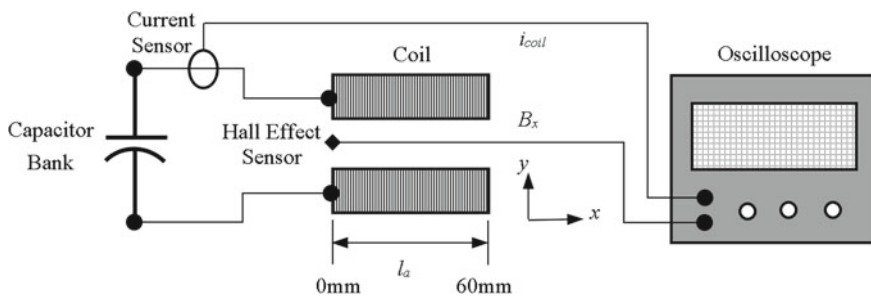
**Table 13.1** Parameters of developed coil

Parameter	Value
Wire size	16 SWG
Number of turn	1033
Resistance	2.5 Ω
Inductance	7.5 mH
Outer diameter	60 mm
Inner diameter	9 mm
Axial length	60 mm

560 and 1120 uF. Then, the Hall-effect is inserted inside the coil at a position near the coil inner surface, i.e. set as 0 mm. The magnetic field of the coil at the current position is measured until its position is equal to the total coil length. The data is recorded and tabulated in a graph. The experimental setup and flowchart is shown in Figs. 13.1 and 13.2, respectively.

A Hall-effect sensor is used to measure the magnetic field inside the coil. The Hall-effect sensor is able to vary its output voltage in response to a magnetic field. The type of Hall-effect sensor that is used for this experiment is from the SS49E series. The Hall-effect sensor is used for the experiment because the cost is lower than other mechanical switches and it can be measured until higher flux densities. Besides that, the Hall-effect sensor also responds to either a positive or a negative Gauss distribution [10]. The transfer characteristics of the magnetic field (gauss) Hall-effect sensor are shown in Fig. 13.3.

Referring to Fig. 13.3, it shows that the Hall-effect sensors provide an output voltage that is proportional to the magnetic field to which it is exposed. It illustrates a ratiometric Hall-effect sensor that accepts a 4.5–10.5 V supply. The ratiometric output voltage is set by the supply voltage and varies in proportion to the strength of the magnetic field. The output voltage of the Hall-effect sensor as shown in Eq. (13.1) is obtained from Fig. 13.3, where  $V_0$  is the output voltage of the Hall-effect sensor and  $B_x$  is the magnetic field. Rearranging Eq. (13.1), then, Eq. (13.2) is used to determine the magnetic field of the coil [10].



**Fig. 13.1** Experimental setup

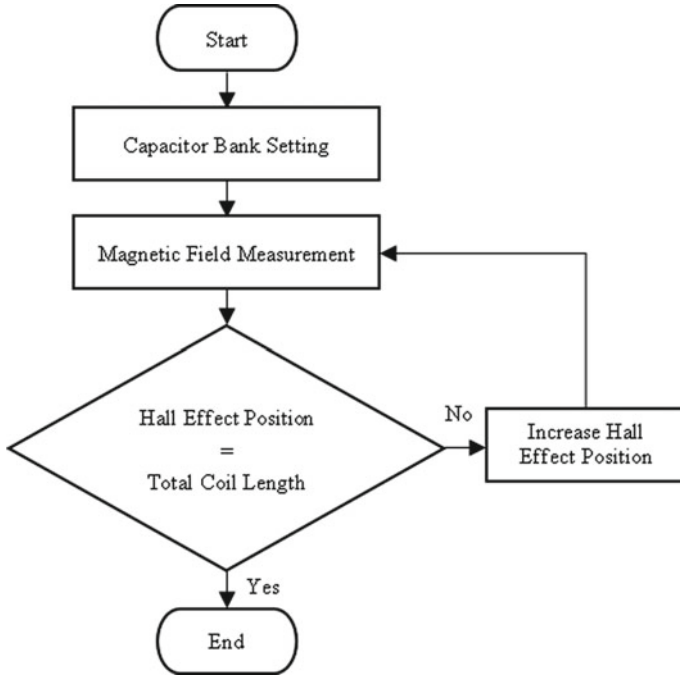
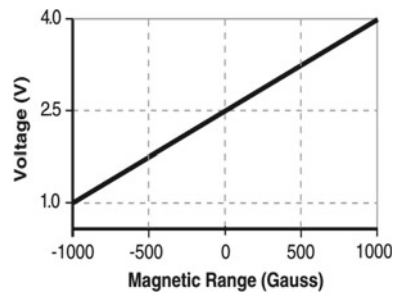


Fig. 13.2 Experimental flowchart

Fig. 13.3 Hall-effect sensor range transfer characteristics

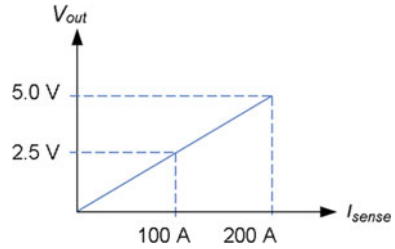


$$V_0 = 0.0015B_x + 2.5 \tag{13.1}$$

$$B_x = \frac{1 \times 10^4 V_0}{15} - \frac{2.5}{1.5 \times 10^{-3}} \tag{13.2}$$

The current that flows into the coil is measured using the current sensor ACS758 [11]. The output response of the current sensor ACS758 is shown in Fig. 13.4. This current sensor has a maximum current sense of 200 A. The output voltage from the current sensor will determine the actual current sense by this current sensor.

**Fig. 13.4** Current sensor output response



Referring to Fig. 13.4, the  $V_{out}$  can be determine using Eq. (13.3).

$$V_{out} = 0.025I_{sense} \quad (13.3)$$

Rearranging Eq. (13.3), then the  $I_{sense}$  can be found using Eq. (13.4).

$$I_{sense} = 40V_{out} \quad (13.4)$$

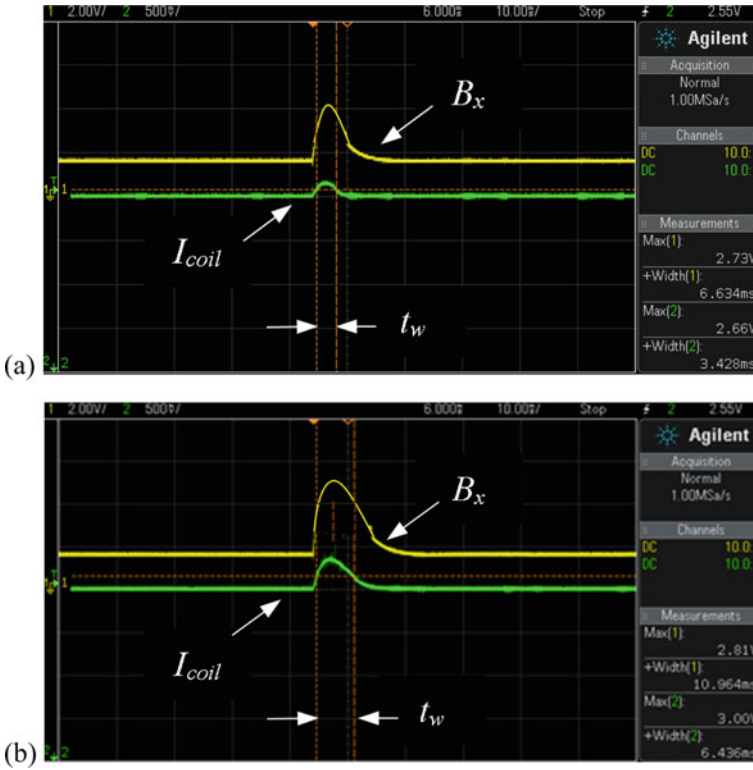
## 13.4 Results and Discussion

The coil's current  $I_{coil}$  and the magnetic field  $B_x$  when it is supplied with 100 V, 560 uF are shown in Fig. 13.5a. The maximum current that flows inside the coil winding at a position of 11 mm inside the coil is 2.66 V, which is equivalent to 106.4 A. The output of the Hall-effect sensor is 4 V, which is equivalent to 0.1 T. The pulse width  $t_w$  is 3.4 ms. The current flows in the coil winding and the magnetic field is shown in Fig. 13.5b when supplied with 200 V, 1120 uF capacitor bank. The maximum current flows inside the coil winding at position of 10 mm inside the coil is 3 V, which is equivalent to 120 A. The output of the Hall-effect sensor is 5 V, which is equivalent to 0.17 T. The pulse width is 6.4 ms.

The actual value of the Hall-effect sensor and the current sensor output is obtained using Eqs. (13.2) and (13.4) respectively. When the voltage of the capacitor bank is increased, the coil's current will be increased. When the capacitance of the capacitor bank is increased, then the pulse width  $t_w$  of the coil current is also increased. The magnetic fields will be stronger if the current is higher and vice versa. Longer pulse width  $t_w$  of the coil's current will create longer pulse width of the magnetic field and vice versa. The coil is supplied with different capacitor bank settings to find the different magnetic field characteristics at every coil position. The experiment was conducted by changing the capacitor one by one where the capacitors are connected in parallel.

Referring to Fig. 13.6a, the highest magnetic fields point for 100 V, 560 uF capacitor bank is at position 10 and 11 mm is 10 mT, whereas for 100 V, 1120 uF capacitor bank is at position 12, 17, 18 and 24 mm is 11 mT. Figure 13.6b illustrated the



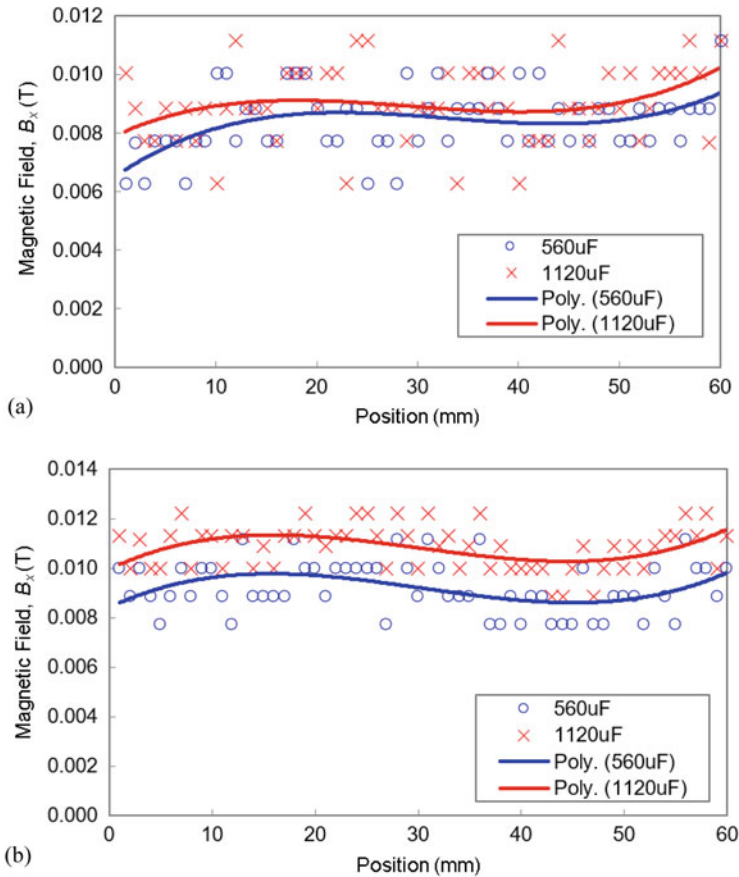


**Fig. 13.5** Coil's current and Hall-effect sensor output **a** when supplied with 100 V, 560  $\mu$ F capacitor bank. **b** when supplied with 200 V, 1120  $\mu$ F capacitor bank

magnetic fields distribution for 200 V, 560  $\mu$ F and 200 V, 1120  $\mu$ F capacitor banks. The highest magnetic fields point for 200 V, 560  $\mu$ F capacitor bank is at position 13 mm is 11 mT, whereas for 200 V, 1120  $\mu$ F capacitor bank is at position 8 mm and 19 mm is 12 mT. Referring to Fig. 13.6, it shows that the magnetic field inside the coil is increased by 25% when the voltage of the capacitor bank is increased by 50%.

### 13.5 Conclusion

This paper has presented a magnetic field distribution for a single coil pulsed linear accelerator. The single coil pulsed linear accelerator is supplied with different settings of capacitor banks. A Hall-effect sensor is used to measure the magnetic field inside the coil. Higher voltage of capacitor bank will generate higher magnetic field inside the coil. Higher capacitance of the capacitor bank will make the magnetic field stay



**Fig. 13.6** Magnetic field distribution inside the coil for 560 uF and 1120 uF capacitor bank. **a** when supplied with 100 V. **b** when supplied with 200 V

longer inside the coil. In addition, to detect the highest magnetic fields, the Hall-effect sensor is suggested to be located less than half of the coil length and for this case, it is between 8 and 15 mm.

## References

1. Martins MN, Silva TF (2014) Electron accelerators: history, applications, and perspectives. Radiat Phys Chem 95:78–85
2. Ising G (1924) Prinzip einer methode zur herstellung von kanalstrahlen hoher voltzahl. Archiv für matematik, astronomioch fysik (in German) 18(30):1–4
3. Widerøe R (1928) Über ein neues prinzip zur herstellung hoher spannungen. Archiv für Elektrotechnik (in German) 21(4):387–406

4. Portugall O, Solane PY, Plochocka P, Maude DK, Nicholas RJ (2013) Beyond 100 tesla: scientific experiments using single-turn coils. *Comptes Rendus Phys* 14(1):115–120
5. Laxdal RE, Boussier B, Fong K, Sekachev I, Clark G, Zvyagintsev V, Eichhorn R (2006) Magnetic field studies in the ISAC-II cryomodule. *Phys C Supercond* 441(1–2):225–228
6. Boggs S (2010) Historical introduction to capacitor technology. University of Connecticut, Institute of Materials Science
7. Movva A, Anoosha N, Singavarapu, (2013) Reliable testing of capacitors. *Innov Technol Explor Eng* 2:149–151
8. Steven M (2000) Magnetic field measurement. Macintyre Electron Des
9. Storr W (2014) Series RLC circuit. <http://www.electronics-tutorials.ws/accircuits/series-circuit.html>. Accessed 10 July 2015
10. Honeywell (2015) Solid state hall effect sensor SS49E series. <https://sensing.honeywell.com/honeywell-sensing-sensors-linear-hall-effect-ics-ss490-series-datasheet-005843-2-en.pdf>. Accessed 20 July 2015
11. Allegro (2015) Current sensor ACS758 series. <https://www.allegromicro.com/~media/Files/Datasheets/ACS758-Datasheet.ashx>. Accessed 20 July 2015

# Chapter 14

## Formulations After Features Extraction of Veltink to Second-Order Critical Damped Black Box Model for Observer Formation Representing Knee Extension



Saharul Arof, Norramlee Mohamed Noor, Emilia Noorsal, Saiful Zaimy, Zakaria Hussein, and Hamzah Arof

**Abstract** Real-world function electrical stimulation (FES) encounters nonlinear effects of fatigue and time delay that cause the FES controller to underperform and sometimes fail. Nonlinearities degrade the muscle performance and change the system, but the FES controller cannot be re-tuned once its parameters are set. System representation using an observer enables the patient's knee extension to be represented in a numerical computation algorithm and can be run or executed in an embedded system. This allows tuning of the closed-loop controller to be made to the imitated system. The formation of an observer requires parameters to be collected through feature extraction process. The transformation of these collected parameters to suitable parameters for the observer formation can be eased with the establishment of a control law made of equations and rules and finally represented in a look-up table. This paper investigates the feasibility of using the second-order system response to

---

S. Arof (✉) · N. M. Noor  
Universiti Kuala Lumpur, Malaysian Spanish Institute Kulim Hi-Tech Park, 09000 Kulim, Kedah, Malaysia  
e-mail: [saharul@unikl.edu.my](mailto:saharul@unikl.edu.my)

N. M. Noor  
e-mail: [noramlee@unikl.edu.my](mailto:noramlee@unikl.edu.my)

S. Arof · E. Noorsal · S. Zaimy · Z. Hussein  
School of Electrical Engineering, College of Engineering, Universiti Teknologi MARA, Cawangan Pulau Pinang, 13500 Kampus Permatang Pauh, Pulau Pinang, Malaysia  
e-mail: [emilia.noorsal@uitm.edu.my](mailto:emilia.noorsal@uitm.edu.my)

S. Zaimy  
e-mail: [saiful053@uitm.edu.my](mailto:saiful053@uitm.edu.my)

Z. Hussein  
e-mail: [zakaria183@uitm.edu.my](mailto:zakaria183@uitm.edu.my)

H. Arof  
Electrical Engineering Department, University of Malaya, Jalan Universiti, 50603 Kuala Lumpur, Malaysia  
e-mail: [ahamzah@um.edu.my](mailto:ahamzah@um.edu.my)

formulate controller setting and observer formation. MATLAB/Simulink software is used to study, and the simulation results are used to establish the formulation of the system for an observer formation representing the knee extension model.

**Keywords** Rehabilitation · FES · Observer · Features extraction · FIR filter · Finite state machine · Black box

## 14.1 Introduction

Despite continuous research, most functional electrical stimulation (FES) devices in the market have practical limitations in terms of size, weight, price, user-friendliness, and operator/helper independence [1–3]. Theoretically, closed-loop control algorithms can improve the performance of open-loop control algorithms for FES applications. However, the actual performance of the closed-loop controllers for the FES devices can degrade significantly when affected by nonlinear effects like fatigue and spasticity [4]. Moreover, all of the feedback controllers are sensitive to variations in the parameters of the muscle recruitment function, which change during real-world FES use [5]. Hence, for better feedback control operation, there is a need to use an accurate muscle system model [6, 7] of the system (patient to be treated). Ideally, nonlinearities should be considered when developing the controller of the electrically stimulated system. When knee and muscle experience fatigue and spasticity their performance degrade [8, 9]. However, it is impossible to tune the closed-loop feedback controllers online when they are directly attached to the patient's leg and knee [10]. The FES in the laboratory was set up and tested according to several pre-determined persons, while FES devices in the market are designed to meet the parameters (related to weight, damping, etc.) of different users which are unknown a priori [11]. These unknown parameters could prevent the system from running at its highest performance, cause the patient to sustain further injuries [12] or the system to fail. This is because it was set up to work efficiently only for the pre-determined subjects in the laboratory test [12]. An accurate model requires the identification process to be established and this is considered as impractical in a clinic setting due to time constraints and fast-changing dynamics [12].

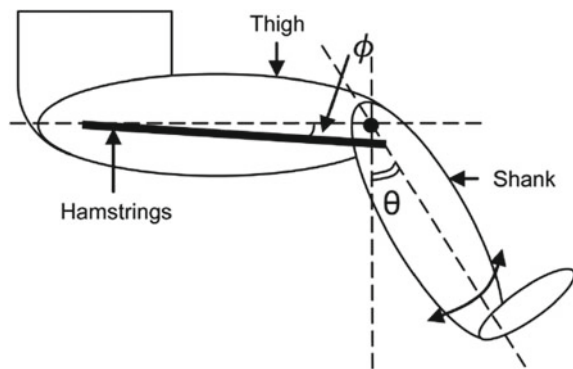
Nonlinearities cause system changes but controller re-tuning is not possible due to degradation of the muscle [13, 14]. A system representation [15] using an observer can enable patient knee extension to be represented in a numerical computation algorithm and can exist, run, or execute in an embedded system. This allows close-loop controller tuning using genetics algorithm [16] or gradient descend [17] to the imitated system. The main objective of this research is to investigate and study the second-order system that matches the Veltink model so that the formulation, control law, and look-up table can be established for the formation of an observer. Once the order of the systems and the system parameters have been determined, the next step is to retrieve the values of  $z\eta$ ,  $wn$ , system gain, and steady state gain. This is to establish linear differential equation form and then convert it into a numerical method

representation. The Taylor series method is used for the numerical representation of the knee extension because its calculation method is much easier. The process of this conversion is not covered in this paper, but it will be covered in a separate paper. In the case the established observer needs some tuning to improve the accuracy, the process can be done using optimization tools. During the process the formulations could be used to ease the process.

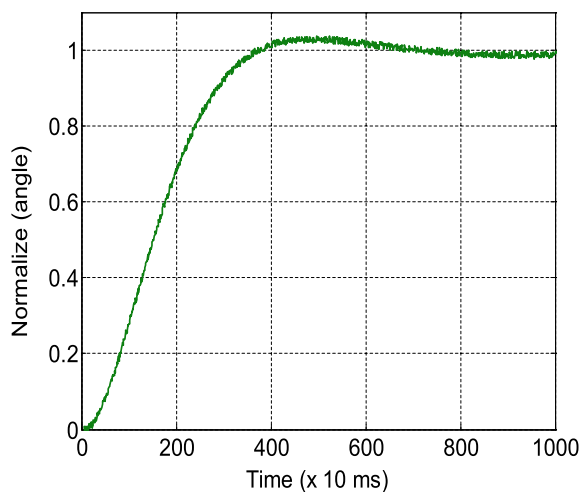
The knee extension model can be represented by a body part and joint dynamic equation, and an electrically stimulated muscle model as depicted in Fig. 14.1 and Eq. (14.1), respectively. Veltink et al. [18] in a controlled study of the ankle joint movement, used a second-order linear system to determine the relation between torque and angle as shown in Fig. 14.2.

$$M = I\ddot{\theta} + B\dot{\theta} + \frac{\theta - \theta^{nom}}{C} \quad (14.1)$$

**Fig. 14.1** Knee extension



**Fig. 14.2** Knee extension angle trajectory



where  $M$  is the joint torque,  $q$  is the joint angle,  $q_{nom}$  is the angle at which the steady state torque equals zero,

$I$  is the inertia,  $B$  is the damping,  $C$  is the compliance of the load.

The Veltink knee extension system can be represented by second-order systems. Second-Order Transfer Function.

$$\frac{C(s)}{R(s)} = \frac{\omega_n^2}{s^2 + 2\zeta\omega_n s + \omega_n^2} \quad (14.2)$$

$\omega_n^2$  = natural frequency,  $\zeta$ =damping.

The characteristics equations can be equated to knee extension as per Eq. (14.1).

$$as^2 + 2\zeta\omega_n^2 = I\ddot{\theta} + B\dot{\theta} + \frac{\theta - \theta_{nom}}{C} \quad (14.3)$$

$$2\zeta\omega_n = B, \left( \omega_n^2 = \frac{\theta - \theta_{nom}}{c} \right), a = I \quad (14.4)$$

$$\omega_n = \frac{\text{steady state output}}{\text{Step input}} \quad (14.5)$$

$$\zeta = 1 \quad (14.6)$$

$$\text{Settling time } T_s = \frac{5.8335}{\omega_n} \quad (14.7)$$

$$\text{Steady state gain} = \text{steady state output/input value} \quad (14.8)$$

The second-order system that matches the Veltink model can fall into four categories which are, under-damped, critical damped, damped, and over-damped. For knee extension, the most probable pattern will be under-damped, over-damped, and critical damped. For the second-order system, natural frequency ( $\omega_n$ ), damping ratio ( $\zeta$ ), system gain, and time constants are the important parameters.

## 14.2 Methodology

To establish formulations after Features Extraction of Veltink to Second-Order Critical Damped Black Box Model for Observer Formation Representing Knee Extension a generalize system identification that classifies the second-order critical damped model requires segregation of the black box model parameters. As the critical damped has only one  $\zeta$  real value, varying gain and natural frequency ( $\omega_n$ ) change the system response.

### 14.3 Result and Analysis

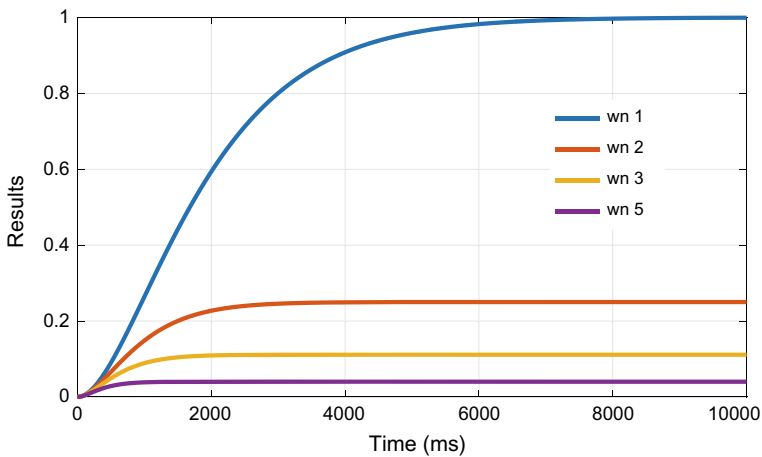
The critical damped second-order black box model can be generally classified with Normal, high gain, and both high gain and high  $wn$  system. In general, the classification according to overshoot and steady state gain as per Table 14.1

As the critical damped has only one real  $zeta$  value, varying/natural frequency ( $wn$ ) changes the system response. Figure 14.3 shows the normalized response upon varying  $wn$ .

The  $wn$  will influence the transient response and steady state value as shown in Fig. 14.3 and listed in Table 14.2. The steady state time is faster, but the steady state value is smaller.

**Table 14.1** General critical damped classification

Settling time	Overshoot	System steady state gain	System under controlled
$T_s = 6\text{ s}$	No	$=1$	Normal Critical damped
$T_s \geq 6\text{ s}$	No	$\geq 1$	Critical damped with high gain/ $wn$
$T_s < 6\text{ s}$	No	$\leq 1$	Critical damped with high gain and high $wn$



**Fig. 14.3** Second-order critical damped dynamic behavior with  $wn$  variation

**Table 14.2** Response of the system to varying gain while maintaining  $zeta$

$wn$	$ssv$	$sst$
1	1	7
2	0.22	2.2
3	0.1	1.6
5	0.04	1.4

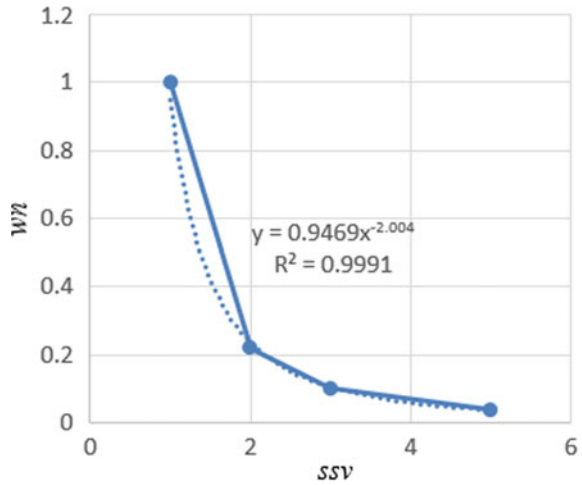


From the table above, the equations that can be used to establish a formulation translated to look-up table formation in finding and representing  $z\theta$  and other variables are as per Figs. 14.4 and 14.5.

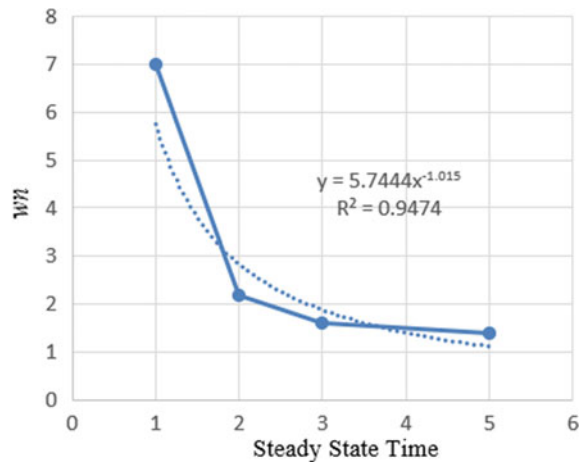
If the  $z\theta$  and  $wn$  are maintained, varying system gain to the possible condition varying steady state gain gain. The simulation result of varying system gain while maintaining the  $z\theta$  and  $wn$  cause steady state gain to increase as shown in Fig. 14.6. The system response as a result of changes made to system gain which is transformed into detailed parameters of the system performance is recorded in Table 14.3.

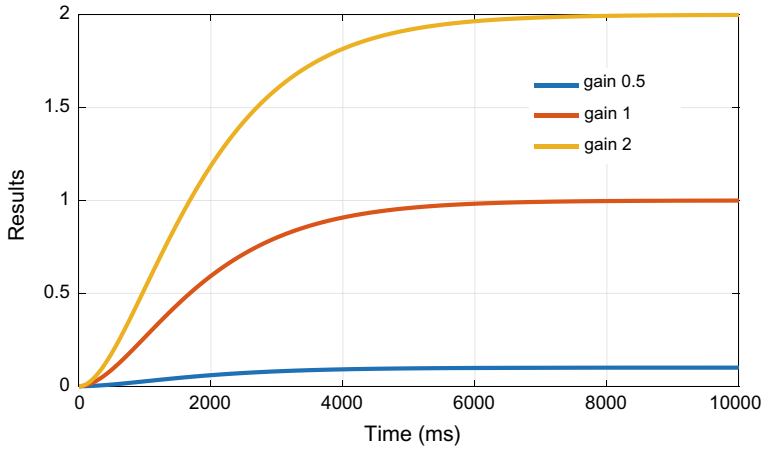
As in Table 14.3, increasing the system gain will increase the steady state time and steady state gain value of the response and vice versa.

**Fig. 14.4** The relationship between  $wn$  and  $ssv$



**Fig. 14.5** The relationship between  $wn$  and steady state time



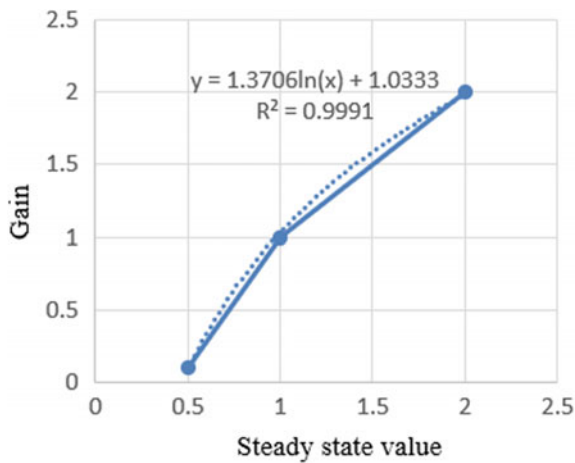


**Fig. 14.6** Second-order critical damped dynamic behavior with a gain variation

**Table 14.3** Varies of gain while maintaining  $\zeta$  and  $\omega_n$

Gain	$ssv$	$sst$
2	2	7
1	1	6
0.5	0.1	2.2

From Table 14.3, the equations that can be used to establish a look-up table in finding and representing  $\zeta$  and other variables are as per Figs. 14.7 and 14.8.



**Fig. 14.7** The relationship between gain and state time

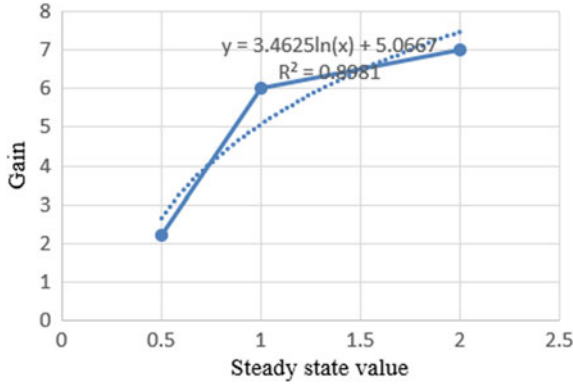


Fig. 14.8 The relationship between gain and steady state value

The possible conditions of critically damped system under varying system gain and  $\omega_n$ , while maintaining the  $\zeta$  are as shown in Fig. 14.9. The results of varying system gain and  $\omega_n$ , extracted parameters corresponding to system performance are recorded in Table 14.4.

As shown in Table 14.4. The natural frequency ( $\omega_n$ ) and system gain will influence the steady state time response system response to be faster.

From the table above, the equations that can be used to establish a look-up table in finding and representing  $\zeta$  and other variables are as per Fig. 14.10.

As part of the process to establish an observer, producing formulation, control law and controller setting, the gathered equation transformed into meaningful equation and simplified as shown in Table 14.5.

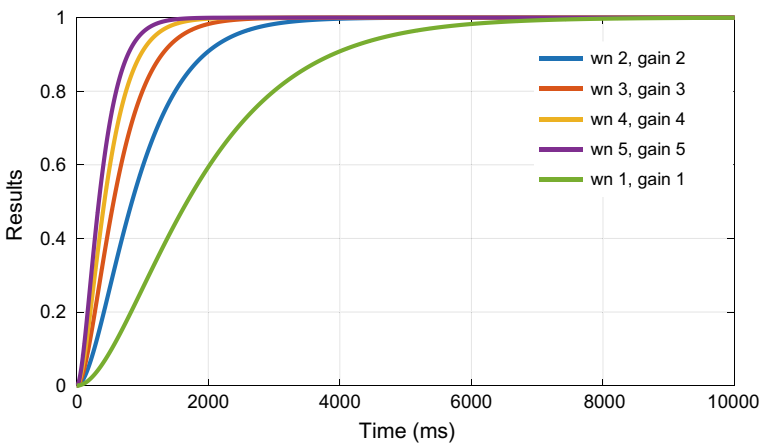
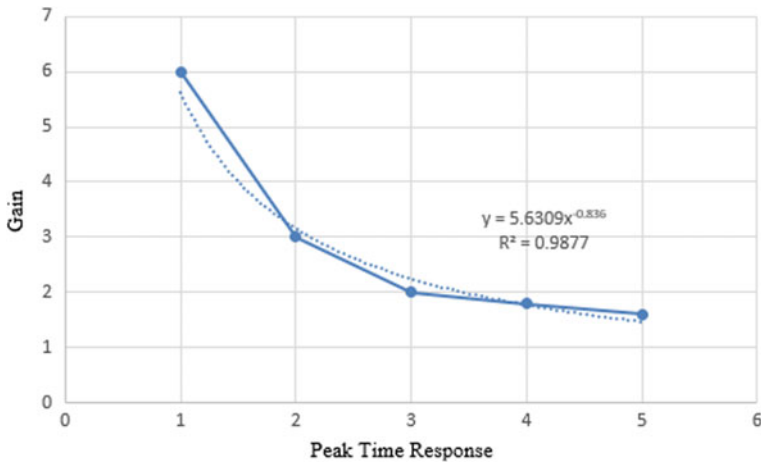


Fig. 14.9 The relationship between gain and steady state value

**Table 14.4** varies of  $\omega_n$  and gain while maintaining  $\zeta$

$\omega_n$	98%Sst (sec)	System GAIN	$\zeta$
1	6	1	1
2	3	2	1
3	2	3	1
4	1.8	4	1
5	1.6	5	1



**Fig. 14.10** The Relationship between gain and peak time response

**Table 14.5** Critical damped system look-up table equations

With high $\omega_n$		With high gain		With high gain and high $\omega_n$
$\omega_n$ to settling time equation	$\omega_n$ to $\zeta$ equation	Gain to settling time equation	Gain to $\zeta$ Equation	$\omega_n$ and gain to settling time
$y = 0.9469x - 2.004$	$y = 5.7444x - 1.015$	$y = 1.3706\ln(x) + 1.0333$	$y = 3.4625\ln(x) + 5.0667$	$y = 5.6309x - 0.836$

The established formulations are used for observer formation and observer tuning. Detail on observer formation and tuning is not discussed in this paper.

**Control law using Rules expert system**

1. If setting time  $< 6$  s and the steady state gain  $\geq 1$ , the  $\zeta$ ,  $\omega_n$  and gain are 1, 0.5, 1.
2. If setting time  $\geq 6$  s and the steady state gain  $> 0.85$  the  $\zeta$ ,  $\omega_n$  and gain equation are 1,  $y = 0.9469x - 2.004$ ,  $y = 5.7444x - 1.015$

3. If setting time  $< 6$  s and the steady state gain  $< 85$  the  $z_{\theta}$ ,  $w_n$  and gain equation are 1,  $y = 1.3706\ln(x) + 1.0333y = 3.4625\ln(x) + 5.0667$
4. If setting time  $\geq 6$  s and the steady state gain  $< 0.85$  the  $z_{\theta}$ ,  $w_n$  with gain equation are 1,  $y = 5.6309x - 0.836$ .

## 14.4 Conclusion

The formulations of second-order critical damped system that matched to Veltink under variation of  $w_n$ , system gain and both have successfully been established. This can be used for observer formation and tuning. The close loop feedback controllers such as Fuzzy Logic [14], PID and sliding mode can use this table, control law and formulations for controller gain setting.

## References

1. Lynch CL, Popovic MR (2012) A comparison of closed-loop control algorithms for regulating electrically stimulated knee movements in individuals with spinal cord injury. *IEEE Trans Neural Syst Rehabil Eng* 20(4)
2. Lynch CL, Popovic MR (2008) Functional electrical stimulation control systems. *IEEE* 28(2):40–50.5
3. Simonsen D, Spaich EG, Hansen J, Andersen OK (2017) Design and test of a closed-loop FES system for supporting function of the hemiparetic hand based on automatic detection, using the microsoft kinect sensor. *IEEE Trans Neural Syst Rehabil Eng* 25(8)
4. Previdi F, Carpanzano E (2003) Design of a gain scheduling controller for knee-joint angle control by using functional electrical stimulation. *IEEE Trans Control Syst Technol* 11
5. Jezernik S, Ruben G, Wassink V, Keller T (2004) Sliding mode closed-loop control of FES: controlling the shank movement. *IEEE Trans Biomed Eng* 51(2)
6. Tu Y, Matthews GI, Lee S-Y, Fang Q (2016) A closed-loop micro-stimulator controlled by muscle fatigue status and function impairment level for upper limb rehabilitation. *IEEE Conf*
7. Alouane MA, Rifai H, Amirat Y, Mohammed S (2018) Cooperative control for knee joint flexion-extension movement restoration. In: 2018 IEEE/RSJ international conference on intelligent robots and systems (IROS), Madrid, Spain, pp 5175–5180
8. Benahmed S, Tadjine M, Kermia O (2017) Adaptive super twisting controller: In search of a universal controller for the paraplegic knee movement using FES. In: The 5th international conference on electrical engineering—boumerdes (ICEE-B)
9. Alibejji N, Kirsch N, Sharma N (2015) Dynamic surface control of neuromuscular electrical stimulation of a musculoskeletal system with activation dynamics and an input delay. In: 2015 American control conference
10. Lynch CL, Sayenko D, Popovic MR (2012) Co-contraction of antagonist muscles during knee extension. In: 34th annual international conference of the IEEE EMBS, pp 1843–1846
11. Abdulla SC, Tokhi MO (2012) Comparative assessment of two fuzzy logic based control approaches for a flywheel and electrical clutch assist mechanism in FES cycling. *IEEE*, pp 246–251
12. Kawai H, Bellman MJ, Downey RJ, Dixon WE (2019) Closed-loop position and cadence tracking control for FES-cycling exploiting pedal force direction with antagonistic biarticular muscles. *IEEE Trans Control Syst Technol* 27(2):730–742

13. Noorsal E, Yahaya SZ, Hussain Z, Boudville R, Ibrahim MN, Ali YM (2020) Analytical study of flexible stimulation waveforms in muscle fatigue reduction. *Int J Electr Comput Eng (IJECE)* 10(1):690–703. <https://doi.org/10.11591/ijece.v10i1>
14. Noorsal E, Arof S, Yahaya SZ, Hussain Z, Kho D, Mohd Ali Y (2021) Design of an FPGA-based fuzzy feedback controller for closed-loop FES in knee joint model. *Micromachines* 12(8):968. <https://doi.org/10.3390/mi12080968>
15. Arof S, Sukiman ED, Diyanah NH, Noor NM, Noorsal E, Mawby PA, Arof H (2020) Discrete-time linear system of new series motor four-quadrant drive direct current chopper numerically represented by taylor series. *Progress in engineering technology II*. In: *Advanced structured materials*, vol 131. Springer, Cham. [https://doi.org/10.1007/978-3-030-46036-5\\_10](https://doi.org/10.1007/978-3-030-46036-5_10)
16. Arof S, Diyanah NHN, Noor NM, Rosyidi M, Mawby PA, Arof H (2019) Genetics algorithm for setting up look up table for parallel mode of new series motor four quadrants dc chopper. In: *Progress in engineering*, pp 155–167. [https://doi.org/10.1007/978-3-030-28505-0\\_12](https://doi.org/10.1007/978-3-030-28505-0_12)
17. Saharul Arof ARA, Shauqee M, Rosyidi NHN, Diyanah PM, Arof H, Noorsal E (2021) Gradient descend for setting up a look-up table of series motor four quadrants drive DC chopper in parallel mode. In: *Progress in engineering technology III*. [https://doi.org/10.1007/978-3-030-67750-3\\_16](https://doi.org/10.1007/978-3-030-67750-3_16)
18. Veltink PH, Chizeck HJ, Crago PE, El-bialy A (1992) Nonlinear joint angle control for artificially stimulated muscle. *IEEE Trans Biomed Eng* 39(4):368–380

# Chapter 15

## Optimization of Process Parameters in Electric Discharge Machining Wire-Cut of Magnesium Alloys Using the Taguchi's Approach



**Ariff Naquiuddin Nazri, Muhammad Al'Hapis Abdul Razak, Mohd Rezal Mohamed, Mohamad Fadzli Haniff, Ahmad Razlee Ab Kadir, Sadaqat Ali, and Abdul'Azeez A. Aliyu**

**Abstract** Electric discharge machining wire-cut is an accurate and cost-effective manufacturing route in numerous applications. Taguchi method was used for the analysis of the effect of EDM wire-cut process parameters on material removal rate, surface roughness and machining time of magnesium alloys. Different parameters like pulse off time, pulse on time, current and voltage are used to optimize the material removal rate, surface roughness and machining time by Minitab 19. Taguchi orthogonal array L9 is used for optimizing three different parameters so that

---

A. N. Nazri · M. A. A. Razak (✉)

Manufacturing Section, Universiti Kuala Lumpur Malaysian Spanish Institute, Kulim Hi-Tech Park, 09000 Kulim, Kedah, Malaysia

e-mail: [alhapis@unikl.edu.my](mailto:alhapis@unikl.edu.my)

A. N. Nazri

e-mail: [ariff.nazri@s.unikl.edu.my](mailto:ariff.nazri@s.unikl.edu.my)

M. R. Mohamed · M. F. Haniff

Electrical, Electronics and Automation Section, Universiti Kuala Lumpur Malaysian Spanish Institute, Kulim Hi-Tech Park, 09000 Kulim, Kedah, Malaysia

e-mail: [mrezal@unikl.edu.my](mailto:mrezal@unikl.edu.my)

M. F. Haniff

e-mail: [mohamadfadzli@unikl.edu.my](mailto:mohamadfadzli@unikl.edu.my)

A. R. Ab Kadir

Mechanical Section, Universiti Kuala Lumpur Malaysian Spanish Institute, Kulim Hi-Tech Park, 09000 Kulim, Kedah, Malaysia

e-mail: [ahmadrazlee@unikl.edu.my](mailto:ahmadrazlee@unikl.edu.my)

S. Ali

National University of Sciences and Technology (NUST), Islamabad, Pakistan

A. A. Aliyu

Mechanical Engineering Department, Bayero University Kano, Kano, Nigeria

e-mail: [aaaliyu.mec@buk.edu.ng](mailto:aaaliyu.mec@buk.edu.ng)

© The Author(s), under exclusive license to Springer Nature Switzerland AG 2022

M. H. Abu Bakar et al. (eds.), *Progress in Engineering Technology IV*,

Advanced Structured Materials 169,

[https://doi.org/10.1007/978-3-030-93250-3\\_15](https://doi.org/10.1007/978-3-030-93250-3_15)

maximum material removal rate and minimum surface roughness and machining time is obtained.

**Keywords** EDM wire-cut · Taguchi method · Process parameters · Optimization · Magnesium alloy

## 15.1 Introduction

A lot of research has been carried out on the usage of material for medical applications. These highly demanding materials that need to be used are very complex for medical application. The material itself needs to be highly biocompatible to the human body and must achieve a long fatigue life. As the human body is naturally highly corrosive, a biocompatible material is really in need to prevent any replacement of the implants. The material also needs to prevent any reaction to the tissue around the implants as an unexpected surgery can increase the risk of complications and are always painful for the patient. One of the most promising materials to be used for biodegradable orthopedic implants is magnesium alloys. The magnesium alloy characteristic of high strength to weight ratio can make implants have a high strength compared to the human bones that consequently have stress-shielding effect near the neighboring tissues [8]. The human body has a high concentration of magnesium ions making a magnesium alloy very biocompatible. Thus, magnesium alloy is the potential material for bio-implant applications. To add the advantage of magnesium alloys to the human body, magnesium forms soluble non-toxic corrosion products that are innocuously excreted through the urine [8].

In the generation of highly demanding and complex medical applications, bio-implants for damaged human body parts use magnesium alloy as they are biocompatible to humans. But there is no specific parameter on magnesium alloy for electrical discharge machining (EDM) wire-cut. However, the default parameters for EDM wire-cutting are only available for conventional material such as aluminum. An experiment needs to be designed using the design of experiment method. The production process and the resulting surface integrity in particular have a significant influence on the biocompatibility as well as the fatigue life of the implant [1]. Therefore, the surface of the material needs to have tailored roughness with non-existence pores and cracks with no toxic substances resulting from the machine process. The data from the experiment needs to be analyzed to verify the experiment.

## 15.2 Literature

Literature reveals findings on EDM wire-cutting of various materials. Most of the work is reported to study the parameters like pulse on time, pulse off time and voltage, wire tension, wire speed, to find out the surface roughness and the material removal



rate (MRR) using different types of tools and with the help of design of experiments and statistical optimization techniques. From the referred papers, some conclusions came out and helped decide the further work to optimize and analyze the given below process parameters on EDM wire-cutting.

### ***15.2.1 Magnesium Alloys***

Magnesium alloys are widely used in electronic devices, automotive applications, aerospace, and power tools as their strength to weight ratio is a critical issue in these applications. The density of some favorable engineering metals such as aluminum (Al, 2.7 g/cm<sup>3</sup>), titanium (Ti, 4.5 g/cm<sup>3</sup>), and iron (Fe, 7.9 g/cm<sup>3</sup>) is significantly higher than magnesium (Mg, 1.7 g/cm<sup>3</sup>) making magnesium the lightest engineering metal available [9]. But the strength of the magnesium alloy is depending on other material properties combined. An additional process needs to be applied to increase the strength of the material. Pure magnesium is the most abundant element in the earth crust thus, ample resources to cover the use of its alloys in various engineering sectors [2]. However, pure magnesium has high reactivity and corrosion in open atmosphere thus proper handling is needed for various engineering sectors to overcome the problem.

### ***15.2.2 Electric Discharge Machine***

Nowadays, the increasing demands of manufacturing industry have led to develop and manufacture new materials that are considered difficult to cut or process by any conventional machining process [3]. As an example, magnesium alloys have a high demand not only in aerospace applications but now in the emerging sector of medical applications used in human bodies. Manufacturing magnesium alloys using conventional machining is extremely difficult due to their characteristic of low thermal conductivity, excessive tool wear, and hardness. Conventional machining also could lead to undesired construction of cracks that can be costly to the manufacturing process. Due to the emerging demands of super-finished products in aerospace or medical applications, manufacturing industries tend to look on other alternative approaches for machining this type of material. The machining process needs to achieve a machine that can machine this material with high production or cutting rate, flattering surface quality, and low costs [4]. To overcome the hurdle in the machining of these superalloys by conventional machining practices, the advanced machining processes such as laser beam machining, electrochemical machining, and discharge machining (EDM) can be successfully exploited [4]. Electric discharge machining wire-cut (WEDM) is a convincing and economical approach for machining magnesium alloys.

### 15.2.2.1 EDM Wire-Cut

The EDM wire-cut process has gained the popularity as a promising thermoelectric cutting mechanism for cutting such difficult-to-cut materials [3]. It is flexible in machining of any complex profile with high accuracy and close dimensional tolerance using computer numerical control (CNC) programming [3, 4]. The spark temperature from this advanced machining process can reach up to 12,000 °C during spark on-time and sudden quenching from dielectric during spark off-time [3, 4]. The spark temperature can cause melting and vaporization of the material. The scrap or remains of the material such as dust or debris produced from the process will be flushed away by the dielectric fluid that is continuously flowing and circulating during the process.

Machining efficiently, high strength, and wear-resistant materials with high accuracy is what EDM wire-cut is capable of doing. The formation of complicated shapes that are difficult to form by conventional means can easily be produced using this cutting technique [3]. Inherent problems like chatter, vibrations, and mechanical stresses which conventional machining processes have, are eliminated in EDM wire-cut where indirect contact between the workpiece and the wire electrode is established [3]. Although, the machining performance of EDM wire-cut has been evaluated for magnesium alloy. But there is no specific research on the optimum parameters for magnesium alloys.

### 15.2.3 Statistical Method

The literature review focus on the statistical method that can optimize the parameters for machining magnesium alloys using EDM wire-cut. Thus, it was difficult to compare the different machining parameters of magnesium alloys using the data in the literature. Most of the reviewed article uses the Taguchi's method as it is reducing the variation in a process through + robust design of experiment.

#### 15.2.3.1 Taguchi's Method

Orthogonal arrays are highly fractional orthogonal designs. These designs can be used not only to two-level factorial experiments but also can investigate main effects when factors have more than two levels [5]. Chandramouli and Eswaraiah [6] have done a research on optimization of EDM process parameters in machining of 17–4 PH steel using the Taguchi method. It uses previous researcher literature to get the optimum parameters for 17–4 PH Steel but not using any magnesium alloy. Kuram and Ozcelik [7] on the other hand, made a research on optimization of machining parameters during micro-milling of Ti6Al4V titanium alloy and Inconel 718 materials using the Taguchi method. The material used in this research is not near the chemical composition of magnesium alloys but the research using Taguchi's method made the difference.

### 15.3 Methodology

Taguchi's method involves reducing the variation in a process through robust design of experiments [6]. Taguchi's method uses a specially designed experiment matrix known as the orthogonal array [7]. This array is to organize the parameters [8–11] affecting the process and the levels at which they should be varied [10, 11]. Finding the optimum level of input parameters within the range is the main aim of Taguchi's method that needs to be taken into consideration. Saving time and resources can be achieved when the data collects only the necessary to determine the most affecting the results with minimum number of experiment using the factors that have been identified. The general steps for using Taguchi's method are as follows:

- Identifying the objective and parameters of the process that affects the process.
- Produce orthogonal array for the designed parameter.
- Conduct the experiment using the orthogonal array
- Analyze the data from the experiment.
- Compute the effect of the different parameters on the performance measure.
- Validate the optimum parameters using conformation test.

For this research experiment, Taguchi's L9 orthogonal array was used to conduct the experiments. Table 15.1 discusses the controllable parameters and their levels that has been considered for this experiment.

For this experiment, a magnesium alloy is chosen as a workpiece material. The workpiece is initially in rectangular shape with the dimensions of length (205 mm), width (20 mm) and thickness (11 mm). The type of wire-cut EDM machine used to conduct this experiment is a FANUC Series 310is-WA. The machine uses a 0.25 mm in diameter of brass cutting wire with a spark diameter of 0.15 mm to cut three pieces of specimen with the dimension of  $5\text{mm} \times 20\text{mm} \times 11\text{mm}$ . A preliminary experiment has been conducted using the default parameters of aluminum. The process parameters such as voltage (V), pulse on time (TON), pulse off (TOFF), and current

**Table 15.1** L9 Orthogonal array using the Taguchi's method

Specimen	Voltage	Pulse on	Pulse off	Current
1	62	5	10	1.4
2	62	10	14	1.6
3	62	15	19	1.8
4	67	5	14	1.8
5	67	10	19	1.4
6	67	15	10	1.6
7	72	5	19	1.6
8	72	10	10	1.8
9	72	15	14	1.4

(I) are selected as the control parameters while surface roughness (Ra), machining time (MT), weight (W), and material removal rate (MRR) are the response variables.

## 15.4 Results and Discussion

The result from the preliminary test with default parameters of aluminum (Al) is shown in Fig. 15.1. The machining parameters for aluminum are shown in Table 15.2. During the preliminary test, FANUC Series 310is-WA machine took several times to determine the datum point using the AI function as magnesium alloy parameters are not included in the machine system.

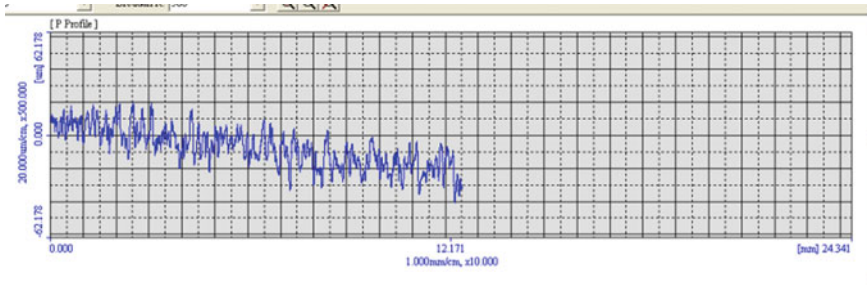
The machining time for machining the 3 specimens was taken in an average time of 1.455 min and the Ra is at  $6.03 \mu\text{m}$ . The surface roughness tester Mitutoyo S3000 probe was not calibrated but the result still can be used. From the results, the parameters of aluminum can be included into the experiment parameters due to the fact that the value of Ra is acceptable. This is because the material properties of magnesium alloys are close to aluminum where the melting point of magnesium is at  $650^\circ\text{C}$  and aluminum is at  $660.3^\circ\text{C}$  (Fig. 15.2).

**Fig. 15.1** Result from cutting the workpiece specimen



**Table 15.2** Default aluminum parameters

Parameters	Level
	1
Voltage (V)	67
Pulse on (Ton)	10
Pulse off (Toff)	14
Current (I)	1.6



**Fig. 15.2** Results of Ra

## 15.5 Conclusions

The experiment is still in the preliminary stage and needs to be continued to the next stage of the experiment. The initial conclusion is that aluminum parameters can be used to cut magnesium alloys but the optimum parameters are yet to be achieved.

## References

1. Klocke F, Schwade M, Klink A, Kopp A (2011) EDM machining capabilities of magnesium (Mg) alloy WE43 for medical applications. *Procedia Eng.* 19:190–195. <https://doi.org/10.1016/j.proeng.2011.11.100>
2. Dziubińska A, Gontarz A, Dziubiński M, Barszcz M (2016) The forming of magnesium alloy forgings for aircraft and automotive applications. *Adv Sci Technol Res J* 10(31):158–168. <https://doi.org/10.12913/22998624/64003>
3. Ishfaq K, Mufti NA, Mughal MP, Saleem MQ, Ahmed N (2018) Investigation of wire electric discharge machining of stainless-clad steel for optimization of cutting speed. *Int J Adv Manuf Technol* 96(1–4):1429–1443. <https://doi.org/10.1007/s00170-018-1630-9>
4. Bisaria H, Shandilya P (2019) Experimental investigation on wire electric discharge machining (WEDM) of Nimonic C-263 superalloy. *Mater Manuf Process* 34(1):83–92. <https://doi.org/10.1080/10426914.2018.1532589>
5. Subrahmanyam M, Nancharaiah T (2020) Optimization of process parameters in wire-cut EDM of Inconel 625 using Taguchi's approach. *Mater Today Proc* 23:642–646. <https://doi.org/10.1016/j.matpr.2019.05.449>
6. Chandramouli S, Eswaraiah K (2017) Optimization of EDM process parameters in machining of 17–4 PH Steel using Taguchi Method. *Mater Today Proc* 4(2):2040–2047. <https://doi.org/10.1016/j.matpr.2017.02.049>
7. Kuram E, Ozelcik B (2017) Optimization of machining parameters during micro-milling of Ti6Al4V titanium alloy and Inconel 718 materials using Taguchi method. *Proc Inst Mech Eng Part B J Eng Manuf* 231(2):228–242. <https://doi.org/10.1177/0954405415572662>
8. Ramalingam VV, Ramasamy P, Das Kovukkal M, Myilsamy G (2020) Research and development in magnesium alloys for industrial and biomedical applications: a review. *Met Mater Int* 26(4):409–430. <https://doi.org/10.1007/s12540-019-00346-8>
9. Esmaily M et al (2017) Fundamentals and advances in magnesium alloy corrosion. *Prog Mater Sci* 89:92–193. <https://doi.org/10.1016/j.pmatsci.2017.04.011>

10. Razak MA, Abdul-Rani AM, Rao TVVLN, Pedapati SR, Kamal S (2016) Electrical discharge machining on biodegradable AZ31 magnesium alloy using Taguchi method. *Procedia Eng* 148:916–922. <https://doi.org/10.1016/j.proeng.2016.06.501>
11. Sonawane SA, Kulkarni ML (2018) Optimization of machining parameters of WEDM for Nimonic-75 alloy using principal component analysis integrated with Taguchi method. *J King Saud Univ Eng Sci* 30(3):250–258. <https://doi.org/10.1016/j.jksues.2018.04.001>

# Chapter 16

## Design of Micro Turbocharger Runners for Automotive Application



**Khairul Shahril, Mohamad Wardi, Shahril Nizam, Muhammad Najib, and Ishak A. Azid**

**Abstract** The turbocharged system is one of the essential components that works in the engine system. It uses exhaust gas to control a turbine. This spins an air compressor that pushes in the cylinders with extra air (and oxygen), allowing them to burn more fuel every second. The intake air system for a motorcycle turbocharger must be correctly configured to minimize the output losses caused by the runner manifold with the regulated air exhaust turbine rule regulation. The paper presents the analysis of the runner manifold configuration parameter design against the engine output and then enhances the traditional runner manifold performance. This research begins with the development of the runner manifold design and modelling, and the runner manifold will use air flow simulation software to be used for simulation purposes. The parametric analysis was carried out to study the effect of the runner manifold parameter design on the engine output after designing the reference engine model. The optimization process was then carried out to achieve the goal of progress that had already been set before the optimization was carried out. The findings show an improvement in speed and pressure of up to 65.20 and 88.09% at the optimal operating range of engine speed.

**Keywords** Exhaust manifold · Runner · Simulation · Modelling

---

K. Shahril (✉) · M. Wardi · S. Nizam · M. Najib · I. A. Azid  
Universiti Kuala Lumpur, Malaysian Spanish Institute Kulim Hi-Tech Park, 09000 Kulim, Kedah, Malaysia  
e-mail: [khairuls@unikl.edu.my](mailto:khairuls@unikl.edu.my)

S. Nizam  
e-mail: [shahrilnizam@unikl.edu.my](mailto:shahrilnizam@unikl.edu.my)

M. Najib  
e-mail: [mnajib@unikl.edu.my](mailto:mnajib@unikl.edu.my)

I. A. Azid  
e-mail: [ishak.abdulazid@unikl.edu.my](mailto:ishak.abdulazid@unikl.edu.my)

## 16.1 Introduction

In this globalization era, to progress the automotive application is very important because of the growing economy in every country. The expanding automotive technology provides more development opportunities for other activities that cannot be archived before this. The motorcycle turbocharger, where a turbocharger is used for the forced induction of an internal combustion engine, is one example of an automobile application. The aim of a turbocharger, like a supercharger, is to increase the mass of air entering the engine in order to produce more fuel. Turbocharger use among motorcycle riders across Malaysia has recently increased in demand due to the advantages and satisfaction of turbocharge users.

Even with a turbocharger, a motorcycle cannot yet achieve one hundred per cent efficiency due to air pressure and velocity loss through the exhaust stroke process which channelled right after it exits the cylinder head straight to the turbocharger turbine, basically this part that channelled throughout from the exhaust port manifold to the turbine wheel in turbocharger is called the runner. The exhaust manifold is one of the most critical components of an internal combustion (IC) engine [8]. Hence this project is focused on designing the runner around exhaust manifold in order to increase the turbo productivity of air pressure inside the runner more sufficiently while maintaining volumetric efficiency of manifold runner flows. The power of the engine greatly depends on the amount of air that can be delivered through the intake. The solution that is used to overcome this problem is to design the tapered runner that has three different parameters which are the elbow diameter, manifold length and tapered diameter [10].

## 16.2 Literature Review

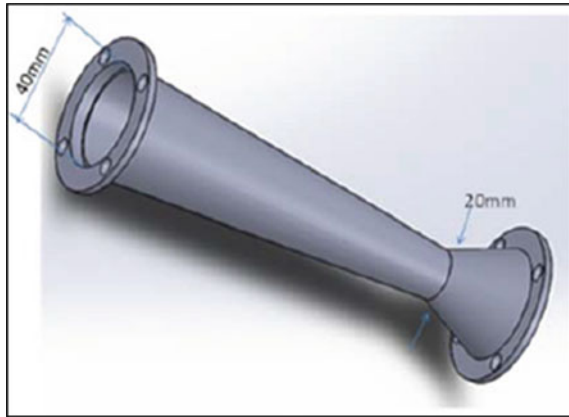
In order to gather all the available sources related to design of micro turbocharger runners for automotive application in one place and to assess them in terms of theory, engineering assessment and other external factors, the previous study that has been done related must be studied in order to have evidence and source that can assist in the project. There are a few main keys that can obtain the idea for the feature of this project in order to progress the modelling method and analyse method of the runner. These main keys are design theory and air flow behaviour.

### 16.2.1 *Design of a New Improved Intake Manifold for F-*SAE* Car*

The output velocity should be high with an even distribution to each cylinder to achieve the maximum mass flow rate for efficient working of the engine. But there



**Fig. 16.1** Final design of restrictor [3]



is a low mass flow rate attributable from higher pressure losses distributed along with the air fuel mixture to each runner that affects the efficiency of IC engine. The performance of the intake manifold must be improved to improve the performance of the internal combustion engine, since the efficiency of an IC engine is highly dependent on the performance of the intake manifold [6].

The geometry of the runner and plenum must be improved to minimize pressure losses in order to demonstrate the efficiency of the model and to improve the performance of the intake manifold, so that high mass flow rate and even fuel/air distribution to each runner must be achieved by using computer simulation on the established model. The example of the model is shown as in Fig. 16.1 [6].

By changing the venturi and throat diameters, the pressure–velocity characteristics of the venturi are not affected too much. But the diameters influence the duration of the venturi non-aerated flow area [3].

### ***16.2.2 Simulation Analysis of Spark Ignition Engine Intake Manifold for Better Performance***

The authors of the paper present the research that explores the impact on the engine efficiency of the intake design parameter and then enhances the performance of the previous intake manifold system. This study begins with the development of the Honda CBR 600RR engine model and intake manifold device model to be used for simulation purposes using the GT-Power engine simulation software. The parametric research was conducted after designing the reference engine model to study the effect of the intake manifold parameter design on the output of the engine [9].

Parametric study is performed on the reference intake manifold system for the main purpose to investigate and identify the relationship of the effect of changing the design parameter of intake system towards the performance of the engine and to

**Table 16.1** Design parameter values for parametric study [9]

Design parameter	Present values	Selected values
Plenum volume	2.3 L	1 L
		3 L
		4 L
		5 L
Runner length	247.6 mm	100 mm
		150 mm
		200 mm
		300 mm
Runner opening diameter	44 mm	30 mm
		40 mm
		50 mm
		60 mm

ensure that this research is producing relevant data compared with previous research from the literature review findings. The parametric study was carried out for the purpose of determining a suitable range of the design parameters and acts as a guide when performing the optimization at a later stage. Table 16.1 shows the design parameter values to be analysed [9].

The optimization process was then carried out to achieve the goal of progress that had already been set before the optimization was carried out. The results show an improvement in the target operating range of engine speed to 4.83 and 4.45% of the torque and air flow rate, respectively [9].

### ***16.2.3 Air Flow Behaviour on Different Intake Manifold Angles for Small 4-Stroke PFI Retrofit Kit System***

In order to deduce the angle at which the air flow conduct is stronger in the intake manifold for a small 4-time PFI retrofit kit device, the author investigates the airflow behaviour. Six intake manifold angles were investigated using the simulation tool CFX (software fluid dynamic) which are 30°, 60°, 90°, 120°, 150° and 180° as shown in Fig. 16.2 [5].

The high intake multiple angles provide better air flow inside the intake manifold based on the shown results. This is because the flexible manifold has lower air resistance. The results of this study showed that 180° is the best choice for multiple angles of input due to better air flow behaviour [5].

Optimization focuses specifically on the optimal configuration of the following parameters: elbow diameter, manifold length and tapered diameter [4]. Valve timing, valve diameter, valve lift profiles, exhaust multi diameter, tube inlet and exhaust tubes

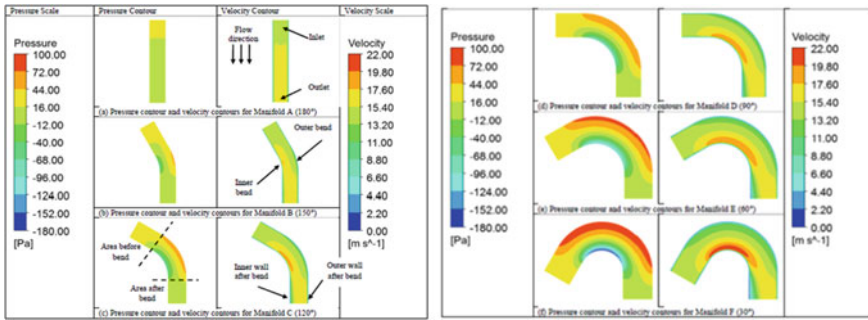


Fig. 16.2 Pressure and velocity contours plots for all intake manifold models continue [5]

lengths and tube junction geometry are parameters which improve the performance significantly [2, 7].

For the prediction of process output and efficiency of multiple systems, flow distribution and pressure drop are vital [11]. One of the important factors that governs the engine output is airflow inside the intake manifold, so the flow phenomenon inside the intake manifold should be completely optimized to generate more engine power with better combustion [1].

### 16.3 Methodologies/Experimental Set-Up/Model Set-Up

This paper aims to explain the flow map, which consists of a research framework that is essentially the work outline, conducive to the design of turbocharger runners. Next is the method of achieving or approaching something, particularly a systematic or established one, which is a specific procedure. Modelling is the method of project design and step-by-step design in CAD, divided by two parts that are modelling and analysis, while the air flow simulation shows the properties and the simulation process in the analysis and also the calculation involving flow rate and velocity in this paper.

#### 16.3.1 Methodology Process

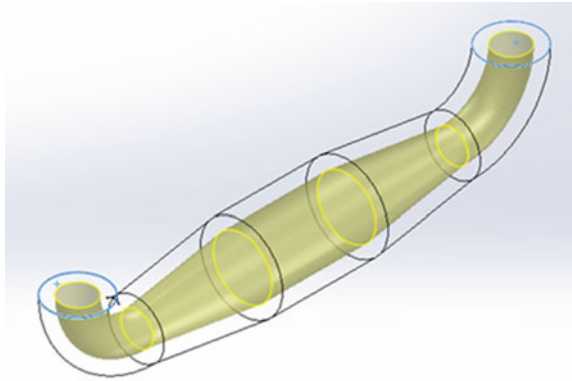
A methodology process is an approach with a defined set of rules, methods, testing operations, deliverables and processes to do something that typically serves to solve a particular problem. There are two parts of the methodology in this project: the first part is modelling and the second part is simulation of analysis.

### 16.3.1.1 Modelling

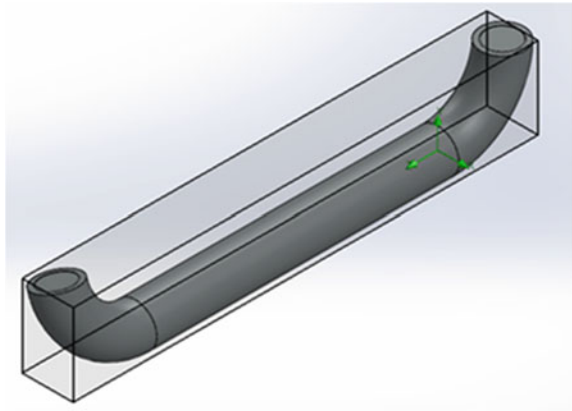
For this research, the modelling was performed using the 3D modelling SolidWorks software to visualize how different geometries affect parameters such as the length of manifold. The 3D modelling is performed at the engine full load condition. The modelling was done to study the result of the parameter differences by improving the design and geometry of every runner part in the exhaust system on the turbocharger performance. The explanation of this research is as below:

- (a) Construct a 3D model of the present exhaust manifold system using SolidWorks.
- (b) Create a component modelling using SolidWorks 3D as shown in Fig. 16.4.
- (c) Assemble the developed complete part and both intake and exhaust system to form a complete manifold runner for the simulation purposes (Fig. 16.3).

**Fig. 16.3** Remove material inside by using shell function



**Fig. 16.4** Computational domain of current runner



### 16.3.1.2 Simulation Analysis

For this research, the simulation was performed using airflow simulation in Solid-Works to visualize how different geometries affect parameters such as the elbow diameter of the runner and to achieve a certain result that will optimize the design. The simulation analysis is performed at the engine full load condition as shown in Fig. 16.5. The simulations were done to investigate the impact of the parameter variations by optimizing the design and properties for the manifold system on the turbocharger system performance. The explanation of this research is as below:

- (a) Develop engine model for this research using the airflow simulation software.
- (b) Run the simulation on the complete system with properties to obtain the performance result of the air flow velocity and pressure.
- (c) Perform a parametric study on the exhaust manifold system.
- (d) Analyse the results from the parametric study and perform the optimization towards the parameter of the intake manifold system by using the method based on the second journal.
- (e) Review the results after implementing the optimization values of the parameter on the present exhaust manifold system.

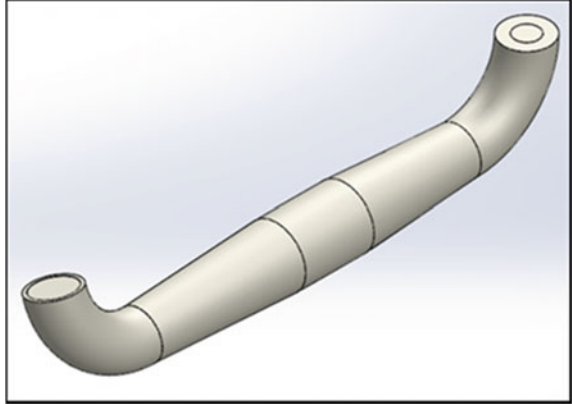
## 16.4 Results and Discussion

After running the optimization process using the simulation air flow method according to the proposed setup in order to achieve the desired target, the values for each of these three design parameters were obtained through the optimization results performed earlier. Figure 16.5 shows the optimizing design which combines the best of the three parameters. Figure 16.6 shows a clear wireframe design to make a view of the inner design and Fig. 16.7 is a simulation on flow trajectories velocity and pressure and the contour for pressure and velocity.

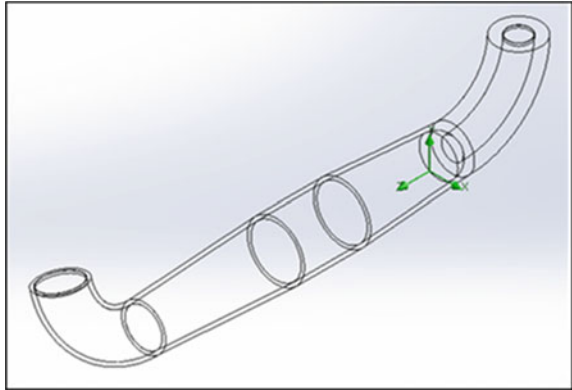
The elbow diameter is the first design parameter where an elbow offers a change in the direction of material flow. This causes the device to lose pressure due to impact, friction and re-acceleration. Manifold length second parameters were one of the important characteristics when concerning intake and exhaust manifold runners. The shape of the runners themselves is perhaps similarly as important. Tapered diameter third parameter is where a process of providing the slope between two surfaces objects with the use of the tapered pipe.

In the first parameters, i.e. elbow diameter, the best velocity would be design ED9 with 65.24% increase whereas for the best pressure it would be design ED9 with 88.09% increase. For the second parameters, i.e. the manifold length, the best velocity would be for design ML15 with 2.05% increases meanwhile the best of pressure would be for design ML1 with 6.13% increases diameter which the best velocity would be for design TD3 with 2.24% increases and for the best pressure would be for design TD4 with 6.91% increases. However, the design TD3 with 6.84%

**Fig. 16.5** Final design of MW



**Fig. 16.6** Wireframe of MW



was selected due to higher velocity value. But the design ML15 with 5.60% was selected due to higher velocity value. Last parameter is tapered as the percentage increases for each parameter but the most significant affecting the result analysis would be the first parameter which is elbow diameter that increases velocity by 65.24% and the pressure by 88.09% which turn into main influence to the air flow inside the runner. Table 16.2 shows the data or result of the final design.

## 16.5 Conclusion

In conclusion, the correlation between each design parameter and the engine output is clearly established by the parametric analysis. The targets for the optimization also were successfully achieved. The improvement of air flow velocity is significant with the highest increment of about 65.24% at design ED9 whereas for the pressure, the most significant improvement also occurred at design ED9 with 88.09%

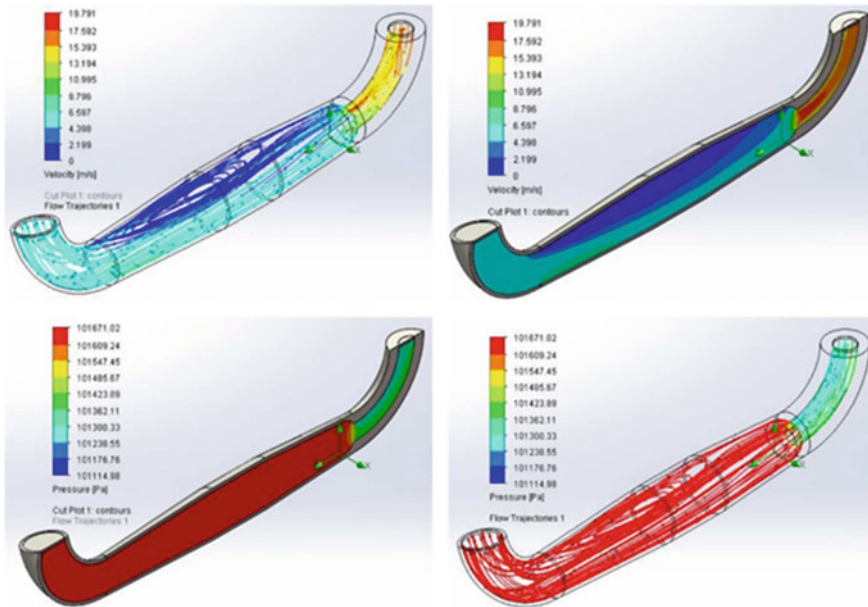


Fig. 16.7 Velocity and pressure of flow trajectories and contour

Table 16.2 Result of final design

Goal Name	Unit	Value	Averaged value	Minimum value	Maximum value
SG Av dynamic pressure 1	[Pa]	28.57	28.57244015	28.57122358	28.5744519
SG Av dynamic pressure 2	[Pa]	240.59	240.5640328	240.3140754	240.8081782
SG Av velocity 1	[m/s]	5.58	5.580028426	5.580028426	5.580028426
SG Av velocity 2	[m/s]	16.09	16.09739693	16.09355366	16.10185785

increment. The most significant parameter affecting the result analysis would be the first parameter which is the elbow diameter that increases both velocity and pressure which turn into the main influence on the air flow inside the runner. To conclude, the overall performance of the engine for the improvement at the runner manifold of the turbocharger has been successfully achieved through the implementation of the optimization approach.

**Acknowledgements** UniKL-STRG Grant (str17042), funded by Universiti Kuala Lumpur and Fundamental Research Grant Scheme (FRGS), Ministry of Science, Technology and Innovation (MOSTI), Malaysia, was financially sponsored with reference number FRGS/1/2019/TK03/UNIKL/01/2. Appreciation for the comments given is also extended to anonymous reviewers, leading to the substantially improved manuscript content.

## References

1. Anilkumar DB, Elia Anoop Kumar G, Bidar (2018) Computational analysis of intake manifold design of a four cylinder diesel engine. *Int J Curr Eng Sci Res (IJCESR)* 5(4):61–69
2. Bajpai K, Chandrakar A, Agrawal A, Shekhar S (2017) CFD analysis of exhaust manifold of SI engine and comparison of back pressure using alternative fuels 14(1):23–29
3. Baylar A, Cihan Aydin M, Unsal M, Ozkan F (2009) Numerical modeling of venturi flows for determining air injection rates using fluent V6.2. *Math Comput Appl* 14(2):97–108
4. Bayas Jagadishsingh G, Jadhav NP (2016) Effect of variable length intake manifold on performance of IC engine 5(5):47–52
5. Hushim MF et al (2015) Air flow behaviour on different intake manifold angles for small 4-stroke Pfi retrofit kit system. *ARPJ Eng Appl Sci* 1–7
6. Jeevanandha P, Ganesh Prasanth M, Rajesh M, Santhos S, Sathish Kumar M (2014) International journal of research in aeronautical and mechanical engineering heat transfer analysis on shell and tube heat. *Int J Res Aeronaut Mech Eng* 2(1):11–26
7. Kanazaki M, Obayashi S, Nakahashi K (2002) Exhaust manifold design with tapered pipes using divided range MOGA 1. *Int Conf Parallel CFD* 2002(1):1–8
8. Krishnara CJ, Rajesh Ruban S, Subramani N (2018) Analysis of exhaust manifold to improve the engine performance. *Int J Eng Technol* 7:539–542
9. Raghuvanshi G, Kakirde A, Sharma S (2018) Design and analysis of exhaust manifold comparing different specifications. *Int J Eng Trends Technol (IJETT)* 62(1):42–45
10. Raj A, Mohanta JC, Paul B, Mohd. Nayab Zafar. (2016) Design of a new improved intake manifold for F-Sae car. *Int J Adv Prod Mech Eng (IJAPME)* 2(4):48–52
11. Wang J (2011) Theory of flow distribution in manifolds. *Chem Eng J* 168(3):1331–1345. <https://doi.org/10.1016/j.cej.2011.02.050>



# Chapter 17

## Study on Ripple Current, Ripple Torque in Parallel Mode of Series Motor Four Quadrants DC Chopper for Electric Vehicles



**Saharul Arof, Mohamad Rosyidi Ahmad, Philip Mawby, Hamzah Arof, and Emilia Noorsal**

**Abstract** Parallel mode operation is one of the modes of operation offered by New series motor four quadrants DC chopper for Electric Vehicles (EV). This paper is to study about the parallel mode and the focus is to reduce ripple current and ripple torque. Matlab/Simulink software is used to establish the system under study and the simulation results indicate that the proposed technique can be used to reduce the ripple current and ripple torque during parallel mode.

**Keywords** DC drive · EV · RL load · Ripple current · Ripple torque · Dc series motor · Buck chopper · Parallel mode

---

S. Arof (✉) · M. R. Ahmad  
Universiti Kuala Lumpur, Malaysian Spanish Institute Kulim Hi-Tech Park, 09000 Kulim, Kedah, Malaysia  
e-mail: [saharul@unikl.edu.my](mailto:saharul@unikl.edu.my)

M. R. Ahmad  
e-mail: [mrosyidi@unikl.edu.my](mailto:mrosyidi@unikl.edu.my)

S. Arof · P. Mawby  
University of Warwick School of Engineering, Coventry CV47AL, UK  
e-mail: [p.a.mawby@warwick.ac.uk](mailto:p.a.mawby@warwick.ac.uk)

H. Arof  
Engineering Department, Universiti Malaya, Jalan Universiti, 50603 Kuala Lumpur, Malaysia  
e-mail: [ahamzah@um.edu.my](mailto:ahamzah@um.edu.my)

E. Noorsal  
School of Electrical Engineering, College of Engineering, Cawangan Pulau Pinang, Universiti Teknologi MARA, Kampus Permatang Pauh, 13500 Pulau Pinang, Malaysia  
e-mail: [emilia.noorsal@uitm.edu.my](mailto:emilia.noorsal@uitm.edu.my)

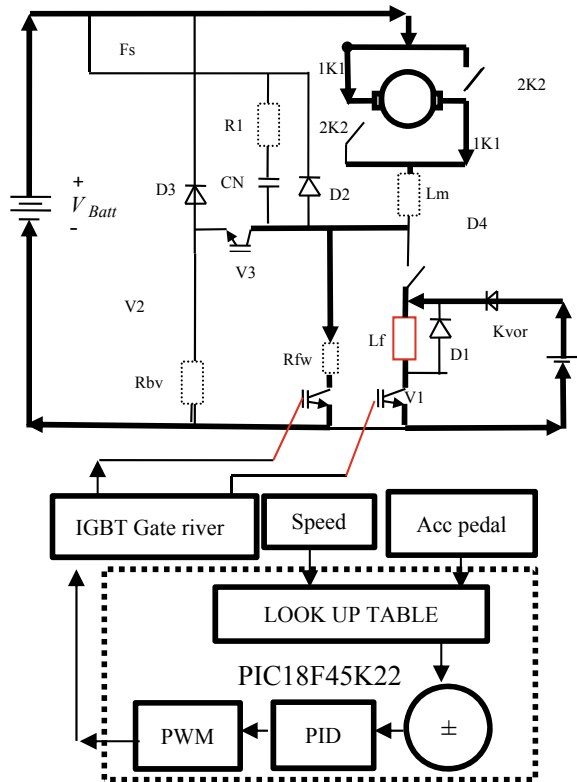
## 17.1 Introduction

The vehicles in use around the world have been producing serious problems to the environment such as air pollution, global warming, and the rapid depletion of the earth's petroleum reservoirs and this will eventually harm human life. Therefore, electric vehicles (EVs), hybrid electric vehicles (HEVs), and fuel cell electric vehicles (FCEVs) are some of the solutions to reduce global hydrocarbon emission and at the same time have higher efficiencies. The concept of EVs is to use a charged battery to energize and converts electrical energy to mechanical energy. In electric vehicles, the primary components are the motor, controller, power source (usually batteries), and transmission. A converter is required to control the power flows between batteries and electric motor.

## 17.2 Review Stage

DC motors have been the subject of interest since a long time because of a simple control and decoupling of the flux and torque. The commutator actually acts as a robust inverter, therefore, power electronics devices can be much simpler and inexpensive. Oak Ridge National Laboratory (ORNL) [1], United States in 2009, had successfully designed a DC brushed motor with high power output (55 kW), high efficiency (92%) that can operate at low operating voltages (13 V) and this has initiated the interest to embark research in DC drive electrical vehicles. A new series motor four quadrants DC chopper, such as shown in Fig. 17.1, was designed and the proposed chopper has multiple operations [2]. Several other studies related to DC drive EVs led to research on EC battery chargers [3–5] and different types of DC drive motors such as separately excited [6]. Detailed investigations on the chopper operation modes and EV design requirement [7] led to the establishment of a simulation model to test the chopper operations for the application of electric car and light rail Transit (LRT) [8]. The simulation model allows further investigations on each of the chopper operations in detail on the specific pattern of voltage, current, torque, speed, of the FQDC running dc series motor have been carried out [9]. This included details in several modes of operation such as driving, field weakening [10], parallel mode [11], regenerative braking [12], resistive braking [13], and overall system fault finding [14]. For DC series motor traction EC application, the speed and torque control has been successfully done and implemented with direct current control [15]. For power regeneration, the FQDC offers the generator mode with several techniques of regenerating power as studied and discussed in [16]. In order for the FQDC to be applied in real world it needs controllers running control algorithm in the embedded system. The controller and its control algorithm are studied and tested using a processor in the loop technique [17]. To improve the new FQDC performance an optimization tool such as artificial intelligence (AI) is introduced to control all of the chopper operations of the proposed FQDC chopper [18–20]. Attempt

**Fig. 17.1** New proposed chopper



of cruising test with specific requirement of remaining distance traverse and battery state of charge using a Fuzzy logic [21] controller shows significant performance in controlling the EV operation. Each operation of FQDC modes performance can be improved using AI optimization tools such as genetics algorithm and gradient descend [22] to set up specific look-up tables [23]. The pole placement method [24] is used to tune close loop PID controller to improve the controller performance while a Fuzzy Logic controller is used to control motor current [25] to improve the control performance and system stability. For fault diagnosis and online system tuning and optimization, a numerical representation using Taylor series [26] is studied and tried for the driving mode. The cascade PID with an ascend descend algorithm and after improvisation was associated to steering [27], brake control [28] and vehicle movement control [29] to be used for autonomous EVs for automatic reverse parking. This paper continues the study about the ripple current, ripple torque, switching frequency and duty ratio of PWM in parallel mode operation.

### 17.3 Methodology

Figure 17.1 shows the circuit in which the electric current flows during parallel mode operation. This parallel mode is used to overcome the disadvantage of series motors in which the speed drops when loaded such when the EV is climbing a steep hill. The following general equations describe the voltage and current for the chopper. Equations (17.1–17.3) are general equations that are applicable to all chopper operation modes.  $B_{emf}$  is the back emf of the motor,  $V_a$  and  $V_f$  are the armature and field voltages,  $K_b$  is the back emf constant,  $K_t$  is the torque motor constant,  $I_f$  is the field current,  $R_a$  and  $R_f$  are the motor coil resistances,  $I_a$  is the armature current,  $\omega$  is the angular speed, and  $T_d$  is the motor torque. Equations (17.4–17.6) are equations during parallel mode.

$$I_a = V_{batt} - I_a(R_a + R_f) - B_{emf} \omega L_a + L F \quad (17.1)$$

$$B_{emf} = K_v I_f \omega \quad (17.2)$$

$$T_d = K_t I_f I_a = J \frac{d\omega}{dt} + B_w + T_L \quad (17.3)$$

The dynamic equations of field and armature current are as shown below.

$$\frac{d}{dt}[I_f] = \left[ -\left(\frac{R_f}{L_f}\right) \right] [I_f] \left[ \frac{1}{(L_f)} \right] [V_{ext} K_{drv}] \quad (17.4)$$

$$\frac{d}{dt}[I_a] = \left[ \frac{-(R_a)}{L_a} \right] [I_a] \left[ \frac{1}{L_a} - \frac{1}{L_a} \right] \left[ \begin{matrix} V_{dc} \\ E_g \end{matrix} \right] \quad (17.5)$$

$$\left[ \begin{matrix} I_f \\ V_c \end{matrix} \right] \left[ \frac{1}{L_f} \ 0 \right] \left[ \begin{matrix} V_{dc} K_{drv} K_{rgb} \\ 0 \end{matrix} \right] \quad (17.6)$$

The proposed DC chopper allows the series motor to operate in parallel mode and in this mode, the field current is separately controlled from the armature current whereby it can be changed or maintained. The armature current is controlled by varying the PWM value for IGBT2 as the simplified circuit shown in Fig. 17.2. Field current is controlled by controlling PWM of IGBT1 as simplified circuit shown in Fig. 17.3. In parallel mode, to overcome the load effect (climbing steep hill), it must have a higher motor torque. To obtain a higher torque, it must increase the armature current by reducing the back emf voltage. To lower  $B_{emf}$  must reduce the field current. To lower the field current, we must reduce the duty ratio of switching IGBTV1. If the duty ratio of PWM IGBTV1 is lowered below the maximum PWM value which is 255, the ripple current will exist. The ripple current causes the ripple torque. The IGBT V2 in the armature circuit is fired at maximum to have the highest armature current. As the switching PWM value is maximum (255), the duty ratio is 1.

Fig. 17.2 Armature circuit

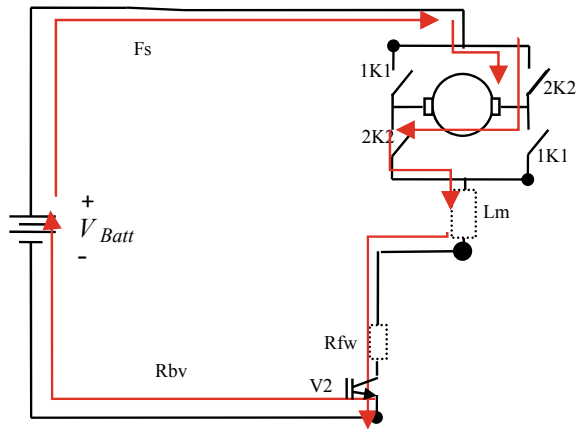
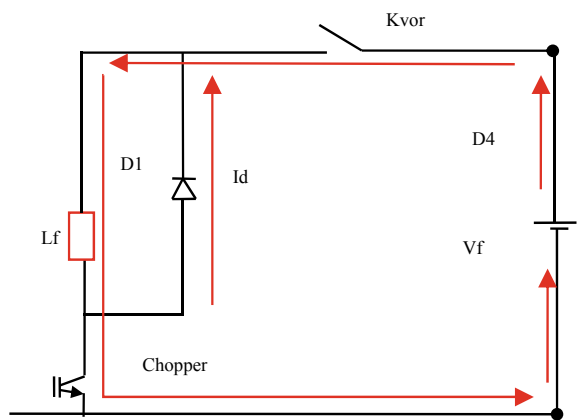


Fig. 17.3 Field circuit



As the parallel mode requirement is to lower the field current the chopper IGBTV1 PWM value is always lower than 255 and the duty ratio is lower than 1. Due to the previous condition, the operation of the chopper can be divided into two modes. During mode 1, the chopper is switched on and the current flows from the supply to the load. The equivalent circuits for these modes are shown in Fig. 17.4.

During mode 2, the chopper is switched off and the field current continues to flow through the freewheeling diode  $D_m$  and is recirculating the load as shown in Fig. 17.5.

The field current for mode 1 can be found from

$$v_f = Ri_f + L \frac{di_f}{dt} + E \tag{17.7}$$

$$\text{Voltage across inductor} = L \frac{di_f}{dt} \tag{17.8}$$

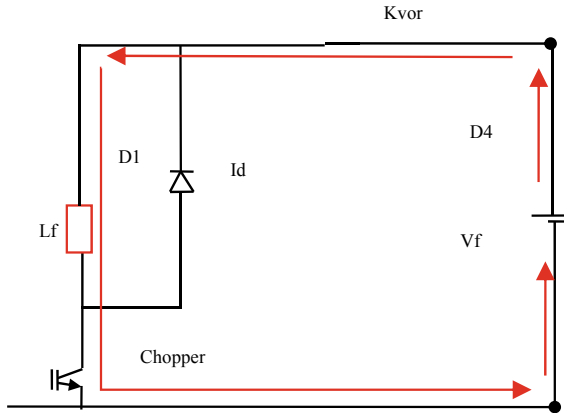


Fig. 17.4 Chopper in mode 1

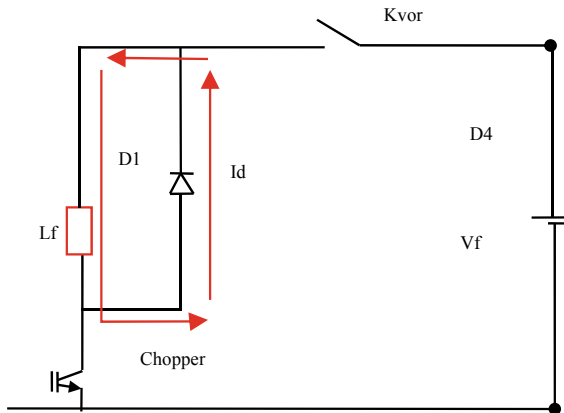


Fig. 17.5 Chopper in mode 2

$$\text{Energy stored in inductor } E = \frac{1}{2} L_f I_f^2 \tag{17.9}$$

With initial condition,  $i(t = 0) = I_1$ ,

In the Laplace's domain of  $s$ , Eq. (17.7) becomes

$$\frac{V_f}{s} = L_f I_{f(s)} - s L_f I_f + R_f I_{f(s)} + \frac{E}{s}, \tag{17.10}$$

$$\frac{V_f}{s} - \frac{E}{s} = L_s I_{f(s)} - s L_f I_f + R_f I_{f(s)} \tag{17.11}$$

$$\frac{V_f}{s} - \frac{E}{s} + L_f I_f = L_s I_{f(s)} + R_f I_{f(s)}, \quad (17.12)$$

$$\frac{V_s - E}{s} + L I_f = I_{f(s)}(L_f + R_f) \quad (17.13)$$

And solving for  $I_{(s)}$  gives:

$$I_{f(s)} = \frac{V_s - E}{(L_s + R)s} + \frac{L I_1}{L_s + R}, \quad (17.14)$$

$$I_{f(s)} = \frac{V_s - E}{(L_s s + R s)} + \frac{L I_1}{L(s + \frac{R}{L})} \quad (17.15)$$

$$I_{f(s)} = \frac{V_s - E}{L_s \left( s + \frac{R s}{L_s} \right)} + \frac{I_1}{\left( s + \frac{R}{L} \right)}, \quad (17.16)$$

$$I_{f(s)} = \frac{V_s - E}{L_s \left( s + \frac{R}{L} \right)} + \frac{I_1}{\left( s + \frac{R}{L} \right)} \quad (17.17)$$

$$I_{f(s)} = \frac{V_s - E}{L_s(s + \beta)} + \frac{I_1}{s + \beta}, \quad \text{where } \beta = \frac{R}{L} \quad (17.18)$$

$$I_{f(s)} = \frac{V_s - E}{R} \left( \frac{R}{L_s(s + \beta)} \right) + \frac{I_1}{s + \beta}, \quad (17.19)$$

$$I_{f(s)} = \frac{V_s - E}{R} \left( \frac{\beta}{s(s + \beta)} \right) + \frac{I_1}{s + \beta} \quad (17.20)$$

$$I_{f(s)} = \frac{V_s - E}{R} \left( \frac{1}{s} - \frac{1}{s + \beta} \right) + \frac{I_1}{s + \beta} \quad (17.21)$$

Taking the inverse Laplace transform, the solution of Eq. (17.21) with initial current  $i_f(t=0) = I_1$  gives the load current as;

$$i_f(t) = I_1 e^{-tR/L} + \frac{V_s - V_E}{R} (1 - e^{-tR/L}) \quad (17.22)$$

The transient response of Energy stored in inductor is as shown in Fig. 17.6, while the current is as in Fig. 17.7.

In case at the beginning of the generated voltage or for back emf  $E = 0$ , the Eq. (17.22) then becomes

$$i_f(t) = I_1 e^{-tR/L} + \frac{V_s}{R} (1 - e^{-tR/L}) \quad (17.23)$$

If there is no initial current on the inductor hence the Eq. (17.23) is

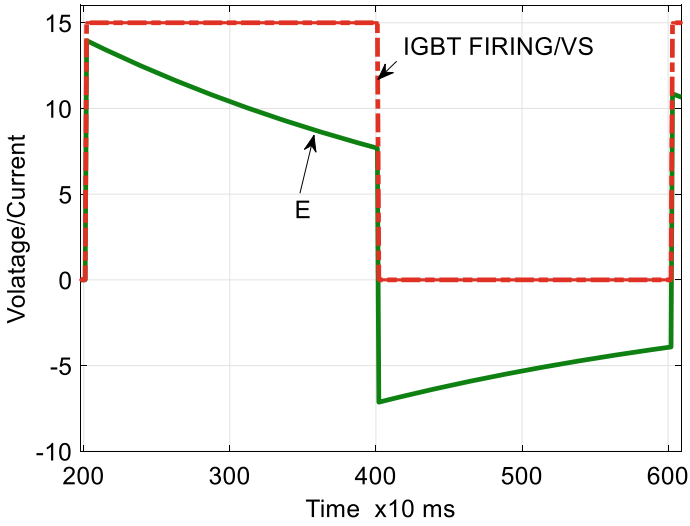


Fig. 17.6 Voltage stored in inductor

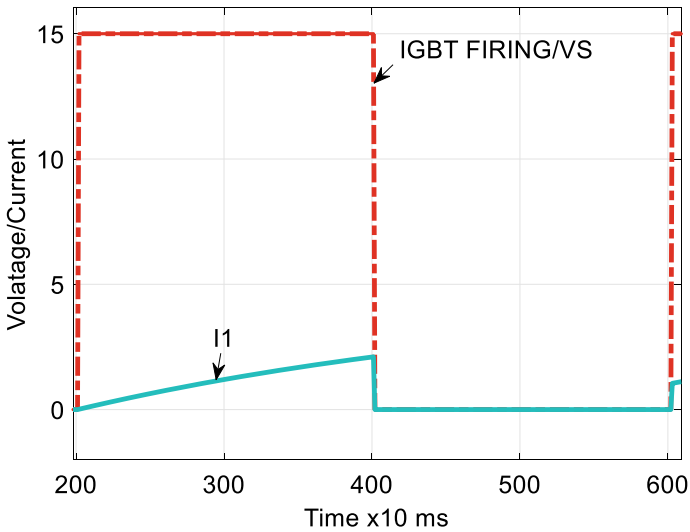


Fig. 17.7 Current in mode 1

$$i_f(t) = \frac{V_s}{R}(1 - e^{-\beta t}) \tag{17.24}$$

In steady state (at  $t = \infty$ ); the Eq. (17.24) is



$$I_{fss} = i(t = \infty) = \frac{V_s}{R} \tag{17.25}$$

This mode is valid for  $0 \leq t \leq t_1 (=kT)$ ; and at the end of this mode, the load current becomes

$$i_1(t = t_1 = kT) = I_2 \tag{17.26}$$

The load current for mode 2 can be found from

$$0 = Ri_2 + L \frac{di_2}{dt} + E \tag{17.27}$$

With initial current  $i_2(t = 0) = I_2$  and redefining the time origin (i.e.;  $t = 0$ ) at the beginning of mode 2, we have

$$i_2(t) = I_2 e^{-tR/L} + \frac{E}{R} (1 - e^{-tR/L}) \tag{17.28}$$

The transient response of current flowing through inductor is as shown in Fig. 17.8, This mode is valid for  $0 \leq t \leq t_2 [(1 - k)T]$  and at the end of this mode, the load current becomes

$$i_2(t = t_2) = I_3 \tag{17.29}$$

At the end of mode 2, the chopper is turned on again in the next cycle after time,

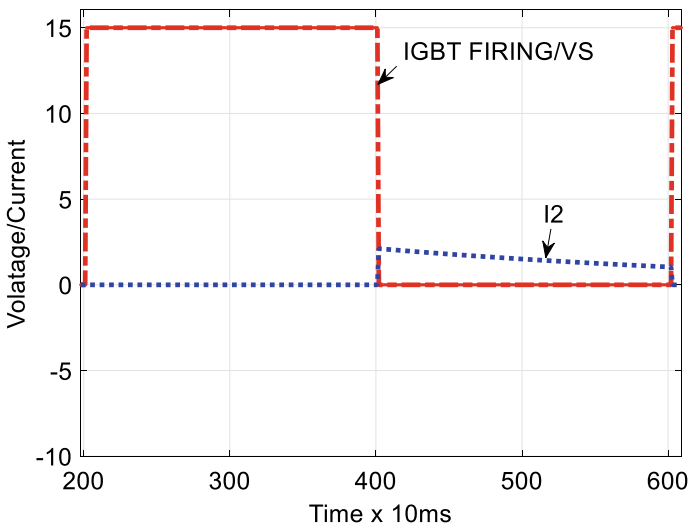


Fig. 17.8 Current in mode 2

$$T = 1/f = t_1 + t_2 \quad (17.30)$$

Under steady state conditions,  $I_i = I_3$ . The peak-to-peak load ripple current  $I_2$  is given by

$$i_2 = i_1 e^{-kTR/L} + \frac{V_s - E}{R} (1 - e^{-kTR/L}) \quad (17.31)$$

$$I_3 = I_1 = I_2 e^{-(1-k)TR/L} - \frac{E}{R} (1 - e^{-(1-k)TR/L}) \quad (17.32)$$

The peak-to-peak ripple current is  $\Delta I = I_2 - I_1$  which after simplifications becomes

$$\Delta I = \frac{V_s}{R} \frac{1 - e^{-kTR/L} + e^{-TR/L} - e^{-(1-k)TR/L}}{1 - e^{-TR/L}} \quad (17.33)$$

The condition for maximum ripple,

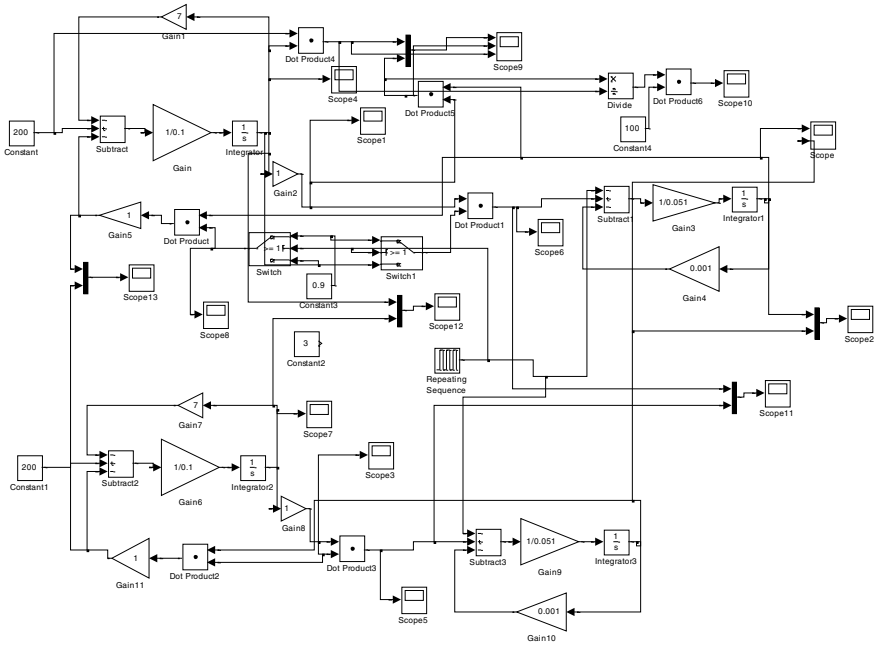
$$\frac{d(\Delta I)}{dk} = 0 \quad (17.34)$$

Gives  $e^{-kTR/L} - e^{-(1-k)TR/L} = 0$  or  $-k = -(1 - k)$  or  $k = 0.5$ .

Ripple in armature or field current produces ripple in torque according to Eq. 17.3. Ripple in torque is unwanted as it causes jerking to the motor drive, EMI and can damage the motor. Some early hypotheses to reduce ripple torque during parallel mode is by reducing field current ripple with several methods proposed are as follows:

1. Increase switching frequency: increasing switching frequency could reduce the ripple current, but it can increase power electronics devices switching losses. If it is the case, a larger heat sink is required and this means extra costs.
2. Increase duty ratio: increase duty ratio can reduce the ripple current, but this also could mean that the expected field current cannot be achieved. As mentioned earlier, the higher torque during Parallel mode is reduced back emf by reducing the field current.
3. Add inductor to the field circuit: adding inductor could cause the rising and falling current to slow down means reducing the ripple current but increasing the inductor cost and weight to the vehicle.
4. Use lower Field voltage supply: this reduces the ripple current but too low voltage causes a lower magnetic field, which generates the motor torque.

The MATLAB/Simulink simulation model is established using mathematical equations for studying the hypotheses of ripple current reduction during parallel mode operation is as shown in Fig. 17.9.



**Fig. 17.9** Simulation model representation of four quadrants DC chopper in parallel mode for mode 1 and mode 2 while studying ripple current and ripple torque

### 17.4 Results

To test the hypothesis, the simulation model is made to turn on and off representing IGBT firing. The obtained result of IGBT firing making on and off which produces ripple torque as a result of ripple armature and field current is shown in Fig. 17.10.

The hypothesis of increasing switching frequency can lower the ripple current is tested by varying the frequency and observing the output ripple current. The result is as shown in Fig. 17.11. The conclusion that can be made is, the higher the frequency, the lower the ripple current.

The hypothesis that an increasing duty ratio lowers the ripple current is tested by varying the duty ratio and observing the output ripple current. The result is as shown in Fig. 17.12. The conclusion that can be made is, the higher the duty ratio, the lower the ripple current.

The hypothesis that increasing inductor value to reduce the ripple current is tested by changing the inductor value and observing the output ripple current. The result is as shown in Fig. 17.13. The conclusion that can be made is, the higher the inductor value, the lower the ripple current.

The hypothesis that lowering the supply voltage value to reduce the ripple current is tested by changing the voltage supply value and observing the output ripple current.

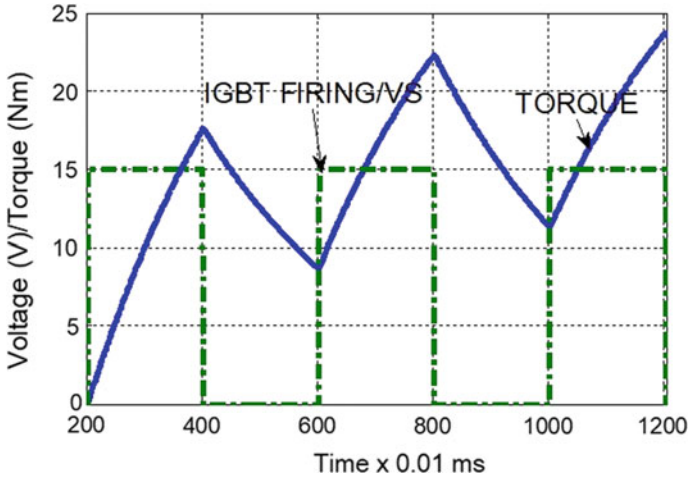


Fig. 17.10 IGBT turning on and off and torque

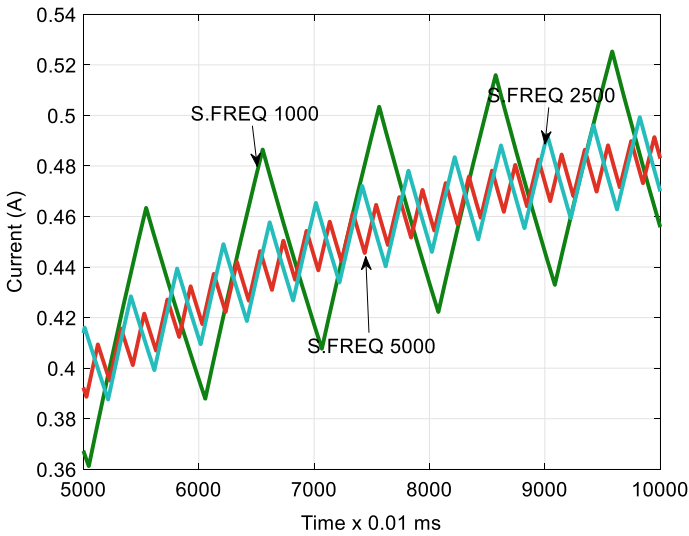


Fig. 17.11 Current with different switching frequencies (Hz)

The result is as shown in Fig. 17.14. The conclusion that can be made is, the lower the supply voltage, the lower the ripple current.

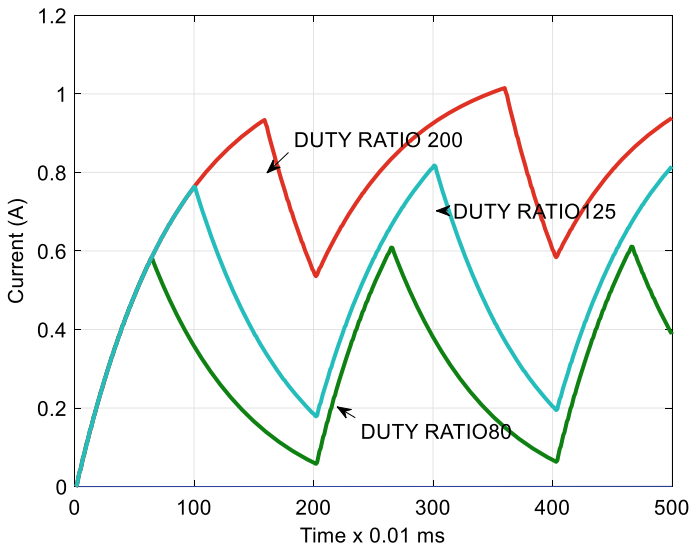


Fig. 17.12 Current with different duty ratio

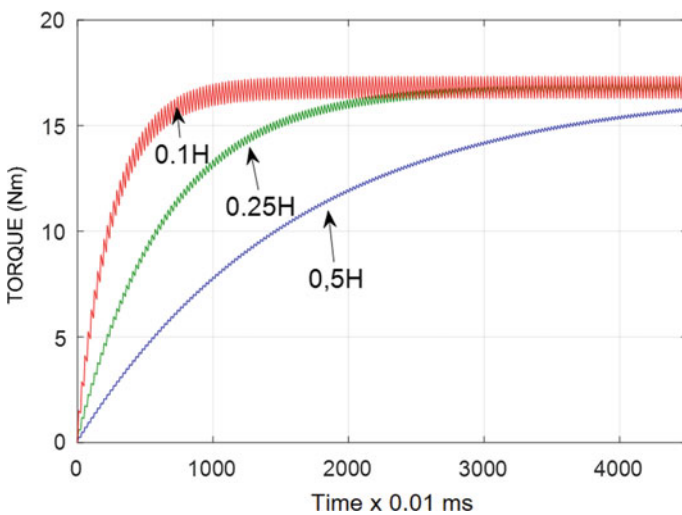
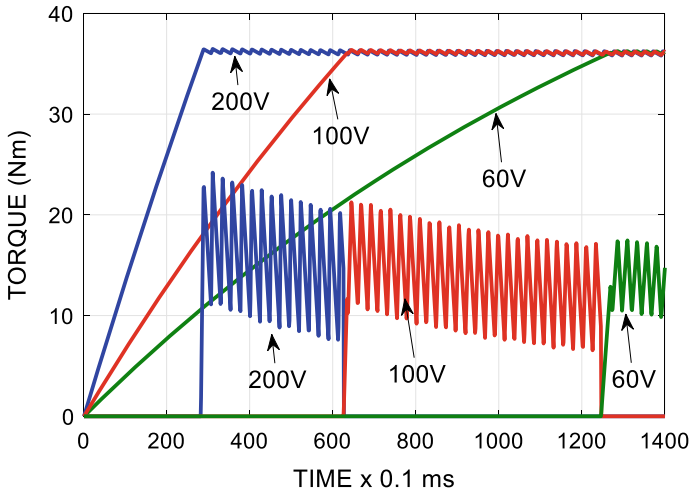


Fig. 17.13 Current with different inductor value

### 17.5 Conclusion

Increased frequency, increased duty ratio, increased inductor value and lower voltage supply can reduce the effect of ripple current and ripple torque of the series motor powered by four quadrants DC chopper. A combination of lowering the field current



**Fig. 17.14** Current with different inductor value

and increasing the duty ratio may be one of the solutions to reduce the field current ripple. In summary DC drive series motor has a high potential to be utilized in EV. This is due to its simple design, low cost and excellent controllability.

## References

1. Oak Ridge National Laboratory (2009) Advanced brush technology for DC motors. <http://peemrc.ornl.gov/projects/emdc3.jpg>
2. Arof S, Jalil JA, Yaakop NM, Mawby PA, Arof H (2014) Series motor four quadrants drive Dc chopper Part 1: overall. In: International conference on power electronics
3. Arof S, Diyanah N, Philip Mawby NH, Arof H, Yaakop NM (2019) Low harmonics plug-in home charging electric vehicle battery charger utilizing multi-level rectifier, zero crossing and buck chopper: Part 1: general overview. In: Progress in engineering technology, pp 103–108. [https://doi.org/10.1007/978-3-030-28505-0\\_9](https://doi.org/10.1007/978-3-030-28505-0_9)
4. Arof S, Ahmad MR, Yaakop NM, Philip Mawby H, Arof EN, Bakar AA, Ali YM (2021) Low harmonics plug-in home charging electric vehicle battery charger utilizing multilevel rectifier, zero crossing, and buck chopper: state of charge estimator using current integration algorithm for embedded system. In: Progress in engineering technology III. [https://doi.org/10.1007/978-3-030-67750-3\\_19](https://doi.org/10.1007/978-3-030-67750-3_19)
5. Saharul Arof MS, Sazali NM, Noor JN, Amirah PM, Noorsal E, Bakar AA, Ali YM (2021) Low harmonics plug-in home charging electric vehicle battery charger utilizing multi-level rectifier, zero crossing, and buck chopper: BMS battery charging control algorithm. In: Progress in engineering technology III. [https://doi.org/10.1007/978-3-030-67750-3\\_18](https://doi.org/10.1007/978-3-030-67750-3_18)
6. Arof S, Diyanah NHN, Noor NM, Jalil JA, Mawby PA, Arof H (2019) A new four quadrants drive chopper for separately excited DC motor in low cost electric vehicle. In: Progress in engineering, pp 119–138. [https://doi.org/10.1007/978-3-030-28505-0\\_10](https://doi.org/10.1007/978-3-030-28505-0_10)

7. Arof S, Noor NM, Nur Diyanah NH, Philip Mawby H, Arof EN (2021) DC drive electric car utilizing series motor and four quadrants drive DC chopper parameter determination from general design requirements. In: Progress in engineering technology III. [https://doi.org/10.1007/978-3-030-67750-3\\_17](https://doi.org/10.1007/978-3-030-67750-3_17)
8. Arof S, Hassan H, Rosyidi M, Mawby PA, Arof H (2017) Implementation of series motor four quadrants Drive dc chopper for dc drive electric car and LRT via simulation model. *J Appl Environ Biol Sci* 7(3S)73–82
9. Arof S, Noor NM, Elias F, Mawby PA, Arof H (2017) Investigation of chopper operation of series motor four quadrants DC chopper. *J Appl Environ Biol Sci* 7(3S)49–56
10. Arof S, Diyanah NHN, Mawby PA, H. Arof Emilia (2021) Series motor four quadrants drive DC chopper Part 3: field weakening mode. *IOP Conf Ser Mater Sci Eng* 1127(1). <https://doi.org/10.1088/1757-899X/1127/1/012028.8>
11. Arof S, Diyanah NHN, Mawby PA, H. Arof Emilia (2021) New series motor four quadrants drive DC chopper for economical EV, Part 5: parallel mode. *IOP Conf Ser Mater Sci Eng* 1127(1). <https://doi.org/10.1088/1757-899X/1127/1/012025>
12. Arof S, Noorsal E, Mawby PA, Arof H (2020) Series motor four quadrants drive DC chopper for DC drive electric vehicle Part 6: regenerative braking. *International Scientific Forum (ISF2019)*, Melaka, Malaysia, eISBN: 978-967-10842-1-2
13. Arof S, Noorsal E, Mawby PA, Arof H (2020) Series motor four quadrants drive DC chopper for DC drive electric vehicle Part 7: resistive braking. *International Scientific Forum (ISF2019)*, Melaka, Malaysia, eISBN: 978-967-10842-1-2
14. Saharul Arof MR, Faiz NHN, Diyanah NM, Yaakop PM, Arof H, Noorsal E (2021) Fault diagnose of DC drive EV utilizing a new series motor four quadrants DC chopper using an expert system and quadratic solver running in embedded: Part 1: during start up. In: Progress in engineering technology III. [https://doi.org/10.1007/978-3-030-67750-3\\_15](https://doi.org/10.1007/978-3-030-67750-3_15)
15. Arof S, Jalil JA, Kamaruddin NH, Yaakop NM, Mawby PA, Arof H (2016) Series motor four quadrants drive Dc chopper Part 2: driving and reverse with direct current control. In: *International conference on power electronics*, pp 775–780. 978-1-5090-2547-3/16. <https://doi.org/10.1109/PECON2016.7951663>
16. Arof S, Diyanah NHN, Noor NMN, Radzi M, Jalil JA, Mawby PA, Arof H (2019) Series motor four quadrants drive DC chopper: Part 4: generator mode. In: Progress in engineering technology, pp 155–167. [https://doi.org/10.1007/978-3-030-28505-0\\_12](https://doi.org/10.1007/978-3-030-28505-0_12)
17. Arof SH, Diyanah N, Yaakop MA, Mawby P, Arof H (2019) Processor in the loop for testing series motor four quadrants drive direct current chopper for series motor driven electric car: Part1: chopper operation modes testing. In: *Advanced engineering for processes and technologies*, pp 59–76. [https://doi.org/10.1007/978-3-030-05621-6\\_5](https://doi.org/10.1007/978-3-030-05621-6_5)
18. Arof S, Muhd Khairulzaman AK, Jalil JA, Arof H, Mawby PA (2015) Self tuning fuzzy logic controlling chopper operation of four quadrants drive DC chopper for low cost electric vehicle. In: *6th international conference on intelligent systems, modelling and simulation*, IEEE computer society, pp 40–24
19. Arof S, Zaman MK, Jalil JA, Mawby PA, Arof H (2015) Artificial intelligence controlling chopper operation of four quadrants drive DC chopper for low cost electric vehicle. *Int J Simul Syst Sci Technol*. <https://doi.org/10.5013/IJSSST.a.16.04.03.2015>
20. Arof S, Diyanah NH, Mawby PA, Arof H (2019) Study on implementation of neural network controlling four quadrants direct current chopper: Part1: using single neural network controller with binary data output. In: *Advanced engineering for processes and technologies*, pp 37–57
21. Arof S, Diyanah NHN, Mawby PA, Arof Emilia Noorsal H (2020) DC drive electric car state of charge (SOC) and remaining distance traverse (RDT) optimized by fuzzy logic. *International Scientific Forum (ISF2019)*, Melaka, Malaysia, eISBN: 978-967-10842-1-2
22. Saharul Arof ARA, Shauqee M, Rosyidi NHN, Diyanah PM, Arof H, Noorsal E (2021) Gradient descend for setting up a look-up table of series motor four quadrants drive DC chopper in parallel mode. In: Progress in engineering technology III. [https://doi.org/10.1007/978-3-030-67750-3\\_16](https://doi.org/10.1007/978-3-030-67750-3_16)

23. Arof S, Diyanah NHN, Noor NM, Rosyidi M, Mawby PA, Arof H (2019) Genetics algorithm for setting up look up table for parallel mode of new series motor four quadrants dc chopper. In: Progress in engineering, pp 155–167. [https://doi.org/10.1007/978-3-030-28505-0\\_12](https://doi.org/10.1007/978-3-030-28505-0_12)
24. Arof S, Noor NM, Alias MF, Noorsal E, Mawby P, Arof H (2020) Digital proportional integral derivative (PID) Controller for closed-loop direct current control of an electric vehicle traction tuned using pole placement. In: Progress in engineering technology II. Advanced structured materials, vol 131. Springer, Cham. [https://doi.org/10.1007/978-3-030-46036-5\\_8](https://doi.org/10.1007/978-3-030-46036-5_8)
25. Arof S, Noor NM, Mohamad R, Noorsal E, Mawby PA, Arof H (2020) Close loop feedback direct current control in driving mode of a four quadrants drive direct current chopper for electric vehicle traction controlled using fuzzy logic. In: Progress in engineering technology II. Advanced structured materials, vol 131. Springer, Cham. [https://doi.org/10.1007/978-3-030-46036-5\\_7](https://doi.org/10.1007/978-3-030-46036-5_7)
26. Arof S, Sukiman ED, Diyanah NH, Noor NM, Noorsal E, Mawby PA, Arof H (2020) Discrete-time linear system of new series motor four-quadrant drive direct current chopper numerically represented by Taylor series. In: Progress in engineering technology II. Advanced structured materials, vol 131. Springer, Cham. [https://doi.org/10.1007/978-3-030-46036-5\\_10](https://doi.org/10.1007/978-3-030-46036-5_10)
27. Saharul A, Said S, Diyanah NHN, Noor NM, Mawby YP, Arof H, Noorsal E (2020) Series motor four-quadrant direct current chopper: reverse mode, steering position control with double-circle path tracking and control for autonomous reverse parking of direct current drive electric car. In: Progress in engineering technology II. Advanced structured materials, vol 131. Springer, Cham. [https://doi.org/10.1007/978-3-030-46036-5\\_12](https://doi.org/10.1007/978-3-030-46036-5_12)
28. Saharul Arof MS, Sazali NHN, Diyanah PM, Arof H, Noorsal E (2021) Series motor four quadrants drive DC chopper: reverse mode with automatic reverse parking of DC drive electric car with constant brake motor control combine to the propulsion motor torque. In: Progress in engineering technology III. [https://doi.org/10.1007/978-3-030-67750-3\\_20](https://doi.org/10.1007/978-3-030-67750-3_20)
29. Saharul Arof S, Said NHN, Diyanah NM, Noor JA, Jalil PM, Arof H, Noorsal E (2020) Series motor four-quadrant DC chopper: reverse mode, direct current control, triple cascade PIDs, and ascend-descend algorithm with feedback optimization for automatic reverse parking. In: Progress in engineering technology II. Advanced structured materials, vol 131. Springer, Cham. [https://doi.org/10.1007/978-3-030-46036-5\\_13](https://doi.org/10.1007/978-3-030-46036-5_13)



# Chapter 18

## Statistical Approach for Predictions of Motorcycle Engine Block Surface Roughness Property After CNC Machining



**Shahrizan Yusoff, Sharifah Nur Anis Ajmal, Nur Nadhirah, and Baizura Zubir**

**Abstract** The engine block is one of the important components in a motorcycle. It plays an important role in ensuring that the motorcycle works properly. The surface roughness of the engine cylinder affects the engine efficiency. Therefore, researchers underwent experiments to find out the goodness of the surface for the engine block. Through the surface roughness test machine and cutting using a CNC milling machine, it shows that the cutting speed and speed rate affect the surface roughness results. Response surface methodology (RSM) and Minitab methods are used to obtain statistical analysis data in completing this project.

**Keywords** Surface roughness · CNC milling and engine block

### 18.1 Introduction

The engine block aims to support the engine's components. Furthermore, the engine block passes heat from friction to the atmosphere and coolant from the engine. The material chosen is either a gray cast iron or an aluminum alloy for the engine block. Optimization of machining parameters needs to determine the most significant parameter for predictions of the motorcycle engine block surface roughness.

---

S. Yusoff (✉) · S. N. A. Ajmal · N. Nadhirah · B. Zubir  
Universiti Kuala Lumpur, Malaysian Spanish Institute Kulim Hi-Tech Park, 09000 Kulim, Kedah, Malaysia  
e-mail: [mshahrizan@unikl.edu.my](mailto:mshahrizan@unikl.edu.my)

S. N. A. Ajmal  
e-mail: [anis.azimuddin@s.unikl.edu.my](mailto:anis.azimuddin@s.unikl.edu.my)

N. Nadhirah  
e-mail: [nadhirah.ramlee@s.unikl.edu.my](mailto:nadhirah.ramlee@s.unikl.edu.my)

B. Zubir  
e-mail: [baizura@unikl.edu.my](mailto:baizura@unikl.edu.my)

The controllable parameters for the CNC milling machine are the cutting tool variables, workpiece material variables, and cutting conditions, whereas the main desired output is a good surface roughness [1]. The present work discusses the findings of an experimental investigation into the effects of cutting speed, feed rate, and tool diameter during CNC milling of an engine block keeping the depth of cut constant. Response surface methodology (RSM) and Minitab were used to accomplish the objective of the experimental study.

## 18.2 Literature

### 18.2.1 Surface Roughness

The following paragraph summarizes some articles regarding the motorcycle engine block surface roughness. A surface roughness measuring device provided the surface roughness parameters in 3D coordinate used by Bulaha et al. [2]. It is therefore important to use a practical way to characterize them to optimize the surface and a study of the roughness parameters (profile) provides knowledge along the x-axis and z-axis. The following properties should have the ideal cylinder liner surface: a smooth friction reducing surface and a quick adjustment of the running clearance significant contact area for exchanging wear all over the surface and avoiding high-pressure areas as well as sealing and deep groove for the preservation of lubrication and collecting debris. Table 18.1 shows the cause and effect of cylinder line surface caused by machining. Surface roughness most commonly refers to the variations in the height of the surface relative to a reference plane. It is measured either along with a single line profile or along with a set of parallel line profiles (surface maps). The value of surface roughness average ( $Ra$ ) is an official standard in most industrialized countries. Surface measurement usually gives the data in two ways, i.e. roughness and waviness. The efficiency and problems of machine tools can be described and predicted using these parameters. The parameters of the surface profile are described by ISO 4287:1997, which covers five groups of texture parameters, including parameters of amplitude (peak and valley), parameters of amplitude (average of ordinates), parameters of spacing, hybrid parameters, curves, and related parameters. The arithmetical mean of five surface profile ( $Ra$ ) is the surface roughness parameter used in this analysis. This parameter is also the surface finish parameter most used by researchers and industries.  $Ra$  is the arithmetic average of the absolute value of the heights from the calculated mean value of roughness irregularities.

**Table 18.1** Summary of most common deviations—the cause and effect

Default	Effect on engine performance	Common major causes
Wide, deep crosshatch grooves	Causes abnormal wear, excessive oil consumption	Stone grit too coarse, poor stone breakdown, coolant viscosity too high, excessive stone pressure
Crosshatch grooves irregular spaced	Poor oil distribution	Stone grade too hard, stone grit too coarse, low stone breakdown
Crosshatch grooves fragmented	Slows ring, cause scratching and high wear, lower life and oil economy, raise ring temperature, cause excessive variation engine to engine	Insufficient dwell strokes at the end of honing cut, stone grit too coarse
One directional cut crosshatch	Cause ring rotation, rapid wear	Excessive play in hone components such as joints or stone holder to body clearance
Low crosshatch angle	Poor oil distribution, high impact forces on rings, excessive wear, shortens life	Tool kinematics

### 18.2.2 CNC Milling

In this subheading of the review, the effect of the cutting speed and feed rate of the CNC milling process are summarized based on the project thesis regarding using the CNC milling in this project. Cutting speed, feed rate and depth of cut are the most significant parameters on the surface roughness. The importance of cutting speed and machine feed rate cannot be overemphasized in machining operation. The right feed can also prolong the life of the unit. The correct speed can mean the difference between burning the end of a drill or other tool, causing time to be lost, or getting several hours of cutting time between sharpening or replacement.

### 18.2.3 Cutting Speed

The cutting speed (CS) is typically provided in cutting tool tables and is based on the surface feet per minute. Surface feet per minute indicates that either the machine moves past the work or the work moves past the tool is a rate dependent on the number of feet moving the instrument in one minute [3]. There are more revolutions per minute of a small cylinder (rpm) than a big one with the same surface speed.

### ***18.2.4 Feed***

The movement of the machine that causes a tool to cut into or along a workpiece's surface is called the feed. In metal cutting, the volume of feed is generally measured in thousands of inches. Feeds on various types of machine tools are represented in slightly different ways. Drills on drill presses rotate, allowing the cutting edges to cut into the workpiece at the end of the drill. The cut depth is not connected to the feed depth. Instead of a vertical one, the horizontal milling machine has a horizontal spindle, but the calculation of the feed rate is the same as the vertical mills. Cutting speeds and rpm are often calculated.

### ***18.2.5 Depth of Cut***

In regards to the depth of cut, previous end-milling studies have viewed the depth of cut as a constant for convenience, but this technique is a distortion of fact. Due to the irregular shape of workpieces, the inaccuracy of identifying workpieces on the unit, and machining errors from previous cutting, it is challenging to monitor depth of cut. The depth of cut makes a massive effect on the surface roughness.

### ***18.2.6 Cemented Carbide***

As a cutting tool for this project, a cemented carbide material was used. The paper details the features of cemented carbides. Carbide is a chemical compound of carbon and a metal. The term carbide is widely used in different combinations to refer to cemented carbides. The cutting instruments are made up of tungsten carbide, titanium carbide or tantalum carbide and cobalt. A standard cemented carbide composition is 85 to 95 tungsten carbide, and the remaining is a cobalt binder for the tungsten carbide powder. Increasing the cobalt binder percentage increases the strength of the tool material and decreases its strength or wear resistance at the same time [4]. In both high and low temperatures, carbides have greater hardness, allowing high-speed steel or cast alloys. This provides for steel machining speeds of approximately 400 fpm. Cemented carbides are used for cutting tough alloy steels in particular. Various grades of carbide and insert shapes are available, and a specific material should be made the correct selection for machining.

### ***18.2.7 Engine Cylinder Block***

One of the main components of vehicle propulsion is the engine cylinder block. The engine block is the engine body made of cast iron or aluminum containing the cylinders. The valve and valve ports were included in the block in all older engines. The water-cooled engine block consists of a water jacket cast around the cylinders. In air-cooled engines, the block's outer surface has cooling fins and an engine cylinder block can make up nearly two percent of the total mass of the vehicle [5]. The cylinder block must ensure that the piston assembly in the cylinders (or liners) is appropriately sealed and preserve the ideal oil reserve needed for the cylinder-piston ring system through the texture given by a unique process such as the honing process [6]. Therefore, since the cylinder block houses the cylinder bores, their surrounding coolant passages and the top half of the crankcase, the block dimensions are defined mainly by the sizes of the cylinders and the spacing between the cylinders.

### ***18.2.8 Response Surface Methodology***

The response surface methodology (RSM) is a mathematical and statistical approach commonly used to model and evaluate a mechanism in which different variables affect the answer of interest, and the purpose of this approach is to optimize the response. Dependent variables are called the parameters that influence the operation, while the responses are called dependent variables. Response surface is a surface placement-based process [7]. Therefore, the key objectives of RSM analysis are to understand the response surface topography, including the local limit, local, minimum and ridgelines, and to define the area where the most appropriate response occurs. The RSM examines a reasonable estimate of input and output variables and determines the ideal operating conditions for a system under analysis or a factor field area that meets the operating requirements [8]. The most significant element of RSM is the design of experiments (DoE). The DoE tries to pick the most relevant points where the reaction can be well studied. The mathematical model of the method is often associated with experimental design. The option of experimental design, therefore has a significant influence on deciding the correctness of the answer on the face of construction. The benefits offered by the RSM can be summed up by evaluating the relationship between the independent variables, mathematically modelling the system, and saving time and expense by reducing the number of trials.

### 18.3 Methodology

#### 18.3.1 Block Diagram of Surface Roughness

Figure 18.1 shows the block diagram for the different steps of using the surface roughness machine, which is used to check the surface roughness of the wall of a motorcycle engine block. Within this project, the researcher only focuses on the surface roughness test for the engine block. The first step is to turn on the computer that connects to the machine and opens the software for the surface roughness. Figure 18.2 shows the step of placing, which places the specimen on the device. After that, Fig. 18.3 shows a step to adjust the stylus axis until it reaches the engine block surface. Next, start the program and tested machine starts to function as shown in Figs. 18.4 and 18.5. Then, the surface reading and graph will be shown on the software. Figure 18.6 shows the example of the surface roughness data.

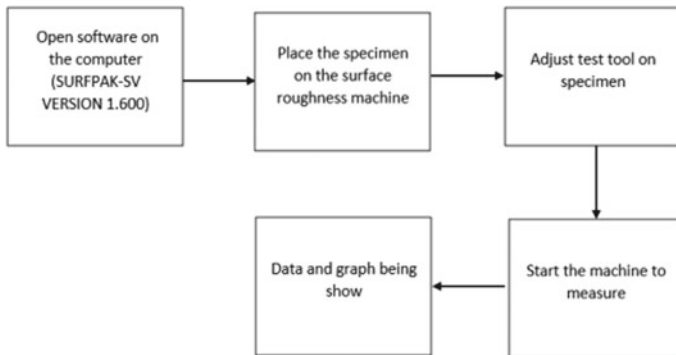
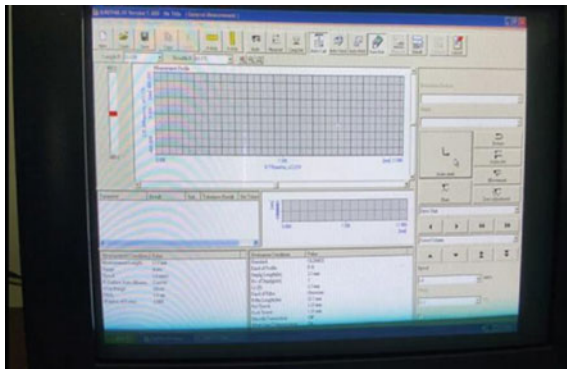


Fig. 18.1 Block diagram for the different steps of using the surface roughness machine

Fig. 18.2 Place specimen on a flat surface



**Fig. 18.3** Adjust the stylus



**Fig. 18.4** Start the process



**Fig. 18.5** Tested surface roughness started

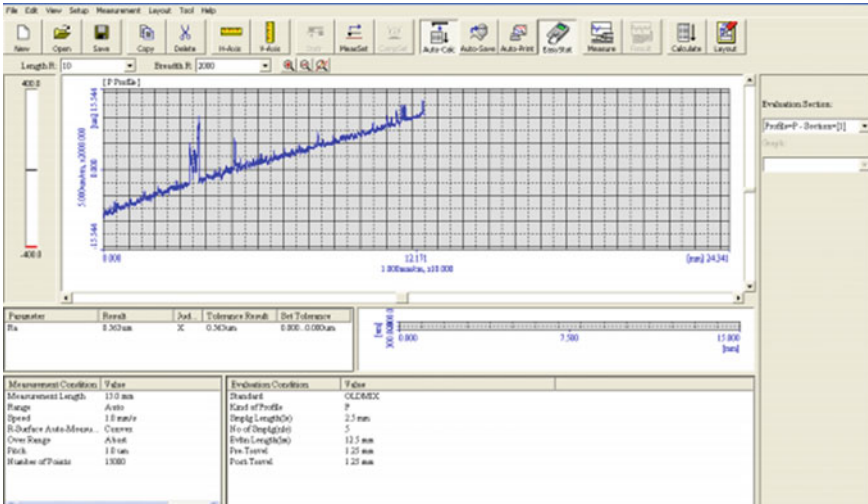


Fig. 18.6 Reading of surface roughness engine block

### 18.3.2 Block Diagram of CNC Milling Cutting

Figure 18.7 shows block diagram CNC milling proceeds from the beginning before cutting starts. First, one needs to set up the specimen into the CNC milling machine, then turn on the machine using edge finder to set X and Y-axis to zero, as shown in Fig. 18.8. Next, key in the radius, feed, rpm, and depth of cut into circular pocket coding. Lastly, in Figs. 18.9 and 18.10 show cutting process start of CNC milling machine for cutting the engine block.

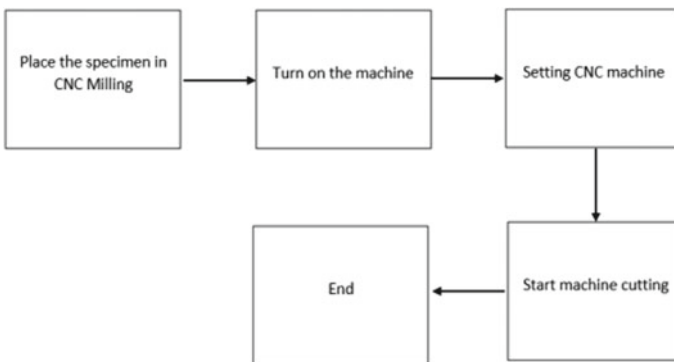
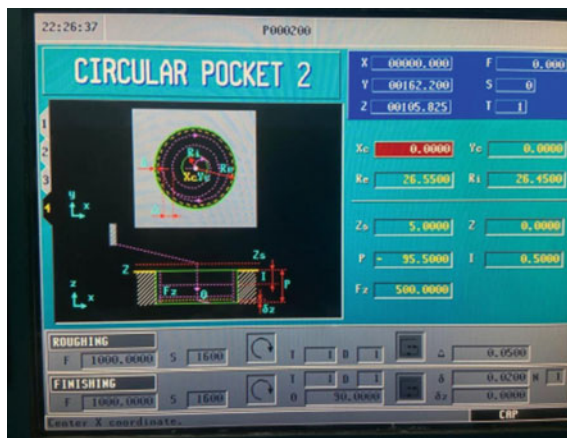


Fig. 18.7 Block diagram of the CNC milling process



**Fig. 18.8** Set up specimens and set all axes to zero



**Fig. 18.9** Coding CNC milling circular pocket 2

## 18.4 Results

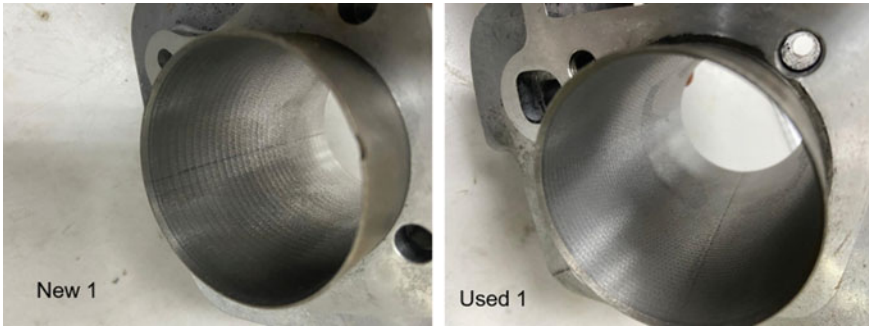
Figure 18.11 shows the surface roughness after first cutting and details are shown in Table 18.2.

Figure 18.12 shows the surface roughness result after second cutting with details shown in Table 18.3.

Tables 18.4 and 18.5 show the reading of the tested surface roughness from the original product until the second cutting of the tested surface roughness. As a result, it can be concluded that the original version has still the best surface roughness after doing some cutting on the surface of the engine block. For the depth of cut it makes a huge effect on the surface roughness as can be seen in the result of the first cutting of the engine block as it is rougher compared to the used, the depth of cut for first cutting engine block new is 3 mm and for used it is 1.5 mm. The surface becomes smoother after the second cutting. The details more smoother than the previous cutting, the details show that RPM and feed have been increased and the depth of cut decreased



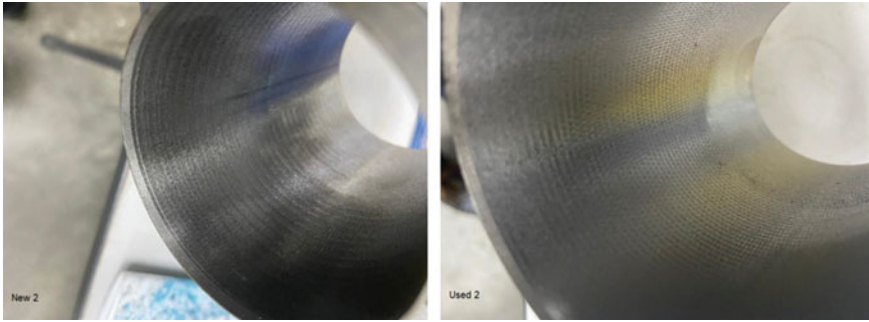
**Fig. 18.10** Starting the cutting



**Fig. 18.11** First cutting result

**Table 18.2** Detail of cutting

Type of engine block	New	Used
Cutting tool	Carbide insert thread turning	Carbide insert thread turning
Time taken	25 minutes	18 minutes
Rpm	800	800
Feed X, Y and Z	500	500
Radius	0.05mm	0.05mm
Depth of cut	3mm	1.5mm
Tool diameter	25mm	25mm



**Fig. 18.12** Second cutting result

**Table 18.3** Details of second cutting

Type of engine block	New	Used
Cutting tool	Carbide insert thread turning	Carbide insert thread turning
Time taken	28 minutes	70 minutes
Rpm	1600	1600
Feed X, Y and Z	1000	1000
Radius	0.05mm	0.05mm
Depth of cut	0.5mm	0.5mm
Tool diameter	25mm	25mm

**Table 18.4** Reading for new engine block

New Engine Block EX-5 Dream 53mm				Average (Ra)
Process	Reading 1 (Ra)	Reading 2 (Ra)	Reading 3 (Ra)	
Original	1.158	1.124	1.096	1.126
First cutting	5.460	5.573	4.627	5.22
Second cutting	4.939	4.618	4.697	4.7513

**Table 18.5** Reading for used engine block

Used Engine Block EX-5 Dream 53mm				Average (Ra)
Process	Reading 1 (Ra)	Reading 2 (Ra)	Reading 3 (Ra)	
Original	0.563	0.854	0.535	0.651
First cutting	2.617	2.302	2.424	2.448
Second cutting	1.017	1.101	1.079	1.0939

and this shows that this is more effective as the details in Table 18.3 indicate in regards a smooth surface.

## 18.5 Conclusion

The objective of output 1 which is to conduct the experiment to determine the surface roughness engine block has been achieved. The value of cutting speed, speed rate, and tool diameter of CNC milling process does affect the surface roughness results. It can be concluded that higher the cutting speed, the lower the surface roughness value. Meanwhile, the higher the speed rate value, the lower the roughness value. The statistical analysis data can be obtained by using RSM and Minitab to complete this project.

## References

1. Access O (2015) Using MINITAB software for teaching measurement uncertainty Using MINITAB software for teaching measurement. <https://doi.org/10.1088/1742-6596/588/1/012025>
2. Bulaha N, Rudzitis J, Lungevics J, Linins O, Krizbergs J (2017) Research of surface roughness anisotropy. *Latv J Phys Tech Sci* 54(2):46–54. <https://doi.org/10.1515/lpts-2017-0012>
3. Dimkovski Z (2006) Characterization of a cylinder liner surface by roughness parameters analysis. *Mech Eng*
4. Dos Santos Filho D (2013) An approach of the engine cylinder block materialx. *SAE Tech Papers* 13:1–10. <https://doi.org/10.4271/2013-36-0113>
5. Gaja H (2011) Analysis and modeling of depth-of-cut during end milling of deposited material
6. Nair Sarath R, Maharnwar AS, Dhananjay D (2016). Significance of aluminium alloys in automobile engine components 7(2)
7. Nwe SS, Yee MM, Cho A (2019) Teaching data analysis using SPSS. 3(5):1752–1755
8. Yüksel A (2009) Utilization of response surface methodology in optimization of extraction of optimization of plant materials. <https://doi.org/10.5772/intechopen.73690>

# Chapter 19

## Contamination Control on Hydraulic Oil Excavator Using an Off-Board Filtering System—Case Study



**Iwan Susanto, Muhammad Al-Hapis Abdul Razak, Azmi Hassan, Surya Atmadyaya, Tumianto, Mohd Shahrizan Yusoff, and Krishnan Subramaniam**

**Abstract** This experiment to identify the contamination control with hydraulic oil used a 250 ton Hitachi hydraulic excavator, which is commonly used in coal mining operations. The aim is to analyze the effectiveness of an off-board filtering system to reduce the particles contaminant PC06 and PC14 in hydraulic oil. The experiment shows the additional flushing activity to clean the hydraulic oil using an off-board. The tool could reduce the particle contaminants in hydraulic oil compared to the normal operating condition. The hydraulic oil is generally filtered by a hydraulic system filter compartment attached to the system itself (on-board at the machine). The signal to noise ratio (SNR) value of the filter factor reaches an optimum when using the off-board with a  $4 \times 10 \mu\text{m}$  filter compared to the standard filtering by machine operation. At the time factor, it comes optimal at level 1 (Time 1000) so that

---

I. Susanto · M. A.-H. Abdul Razak (✉) · S. Atmadyaya · Tumianto · M. S. Yusoff  
Manufacturing Section, Universiti Kuala Lumpur Malaysian Spanish Institute, Kulim Hi-Tech Park, 09000 Kulim, Kedah, Malaysia  
e-mail: [alhapis@unikl.edu.my](mailto:alhapis@unikl.edu.my)

I. Susanto  
e-mail: [iwan.susanto@s.unikl.edu.my](mailto:iwan.susanto@s.unikl.edu.my)

S. Atmadyaya  
e-mail: [atmadyaya.surya@s.unikl.edu.my](mailto:atmadyaya.surya@s.unikl.edu.my)

Tumianto  
e-mail: [tumianto@s.unikl.edu.my](mailto:tumianto@s.unikl.edu.my)

M. S. Yusoff  
e-mail: [mshahrizan@unikl.edu.my](mailto:mshahrizan@unikl.edu.my)

A. Hassan  
Electrical, Electronics and Automation Section, Universiti Kuala Lumpur Malaysian Spanish Institute, Kulim Hi-Tech Park, 09000 Kulim, Kedah, Malaysia  
e-mail: [azmi.hassan@unikl.edu.my](mailto:azmi.hassan@unikl.edu.my)

K. Subramaniam  
Mechanical Engineering Department, School of Engineering, Manipal International University, Putra Nilai, 71800 Nilai, Malaysia  
e-mail: [krishnan.subramaniam@miu.edu.my](mailto:krishnan.subramaniam@miu.edu.my)

the combination of filter and time can optimize the critical parameters PC06, PC14, and V100 in hydraulic oil.

**Keywords** Hydraulic · Oil · Contamination · Control · Filter · Maintenance · Excavator · ISO CODE · Particle

## 19.1 Introduction

Hydraulic oil is one of the important things in hydraulic systems operation. If there is less attention to hydraulic oil, then it will quickly decrease the quality. Degradation and contamination are some of the factors causing the decline in the quality of the oil. Excessive degradation and contamination will affect the durability (in overall hydraulic components life). Degradation and contamination is a common condition and harmful for hydraulic systems.

The attention to repair and maintenance strategy is to keep changing over time. In the early days of production, the maintenance method was to “fix the issue after it has a problem.” This type of maintenance is called a corrective maintenance repair approach [1].

Maintenance costs can be an important part of the organization’s profit. In practice, maintenance costs can take up 2–10% of corporate revenue and reach 24% in the transport industry. Modern management considers maintenance a key component in achieving the production process and high-quality products while maintaining the necessary equipment and reliability of machinery as required in modern times. Automation, simple and flexible production processes, “lean production” and “just-in-time” operation [2].

Oil (fluid) in a hydraulic system functions as a medium to transfer energy. Mineral oil is a type of liquid fluid commonly used. The basic principle of hydraulics is a simple liquid fluid, and the substance property of a liquid does not have a fixed form but always adjusts the shape it occupies. Because liquid nature constantly adapts to one’s shape, it will flow to multiple directions and pass in various sizes and shapes so that the liquid can transfer power and force. In other words, another hydraulic system is the displacement system and controlling force and movement with liquid fluid, in this case, oil. The fluid used in hydraulic systems is oil. Requirements for the hydraulic fluids used must have sufficient viscosity, a good viscosity index, fireproof, non-foaming, cold-resistant, resistant to corrosion and wear-resistant, and cannot be compressed.

Referring to Singh et al. [3], in hydraulic oil contamination, the previous study proved that the oil could cause wear and tear on parts of the hydraulic system. That study analyzed that about 70% of hydraulic system failures are caused by not cleaning oil. A detailed analysis reveals that the leading cause of damage to pumps, valves, and actuators is contamination. Contamination that occurs in the system can damage the components’ surface or stop the movement of moving parts, causing system damage. Another study by Marko Orošnjak et al. [4] regarding the hydraulic contamination

control in condition-based maintenance systems stated that there would be three fundamental steps of CBM related to contamination in hydraulic systems. The first is data acquisition, the second is data processing, and the last one is decision making to decide necessary actions to prevent failure in the future. That is why contamination control for hydraulic oil in a machine is crucial.

The cleanliness of hydraulic oil affects the system performance in general, such as the cylinder's response, the inner parts of the components, impact on movement and pressure, component stability, environmental impact, energy loss caused by the effects of the oil contamination. The effect of lack of hydraulic power for working or, in some cases, to avoid unnecessary breakdown, a proper maintenance strategy must be implemented to meet the machine's requirements [4]. Oil monitoring and schedule oil sampling play an important role in ensuring that the equipment can be operated optimally without disruption from oil-related issues, especially in hydraulic systems. The maintenance team and engineers should understand equipment performance, cycles, cleanliness and contamination controls, operating environment, operating system temperature, and oil characteristics to predict and evaluate the process. The reason is that oil contamination can destroy the mechanism in many ways.

A study was carried out in the past to measure contamination particles' level of hydraulic oil in the system while the machine is operating (on-board system), Ng et al. [5]. This experimental process aims to analyze the correlation of filtering size and oil operating hour effect in reducing contaminants in hydraulic oil at acceptable level parameters as equipment manufacturing recommendation by using a developed off-board filtering system, instead of on-board with particle counters.

Contamination in the hydraulic system will harm the performance and service life of the hydraulic equipment; it can cause system failures, which include:

- a. Deterioration in performance: this is due to the interaction between contaminant particles that can damage the two moving surfaces, causing aeration, abrasive wear, and corrosion.
- b. Intermittent: temporary resistance caused by contaminants that occur in the poppet movement or valve spool, which functions to open and close the systems' oil flow.
- c. Severe damage that occurs due to the presence of a few large particles or a large number of small particles causing a jamming of moving parts.

Once hydraulic oil is contaminated with pollutants either from inside or outside the system, this can cause a system failure. In general, there are three primary sources of contaminants in a hydraulic system.

- a. Internal contaminants, which can come from manufacturing, assembling, and testing hydraulic components.
- b. External contamination often occurs due to inadequate system sealing or inadequate filtration of the oil reservoir air caps. Machines used in the mining industry tend to have high silicon levels, dirt, and water in the hydraulic system. Contamination can also occur during maintenance, especially when refilling hydraulic oil if environmental contamination is not considered.

- c. The resulting contamination, also known as abrasion, is caused by contact with hydraulic components during use and cannot always be avoided [5].

Fluid cleanliness can be measured by taking fluid samples from various machine compartments. Particle counters typically measure particle contaminants (PC). The number of particles in fluids is expressed in “ISO (International Organization for Standardization)” ratings. This standard classifies fluid cleanliness by the number and size of particles in 1 ml of fluid. It measures the particle size in  $\mu\text{m}$  (microns) and reports the resulting count in three code ranges X, Y & Z. The three code range defines the size and distribution of particles in 1 ml of fluid:

- a. The first code range, X, represents the number of particles equal to or larger than  $4\ \mu\text{m}$  per milliliter of fluid. This is commonly identified as PC04.
- b. The second code range, Y, represents the number of particles equal to or larger than  $6\ \mu\text{m}$  per milliliter of fluid. This is commonly identified as PC06
- c. The third code range, Z, represents the number of particles equal to or larger than  $14\ \mu\text{m}$  per milliliter of fluid [6]. This is commonly identified as PC14.

The three code range follows “ISO 4406” definitions and is used for liquid fuels such as diesel and gasoline. For example, the two code systems, “ISO -/16/13,” are used for specific lubricant systems. In the two code system, the first number is the number of particles equal to or larger than  $4\ \mu\text{m}$  per milliliter of fluid. This number is not required and may be represented by a dash (-). The second number (Y) and the third number (Z) follow “ISO 4406” definitions [6].

For hydraulic oil in this study, the Y and Z codes were represented by.

- a. PC06 represents the number of particles equal to or larger than  $6\ \mu\text{m}$  per milliliter of fluid with the standard specification limit, which is  $<2500$  particle count (ISO Code 18).
- b. PC14 represents the number of particles equal to or larger than  $14\ \mu\text{m}$  per milliliter of fluid with a standard specification limit, which is  $<320$  particle count (ISO code 15).

Other than oil contamination, the oil’s viscosity also has an important role in ensuring that the hydraulic system is working properly. Viscosity is a temperature-dependent characteristic of lubricants that describes how the oil will flow. Viscosity is usually measured at 100 degrees Celsius (V100). At high operating temperatures, a lubricant must be able to maintain an appropriate film thickness. If the viscosity becomes too low, wear will occur within the compartment. If viscosity is too high, the oil will not flow to areas needing lubrication.

Taguchi is used for reviewing and analyzing the experiment. Taguchi’s approach involves reducing operational variables with a robust experimental design. Taguchi’s experimental technique includes the use of orthogonal groups to organize the phases that affect the process and the conditions in which they should differ [3]. This method uses orthogonal arrays that use a small number of experiments to extract the complete information about functional components. These test products are generally selected based on trade between the price (time or materials) of the test and the accuracy of the results [7].



Taguchi's method allows for the analysis of different phases without much higher experiments. For example, a process of 8 factors, each with three levels, would require 6561 ( $3^8$ ) trials to test all parameters. However, only 18 experiments are needed using Taguchi orthogonal arrays, or less than 3% of the original experiments. In this way, it allows for identifying critical conditions that significantly impact the quality of the process so that further tests can be performed and invalid conditions can be ignored [8].

## 19.2 Methodologies

Methodologies on the research will be described as follow.

### 19.2.1 Data Collection Method

This research is taken from the context of hydraulic oil inspection to maintain mining equipment at a coal mine in Indonesia. The number of samples is taken from four excavators, 250 tons of Hitachi, where each of them used four samples of hydraulic oil reports from SOS's laboratory to be analyzed.

### 19.2.2 Data Analysis

The variables used in the analysis consisted of two types of variables, namely the response variable and the independent variable. The response variable used is a variable that indicates the quality of the oil. In this case, three response variables were chosen, namely:

- a. PC06, with the normal specification limit, is  $<2500$ , where smaller is better characters.
- b. PC14, with a normal specification limit, is  $<320$ , where smaller is better characters.

The signal to noise ratio (SNR) of the two above variables (PC06 and PC14) will be measured as follow;

Smaller is the better characteristic

$$SNR: -10 \log \frac{1}{n} \left( \sum y^2 \right) \quad (19.1)$$

- c. V100, with normal specifications  $>7$ , so it has larger is better characters.  
The signal to noise ratio (SNR) of V100 variables will be measured as follow:  
Larger is the better characteristic

**Table 19.1** Factors and levels used

Level	Filter set	Time interval (Hrs)
1	With no off-board	1000
2	Filter set A	2000

$$SNR: -10\log\frac{1}{n}\left(\sum\frac{1}{y^2}\right) \tag{19.2}$$

$n$  is the sample observed

$y_1, y_2, \dots$  is the data results

While the independent variables in this analysis are the variables used to optimize the quality of oil, and each has two levels, namely:

- a. The filter consists of the level filter set A (4 × 10 m filters) and no filter set, meaning that no off-board facility is used.
- b. Time interval, which consists of levels 1000 (interval hour) and 2000 (interval hour).

Table 19.1 summarizes the factors and levels used.

Based on the available data, this analysis uses four data for each combination of factor levels, filter and time interval. The data are taken from the first time the oil is used (after the oil is changed) until it is replaced again. Four data were taken because there were four data, which made it possible to have the same number of replications for each level combination. Data are presented in Table 19.2.

### 19.3 Discussion

Results of the experimental analysis of particles contamination using the off-board filtering system are as follow.

#### 19.3.1 Taguchi Analysis of PC06 Response

##### 19.3.1.1 Orthogonal Array on PC06 Response

The analysis used two factors that are thought to influence the response (PC06), namely filter (X1) and hour (X2), where each factor has two levels. This analysis used an orthogonal array of 4 experiments with four repetitions for each experiment (a combination of factors on each level). The orthogonal arrangement design, as follows:  $x = \text{experiment} = 4$ ,  $n = \text{sample observed} = 4$ ,  $a = \text{factor level X1} = 2$ ,  $b = \text{factor level X2} = 2$ .

**Table 19.2** Experimental data from hydraulic scheduled oil sampling analysis

Machine ID	Oil code	Filter set	Time interval (Hrs)	Sample 1	Sample 2	Sample 3	Sample 4
EX57	PC06	With No Off Board	1000	2887	3517	4221	2819
EX54	PC06	With No Off Board	2000	4226	4807	4793	3969
EX78	PC06	Filter Set A	1000	3414	3203	3089	2313
EX55	PC06	Filter Set A	2000	4836	3557	3989	2167
EX57	PC14	With No Off Board	1000	275	267	260	302
EX54	PC14	With No Off Board	2000	347	446	467	508
EX78	PC14	Filter Set A	1000	228	301	290	227
EX55	PC14	Filter Set A	2000	326	317	294	342
EX57	V100	With No Off Board	1000	7.36	7.24	7.27	7.31
EX54	V100	With No Off Board	2000	7.33	7.22	7.31	7.26
EX78	V100	Filter Set A	1000	7.36	7.34	7.47	7.64
EX55	V100	Filter Set A	2000	7.33	7.49	7.38	7.37

**Table 19.3** SNR on PC06 response

No	Set filter	Time interval (Hrs)	Y Bar	S/R ratio for PC06
	(X1)	(X2)		
1	N	1000	3361.000	70.651
2	N	2000	4448.750	72.994
3	A	1000	3004.750	69.639
4	A	2000	3637.250	71.511
Average			3612.938	71.199

**19.3.1.2 Signal to Noise Ratio (SNR) on PC06 Response**

SNR measures the level of performance and also the obscurity of the output quality characteristics. The higher the performance as measured by the higher SNR is the same as, the smaller the loss. The PC06 response is presented in Table 19.3.

**19.3.1.3 ANOVA on PC06 Response**

The results of the ANOVA analysis can be explained as shown in Table 19.4.

**Table 19.4** ANOVA on PC06 response

CF	DOF	SS	V	F ratio	F (0.95;dof1;dof2)	P value	%C
X1	1	1,363,640.063	1,363,640.063	2.627	4.747	0.131	12.673
X2	1	2,959,260.063	2,959,260.063	5.700	4.747	0.034	27.501
X1*X2	1	207,252.563	207,252.563	0.399	4.747	0.539	1.926
ERROR	12	6,230,214.250	519,184.521				
TOTAL	15	10,760,366.938					

**Table 19.5** Response SNR on PC06

Level	X1	X2
1	71.82	70.14
2	70.57	72.25
Delta	1.25	2.11
Optimal	2	1
Rank	2	1

**19.3.1.4 Large Factor Contributions**

The proportion of each factor’s contribution to the response: The filter factor affects 12.673% on PC06. The time factor has an impact of 27.501% on PC06. The filter interaction factor and time have an impact of 1.926% on PC06.

**19.3.1.5 Response SNR on PC06**

The effect table calculation is by calculating the SNR average value at each level of each corresponding factor, see Table 19.5.

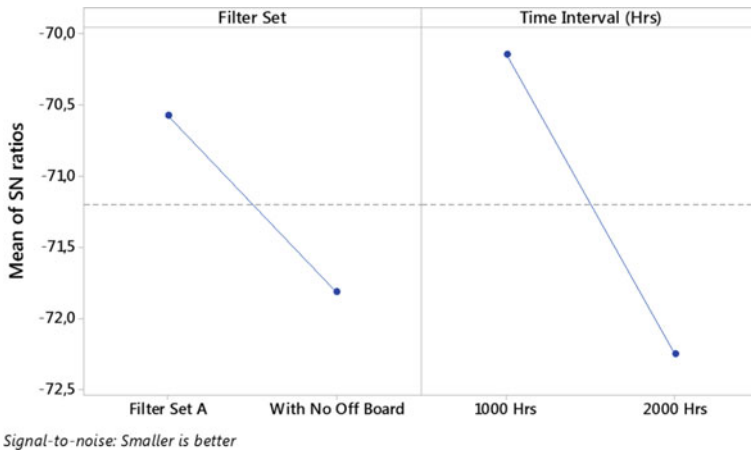
The design that produces the best SNR value is the design with filter A (level 2) and 1000 h (level 1). The graphs of the average SNR of PC06 are shown in Fig. 19.1.

The SNR value on the filter factor reaches its optimum at level 2 (Filter A). At the time factor, it becomes optimal at level 1 (1000 h) so that the combination of filter and time can optimize (minimize) the PC06 content in the oil by using filter A and 1000 h.

**19.3.1.6 PC06 and SNR Predictions**

The prediction value of PC06 in oil is carried out if the optimal design is used with filter A for 1000 h. The prediction results are as follows:

$$\hat{y} = \overline{X1}_a + \overline{X2}_{1000} - \bar{y}_{..} = 2891 \tag{19.3}$$



**Fig. 19.1** Average SNR response on PC06

The average PC06 oil content is 2891.

### 19.3.2 Taguchi Analysis of PC14 Response

#### 19.3.2.1 Orthogonal Array on PC14 Response

The analysis used two factors that are thought to influence the response (PC014), namely filter (X1) and hour (X2), where each factor has two levels. This analysis used an orthogonal array of 4 experiments with four repetitions for each experiment (combining factors on each level). The orthogonal arrangement design,  $x = \text{experiment} = 4$ ,  $n = \text{sample observed} = 4$ ,  $a = \text{factor level X1} = 2$ ,  $b = \text{factor level X2} = 2$ .

#### 19.3.2.2 Signal to Noise Ratio (SNR) on PC14 Response

SNR measures the level of performance, and it is presented in Table 19.6.

#### 19.3.2.3 ANOVA on PC14 Response

The results of the ANOVA PC14 analysis can be explained as shown in Table 19.7.

**Table 19.6** SNR on PC14 response

No	Set filter	Time interval (Hrs)	Y Bar	S/R ratio for PC14
	(X1)	(X2)		
1	N	1000	276.000	-48.833
2	N	2000	442.000	-52.986
3	A	1000	261.500	-48.423
4	A	2000	319.750	-50.109
Average			324.813	-50.088

**Table 19.7** ANOVA on PC14 response

CF	DOF	SS	V	F ratio	F(0.95;dof1;dof2)	P-Value	%C
X1	1	18,700.563	18,700.563	10.724	4.747	0.007	18.420
X2	1	50,288.063	50,288.063	28.838	4.747	0.000	49.533
X1*X2	1	11,610.063	11,610.063	6.658	4.747	0.024	11.436
ERROR	12	20,925.750	1743.813				
TOTAL	15	101,524.438					

**19.3.2.4 Large Factor Contributions**

The proportion of each factor’s contribution to the response: filter factor has an effect of 18.420% on PC14. The time factor has an impact of 49.533% on PC14. The filter interaction factor and time have an effect of 11.436% on PC14.

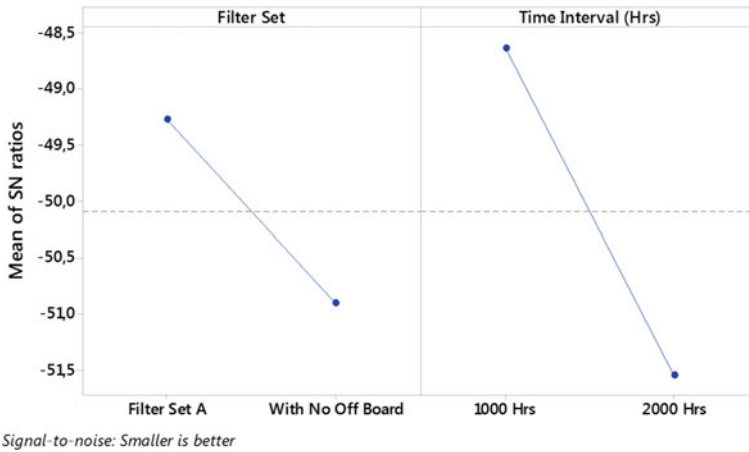
**19.3.2.5 Response SNR on PC14**

The effect table calculation is by calculating the SNR average value at each level of each corresponding factor as shown in Table 19.8.

The design that produces the best SNR value is the design with filter A (level 2) and 1000 h (level 1), as shown in the graphs of the average SNR of PC14 in Fig. 19.2.

**Table 19.8** Response SNR on PC14

Level	X1	X2
1	50.91	48.63
2	49.27	51.55
Delta	1.643	2.919
Optimal	2	1
Rank	2	1



**Fig. 19.2** Average SNR response on PC14

The best SNR value is the design with filter A (level 2) and 1000 h (level 1) so that the combination of filter and time can optimize (minimize) the PC14 content in the oil by using filter A and a time of 1000 h.

**19.3.2.6 PC14 and SNR Predictions**

Furthermore, the prediction of the value of PC14 in oil will be carried out if the optimal design is used, namely, filter B with 1000 h.

$$\hat{y} = \overline{X1}_a + \overline{X2}_{1000} - \overline{y}_{..} = 235 \tag{19.4}$$

The average of PC14 in the oil is 235.

**19.3.3 Taguchi Analysis of V100 Response**

**19.3.3.1 Orthogonal Array on V100 Response**

The analysis used two factors that are thought to influence the response (V100), namely filter (X1) and hour (X2). Each factor has two levels. This analysis used an orthogonal array of 4 experiments with four repetitions for each experiment (a combination of factors on each level). The orthogonal arrangement design, x = experiment = 4, n = sample observed = 4, a = factor level X1 = 2, b = factor level X2 = 2.

**Table 19.9** SNR on V100 response

No	Set Filter	Time Interval (Hrs)	Y Bar	S/R Ratio for V100
	(X1)	(X2)		
1	N	1000	7.295	17.260
2	N	2000	7.280	17.242
3	A	1000	7.453	17.443
4	A	2000	7.393	17.375
Average			7.355	17.330

**Table 19.10** ANOVA on V100 response

CF	DOF	SS	V	F ratio	F(0.95;dof1;dof2)	P-Value	%C
X1	1	0.073	0.073	10.143	4.747	0.008	43.705
X2	1	0.006	0.006	0.783	4.747	0.394	3.372
X1*X2	1	0.002	0.002	0.282	4.747	0.605	1.214
ERROR	12	0.086	0.007				
Total	15	0.167					

**19.3.3.2 Signal to Noise Ratio (SNR) on V100 Response**

The higher the performance as measured by the higher SNR is the same as, the smaller the loss. SNR measures the level of performance, and it is presented in Table 19.9.

**19.3.3.3 ANOVA on V100 Response**

The results of the ANOVA V100 analysis can be explained as shown in Table 19.10.

**19.3.3.4 Large Factor Contributions**

The proportion of each factor’s contribution to the response: filter factor has an effect of 43.705% on V100. The time factor has an effect of 3.372% on V100. The filter interaction factor and time have an impact of 1.214% on V100.

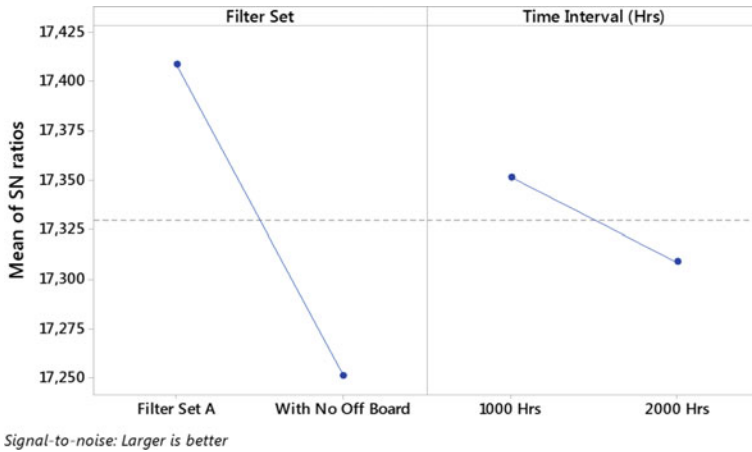
**19.3.3.5 Response SNR on V100**

The effect table calculation is by calculating the SNR average value at each level of each corresponding factor, see Table 19.11.



**Table 19.11** Response SNR on V100

Level	X1	X2
1	17.25	17.35
2	17.41	17.31
Delta	0.158	0.043
Optimal	2	1
Rank	1	2



**Fig. 19.3** Average SNR response on V100

The design that produces the best SNR value is the design with filter A (level 2) and 1000 h (level 1), as shown in Fig. 19.3.

The SNR value on the filter factor reaches optimal at level 2 (Filter A). At the time factor, it becomes optimal at level 1 (Time 1000) so that the combination of filter and time that can optimize (minimize) the V100 content in the oil by using filter A and time 1000 h.

**19.3.3.6 and SNR Predictions**

The prediction of the value of V100 in oil is carried out if the optimal design is used, namely, filter A in 1000 h. The prediction results are as follows:

$$\hat{y} = \overline{X1}_a + \overline{X2}_{1000} - \bar{y}_{..} = 7.44 \tag{19.5}$$

The average V100 content in the oil is 7.44.

## 19.4 Conclusions

The SNR value on the filter factor reaches its optimum at level 2 (Filter A). At the time factor, it becomes optimal at level 1 (1000 h) so that the combination of filter and time can optimize (minimize) the PC06 content in the oil by using filter A and 1000 h. The filter factor has an effect of 12.673% on PC06. The time factor has an impact of 27,501% on PC06. The filter interaction factor and time have an impact of 1.926% on PC06.

The filter factor has an effect of 18.420% on PC14. The time factor has an impact of 49.533% on PC14. The filter interaction factor and time have an effect of 11.436% on PC14. The best SNR value is the design with filter A (level 2) and 1000 h (level 1) so that the combination of filter and time that can optimize (minimize) the PC14 content in the oil by using filter A and a time of 1000 h.

The SNR value on the filter factor reaches its optimum at level 2 (Filter A). At the time factor, it becomes optimal at level 1 (Time 1000) so that the combination of filter and time can optimize the V100 content in the oil by using filter A and time 1000 h. The proportion of each factor's contribution to the response: The filter factor has an effect of 43.705% on V100. The time factor has an effect of 3.372% on V100. The filter interaction

The experiment showed that the additional flushing activity to clean hydraulic oil using an off-board system could reduce particle contaminant in hydraulic oil compared to the normal operating condition. The hydraulic oil is typically filtered by a combination of hydraulic system filter compartments attached to the system itself (on-board at the machine).

A further experiment is worth being carried out to identify the effect of different filter size ratings on an off-board filtering system, including a filter set that can control particle contaminants better.

## References

1. Ayo-Imoru RM, Cilliers AC (2018) A survey of the state of condition-based maintenance (CBM) in the nuclear power industry. *Ann Nucl Energy* 112:177–188
2. Ben-Daya M, Duffuaa SO (2009) Handbook of maintenance management and engineering
3. Singh M, Lathkar GS, Basu SK (2012) Failure prevention of hydraulic system based on oil contamination. *J Inst Eng (India): Series C*. **93**(3):269–274
4. Marko Orošnjak TP, Jocanović M, Karanović V, Horvatić Novak A (2017) Using contamination control in condition based maintenance of a hydraulic system
5. Ng F, Harding JA, Glass J (2017) Improving hydraulic excavator performance through in line hydraulic oil contamination monitoring. *Mech Syst Signal Process* 83:176–193
6. Caterpillar (2017) Caterpillar machine fluids recommendation, pp 141–143
7. Mohsin I et al (2020) Optimization of the polishing efficiency and torque by using Taguchi method and ANOVA in robotic polishing. *Appl Sci* 10(3):824
8. Stephanie Fraley MO, Terrien B, Zalewsk J (2020) Design of experiments via taguchi methods—orthogonal arrays

# Chapter 20

## Hardware Development for Zero Crossing of a Multilevel Single Phase Rectifier Chopper for Plug-In Electric Car Battery Charger Using a PIC Microcontroller



Saharul Arof, Fathul H. Ahmad, Nurazlin M. Yaakop, Julaida A. Jalil, Philip Mawby, Hamzah Arof, and Emilia Noorsal

**Abstract** This paper focuses on developing the hardware for a controller and of a zero crossing circuit for an electric car battery charger. A novel topology of a battery charger is studied and tested. A conventional rectifier has drawbacks in terms of harmonic currents. This paper describes a five-level single-phase rectifier associated with buck chopper with a control signal which draws a clean sinusoidal line current for the application in a plug-in battery charger. The MATLAB/Simulink results reveal that the proposed battery charger performance is better compared to the conventional method.

---

S. Arof (✉) · F. H. Ahmad · N. M. Yaakop · J. A. Jalil  
Universiti Kuala Lumpur, Malaysian Spanish Institute Kulim Hi-Tech Park, 09000 Kulim, Kedah, Malaysia  
e-mail: [saharul@unikl.edu.my](mailto:saharul@unikl.edu.my)

F. H. Ahmad  
e-mail: [fathulhazrimy@unikl.edu.my](mailto:fathulhazrimy@unikl.edu.my)

N. M. Yaakop  
e-mail: [nurazlin@unikl.edu.my](mailto:nurazlin@unikl.edu.my)

J. A. Jalil  
e-mail: [julaida@unikl.edu.my](mailto:julaida@unikl.edu.my)

S. Arof · P. Mawby  
University of Warwick School of Engineering, Coventry CV47AL, United Kingdom  
e-mail: [p.a.mawby@warwick.ac.uk](mailto:p.a.mawby@warwick.ac.uk)

H. Arof  
Engineering Department, Universiti Malaya, Jalan Universiti, 50603 Kuala Lumpur, Malaysia  
e-mail: [ahamzah@um.edu.my](mailto:ahamzah@um.edu.my)

E. Noorsal  
School of Electrical Engineering, College of Engineering, Universiti Teknologi MARA, Cawangan Pulau Pinang, Kampus Permatang Pauh, 13500 Pulau Pinang, Malaysia  
e-mail: [emilia.noorsal@uitm.edu.my](mailto:emilia.noorsal@uitm.edu.my)

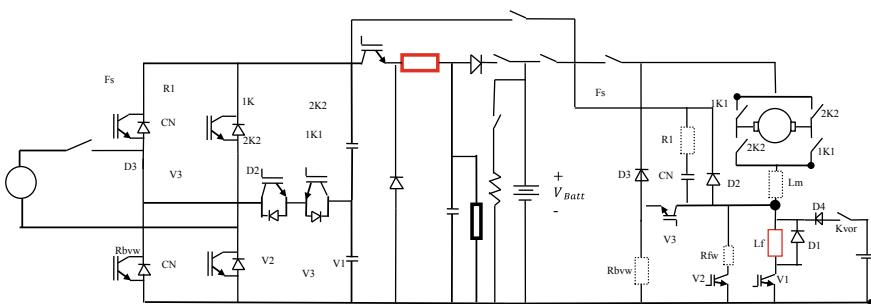
**Keywords** Multilevel inverter · Battery charger · Multilevel rectifier · Buck chopper · PWM · THD

## 20.1 Introduction

The emission of hydrocarbons does not only pollute the environment but also contributes to global warming which melts icebergs and increases the sea level. Using efficient electric vehicles (EV) and hybrid electric vehicles (HEV) for transportation is one of the solutions to reducing global hydrocarbon emissions [1]. All electric vehicles including DC drive EVs require battery charging. The charging operation happens while the EV is moving and when it is at standstill. Vehicle inertia provides a source for charging while moving, while electricity provides power when the vehicle is not moving.

## 20.2 Review Stage

Oak Research National Laboratory (ORNL) [1], United States, in 2009, successfully designed DC brushed motor with high power output (55 kW), high efficiency (92%) that can operate at low operating voltages (13 V) and this has initiated the interest in DC drive electrical vehicles. Attempts to improve the conventional bridge chopper by increasing the operations or allowing the motor reverse action have been continuously carried out but ever since the development of the new motor by the ORNL, a new series motor four quadrants DC chopper such as shown in Fig. 20.1, was designed and the proposed chopper has multiple operations [2–6]. Several other studies related to DC drive EVs led to research on EC battery chargers [7–9] and different types of DC drive motors that can be used for motor traction for DC EVs such as separately excited [10]. Detail investigations on the chopper operation modes led to the establishment of a simulation model to test the chopper operations for the application of electric car and light rail transit (LRT) [11]. This simulation model led to further detailed



**Fig. 20.1** Integrated FQDC chopper and battery charger

investigations on each of the chopper operations and on the specific pattern of motor voltage, current, torque, speed and FQDC running for DC drive EC application have been continuously carried out [12, 13]. For DC series motor traction of EC application, the speed and torque control for the series motor, in an attempt to reduce jerk and tire slip, has been successfully done and implemented with the direct current control technique [14]. For power regeneration, the FQDC offers the generator mode with several techniques of starting the regenerated power and voltage control is studied and discussed in [15]. In order for the FQDC to be applied in real world, it needs controllers running control algorithms in the embedded system. The controller and its control algorithm are studied and tested using the processor in the loop (PIL) technique [16]. To improve the new FQDC performance, optimization tools such as artificial intelligence (AI) are introduced to control all of the chopper operations of the proposed FQDC chopper [17–20]. Among the three AI controllers, ANFIS shows the best performance followed by a neural network and the self-tuning Fuzzy logic controller. Studies on a neural network controller to uncover the proper method of tuning have been carried out based on using a single controller with binary output [21]. On each specific FQDC chopper operation mode the performance can be further improved using an AI optimization tool such as genetics algorithm to set up specific look-up tables for the field current [22, 23]. The pole placement method [24] was used to tune the close loop PID controller to improve the controller performance while fuzzy logic controller is used to control the motor current [25] and to improve the control performance and system stability. For fault diagnosis and online system tuning and optimization, a numerical representation using Taylor series [26] is studied and tried for driving mode. The cascade PID with an ascend descend algorithm and after improvisation was associated with steering [27] and vehicle movement control [28] and brake control [29] to be used for autonomous EV for automatic reverse parking.

Connection to an electric power grid allows opportunities such as ancillary services, reactive power support, tracking of output from renewable energy sources and load balance. Battery chargers generally consists of the transformer, rectifier and buck or boost chopper [30–32]. A good, efficient and reliable battery charger should be characterized by high power density, low cost, low volume and less weight [33]. The battery charger operation relies on its components, control technique and switching strategies [34]. In general, the battery charger and its control algorithm are implemented using microcontrollers, digital signal processors and integrated circuits [35].

Two critical aspects of charging batteries are the charging time and battery life. A decrease in the power factor due to an increase in the firing angle and relatively high harmonic currents are the inherent drawbacks of the conventional battery charger designs. Due to that, multilevel converters are introduced in recent years to attain high power quality, low switching losses, high voltage capability and better efficiency. H-bridge multilevel rectifier and the cascade type are the most popular. The significance of this research work is that the adopted five-level single-phase shall contribute to an improvement of the power factor as well as a reduction in the total harmonic

distortion (THD) [34–36]. Thus, a combination of multilevel and buck chopper is suitable for electric car battery charger application.

### **20.2.1 Literature on Zero Crossing**

Zero crossing is a point where the sign of a mathematical function changes from a positive to a negative value or else. In this study, the zero crossing point from negative to positive value is the only used and important. Zero cross (ZC) detection has three functions, first it is to synchronize the firing angle of the carrier signal (triangular wave signal) and reference signals. Without zero crossing the multilevel rectifier will not start at the exact point. Second, is to point to the start of the comparison process, there might be a delay or offset between both references (sine and carrier signal) at every zero cross point without it. Third, is to refresh and reload the carrier signals value at every complete cycle. The action of synchronizing the firing angle to incoming AC supply can result in better performance (efficiency, PF, THD) of MLR for the battery charger.

A zero crossing circuit has been designed using UA741, an operational amplifier, which is not affected owing to instant spikes and sags on the signals of the current or voltage. The zero crossing detector designed has been tested under various conditions and signals including 19.8% of total harmonic distortion (THD). It has been observed by the test results that the detector operates with optimum performance. The project explored techniques in developing the low voltage CMOS analog building blocks such as operational amplifiers using low voltage single supply CMOS operational amplifiers for zero cross detector application. All the designs had been done using the Tanner EDA with 0.25  $\mu\text{m}$  technology where simulation had been carried out using the SPICE simulator and layout had been made using the Tanner layout editor (Ledit). Analyses of the domestic user's energy consumption behavior under the application of the pulse width modulation and zero crossing Width Modulation and Zero Crossing detection techniques for load management has been conducted and confirmed on the successfulness.

## **20.3 Methodology**

A zero crossing circuit requires a combination of few circuits such as voltage sensor, offset circuit, amplifier circuit and a digital or analog controller that can be used. However, this study used a digital controller for better use, but in this study a digital controller is used for better control and flexibility. The voltage sensor is used to capture the AC voltage grid signal and to transform it to a lower voltage which is safe and usable for control and signal conditioning purposes. An offset circuit is to offset the transformed AC voltage to complete DC voltage so that a digital controller such as a PIC microcontroller can be used to process the signals. Without

the offset circuit, the microcontroller is unable to read the negative part of the AC signal. Finally, the amplifier is used to amplify the voltage to the desired value for the microcontroller. An offset circuit is shown in Fig. 20.2.

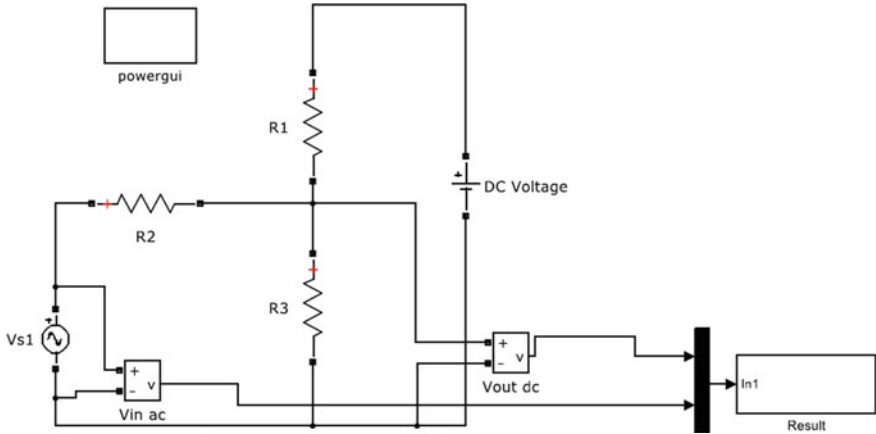


Fig. 20.2 Complete offset circuit

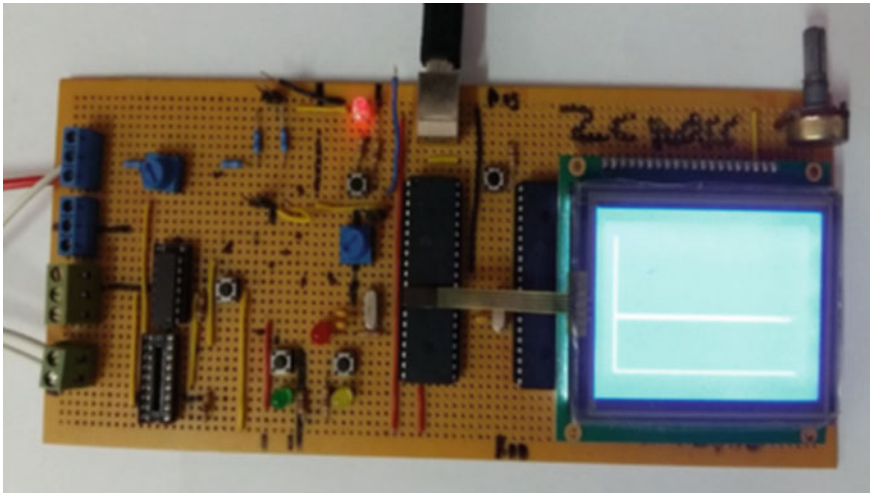
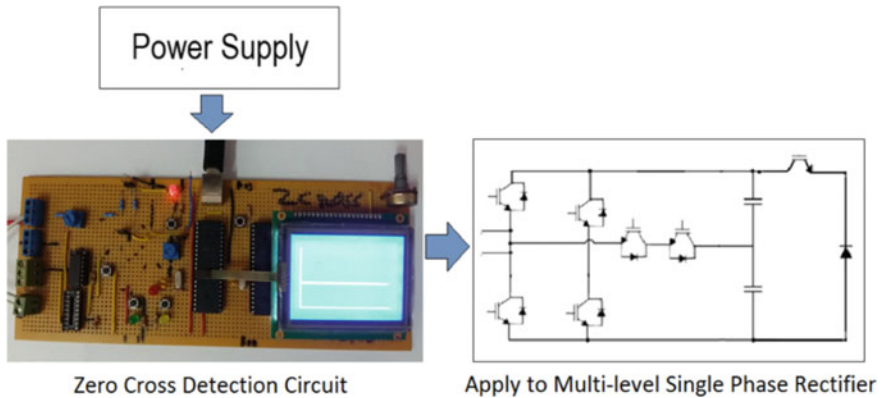


Fig. 20.3 Developed zero crossing detector hardware



**Fig. 20.4** Block diagram of zero crossing detector hardware applications

### 20.3.1 Hardware Application Circuit

Figure 20.3 shows the zero cross detection hardware circuit. The connections could be referred in Fig. 20.4, the schematic shows the connection of the hardware development it details. Two PIC microcontrollers are used. The one which is closed to the display is used to display the sine and the zero cross signal. The other one which is next to it is the one who is used to generate zero cross and to start the signal. The sine AC input from the transformer/sensor input signal is converted to DC voltage and amplify using the offset and amplify circuit. The final voltage is five volts DC. This voltage is read by the two pic microcontrollers using an analog pin at ten bits resolutions ADC pin. The ADC\_Read command is used to read this signal. From 0 to 5 V DC, the signal is converted to zero (0) to 1,024. A ready signal is set once the input signal reading is between zero and ten. Once the reading is between 500 to 512 the zero cross signal is fired.

### 20.3.2 Coding for Zero Crossing

The C Code using MikroC PRO compiler software for both of the algorithms is as below.



```

unsigned int adc_rd=0,ready=0;

void main() {
  ANSELA = 0x03;      // Configure RA1 pin as analog
  ANSELC = 0;        // Configure PORTC pins as digital
  ANSELD = 0;        // Configure PORTD pins as digital

  TRISA = 0x03;      // Set RA1 pin as input
  TRISC = 0x00;      // Set PORTC as output
  TRISD = 0x00;      // Set PORTD as output
  LATD=0;
  LATC=0;
  ADC_init();

  while (1) {  adc_rd = ADC_Read(0);
  if (ready==0){ fire=0;}
  if(adc_rd >0 && adc_rd <40) {ready=1;}
  if (ready==1 ) {
  if (adc_rd>460 && adc_rd<560) { fire=1;} }
  if (adc_rd>560 && adc_rd<660) { ready=0;} }
  //
  }
}

```

## Coding for Display

```

int cnt=0,cnt1=0;int rcheck=0,adc_rd=0,tmp=0,tmp1=0,longitude=0,latitude=0;
signed int a1=0, a2=0;
  bit ready,enable; int mtmp=0;
//Declarations-----
const code char dyana_128_64[1024];
//-----end-declarations

// Gled module connections
char GLCD_DataPort at PORTD;

void delay2S(){          // 2 seconds delay function
  Delay_ms(2000);
}

void main() {

```

```

ANSELA = 0x03;           // Configure RA1 pin as analog
TRISA = 0x03;           // Set RA1 pin as input

Glcd_Init();             // Initialize GLCD
Glcd_Fill(0x00);        // Clear GLCD
Glcd_Image(dyana_128_64);
while(1) {
  cnt=cnt+1;
  if (cnt>=40) {cnt=0;cnt1=cnt1+1;enable=~enable;}

  if (cnt1>=120) {cnt1=0;Glcd_Fill(0x00);
  Glcd_Image(dyana_128_64); }           // Draw image
  // Clear GLCD

  tmp = ADC_Read(0);
  adc_rd=tmp;
  if(adc_rd >0 && adc_rd <40) {ready=1;}
  if (ready==0) {fire=0;}
  if (ready==1 ) {
    if (adc_rd>460 && adc_rd<560) { fire=1;} }
    if (adc_rd>560 && adc_rd<660) { ready=0;}
  tmp1=tmp;
  //tmp1=tmp1*2;
  if (enable==1) {
  longitude=cnt1+7;
  latitude= 36-tmp;//20-tmp1;

  Glcd_Dot(longitude,latitude,1);      // Center dot

  if (tmp1>=0 &&tmp1 <=5) {ready=1;}
  if (ready==1 && tmp1>= 15 && tmp1<=18) {
  Glcd_Line(longitude, 49, longitude, 57, 1);

  ready=0;
  } }

```

### 20.3.3 Hardware Applications

Figure 20.4 shows the block diagram of the zero crossing detector for hardware applications. To apply the algorithms to the zero cross circuit, the program has to be downloaded into the peripheral interface controller (PIC) by using the programming compiler software. By connecting the power supply to the installed zero cross detection systems with the ready hardware multilevel single-phase rectifier, the zero cross detection system is ready to operate.

The flow chart in Fig. 20.5 shows the working operation function for the algorithm 1. At the beginning there will be two input values which are  $u$  and  $\sin$ . In case of 0, there will be decisions only if  $\sin$  is greater than 0,  $\sin$  less than 0.10,  $u$  is greater or equal to 1 and  $\text{rst}$  is equal to zero then the state will bring out the output of 1. If

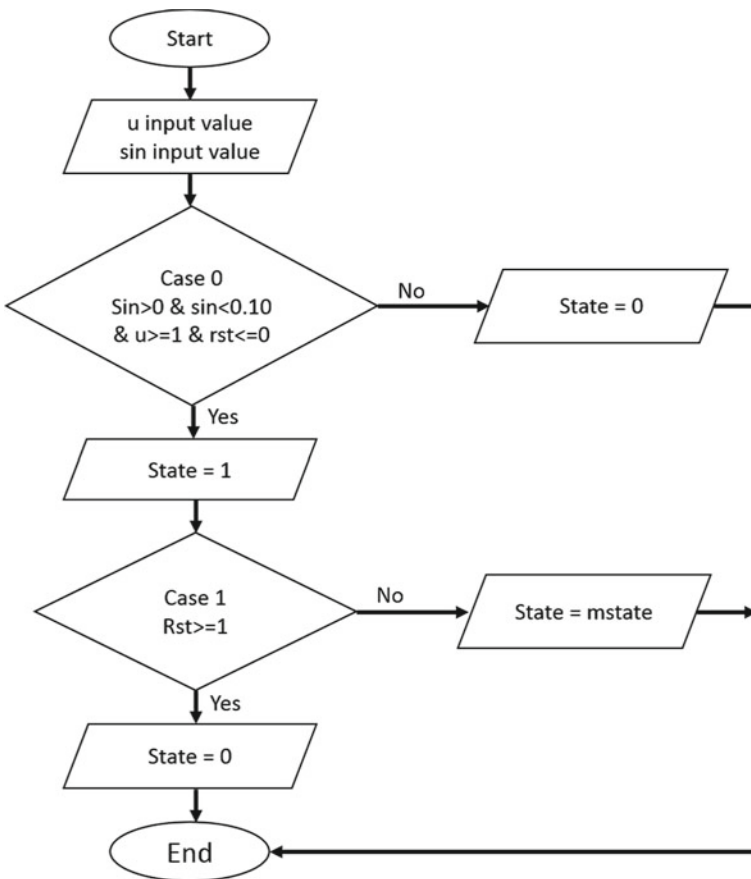


Fig. 20.5 Flow chart of function in Algorithm 1

else the state will be 0. In case of 1, if rst is greater or equal to 1 then the state output will be 0. If else, state output will be the memory state.

### 20.3.4 Algorithm 2

The flow chart in Fig. 20.6 shows the working operation for function in algorithm 2. The input for algorithm 2 is the following output from algorithm 1. So there also will be two input values which is  $u$  and  $sin$ . In case of 0, there will be decisions only if  $sin$  is greater than 0,  $sin$  less than 0.25 and  $u$  is greater or equal to 1 then the state will bring out the output of 1. If else the state will be 0. In case 1, if  $sin$  is greater than 2.5 and  $sin$  is less than 2.65 then the state output will be 2. If else, the state output

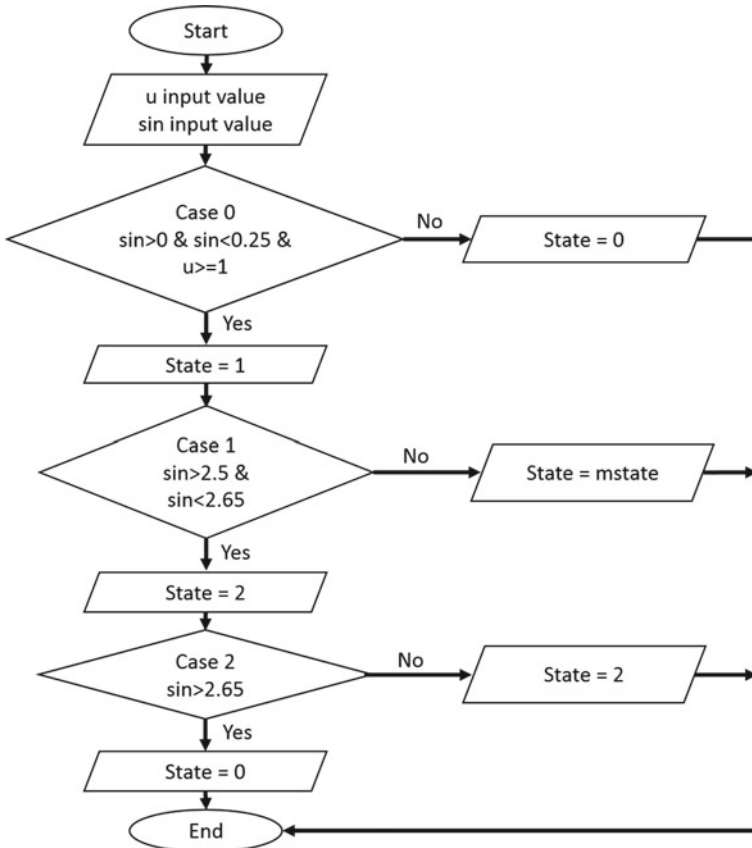


Fig. 20.6 Flow chart of functions in Algorithm 2

will be the memory state. In case 2, if  $\sin$  is greater than 2.65 then the state output will be 0. If else, the state output will bring out the output of 2.

### 20.3.5 Simulation Applications

Figure 20.7 shows the step-by-step illustration of the zero crossing detection output signals. First, the alternating current (AC) voltage if from the source grid of 240 V. Then it becomes 5 V after passing through the voltage sensor. After the voltage offset, it becomes about 2.5 V. After voltage amplification it becomes 5 V again. Next, is detecting the first reference point. After that, from the following output of reference point detection, the actual zero cross point detection will be processed. Finally, there will be the zero crossing output signal.

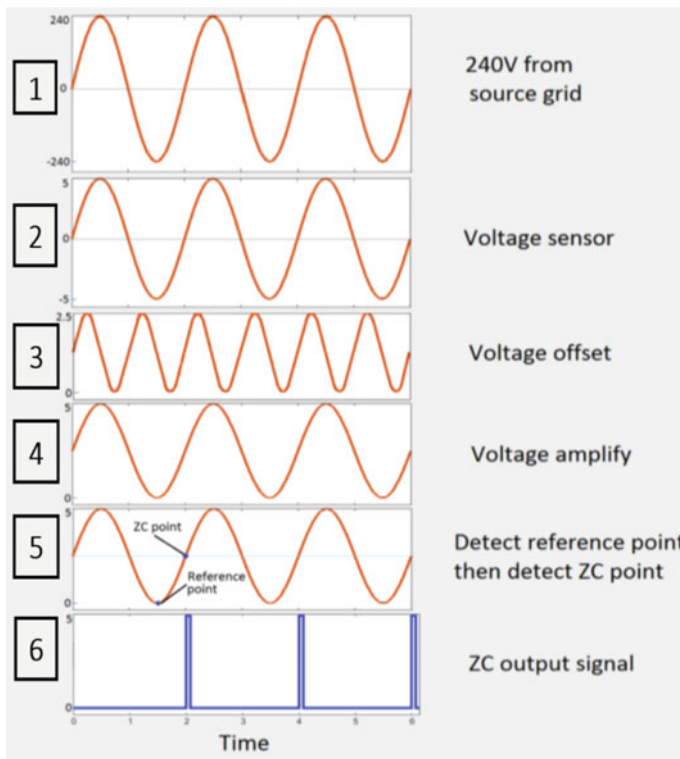


Fig. 20.7 Process of zero cross detection output signals

### 20.3.6 Hardware Development

This subtopic discusses the hardware development regarding the zero crossing circuit and the applications of the hardware.

#### 20.3.6.1 Hardware Zero Crossing Circuit

##### Offset Circuit

Figure 20.8 shows the zero crossing detector circuit which will be applied to the hardware applications. Inside the circuit, there are three resistors that come from different sides and are connected to each other at one of their terminals. It is also known as the offset circuit.

In terms of theoretical modeling, the offset or voltage divider circuit could be represented in the mathematical term [14].

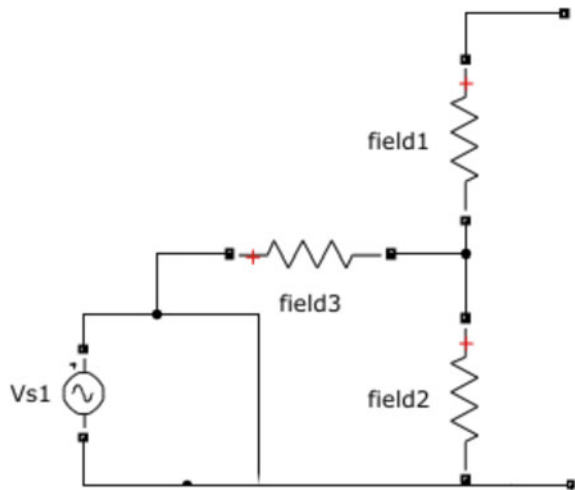
By referring to the offset circuit in Fig. 20.9 which is originally from circuit 20.2, to determine the resistors value, we consider two AC voltage limit situations, one with  $V_{IN} = -5\text{ V}$  and another one with  $V_{IN} = +5\text{ V}$ . While  $R_2$  is set at  $30\text{ k}\Omega$ .

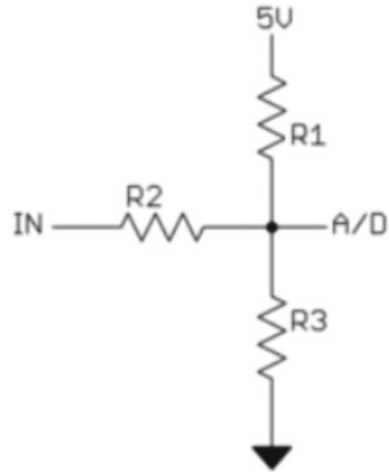
First,  $V_{IN} = 15\text{ V}$ . The ADC should then be at  $0\text{ V}$ . That means that there would not be any current through  $R_3$ , since there is no voltage difference.  $R_2$  and  $R_1$  then form a voltage divider with

$$\frac{0\text{ V} - (-5\text{ V})}{R_2} = \frac{5\text{ V} - 0\text{ V}}{R_1}$$

or

Fig. 20.8 Zero cross circuit



**Fig. 20.9** Offset circuit

$$R1 = \frac{5 \text{ V}}{5 \text{ V}} = 30 \text{ K}\Omega = 30 \text{ K}\Omega$$

Then in the second situation,  $V_{IN} = + 5.1 \text{ V}$ . The ADC should then be at  $+ 5 \text{ V}$ . That means there won't be any current through  $R1$ , since there's no voltage difference.  $R2$  and  $R3$  then form a voltage divider with

$$\frac{5.1 \text{ V} - 5 \text{ V}}{R2} = \frac{5 \text{ V} - 0 \text{ V}}{R3}$$

or

$$R3 = \frac{0.1 \text{ V}}{5 \text{ V}} = 30 \text{ K}\Omega = 600\Omega$$

$$R1 = 30 \text{ k}\Omega,$$

$$R2 = 30 \text{ k}\Omega,$$

$$R3 = 600\Omega.$$

## 20.4 Conclusion

The proposed hardware development of zero crossing circuit and the control algorithm written using MikroC PRO downloaded to PIC Microcontroller 18F46K22 is successfully tested and suitable to use in combination with MLR and Buck chopper and the combination will produce low harmonis and low THD of Plug-in home charging EV battery charger.

## References

1. Oak Ridge National Laboratory (2009) Advanced brush technology for DC motors. <http://pee.mrc.ornl.gov/projects/emdc3.jpg>
2. Arof S, Jalil JA, Yaakop NM, Mawby PA, Arof H (2014) Series motor four quadrants drive Dc chopper Part1: Overall. Int Conf Power Elect
3. Arof S, Noorsal E, Mawby PA, Arof H (2020) Series motor four quadrants drive DC Chopper for DC drive electric vehicle Part7: resistive braking. International Scientific Forum (ISF2019), Melaka, Malaysia, eISBN: 978-967-10842-1-2
4. Arof S, Noorsal E, Mawby PA, Arof H (2020) Series motor four quadrants drive DC chopper for DC drive electric vehicle Part6: regenerative braking. Int Sci Forum (ISF2019), Melaka, Malaysia, eISBN: 978-967-10842-1-2
5. Arof S, Diyanah NHN, Mawby PA, Arof Emilia Noorsal H (2021) Series motor four quadrants drive DC chopper Part3: field weakening mode. IOP Conf Series Mater Sci Eng 1127(1):012028. <https://doi.org/10.1088/1757-899X/1127/1/012028>
6. Arof S, Diyanah NHN, Mawby PA, Noorsal AE (2021) New series motor four quadrants drive DC chopper for economical EV, Part5:parallel mode. IOP Conf Series Mater Sci Eng 1127(1):012025. <https://doi.org/10.1088/1757-899X/1127/1/012025>
7. Arof S, Diyanah NH, Mawby P, Arof H, Mohd Yaakop N (2019) Low harmonics plug-in home charging electric vehicle battery charger utilizing multi-level rectifier, zero crossing and buck chopper: Part 1: general overview. In: Progress in engineering technology, pp. 103–108. <https://doi.org/10.1007/978-3-030-28505-09>
8. Arof S, Ahmad MR, Yaakop NM, Mawby P, Arof H, Noorsal E, Bakar AA, Ali YM (2021) Low harmonics plug-in home charging electric vehicle battery charger utilizing multilevel rectifier, zero crossing, and buck chopper: state of charge estimator using current integration algorithm for embedded system. Prog Eng Technol III. [https://doi.org/10.1007/978-3-030-67750-3\\_19](https://doi.org/10.1007/978-3-030-67750-3_19)
9. Arof S, Sazali MS, Noor NM, Nur Amirah J, Mawby P, Noorsal E, Bakar AA, Mohd Ali Y (2021) Low harmonics plug-in home charging electric vehicle battery charger utilizing multi-level rectifier, zero crossing, and buck chopper: BMS battery charging control algorithm. Prog Eng Technol III. [https://doi.org/10.1007/978-3-030-67750-3\\_18](https://doi.org/10.1007/978-3-030-67750-3_18)
10. Arof S, Diyanah NHN, Noor NM, Jalil JA, Mawby PA, Arof H (2019) A new four quadrants drive chopper for separately excited DC motor in low cost electric vehicle. Prog Eng 119–138. [https://doi.org/10.1007/978-3-030-28505-0\\_10](https://doi.org/10.1007/978-3-030-28505-0_10)
11. Arof S, Hassan H, Rosyidi M, Mawby PA, Arof H (2017) Implementation of series motor four quadrants drive dc chopper for DC drive electric car and LRT via simulation model. J Appl Environ Biol Sci 7(3S):73–82
12. Arof S, Noor NM, Nur Diyanah NH, Mawby P, Arof H, Noorsal E (2021) DC drive electric car utilizing series motor and four quadrants drive DC chopper parameter determination from general design requirements. Prog Eng Technol. [https://doi.org/10.1007/978-3-030-67750-3\\_17](https://doi.org/10.1007/978-3-030-67750-3_17)
13. Arof S, Noor NM, Elias F, Mawby PA, Arof H (2017) Investigation of chopper operation of series motor four quadrants DC chopper. J Appl Environ Biol Sci 7(3S):49–56
14. Arof S, Jalil JA, Kamaruddin NH, Yaakop NM, Mawby PA, Arof H (2016) Series motor four quadrants drive DC chopper Part2:driving and reverse with direct current control. Int Conf Power Elect. 978-1-5090-2547-3/16, pp 775–780. <https://doi.org/10.1109/PECON2016.7951663>
15. Arof S, Diyanah NHN, Noor NMN, Radzi Md, Jalil JA, Mawby PA, Arof H (2019) Series motor four quadrants drive DC chopper: Part 4: generator mode. Prog Eng 155–167. [https://doi.org/10.1007/978-3-030-28505-0\\_12](https://doi.org/10.1007/978-3-030-28505-0_12)
16. Arof S, Diyanah NH, Yaakop M, Mawby PA, Arof H (2019) Processor in the loop for testing series motor four quadrants drive direct current chopper for series motor driven electric car: Part1: chopper operation modes testing. In: Advanced Engineering for Processes and Technologies, pp 59–76. [https://doi.org/10.1007/978-3-030-05621-6\\_5](https://doi.org/10.1007/978-3-030-05621-6_5)



17. Arof S, Zaman MK, Jalil JA, Mawby PA, Arof H (2015) Artificial intelligence controlling chopper operation of four quadrants drive DC chopper for low cost electric vehicle. *Int J Simul Syst Sci Technol*. <https://doi.org/10.5013/IJSSST.a.16.04.03,2015>
18. Arof S, Muhd Khairulzaman AK, Jalil JA, Arof H, Mawby PA (2015) Self tuning fuzzy logic controlling chopper operation of four quadrants drive DC chopper for low cost electric vehicle. In: 6th International conference on intelligent systems, modeling and simulation, IEEE computer society, pp 40–24
19. Arof S, Faiz MR, Diyanah NHN, Yaakop NM, Mawby P, Arof H, Noorsal E (2021) Fault diagnose of DC drive EV utilizing a new series motor four quadrants DC chopper using an expert system and quadratic solver running in embedded: Part 1: during start up, progress in engineering technology III. [https://doi.org/10.1007/978-3-030-67750-3\\_15](https://doi.org/10.1007/978-3-030-67750-3_15)
20. Arof S, Diyanah NHN, Mawby PA, Arof Emilia Noorsal H (2020) DC drive electric car State of Charge (SOC) and Remaining Distance Traverse(RDT) optimized by fuzzy logic. *International Scientific Forum (ISF2019)*, Melaka, Malaysia, eISBN: 978-967-10842-1-2
21. Arof S, Diyanah NH, Mawby PA, Arof H (2019) Study on implementation of neural network controlling four quadrants direct current chopper: Part1: using single neural network controller with binary data output. In: *Advanced engineering for processes and technologies*, pp 37–57
22. Arof S, Diyanah NHN, Noor NM, Rosyidi M, Mawby PA, Arof H (2019) Genetics algorithm for setting up look up table for parallel mode of new series motor four quadrants dc chopper. *Prog Eng* 155–167. [https://doi.org/10.1007/978-3-030-28505-0\\_12](https://doi.org/10.1007/978-3-030-28505-0_12)
23. Arof S, Shauqee ARA, Rosyidi M, Diyanah NHN, Mawby P, Arof H, Noorsal E (2021) Gradient descend for setting up a look-up table of series motor four quadrants drive DC chopper in parallel mode. *Prog Eng Technol*. [https://doi.org/10.1007/978-3-030-67750-3\\_16](https://doi.org/10.1007/978-3-030-67750-3_16)
24. Arof S, Noor NM, Alias MF, Noorsal E, Mawby P, Arof H (2020) Digital Proportional Integral Derivative (PID) controller for closed-loop direct current control of an electric vehicle traction tuned using pole placement. In: *Progress in engineering technology II. Advanced structured materials*, vol 131. Springer, Cham. [https://doi.org/10.1007/978-3-030-46036-5\\_8](https://doi.org/10.1007/978-3-030-46036-5_8)
25. Arof S, Noor NM, Mohamad R, Noorsal E, Mawby PA, Arof H (2020) Close loop feedback direct current control in driving mode of a four quadrants drive direct current chopper for electric vehicle traction controlled using fuzzy logic. In: *Progress in engineering technology II. Advanced structured materials*, vol 131. Springer, Cham. [https://doi.org/10.1007/978-3-030-46036-5\\_7](https://doi.org/10.1007/978-3-030-46036-5_7)
26. Arof S, Sukiman ED, Diyanah NH, Noor NM, Noorsal E, Mawby PA, Arof H (2020) Discrete-time linear system of new series motor four-quadrant drive direct current chopper numerically represented by taylor series. In: *Progress in engineering technology II. Advanced structured materials*, vol 131. Springer, Cham. [https://doi.org/10.1007/978-3-030-46036-5\\_10](https://doi.org/10.1007/978-3-030-46036-5_10)
27. Arof S, Said S, Diyanah NHN, Noor NM, Yaakop NM, Mawby P, Arof H, Noorsal E (2020) Series motor four-quadrant direct current chopper: reverse mode, steering position control with double-circle path tracking and control for autonomous reverse parking of direct current drive electric car. In: *Progress in engineering technology II. Advanced structured materials*, vol 131. Springer, Cham. [https://doi.org/10.1007/978-3-030-46036-5\\_12](https://doi.org/10.1007/978-3-030-46036-5_12)
28. Arof S, Said S, Diyanah NHN, Noor NM, Jalil JA, Mawby P, Arof H, Noorsal E (2020) Series motor four-quadrant DC chopper: reverse mode, direct current control, triple cascade PIDs, and ascend-descend algorithm with feedback optimization for automatic reverse parking. In: *Progress in engineering technology II. Advanced structured materials*, vol 131. Springer, Cham. [https://doi.org/10.1007/978-3-030-46036-5\\_13](https://doi.org/10.1007/978-3-030-46036-5_13)
29. Arof S, Sazali MS, Diyanah NHN, Mawby P, Arof H, Noorsal E (2021), Series motor four quadrants drive DC chopper: reverse mode with automatic reverse parking of DC drive electric car with constant brake motor control combine to the propulsion motor torque. *Prog Eng Technol*. [https://doi.org/10.1007/978-3-030-67750-3\\_20](https://doi.org/10.1007/978-3-030-67750-3_20)
30. Manjrekar MD, Steimer PK, Lipo TA (2000) Hybrid multilevel power conversion system: a competitive solution for high power applications. *IEEE Trans Ind Appl* **36**(3):834–841
31. Carlton D, Dunford WG (2001) Multilevel, unidirectional AC-DC converters, a cost effective alternative to bi-directional converters. In: *Proceedings of the IEEE Power Electronics Conference (SPEC)* **2001**:1911–1917

32. Calais M, Myrzik J, Spooner T (2002) Inverters for single phase grid connected photovoltaic systems an overview. *IEEE Proc Power Elect Spec Conf* 4:1995–2000
33. Carrara G, Gardella S, Marcheconi M, Salutari R, Sciutto G (1992) A new multilevel PWM method; a theoretical analysis. *IEEE Trans Power Elcet* 7(3):497–505
34. Du Z, Tolbert LM, Chiasson JN, Ozpineci B (2006) A cascade multilevel inverter using a single dc source. *IEEE Proc Appl Power Elect* 5:426–430
35. Lai JS, Peng FZ (1996) Multilevel converters—a new breed of power converters. *IEEE Trans Ind Appl* 32(3):509–517
36. Yilmaz M, Krein PT (2013) Review of battery charger topologies, charging power levels, and infrastructure for plug-in electric and hybrid vehicles. *IEEE Trans Power Elect* 28

# Chapter 21

## Topology Optimization of an Engine Mounting Bracket Using Finite Elements



Akief Khan Ayob Khan, Ahmad Razlee Ab Kadir, Zainal Nazri, T. A. A. Razak, and M. N. Ahmad

**Abstract** This project entitled topology optimization of an engine mounting bracket using the finite elements method focusing on an issue for engine mounting problem. The main objective for this project is to improve the performance of mounting bracket in term of vibration and design by using finite elements analysis (FEA) and topology method. The second objective is to develop 3D model of engine mounting basket. Finally, is to choose the best design of engine mounting with to have less of stress and magnitude. The purpose of an engine mounting bracket is to safely support the power-train system in all conditions. An engine mounting bracket is to properly balance the power pack (engine and transmission) on the vehicle chassis for good motion control as well as good isolation. A significant aspect of automotive research has always been to reduce the engine vibration and the dynamic forces transmitted from the engine to the body structure. In order to withstand these vibrations and have a smooth ride, automotive engineers face the challenge of designing mechanisms. The design of engine mounting bracket is built in SolidWorks and was analyzed and simulated by using FEA.

**Keywords** Topology optimization · FEA · SolidWorks · Engine mounting

### 21.1 Introduction

The component that keeps the engine to the body or to the car's engine cradle (sub-frame) is the engine mount. In a typical automobile, the engine and transmission are

---

A. K. A. Khan (✉) · A. R. A. Kadir · Z. Nazri · T. A. A. Razak · M. N. Ahmad  
Universiti Kuala Lumpur, Malaysian Spanish Institute Kulim Hi-Tech Park, 09000 Kulim, Kedah, Malaysia

e-mail: [auzaie.ayob@s.unikl.edu.my](mailto:auzaie.ayob@s.unikl.edu.my)

A. R. A. Kadir

e-mail: [ahmadrazlee@unikl.edu.my](mailto:ahmadrazlee@unikl.edu.my)

Z. Nazri

e-mail: [zainalnazri@unikl.edu.my](mailto:zainalnazri@unikl.edu.my)

bolted together and kept in place by three or four attachments. Engine mounts are designed with a rubber substance so that the engine and the car body do not have direct metal-to-metal contact. A better mounting system distinguishes the engine from the vehicle body, producing friction, and suppresses the effect on the vehicle driver of rough ground surface inputs. This situation becomes worse if the frequency of the system during operation reaches the natural frequency of the system. A poor bracket can also contribute to the rolling vibration of the shock of an engineer from deceleration and acceleration. Engine mounts have the main purpose of isolating the engine from the chassis and aligning the vehicle's power-train configuration according to specifications. In the other case, a high-frequency range of 30–250 Hz must be absorbed from the engine by the bracket. It is very necessary that the engine mounting bracket has appropriate stiffness and strength because of these factors. To check the bracket properties early in the design stage, strength analysis needs to be performed. The strength analysis measures the magnitude of a load from the engine mass, including the safety factor, and applies the load to each mounting bracket of the engine. Noise, vibration and harshness are critical features of vehicles and decreasing these features motivates manufacturers to achieve customer satisfaction.

The general outline of this investigation is stated in the following. In accordance with the research goals, history information related to the topology optimization of the engine mounting bracket using the finite element method is provided. Chaudhari and Panchagade [1] concentrate primarily on lightweight vehicle products to improve fuel economy and reduce emissions. Bankar et al. [2] carried out their research in which the architecture involves the modeling with a full restriction of engine mounting brackets, this work is carried out using aluminum and magnesium alloys. The outcomes for stress and deformation are evaluated.

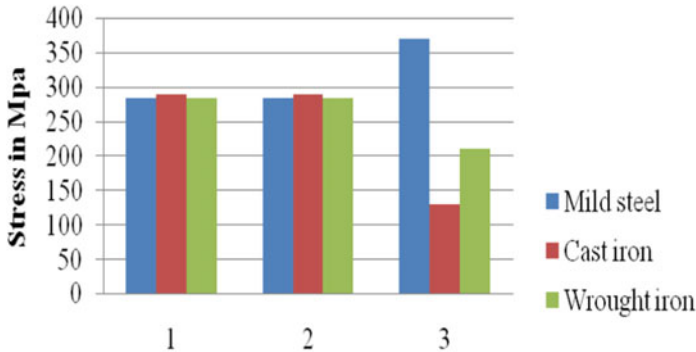
Kala et al. [3] paper outlines the methodology of minimizing the normal frequency of the engine bracket by finite element analysis using various lightweight materials. Evaluation of engine mount bracket assembly was carried out using FEA and modal analysis methodology, resulting in an optimized frequency of bracket produced with Mg alloy.

Ghorpade et al. [4] modeled a car engine mount bracket paper and concentrated on evaluating the normal frequencies of car engine mount brackets. When modal analysis is done, they considered the three engine mount bracket materials that are aluminum alloy, magnesium alloy and gray cast iron. The natural frequencies of gray cast iron are found to be low, which would show more hindrance in engine mount bracket vibration so that gray cast iron has been removed. Aluminum alloy and magnesium alloy show almost near natural frequency value in realistic terms in terms of research, as the magnesium alloy has a better strength with a low-stress value, so magnesium alloy is ideally chosen by the study as a better material.

FEA analysis of an engine mounting bracket is discussed by Jadhav, Ramakrishna [5]. This involves the modeling of the mounting brackets by adjusting the relevant current component material. Magnesium alloy and aluminum alloy are the components used for mounting brackets. The study reveals that compared to normal aluminum alloy material, this bracket would have greater weight reduction and withstand high stress. It has been concluded that magnesium can be chosen as a material

**Table 21.1** Comparison for stress of the engine mount bracket for different material

Different materials	Stress for pretension load in N/mm <sup>2</sup>	Stress for service load in N/mm <sup>2</sup>	Yield strength in N/mm <sup>2</sup>	Ultimate strength in N/mm <sup>2</sup>
Mild steel	284.39	283.53	370	440
Cast iron	289.20	289.05	130	220
Wrought iron	284.44	283.93	210	320



**Fig. 21.1** Stress analysis for different material bracket

for an engine mounting bracket over aluminum. In different working conditions, mounting brackets containing magnesium material are good.

It is evident from the above studies that several works have been conducted primarily on design aspects and material selection on engine mounts. There is still space for improvement by modifying the form of the mount material and design. It is known that all engine mounts that have been discovered and researched are based on their operating theory and area of operation. Nevertheless, no one attempted to use multiple material combinations. Alloys of various materials with high damping coefficients are found to withstand more vibrations than individual materials. Depending on the type of engine, based on the number of cylinders and the type of vehicles used, special designs may also be made for various types of applications. Table 21.1 and Fig. 21.1 show the comparison of stresses of the engine mount bracket for different materials.

### 21.1.1 Based on Application Aspects of Mounts

In evaluating the fatigue life cycle configuration of the engine mount, a stochastic approach is used. It has been proposed that fatigue life is often calculated by using

models of non-linear regression. The benefit of using hydraulic mounts was clarified by Jansson and Johansson [6]. Promising innovations and concepts for actuators are specifically defined. It is also discussed that the type of mount can be used for better performance depending on the type of operation. A parameterized model has been developed for frequencies ranging from zero to 300 Hz. Hafidi et al. [7] reconstructed the excitation force of the working diesel engine is reconstructed by semi-experimental approach with the aid of acceleration data calculated at the mounting sections. Using three uncoupling methods, low-frequency vibration can be reduced; a dynamics model is designed to explain the complicated behavior of the whole system, including the power train and its mounts.

Marzbani et al. [8] concluded that ideal mounts must provide high damping at low excitation frequency and low damping and soft suspension at high excitation frequency. It is noted that the use of hydraulic mounts is due to the dual behavior requirement, and it is found that the use of high damping coefficient of materials and analysis equipment will make hydraulic mounts more effective and functional. The role of the bracket supporting the engine mount was defined by Kala and Kiran [9]. The important function of the engine mounting bracket is to align the engine and transmission on the frame of the car, there using CAD software to model the engine mounting bracket, and finite element analysis. The work of Kumar et al. [10] deals with the engine mount design to eliminate vibrations by using the Hyperworks and CAE software, which is used to find the model solution. In this, hypermesh and hyperview, respectively, carry out the post-processing and pre-processing.

Depending on the type of application, Asker [11] suggested two new models. To do statistical analysis, Ansys11 is used. Compared to the current engine mounting model, 51.5 % of the weight is eliminated. Even the stress caused during vibrations in the proposed model is very minimal. The stiffness and damping values of the mount are understood until the mount is developed, and the next step is to convert these numerical values into actual mount values. This involves determining the mount's geometrical dimensions in such a way that stiffness and damping characteristics are necessary. Optimization modeling has been widely used in the world of engineering for the advancement of finite element technologies and design principles, using the approach of numerical simulation on the structure. Not only does this lower manufacturing costs, but it can also shorten the design period, with high economic benefits.

In this author, Walunje and Kurkute [12] state that the engine rests on the bracket of an automobile vehicle that is attached to the main frame or chassis of the car. In cars, mounting the engine plays an important function. The right geometry offers good ride quality and performance. The simulation techniques finite element analysis, modal analysis and optimization of the engine bracket for the car are used in this article. Since the FSAE car is a high-performance automobile bracket, constant vibration continues to occur, so fatigue strength and reliability measurements have also been conducted to guarantee engine protection.

## 21.2 Methodology

The engine mounting bracket was design by using SolidWorks and the design was imported to the CAE software. The development and creating steps of the current design from the engine mounting Honda FD are very important to be analyzed and were simulated using FEA and topology method.

### 21.2.1 Design Model 3D of Engine Mounting Bracket

#### 21.2.1.1 SolidWorks 2019

The engine mounting bracket was modeled in the SOLIDWORKS 2019 software. This engine mounting bracket was modeling based on the measurement of the actual engine mounting bracket by Honda FD. The material used for the engine mounting bracket for this design is an aluminum alloy. Figure 21.2 shows the 3D drawing of the engine mounting bracket Honda FD by using SolidWorks.

### 21.2.2 Finite Element Analysis (FEA)

The assembly modeling was done by using SOLIDWORKS software and import the file to the FEA. For the final year project, the main objective is to optimize the engine mounting bracket by using Finite Element Analysis. The design from the SOLIDWORKS is saved as Initial Graphic Exchange Specification (IGIS) file, which can be imported easily into the FEA software. This is very important part because to

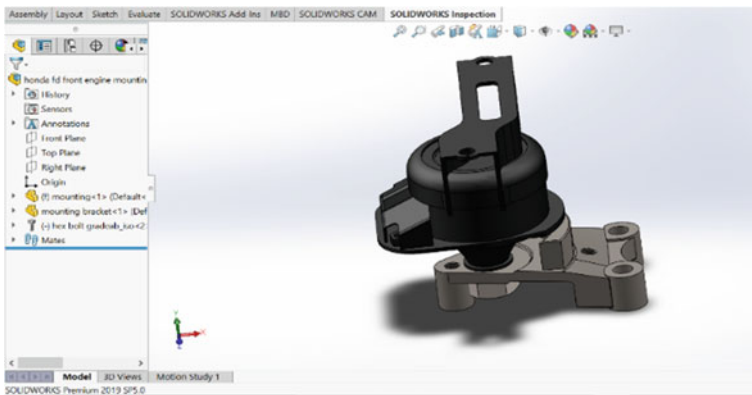


Fig. 21.2 3D Drawing of the engine mounting bracket Honda FD

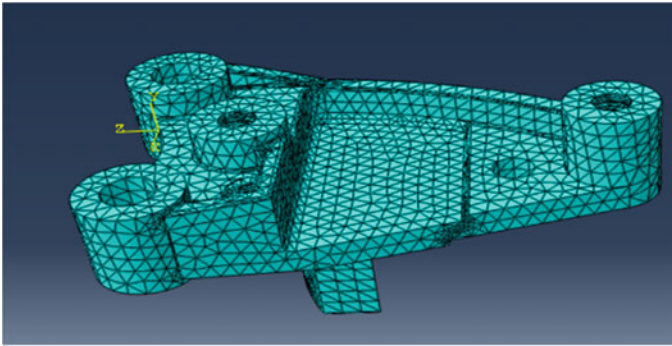


Fig. 21.3 Mesh the engine mounting

run the simulation and to get the result from the FEA the file from the SOLIDWORKS must be converted into IGIS file. By using the FEA software it easily can determine how the critical factors might affect the entire structure and why failure might occur. Figure 21.3 shows the meshing process of engine mount bracket.

### 21.2.3 Modal Analysis

The modal analysis was conducted using effect tests to achieve the performance results. This experiment was done to validate the result from the simulation by using finite element analysis. A specific hammer is used to conduct this test which cell load was put in its tip to obtain the force of impact. Figure 21.4 is shown as an experimental

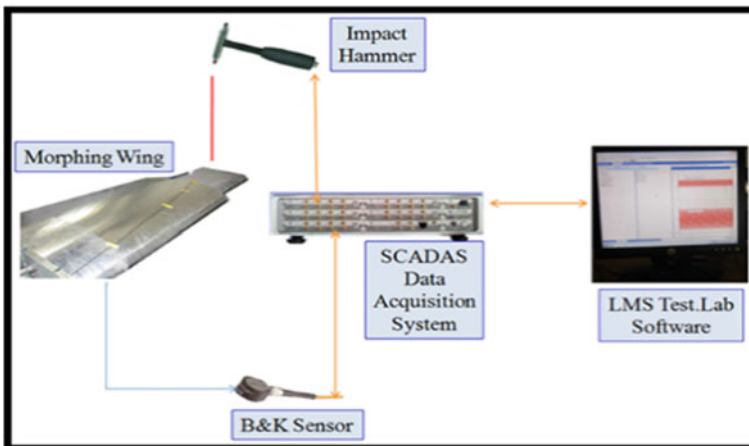


Fig. 21.4 Experiment setup



setup to conduct experiment. In this project, the accelerometer used has a reasonable accuracy capability, with a sensitivity of 50.81 mV/g, the round accelerometer delivers a frequency from 0.5 Hz to 5,000 Hz at a certain time. Figure 21.4 shows the experiment setup devices for testing process. The accelerometer, laptop, NI Acoustic and Vibration Data Recorder, effect hammer and frame structure are the equipment that was used.

Figure 21.5 shows the drawing of the engine mount structure that has been created in LMS Test Lab software using drawing tool according to the coordinate of actual engine mounting bracket that has been measured. After finishing the drawing, need to label the node points at the drawing. Besides, Fig. 21.6 shows the result from EMA after complete testing process.



Fig. 21.5 The drawing of engine mount bracket in LMS test lab

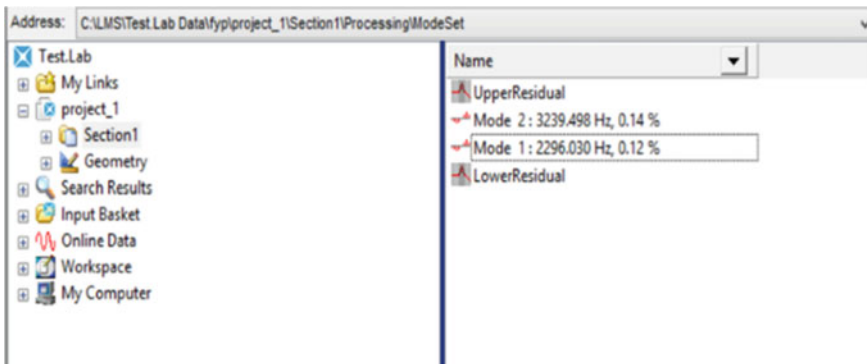
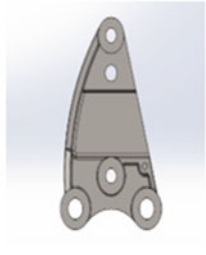

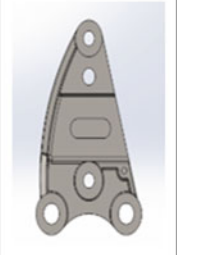


Fig. 21.6 The result from EMA

### 21.2.4 Topology Optimization

Topology optimization is a method that determines the best content structure for a given design space and loading case. Topology optimization is the process of determining the best direction for material delivery in a continuous domain to satisfy the structure’s displacement and stress conditions and achieve the best possible results. The different modification with different thickness is shown in Table 21.2. From this modification the topology optimization will be done to study with one is the most suitable design for engine mounting bracket.

**Table 21.2** Different model of engine mounting

Engine Mounting Model			
Modification	No pocket	With pocket	With pocket
Thickness	36.00 mm	36.00mm	46.00mm
Material to optimization	<ol style="list-style-type: none"> <li>1. Aluminum alloy</li> <li>2. Cast iron</li> <li>3. Wrought iron</li> </ol>	<ol style="list-style-type: none"> <li>1. Aluminum alloy</li> <li>2. Cast iron</li> <li>3. Wrought iron</li> </ol>	<ol style="list-style-type: none"> <li>1. Aluminum alloy</li> <li>2. Cast iron</li> <li>3. Wrought iron</li> </ol>
Model			

**Table 21.3** Comparison result for FEA and EMA

Mode	Natural frequency (Hz)		Deviation (%)
	FEA	EMA	
1	2,231.8	2,296.030	2.8
2	3,299.6	3,239.498	1.8
Average percentage error (%)			2.3

## 21.3 Result and Discussion

### 21.3.1 Comparison Result from FEA and EMA

The percentage error for each mood between EMA and FEA is shown in Table 21.3. This experiment shows that below 2.3% is because when doing the experiment, there are a few factor errors. A mistake in the modeling of the engine mounting bracket, such as noise or experiment configuration. When the experimental modal analysis is done, one of the difficulties occur is the noise. It is possible to wait the part to stop and no further vibration on the engine mount part after knocking in the knocking process. Before the next knocking starts, the engine mount also has previous vibration on the first knocking since minimal vibration cannot be seen by the eyes. It will take longer to ensure no further vibration, and it will take longer to complete the knocking process to complete all the 19 points on the final mounting of the engine.

### 21.3.2 Optimized Design Engine Mounting Bracket

The optimized design was selected with three different materials which is aluminum alloy, cast iron and wrought iron. There are three designs that will be optimized. The optimization process is done by using FEA software. The result of S, Misses and U, Magnitude will be study for the optimization process. Figures 21.7 and 21.8 show the example of the result in topology optimization for U, magnitude and S, Stress.

#### 21.3.2.1 Result for Topology Optimization

From Table 21.4, it can be easy to compare all the engine mounting design with different material simulation within s, misses and u magnitude. From this table we can conclude that the best among design for engine mounting is design 3 which is the material use and are aluminum alloy. The stress that acted on the engine mounting is only  $5.211e^1$  and deflection occur on the engine mount is only  $1.999e^4$  that can withstand the high magnitude due to load attach on the engine mount. Even though the stress and magnitude for cast iron and wrought iron has lower value than aluminum alloy but aluminum alloy have the highest quality in term of corrosion

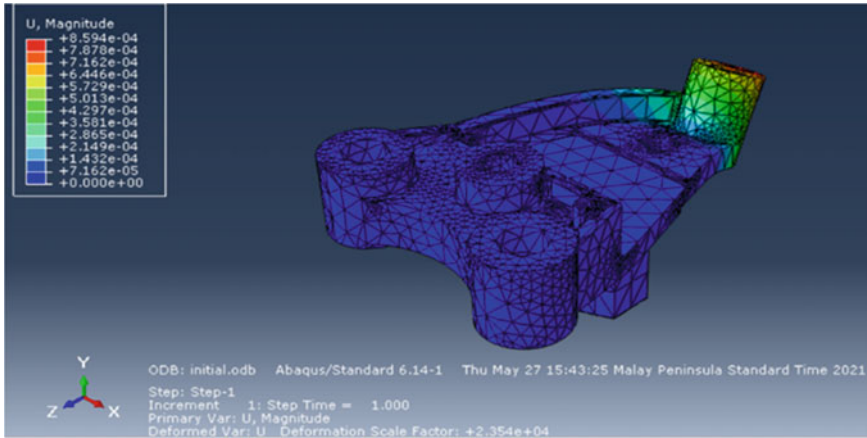


Fig. 21.7 Topology optimization for U, magnitude

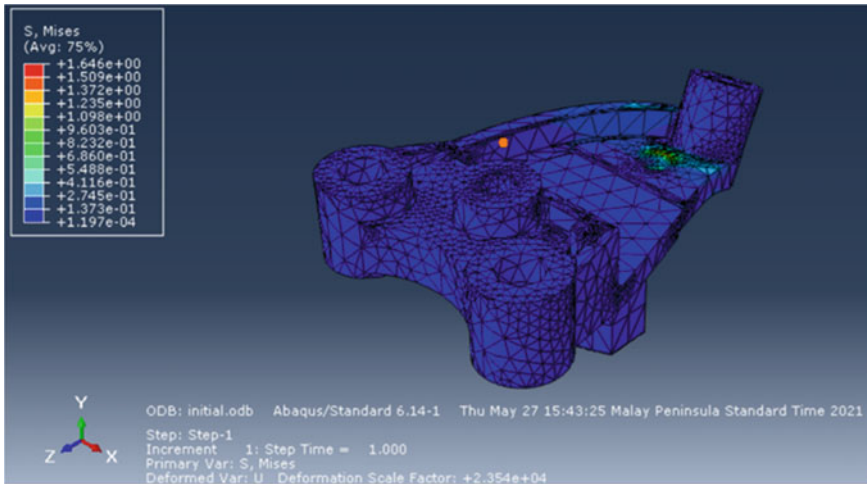


Fig. 21.8 Topology optimization for S, mises

because when it comes to oxidation, cast iron oxidizes more quickly in humid or moist air, and it will continue to oxidize if left outside. Aluminum, on the other hand, frequently develops an imperceptible coating of aluminum oxide that shields it from further oxidation. Besides, aluminum is notable for its low density. As a result, it has become an important component in the manufacture of a wide range of products used in automotive. From the previous study, it has been shown that aluminum is also more impact-resistant than iron, which is known for being brittle. Besides, it was proved that the lower stress acted on the engine mount, it will increase the safety factor for the engine mount.

**Table 21.4** Comparison between existing and modified design with different material

Design	Material	Max, s	Min, s	Max, u	Min, u
1	Aluminum Alloy	1.646e <sup>+00</sup>	1.197e <sup>-4</sup>	8.594e <sup>-4</sup>	0.000e <sup>+00</sup>
	Cast iron	1.661e <sup>+00</sup>	0.000e <sup>+00</sup>	5.035e <sup>-4</sup>	0.000e <sup>+00</sup>
	Wrought iron	1.661e <sup>+00</sup>	0.000e <sup>+00</sup>	3.180e <sup>-4</sup>	0.000e <sup>+00</sup>
2	Aluminum Alloy	1.373e <sup>+00</sup>	0.000e <sup>+00</sup>	8.572e <sup>-4</sup>	0.000e <sup>+00</sup>
	Cast iron	1.379e <sup>+00</sup>	0.000e <sup>+00</sup>	5.049e <sup>-4</sup>	0.000e <sup>+00</sup>
	Wrought iron	1.379e <sup>+00</sup>	0.000e <sup>+00</sup>	3.189e <sup>-4</sup>	0.000e <sup>+00</sup>
3	Aluminum Alloy	5.211e <sup>-1</sup>	0.000e <sup>+00</sup>	1.999e <sup>-4</sup>	0.000e <sup>+00</sup>
	Cast iron	5.145e <sup>-1</sup>	0.000e <sup>+00</sup>	1.168e <sup>-4</sup>	0.000e <sup>+00</sup>
	Wrought iron	5.145e <sup>-1</sup>	0.000e <sup>+00</sup>	7.337e <sup>-5</sup>	0.000e <sup>+00</sup>

## 21.4 Conclusions

The purpose of this chapter is to verify the relationship between the outcome of both FEA and EMA also in the modification of the engine mounting bracket for Honda FD. Besides, to achieve the objective of topology optimization the process was done by using Abaqus software. For the optimization, the comparison result between the existing model of engine mounting will be compare with another two different designs with different material. The objective of this final year project was achieved. By using SolidWorks software, the three different design of engine mounting bracket was modeled. Throughout on simulation by using ABAQUS the optimization result for engine mounting was done and it will be compared with the value for modification by referring to the maximum stress, and deflection occur on the engine mount. From the simulation of engine mounting bracket, the result can be seen clearly and easy to compare with other design on different material. From the FEA software it also can be calculate the result of job frequency. Besides, the lower stress acted on the engine mounting bracket will increase the safety factor. By changing the thickness and made some pocket for the engine mounting bracket, it will produce the good strength for engine mounting bracket of the vehicle.

## References

1. Chaudhari, Panchagade et al (2012) Comparison of magnesium, aluminium and cast iron to obtain optimum frequency for engine bracket using finite element analysis. *Int J Eng Res Appl (IJERA)*, 2248-9622 2(5):1016–1020
2. Bankar (2017) Study and experimental analysis of engine mounting bracket of light commercial vehicle. *Int J Sci Res Dev* 2321-0613, 4(12):512–517
3. Kala, Kiran et al (2015) Modeling and analysis of V6 engine mount bracket. *IJRSET*, 4(7):5907–5914
4. Ghorpade et al (2012) Finite element analysis and natural frequency optimization of engine bracket. (*IJMIE*) ISSN No. 2231-6477, 2(3)

5. Jadhav PD, Ramakrishna et al (2014) Finite element analysis of engine mount bracket. *Int J Adv Eng Technol* **1**:2349–3224
6. Narayanan G, Rezaei K, Nackenhorst U (2015) Fatigue life estimation of aero engine mount structure using monte carlo simulation. *Int J Fatigue* **83**:53–58
7. Jansson F, Johansson O et al (2003) A study of active engine mounts. Reg no: LITH ISY-EX-3453-2003 Linköping
8. Ali El Hafidi H, Martin B, Loredo A, Jego E. Vibration reduction on city buses: determination of optimal position of engine mounts. *Mech Syst Signal Process* **24**:2196–2209
9. Lakshmi Kala P, Ratna Kiran V et al (2015). Modelling and analysis of V6 engine mount bracket. *Int J Innov Res Sci Eng Technol* 3297:2007, **4**(7):5907–5914
10. Kumar AL, Balasivaramareddy K, Sathiskumar A, Kuthus N et al (2017) Stress analysis and optimization of engine mount. *Int J Mech Eng Technol* **8**(6):148–155
11. Asker HK et al (2003) Comparison of the mechanical properties of different models of automotive engine mounting. *ARNP J Eng Appl Sci* 1819 6608, **8**(6):401–406
12. Walunje P, Kurkute VK et al (2013) Optimization of engine mounting bracket using FEA. *IJR* **2**(12):72–75
13. Dhillon JS, Rao P, Sawant VP, Design of engine mount bracket for a FSAE car using finite element
14. Ali A, Hosseini M, Sahari BB et al (2010) A Review of constitutive models for rubber like materials. *Am J Eng Appl Sci* 3:232–239
15. Lin DY et al (2013) Automotive engine bracket topology optimization and finite element analysis. Zhejiang University of Technology, Hangzhou
16. Babu P, Vijaya Kumar Y, Udaya Kiran C et al (2014) Topology optimization in design of engine mounting bracket. *Int Conf Emerg Trends Mech Eng* **1**

# Chapter 22

## Air Conditioning System Comfort Level and Power Consumption Monitoring Device with RF-Based Wireless Sensor Modules and Android Mobile Application



**Norzalina Othman, Mohamad Fadzli Haniff, Hazlina Selamat, Tuan Muhammad Syahmi Tuan Saha'Arif, Muhammad Al'Hapis Abdul Razak, Mohd Usairy Syafiq Sama'in, and Julaida Abdul Jalil**

**Abstract** Nowadays, electric consumption especially in Malaysia has increased over the years caused by the usage of air conditioning (AC). Conventional AC remote devices are unable to monitor the actual comfort index of the building and the power consumption that has been used of the system by using Android mobile applications. Knowing the actual comfort index and power consumption is necessary for the user

---

N. Othman (✉) · T. M. S. T. Saha'Arif · M. A. A. Razak · J. A. Jalil  
System Engineering and Energy Laboratory (SEELab), Universiti Kuala Lumpur Malaysia  
Spanish Institute (UniKL MSI), Kulim Hi-Tech Park, 09000 Kulim, Kedah, Malaysia  
e-mail: [norzalina@unikl.edu.my](mailto:norzalina@unikl.edu.my)

T. M. S. T. Saha'Arif  
e-mail: [tsyahmi.sahaarif@s.unikl.edu.my](mailto:tsyahmi.sahaarif@s.unikl.edu.my)

M. A. A. Razak  
e-mail: [alhapis@unikl.edu.my](mailto:alhapis@unikl.edu.my)

J. A. Jalil  
e-mail: [julaida@unikl.edu.my](mailto:julaida@unikl.edu.my)

M. F. Haniff  
Intelligent Dynamics & System (IDS) i-Kohza, Malaysia-Japan International Institute of  
Technology, Universiti Teknologi Malaysia, 54100 Kuala Lumpur, Malaysia  
e-mail: [mfadzlihaniff@utm.my](mailto:mfadzlihaniff@utm.my)

H. Selamat  
Faculty of Engineering, School of Electrical Engineering, Centre for Artificial Intelligence &  
Robotics, Universiti Teknologi Malaysia, 81310 Skudai, Johor, Malaysia  
e-mail: [hazlina@utm.my](mailto:hazlina@utm.my)

M. U. S. Sama'in  
Quality Engineering Section, Universiti Kuala Lumpur Malaysian Institute of Industrial  
Technology (UniKL MITEC), Bandar Seri Alam, 81750 Masai, Johor, Malaysia  
e-mail: [usairy@unikl.edu.my](mailto:usairy@unikl.edu.my)

to come up with strategies to use the AC system economically. Besides, conventional AC remote devices do not have temperature and humidity sensors that can monitor the comfort index and power consumption. Users do not know the actual comfort level and power consumption, thus causing discomfort and maybe waste of energy. To overcome these problems, an air conditioning system comfort level and power consumption monitoring device with RF-based wireless sensor modules and Android mobile application were produced. Indoor air quality (IAQ) and predicted mean vote (PMV) are the types of comfort index that have been used to measure the comfort level. In this project, the methods used for completing the project of monitoring the air conditioning system by using the predicted mean vote (PMV) algorithm. PMV has six parameters, which are the air temperature, mean radiant temperature, clothing insulation, metabolism rate, relative air velocity and relative air humidity. This monitoring system can monitor various variables at the same time such as the indoor temperature, outdoor temperature, relative temperature, relative humidity, PMV and power consumption. With a monitoring system, the energy consumption can be minimized while retaining the comfort level. In this project, a monitor box, wireless humidity sensor box and wireless temperature sensor box were produced. This research elaborates on the entire process of hardware design. It also discusses the software developed for monitoring parameters such as the power consumption using a mobile phone. The AC system can be better monitored and controlled with the developed tool in this project.

**Keywords** Energy consumption · Temperature · Monitoring · Air conditioning · Thermal comfort · Predicted mean vote

## 22.1 Introduction

Today, most environmental issues are closely linked to the consumption of energy. In buildings, energy consumption constitutes 40% of the overall energy consumed worldwide [1]. Air conditioning systems also consume about 40–50% of the total energy usage in buildings [1]. Energy management of air conditioning systems in houses, therefore, requires comprehensive studies. According to research in [2, 3], the AC system is one of the most substantial households that consume electricity in housing and business office sectors. The number of air conditioners expected will increase to 1.5 million in the private sector by 2020 [4]. This means the air conditioner consumer will increase by the year. Due to this problem, of course, electric consumption will be increased. To overcome this problem, an air conditioning system comfort level and power consumption monitoring device with RF-based wireless sensor modules and Android mobile application were developed and produced.

This system can monitor the actual comfort level and power consumption. At the same time, the user can also know the current indoor temperature, outdoor temperature and indoor humidity. Thus, the users can properly plan their AC for comfort. Therefore, with this monitoring system, the rate of energy consumption



can be reduced and cost-effective operation will occur. It is vital to use energy in an optimal way to make the system more efficient and effective without any waste of energy. A lot of research was already conducted to increase the performance and maximize the thermal comfort indoors and reduce power consumption.

By contrast, this paper presents the development of a comfort index and power consumption monitoring device for AC system using two types of sensor modules which is the temperature sensor and the humidity sensor. In this project, one of the comfort indices that has been used is the PMV. PMV values can be obtained through calculation using six parameters which are the air temperature, mean radiant temperature, metabolism rate, clothing insulation, relative air velocity and relative air humidity. This monitoring system can monitor various variables at the same time. With this monitoring system, the energy consumption can be minimized while retaining the comfort level. To make this project a success, an experiment was conducted for two days. The main purpose of this experiment is to monitor the variables such as indoor temperature, outdoor temperature, relative humidity, relative temperature, PMV value and power consumption. Monitor box, wireless humidity sensor box and wireless humidity sensor box have been produced in this project. The monitor box is also connected to the Android app, where the user can monitor outside of the room using a mobile phone.

## 22.2 Literature

### 22.2.1 *Thermal Comfort*

According to the American Society of Heating, Refrigerating and Air-Conditioning Engineers (ASHRAE) (2004), thermal comfort is a term used to indicate data on the thermal state of the thermal environment of a body and the main methods known as physiological and physical considerations are the thermal comfort. Specific comfort climate devices can be used to measure those physical factors and then send them to an AC system to monitor the airflow in the room and to provide thermal comfort conditions in the room. The air conditioning system could be used for room control to create a thermally comfortable condition in the room when parameters are measured correctly. The current AC system control approach makes it possible for the occupant to bring extra cooling that does not create a thermal comfort environment, plus this will harm humans.

Most researchers have utilized the PMV model, as a thermal comfort index to measure thermal comfort, and PMV has been taken into consideration under ISO 7730 [5–7]. PMV comprises six parameters, which are the metabolic rate, clothing insulation, air temperature, mean radiant temperature, air velocity and humidity. PMV values represent thermal sensation in accordance with these parameters. The metabolism and clothing insulation values are usually assumed to be constant. The metabolic rate is estimated for workplace tasks to be  $60 \text{ W/m}^2$ , and clothing insulation

**Table 22.1** PMV scale

PMV	Sensation
+3	Hot
+2	Warm
+1	Slightly warm
0	Neutral
-1	Slightly cool
-2	Cool
-3	Cold

for a short-sleeved shirt, including trousers, is estimated to be 0.57 clo. In some studies, because of the need for multiple sensors and the complexity of calculation, the mean radiant temperature was assumed to be equal to the air temperature [7]. The clothing insulation can be calculated by measuring on heated mannequins to accurate estimation and a person's expired air can be used to estimate the metabolic rates by measuring CO<sup>2</sup> and O<sup>2</sup> [8]. Besides, time changes in human activity. However, it is not easy to estimate metabolic levels and clothing insulation. Therefore, wearable or non-contact sensors are to be designed in various projects for measuring metabolic rates and clothing insulation and for improving the measuring process of the human factor. Table 22.1 shows that the PMV comfort ranges from -3 (cold) to +3 (hot).

Indoor air quality (IAQ), particularly when it relates to the safety and comfort of people, refers to the air quality inside and around buildings and structures. Comprehension and monitoring of increasing indoor pollutants will help to reduce the risk of indoor health problems. The device can continuously measure and record air quality including temperature and humidity, thus enabling it to monitor. The indoor air quality is a measure of air quality by defining such volatile compounds as paint, furniture, office equipment, waste, cooking compounds, food intake, ventilation and/or sweater. IAQ measurements are important to track air continuously throughout the day to effectively investigate IAQ and at least two areas of air should be monitored the air in the region of concern and the air in the exterior as a reference. IAQ measuring devices are unfortunately expensive. Thus, devices for better choices must be investigated to continue this research. Table 22.2 shows the IAQ rating index.

### 22.2.2 *Mobile Applications*

A mobile app was built based on the Android operating system to control a fresh air conditioner with mobile termination [9]. To control fresh air conditioners with mobile terminator, which is a smartphone or a tablet computer, a client software was developed. In order to regulate a fresh air conditioner, a mobile phone uses customer software to first connect via an internet router to a host computer in a building. The host computer then transfers data via RS-232 to RS485 with the fresh

**Table 22.2** IAQ rating index

Rating	Excellent (5 points each)	Good (4 points each)	Fair (3 points each)	Poor (2 points each)	Inadequate (1 point each)
Temperature (°C)	18–21 °C	Plus or minus 1 °C (including variance rooms, seasons and times of day)	Plus or minus 2 °C (including variance rooms, seasons and times of day)	Plus or minus 3 °C (including variance rooms, seasons and times of day)	Plus or minus 4 °C (including variance rooms, seasons and times of day)
Carbon dioxide (PPM)	<600	601–800	801–1,500	1,501–1,800	>1801
Relative humidity (%RH)	40–60	<40/>60	<30/>70	<20/> 80	<10/>90
Carbon monoxide (mg/m <sup>3</sup> )	0	–	1–7	–	7>
Nitrogen dioxide (mg/m <sup>3</sup> )	<0.2	–	0.2–0.4	–	0.4>
TVOC (mg/m <sup>3</sup> )	<0.1	0.1–0.3	0.3–0.5	0.5–1.0	1.0>

air device controller. Customer software includes user management features, scene control, monitoring energy consumption, security guards and equipment monitoring. Besides, a mobile terminator client software was developed based on Android.

A high volume of energy consumption can be minimized if the preset temperature is regulated in a gentle way [10]. The relation from preset temperature to electricity consumption has historically to be manually controlled in order to save energy. Several electrical management systems have been built in the smart house to avoid the loss of electricity from the manual control process in order to increase energy efficiency. The remote control provides a means of contact through the internet to minimize power from air conditioners that consume the most power in regular household appliances [11].

Wireless technology is a technology that allows us without cables or wires to communicate. With this type of technology, people and other organizations can interact over very long distances. The esp8266 module is used to send Arduino data to the IoT platform from which the user is able to connect. The Wi-Fi module has TC/IP and SOC incorporated. This module easily provides Wi-Fi access when it is linked to an Arduino board because of its software significance. Bluetooth devices (HC-05 module) with a common sequence can form a piconet. The piconet is a network made up of one master and slave, and the topology is a star. The master is Bluetooth device that deliberately connects to other Bluetooth devices that are slaves.

The hopping sequence of the piconet is determined by the Bluetooth device address (BD ADDR) master, which is unique and 48-bit in length. Radiofrequency module (nRF24L01) that can operate in the 2.4 GHz band is commonly used, while others use the ISM band 433/470/868/915 MHz. Nowadays, state of art is to use fully and low-cost hardware for reliable telemetry and consumer applications. The range of the coverage is between 10 and 150 m. It provides a broad range of applications in the field of high-quality image transmission, wireless monitoring system, LED toning and wireless sensor network (WSN). The nRF24L01 configuration is achieved via the serial peripheral interface (SPI) which is a synchronous serial communication. The wireless systems being used are Bluetooth and NRF24L01 for transmitting the data. The Bluetooth module will be used to transmit data from the monitor box to the mobile phone. The NRF24L01 module also will be used to communicate between the monitor box and the sensor box. In this project, the Wi-Fi module is not suitable because it is too complex to use and this project also does not use the IOT.

## 22.3 Methodology

### 22.3.1 Project Planning

Below is the PMV equation that has been used in this project.

$$PMV = (0.303 \cdot e^{-0.036M} + 0.028) \cdot L$$

$$\begin{aligned} L = & M - W - 3.05 \cdot 10^{-3} \cdot (5733 - 6.99 \cdot (M - W) - p_a) - 0.42 \cdot ((M - W) - 58.15) \\ & - 1.7 \cdot 10^{-5} \cdot M \cdot (5687 - p_a) - 0.0014 \cdot M \cdot (34 - t_a) \\ & - 3.69 \cdot 10^{-8} \cdot f_{cl} \cdot ((t_{cl} + 273)^4 - (t_r + 273)^4) - f_{cl} \cdot h_{cl} \cdot (t_{cl} - t_a) \end{aligned}$$

$$\begin{aligned} t_{cl} = & 35.7 - 0.028(M - W) \\ & - (3.69 \cdot 10^{-8} \cdot f_{cl} \cdot ((t_{cl} + 273)^4 - (t_r + 273)^4) - f_{cl} \cdot h_{cl} \cdot (t_{cl} - t_a)) \end{aligned}$$

$$p_a = \frac{p_s RH}{100}$$

$$\ln p_s = \frac{C_1}{T} + C_2 + C_3 \cdot T + C_4 \cdot T^2 + C_5 \cdot T^3 + C_6 \cdot \ln T$$

where

$$C_1 = -5.8002206 \cdot e^3$$

$$C_2 = 1.3914993$$

$$C_3 = -4.8640239 \cdot e^{-2}$$

$$C_4 = 4.1764768 \cdot e^{-5}$$

$$C_5 = -1.4452093 \cdot e^{-8}$$

$$C_6 = 6.5459673$$

$$T = t_a + 273.15$$

$$h_{cl} = \begin{cases} 2.38(t_{cl} - t_r)^{0.25} \text{ for } 2.38(t_{cl} - t_r)^{0.25} > 12.1\sqrt[3]{v_a} \\ 12.1\sqrt[3]{v_a} \text{ for } 2.38(t_{cl} - t_r)^{0.25} < 12.1\sqrt[3]{v_a} \end{cases}$$

$$f_{cl} = \begin{cases} 1.00 + 0.2I_{cl} \text{ for } I_{cl} < 0.5clo \\ 1.05 + 0.1I_{cl} \text{ for } I_{cl} > 0.5clo \end{cases}$$

PMV is a one-value comfort index that is calculated using six parameters where:

- **Air temperature ( $T_{air}$ ):** Air temperature is an indicator of how cold or hot air is. That is the environmental parameter that is most frequently measured.
- **Mean radiant temperature ( $T_r$ ):** is known as the uniform temperature of an imaginary enclosure where radiant heat transfer in the real, non-uniform enclosure from the human body is equal to radiant heat transfer.
- **Metabolism rate ( $M$ ):** used to describe all chemical reactions involved in maintaining the living state of the cells and the organism.
- **Clothing insulation ( $I_{cl}$ ):** is the thermal insulation provided by clothing.
- **Relative air velocity ( $V_a$ ):** is the absolute value of the difference between walking and wind speeds.
- **Relative air humidity ( $RH$ ):** is the ratio of the partial pressure of water vapour to the equilibrium vapour pressure of water at a given temperature.

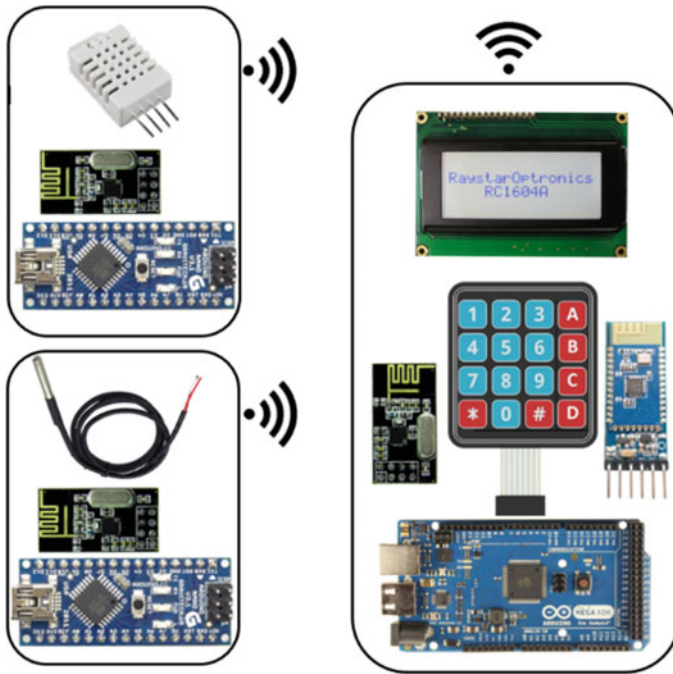
Using the following equation that has been shown below to calculate the power after the PMV value has been obtained:

$$Power (W/h) = \frac{BTU/h}{0.1 \times COP \times 3.41}$$

$$COP_{MAX} = \frac{T_{COOLING}}{T_{OUTDOOR} - T_{COOLING}}$$

$$COP = 0.1 \times COP_{MAX}$$

The main components that have been used in this project are the Arduino MEGA 2560, Arduino Nano, LCD  $20 \times 4$  with I2C interface, temperature sensor (DS18B20), humidity sensor (DHT22),  $4 \times 4$  matrix keypad, NRF24L01, HC-05 and switch button. In this project, we used a monitor box, wireless temperature sensor box and wireless humidity sensor box. Inside of the monitor box are included the components such as the  $20 \times 4$  LCD, keypad, Arduino Mega, HC-05 Bluetooth module and NRF24L01 wireless module. Two sensor boxes have different components. Inside of the wireless humidity sensor box, Arduino Nano, DHT22 and NRF24L01 were



**Fig. 22.1** System framework

included. Arduino Nano, DS18B20 and NRF24L01 were included inside of the wireless temperature sensor box. Figure 22.1 shows the system framework of this project.

Figure 22.2 shows the project layout that had been fabricated in this project. The monitor box and wireless humidity sensor box will be placed indoors. The main purpose of the wireless humidity sensor placed indoor is to measure indoor humidity and temperature. The monitor box will be controlled and observed by the user. To obtain an outdoor temperature reading, the wireless temperature sensor will be placed outside.

The circuit design consists of some of the components, which are the Arduino board, keypad, temperature sensor, humidity sensor, LCD and switch button. In the prototype, the breadboard has to be used to make quick electrical connections between the components. Thus, the user can test the circuit before permanently soldering it together. In this project, three different types of circuit connections were implemented. Figure 22.3 shows the circuit connection for monitor box. Each component has a different connection depending on the specification of the component used. For monitor box connection, it contains a few components such as keypad, LCD, Bluetooth module and NRF24L01 wireless module. Arduino Mega as main microcontroller for this monitor box.

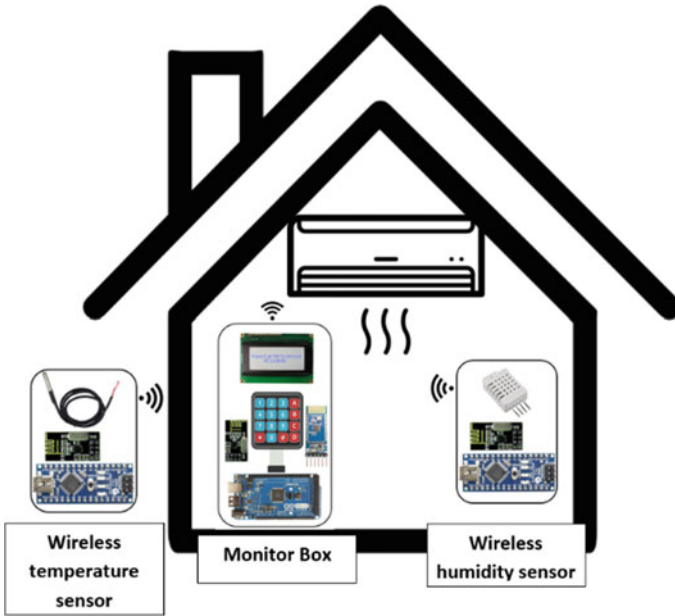


Fig. 22.2 Project layout

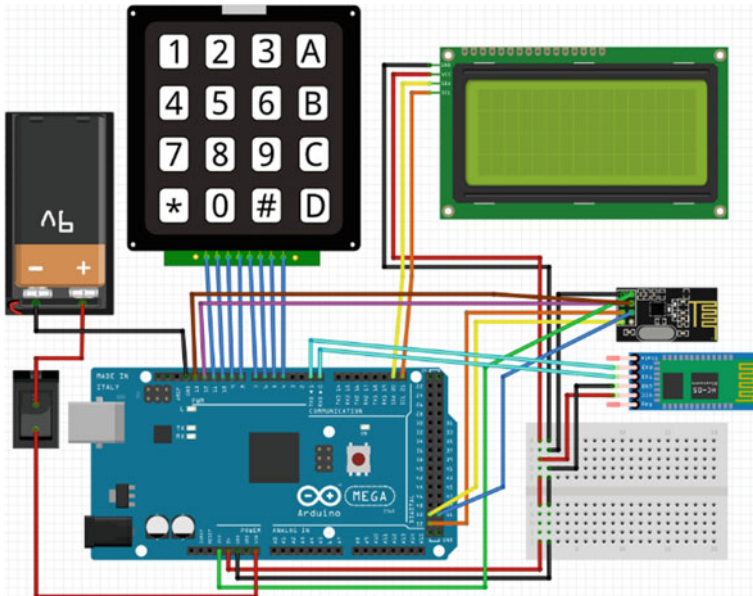


Fig. 22.3 Circuit connection for the monitor box

Circuit connection that has been shown in Fig. 22.4 is for wireless humidity sensor. This circuit also same goes to circuit connection for temperature sensor, but it uses one breadboard only.

Figure 22.5 shows the circuit connection for wireless temperature sensor. Arduino Nano as a microcontroller for this circuit. In this circuit connection, two mini breadboards need to use because single breadboard not enough to connect the resistor for temperature sensor.

### 22.3.2 Fabrication

This phase reveals the method to manufacture the product from initial ideas to the completed device. It consists of a few steps on doing the fabrication stage. Start by connecting LCD, HC-05, NRF24L01, switch button and keyboard with the Arduino Mega board. Then connect the temperature sensor, NRF24L01 and switch to the Arduino Nano Board. Humidity sensor, NRF24L01 and switch button are connected to the Arduino Nano board. The entire terminal is connected to the right place. Ensure the jumper wire is connected to the selected pot. In this subtopic, we also show some pictures of fabricating the monitor box, wireless temperature sensor box and wireless humidity sensor box. Design the casing for each wireless sensor circuit and monitor box (Figs. 22.6, 22.7 and 22.8).

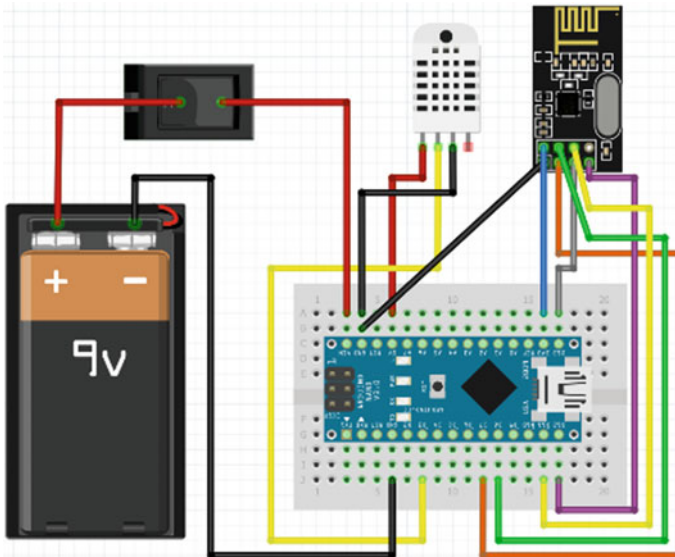


Fig. 22.4 Circuit connection for the wireless humidity sensor



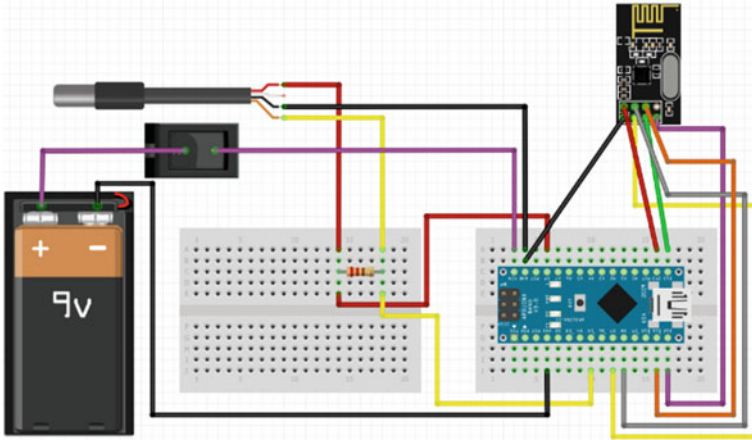
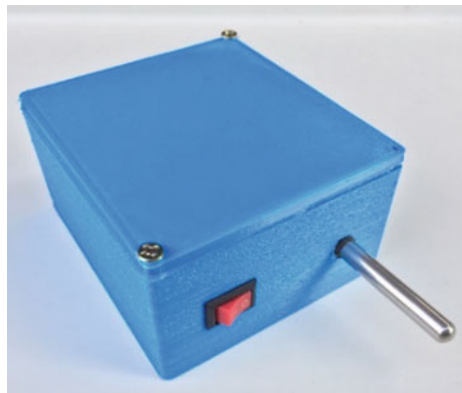


Fig. 22.5 Circuit connection for the wireless temperature sensor

Fig. 22.6 Wireless temperature sensor



Fig. 22.7 Monitor box



**Fig. 22.8** Wireless humidity sensor



**Fig. 22.9** Type of activity



### 22.3.3 LCD Display Sample

The interface of this monitoring device relates to data and information on the LCD. As shown in Fig. 22.9, the first step the user needs to choose is the metabolism of the activity. At the metabolism selection, it has three options of activity which are, for the first options exhibit sit and working while second option is walking. The third option is sit, working and talk. The choice depends on the user to choose the appropriate option to the current situation. Figure 22.10 shows the second step that the user needs to choose is the clothing insulation. The options were divided into three options which is first option is thin, second is medium and third option is thick. Figure 22.11 shows the user needs to enter the BTU value. BTU depends on the types of air conditioners. Each air conditioner has a different BTU. As shown in Fig. 22.12, the monitoring device displayed the indoor temperature ( $T_a$ ), outdoor temperature ( $T_o$ ), relative temperature ( $T_r$ ), relative humidity ( $RH$ ), PMV and power consumption. Figure 22.13 shows the interface of a mobile app consisting of eight variables at the same time that can we monitor.

**Fig. 22.10** Clothing insulation



### 22.3.4 Experimental Setup

This experiment was conducted for two days. The main purpose of this experiment was to monitor the indoor temperature ( $T_a$ ), outdoor temperature ( $T_o$ ), relative temperature ( $T_r$ ), relative humidity ( $RH$ ), PMV and power consumption. One of the reasons why this experiment was conducted for two days was to find out the difference between the actual temperature from the AC system. On the first day of the

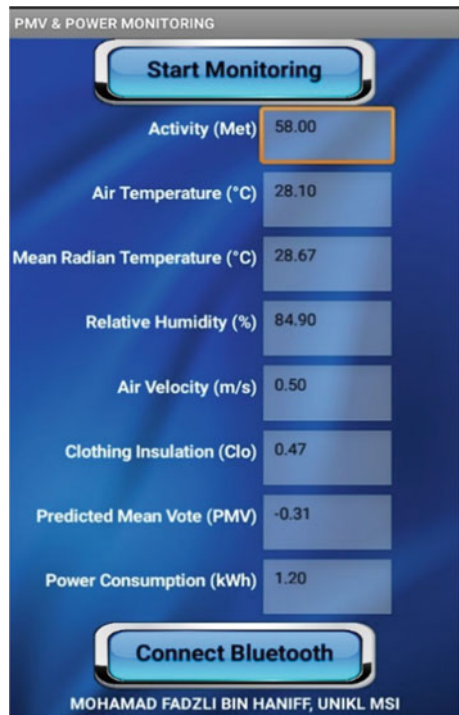
Fig. 22.11 BTU value



Fig. 22.12 Monitoring interface



Fig. 22.13 Mobile app interface



experiment, the actual temperature from the AC system was set up to 22 °C. The next day, the actual temperature from AC was set up to 24 °C. The experiment started at 7:50 am until 3:50 pm. The experiment started at 7:50 am but the AC switched on at 8:00 am and switched off at 3:00 pm. Highest fan speed of the AC system also was set in this experiment. One HP AC system has been used. The area of the room that has been used in this experiment was 2.9 m × 2.2 m, and the room height was 2.5 m.

### 22.4 Results and Discussion

In this experiment that had been conducted,  $T_o$ ,  $T_a$ ,  $RH$ ,  $PMV$  and power consumption was monitored. This experiment is performed to identify the relationship or impact of  $T_o$  on  $T_a$ ,  $RH$ ,  $PMV$  and power consumption. BTU value has been set to 10,000 BTU in this experiment.

As shown in Fig. 22.14, the blue colour line indicates the detections of outdoor temperature ( $T_o$ ) on the first day of experiment, the grey line indicates the reading of  $T_o$  value on the second day of experiment, the orange line indicates the reading of indoor temperature ( $T_a$ ) on the first day of experiment and the last one is the yellow line that indicates the reading of  $T_a$  on the second day of experiment. The  $T_o$  reading pattern on the first day of the experiment is the same as the graft pattern on the second day. The  $T_o$  reading value on the second day decreased slightly from 10:30 am to 10:50 am due to rain for 15 min. The graph pattern shown by the yellow line is higher than the orange line because on the second day the temperature set by the air conditioner is high compared to the first day.

Figure 22.15 shows two lines showing the difference between the outdoor temperature and the indoor temperature. The temperature difference on the first day was

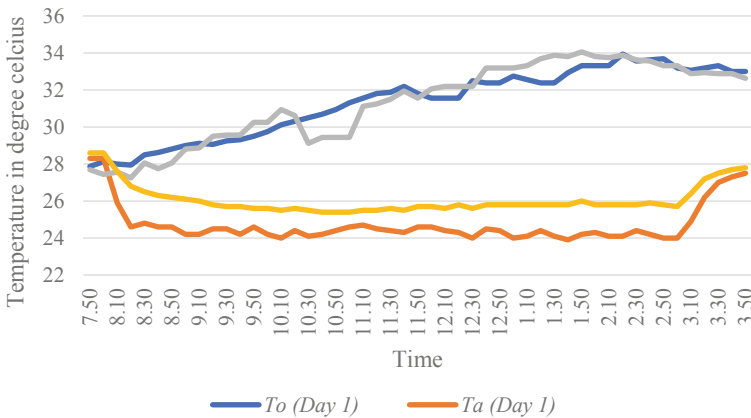


Fig. 22.14 Temperature versus time

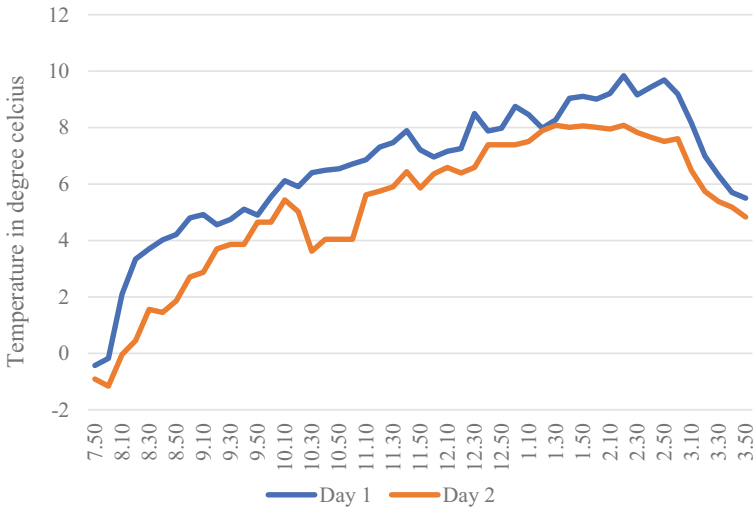


Fig. 22.15 Temperature different between  $T_o$  and  $T_a$

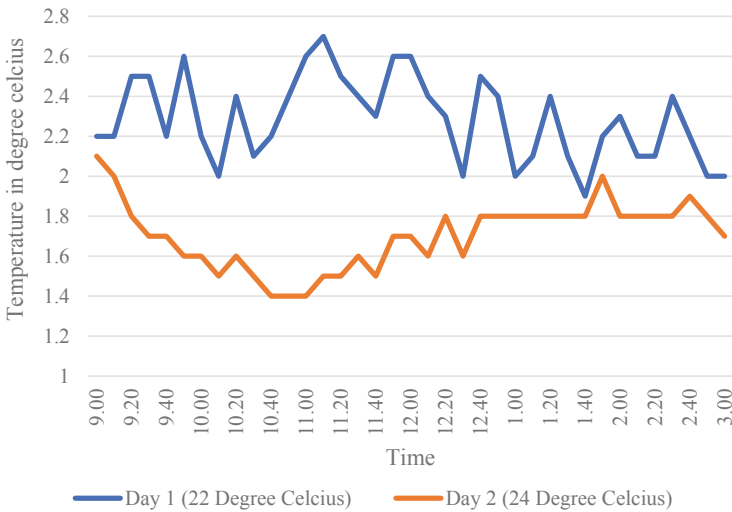
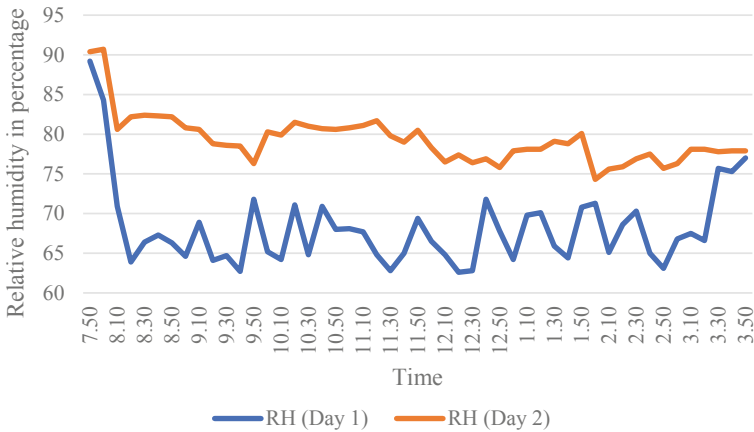


Fig. 22.16 Value difference between indoor temperature ( $T_a$ ) and actual temperature form AC

very significant because the indoor temperature is low, and the outdoor temperature is high. On the second day of the experiment, the difference in graft shows a lower graph pattern compared to the first day of the experiment.

Figure 22.16 shows the value difference between  $T_a$  and the actual temperature from AC. On the first day of the experiment, the actual temperature from AC was 22 °C while on the second day, the actual temperature from AC was 24 °C. The



**Fig. 22.17** Relative humidity

differences between  $T_a$  and the actual temperature from AC system is highest on the first day compared to the second day.

Figure 22.17 shows the relative humidity in percentage collected by the DHT22 sensor during this experiment. The blue colour line indicates the detections of relative humidity value on the first day of experiment and the orange line indicates the reading of relative humidity value on the second day of experiment. The relative humidity is an indication of how much moisture (or vapour) is present in the air and how much air will retain at that temperature. RH readings on the second day were higher than on the first day. This is because the temperature set by the air conditioner is higher than on the first day which is 24 °C. The higher the temperature the higher the relative humidity.

PMV readings are taken from 7:50 am until 3:50 pm as shown in Fig. 22.18. The air conditioner is switched on at 8:00 am and switched off at 3:00 pm. PMV on the first day of the experiment was higher than on the second day due to the difference between  $T_o$  and  $T_a$  is far away.

Power consumption is the form of energy consumption that uses electric energy. Power consumption also influences the actual energy demand made on the existing electricity supply. Figure 22.19 shows two bars of different colours, the blue colour represents the power consumption that had been measured on the first day of experiment and the orange colour represents the power consumption that had been measured on the second day of experiment. The blue colour is higher than the orange colour because the temperature setting of the air conditioner is low. So, power consumption is needed a lot to get the desired temperature.

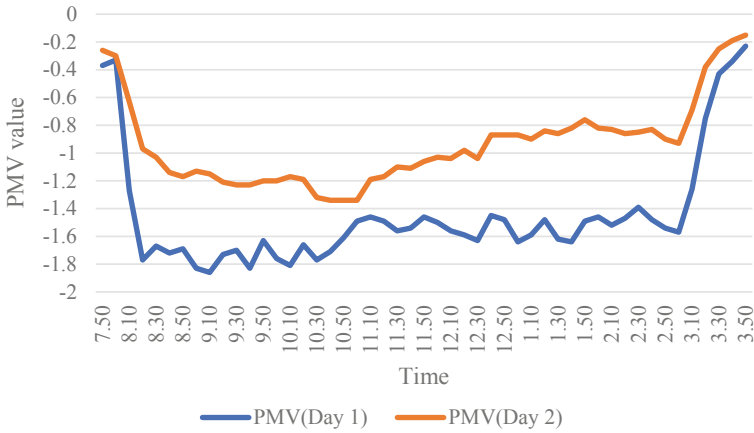


Fig. 22.18 PMV

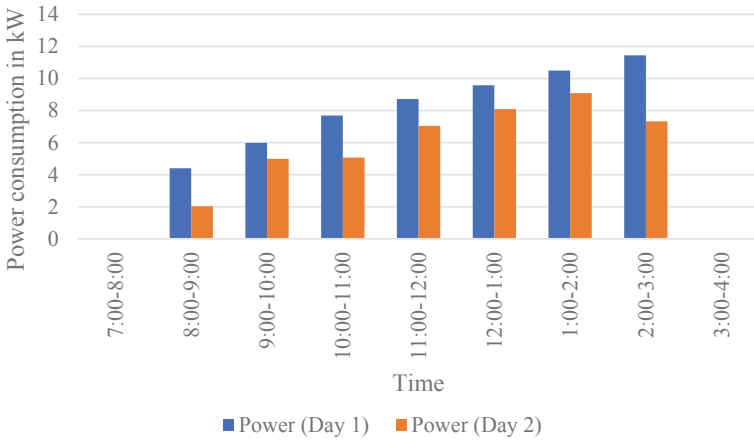


Fig. 22.19 Graph of power consumption

## 22.5 Conclusions

In conclusion, this project had given a positive result regarding developing a comfort index and power consumption monitoring device for AC system using two types of sensors, i.e. the temperature sensor and the humidity sensor. In this project, one of the comfort index had been used, that is, the PMV. PMV values can be obtained through a calculation using six parameters which are the air temperature, mean radiant temperature, metabolism rate, clothing insulation, relative air velocity and relative air humidity. This monitoring system can monitor various variables at the same time. With a monitoring system, the energy consumption can be minimized while retaining

the comfort level. To make this project a success, an experiment was conducted for two days. The main purpose of this experiment was to monitor the variables such as indoor temperature, outdoor temperature, relative humidity, relative temperature, PMV value and power consumption. A monitor box, wireless humidity sensor box and wireless humidity sensor box has been produced in this project. The monitor box is connected to the Android app, where the user can monitor outside of the room using a mobile phone.

## References

1. Sun B, Luh PB, Jia QS, Jiang Z, Wang F, Song C (2013) Building energy management: integrated control of active and passive heating, cooling, lighting, shading, and ventilation systems. *IEEE Trans Autom Sci Eng* 10(3):588–602. <https://doi.org/10.1109/TASE.2012.2205567>
2. Saidur R, Masjuki HH, Jamaluddin MY (2007) An application of energy and exergy analysis in residential sector of Malaysia. *Energy Policy* 35(2):1050–1063. <https://doi.org/10.1016/j.enpol.2006.02.006>
3. Song GS, Lim JH, Ahn TK (2012) Air conditioner operation behaviour based on students' skin temperature in a classroom. *Appl Ergon* 43(1):211–216. <https://doi.org/10.1016/j.apergo.2011.05.009>
4. Mahlia TMI, Masjuki HH, Choudhury IA (2002) Potential electricity savings by implementing energy labels for room air conditioner in Malaysia. *Energy Convers Manag* 43(16):2225–2233. [https://doi.org/10.1016/S0196-8904\(01\)00160-1](https://doi.org/10.1016/S0196-8904(01)00160-1)
5. Liang J, Du R (2008) Design of intelligent comfort control system with human learning and minimum power control strategies. *Energy Convers Manag* 49(4):517–528. <https://doi.org/10.1016/j.enconman.2007.08.006>
6. Fanger P (1984) Moderate thermal environments determination of the PMV and PPD indices and specification of the conditions for thermal comfort
7. Farzaneh Y, Tootoonchi AA (2008) Controlling automobile thermal comfort using optimized fuzzy controller. *Appl Therm Eng* 28(14–15):1906–1917. <https://doi.org/10.1016/j.applthermaleng.2007.12.025>
8. Turner SC, Paliaga G, Lynch BM, Arens EA, Aynsley RM, Brager GS, Deringer JJ, Ferguson JM, Filler JM, Hogeling JJ, Int-hout D, Kwok AG, Levy HF, Sterling EM, Stoops JL, Taylor ST, Tinsley RW, Cooper KW, Dean KW, Peterson JC (1979) American society of heating, refrigerating and air-conditioning engineers. *Int J Refrig* 2(1):56–57. [https://doi.org/10.1016/0140-7007\(79\)90114-2](https://doi.org/10.1016/0140-7007(79)90114-2)
9. Shi Z, Wei J, Wang C (2020) Design of control system for fresh air conditioner. *J Phys: Conf Ser* 1646(1):5670–5675. <https://doi.org/10.1088/1742-6596/1646/1/012115>
10. Kindaichi S, Nishina D, Murakawa S, Ishida M, Ando M (2017) Analysis of energy consumption of room air conditioners: an approach using individual operation data from field measurements. *Appl Therm Eng* 112:7–14. <https://doi.org/10.1016/j.applthermaleng.2016.10.017>
11. Marinakis V, Karakosta C, Doukas H, Androulaki S, Psarras J (2013) A building automation and control tool for remote and real time monitoring of energy consumption. *Sustain Cities Soc* 6(1):11–15. <https://doi.org/10.1016/j.scs.2012.06.003>



# Chapter 23

## A Key Comparative Study Between a Self-Aspirated and an Air-Induced Porous Medium Burner



Ahmad Kamal Ismail, Chan Ping Yi, Mohd Zulkifly Abdullah, Mazlan Mohamed, and Ayub Ahmed Janvekar

**Abstract** Burners have a very vital role in both industrial as well as domestic sector, hence involvement of porous media within them makes their features very efficient and eco-friendly. Most of the conventional porous media burners (PMB) require auxiliary equipment to supply sufficient air in order to assure complete combustion. Though the PMB offer high efficiency, the equipment such as air compressor consumes extra energy that causes the impracticality for domestic use. The self-aspirating technique works by promoting air into the burner system by using the momentum of the fuel jet normally by the fuel nozzle in the burner. In this work, comparative assessment between a self-aspirating and an air-induced PMB has been done. The self-aspirated PMB is capable of producing a flame temperature up to 540 °C while the air-induced PMB maximum flame temperature is 634 °C for uncoated PM and 750 °C for SiC-coated PM. Surface temperatures of the PMB were visualized by a thermal imager which clearly distinguished the flame pattern and concentration between the self-aspirated and air-induced PMB.

---

A. K. Ismail (✉)  
Universiti Kuala Lumpur, Malaysian Spanish Institute, Kulim Hi-Tech Park, 09000 Kulim, Kedah, Malaysia  
e-mail: [ahmadkamal@unikl.edu.my](mailto:ahmadkamal@unikl.edu.my)

A. K. Ismail · C. P. Yi · M. Z. Abdullah  
Universiti Sains Malaysia, Engineering Campus, 14300 Nibong Tebal, Penang, Malaysia  
e-mail: [chan.pingyi@monash.edu](mailto:chan.pingyi@monash.edu)

M. Z. Abdullah  
e-mail: [mezul@usm.my](mailto:mezul@usm.my)

C. P. Yi  
School of Engineering, Monash University, 47500 Subang Jaya, Malaysia

M. Mohamed  
Universiti Malaysia Kelantan, Jeli Campus, 17600 Jeli, Kelantan, Malaysia  
e-mail: [mazlan.m@umk.edu.my](mailto:mazlan.m@umk.edu.my)

A. A. Janvekar  
School of Mechanical Engineering, VIT University, Chennai, TN 600127, India

**Keywords** Combustion · Burner · Porous media combustion · Porous media burner · Cogeneration

## 23.1 Introduction

The emission of hydrocarbons not only pollutes the environment but also contributes to global warming. To tackle this issue, porous medium combustion (PMC) technology has been introduced to minimize the effect of combustion by using conventional burners. The excess enthalpy of combustion produced by PMC has been proven by numerous works to reduce the hydrocarbon fuel usage as well as increase the combustion efficiency and less pollutants.

## 23.2 Literature

Combustion in porous media, which is termed as porous media combustion (PMC), is an interesting technology and is proven to tackle the problem of the environmental pollution and depletion of natural fuel resources compared to free flame combustion [1, 2]. It has the ability to burn ultra-clean fuel mixtures or fuel with lower calorific value, higher power density and lower pollutant emission [3]. Immense work can be found under the hood of porous medium burners [4–6]. For coated PMB, interesting findings can be found from other works [7, 8]. Many investigations have been reported by considering experimental and or numerical approaches [9]. The conventional PMBs are mostly supplied by compressed air which requires an external source of energy to produce efficient burners. There is a need to continuously study the optimum air–fuel ratio for self-aspirated PMB so as to produce a burner with low  $\text{NO}_x$  and CO production as well as good burner efficiency. For combustion using self-aspirating porous media, the problem discovered is the long transition period, i.e. around 1 h for the flame to be changed to steady condition [6, 10–12]. This work provides a comparison between a self-aspirated and an air-induced PMB in terms of equivalence ratio,  $\text{NO}_x$  emission, surface flame temperature and flame concentration for both PMB.

## 23.3 Methodology

Figures 23.1 and 23.2 describe the experimental set up used for the self-aspirating PMB. For the supply or induced air PMB, it can be found from previous work [13] by using compressed air.

In this work, a concept of stoichiometric air–fuel was undertaken. With which the equivalence ratio is attained by supplying the controlled volume of butane and air via

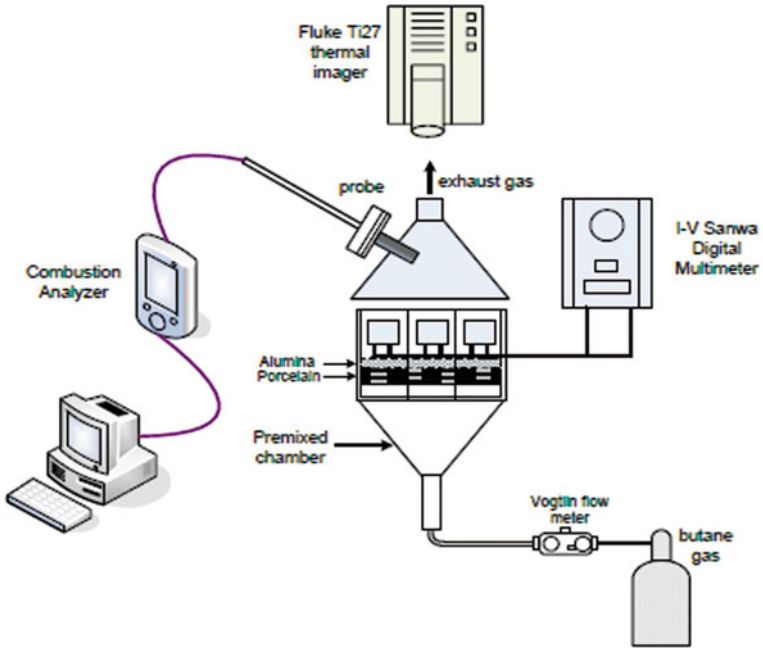


Fig. 23.1 Schematic diagram of the self-aspirating PMB

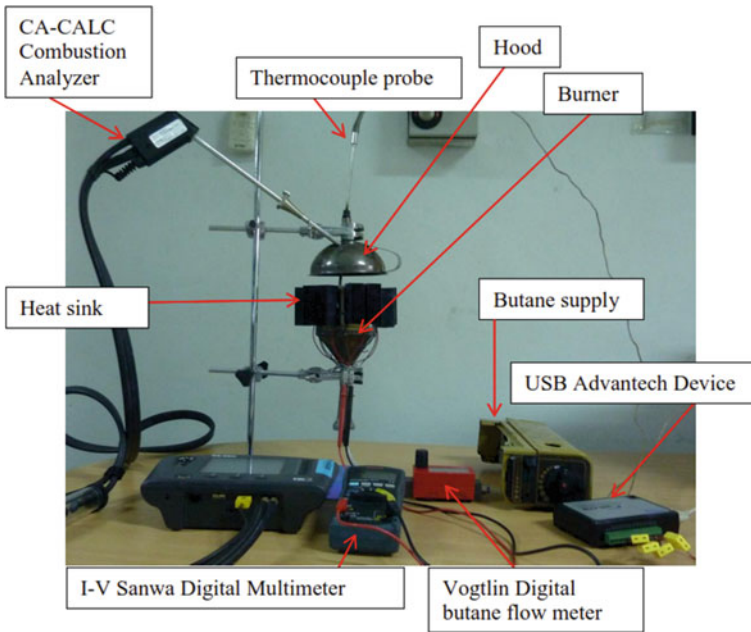


Fig. 23.2 Actual photo of the PMB

proper channels. To track the oxygen content, the gas analyzer was set to the standard oxygen content [14]. It can be noted that in the present scenario the combination of butane-air has the stoichiometric air–fuel ratio by volume which can be taken as 30.95. The other part refers to the actual air–fuel ratio taken, which is directly taken from experimental trials. Furthermore, the mathematical equivalence ratio is denoted as  $\phi$  for the combustion in the self-aspirated PMB by using Eqs. (23.1) and (23.2) [15] where  $O^2$  is the oxygen content,  $A/F$  is the air–fuel ratio,  $PA$  refers to the primary aeration, while  $SA$  is the secondary aeration.

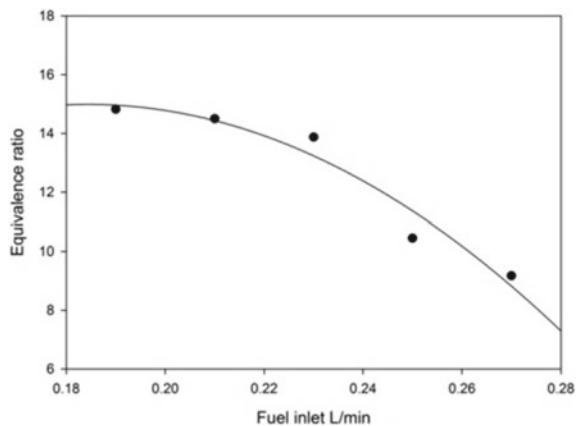
$$PA = \frac{\%O^2}{(A/F)_{stoi} \times [21 - \%O^2]} \times 100 \tag{23.1}$$

$$\phi = \frac{100}{PA \times SA} \tag{23.2}$$

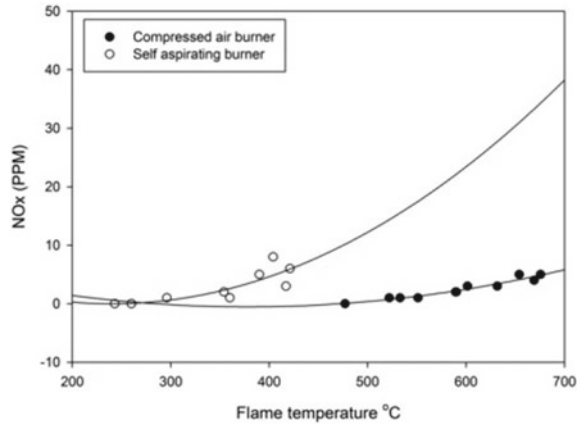
### 23.4 Results and Discussion

Figure 23.3 describes the equivalence ratio of the self-aspirated PMB. It shows that the higher the fuel inlet, the leaner combustion exists due to lower equivalence ratio from 15 to less than 10.  $NO_x$  emission was also lower for the induced air PMB compared to the self-aspirated PMB (Fig. 23.4). Figures 23.5 and 23.6 compare the flame temperature of both PMBs. It was found that at randomly equivalence ratio between 10 to 15, the highest flame temperature for the self-aspirating PMB was lower than 600 °C while for the air-induced PMB using compressed air, the maximum flame temperature was almost 700 °C and higher for the coated PMB at equivalence ratio 1.3 and 1.6. Obviously, the self-aspirating PMB will produce

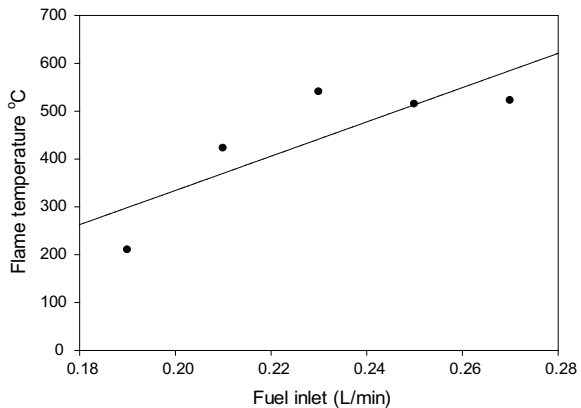
**Fig. 23.3** Equivalence ratio of the self-aspirated PMB



**Fig. 23.4** Measurement of NO<sub>x</sub> released by self-aspirated and air-induced PMB



**Fig. 23.5** Flame temperature produced by the self-aspirated PMB



lower combustion and thermal efficiency and higher NO<sub>x</sub>. Therefore, the design of the self-aspirating PMB needs to be improved to be used for domestic applications.

From Figs. 23.7, 23.8, 23.9 and 23.10 the distinctive characteristics between self-aspirated and air-induced type of porous media burner can be noticed. This was achieved using a digital thermal imager. The device model used to get these digital images was the Fluke Ti27. A clear distribution of color across the selected contour helps to portrait the variations of temperature distributions. The red color indicates the maximum temperature. In addition, the device capability was to measure a maximum of 620 °C. When the temperature reading with respect to the self-aspirated PMB was lower than the maximum capacity of the thermal imager, the reading was found out to be 595.3 °C at a fuel input of 0.19 L/min. While with a fuel input of 0.25 L/min, the temperature recorded was 550 °C for self-aspirating PMB. At 0.19 to 0.25 L/min, temperature on the surface of the burner was more than >620 °C for the air-induced PMB. A unique observation can be made by comparing the image that the color distribution is more scattered. The scattering of color was due to the

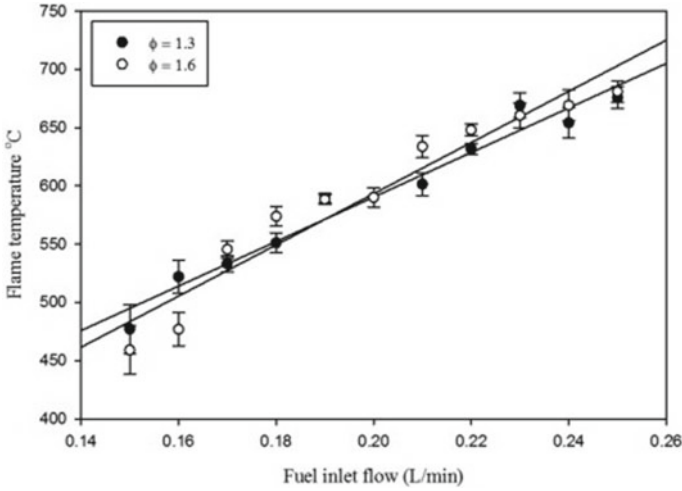
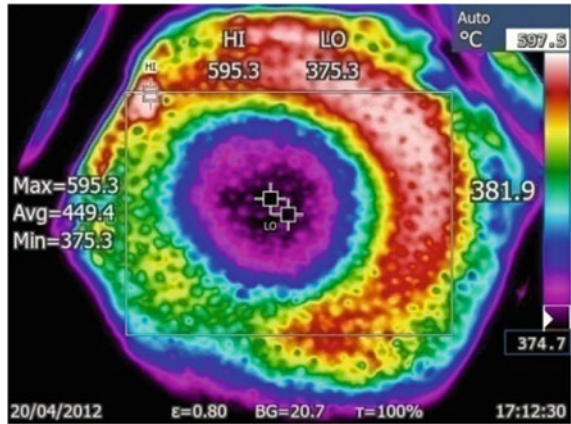


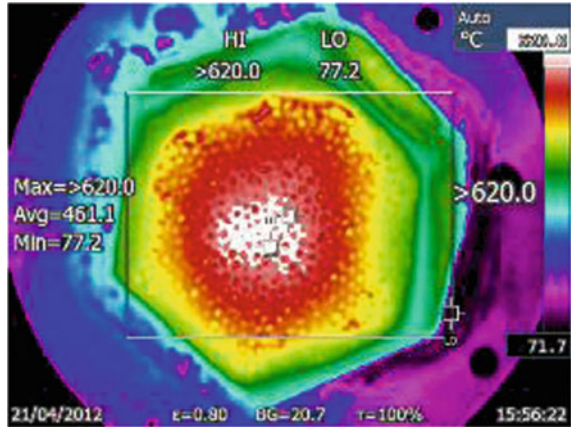
Fig. 23.6 Flame temperature produced by the air-induced PMB

Fig. 23.7 Self-aspirating at fuel input 0.19 L/min

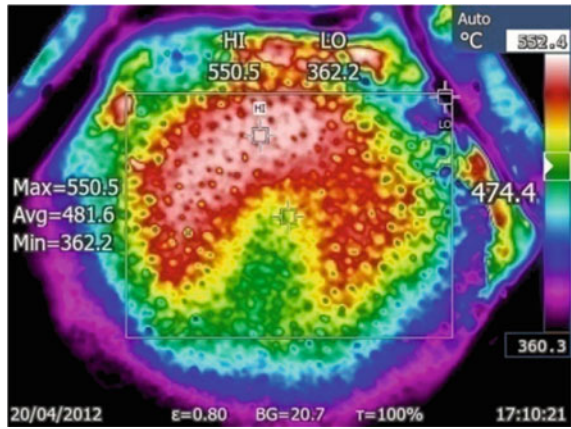


low inlet pressure produced by the self-aspirated PMB. On the other hand, the flame concentration and intensity were very significant and can be seen clearly for the induced air PMB.

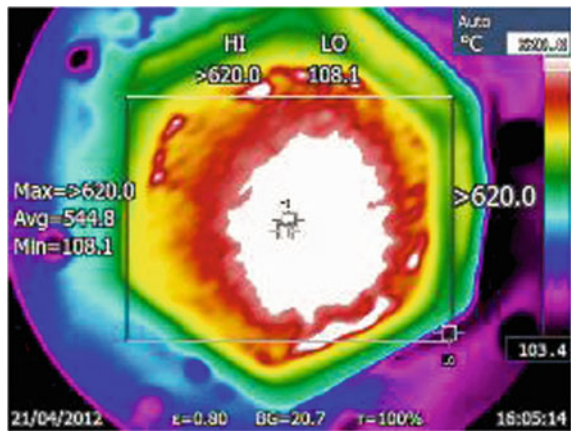
**Fig. 23.8** Air-induced at fuel input 0.19 L/min



**Fig. 23.9** Self-aspirating at fuel input 0.25 L/min



**Fig. 23.10** Air-induced at fuel input 0.25 L/min



## 23.5 Conclusions

The addition of porous media results in an increased, i.e. an improved performance of the burner. It was clearly observed that the PMB with self-aspirated air supply has lower flame temperature compared to the air-induced PMB while the  $\text{NO}_x$  produced was also higher. This indicated that the incomplete combustion in the self-aspirated PMB occurred while the air-induced PMB achieved proper combustion. The flame stabilization and concentration in the self-aspirated PMB were also poor compared to the air-induced PMB by using an air compressor. Further investigation in the design of the self-aspirated PMB is needed in order to improve the performance as well as reduce the emission. Therefore, the self-aspirated PMB can be used for domestic applications.

## References

1. Mujeebu MA, Abdullah MZ et al (2009) Combustion in porous media and its applications—a comprehensive survey. *J Environ Manage* 90(8):2287–2312
2. Mujeebu MA, Abdullah MZ et al (2010) Trends in modeling of porous media combustion. *Prog Energy Combust Sci* 36(6):627–650
3. Wood S, Harris AT (2008) Porous burners for lean-burn applications. *Prog Energy Combust Sci* 34(5):667–684
4. Janvekar AA, Abdullah MZ et al (2018) Experimental and numerical studies of porous media combustion in micro burner. *J Adv Res Fluid Mech Thermal Sci* 43(1):112–120
5. Janvekar AA, Abdullah M, et al (2018) Investigation of micro burner performance during porous media combustion for surface and submerged flames. *IOP conference series: Materials science and engineering*
6. Janvekar AA, Abdullah M, et al (2019) Development of foam porous media to undergo surface and submerged flame during premixed combustion. *IOP conference series: Materials science and engineering*, IOP Publishing
7. Ismail AK, Abdullah MZ et al (2016) Effect of ceramic coating in combustion and cogeneration performance of  $\text{Al}_2\text{O}_3$  porous medium. *J Energy Inst* 89(1):81–93
8. Janvekar AA, Abdullah M, et al (2017) Assessment of porous media burner for surface/submerged flame during porous media combustion. *AIP conference proceedings*. AIP Publishing LLC
9. Ismail A, Ibrahim N, et al (2018) A practical approach in porous medium combustion for domestic application: a review. *IOP conference series: Materials science and engineering*. IOP Publishing
10. Janvekar AA, Abdullah M, et al (2018) Experiential study on temperature and emission performance of micro burner during porous media combustion. *IOP conference series: Materials science and engineering*
11. Janvekar AA, Abdullah M et al (2018) Assessment of porous media combustion with foam porous media for surface/submerged flame. *Mater Today Proc* 5(10):20865–20873
12. Yoksenakul W, Jugjai S (2011) Design and development of a SPMB (self-aspirating, porous medium burner) with a submerged flame. *Energy* 36(5):3092–3100
13. Ismail AK, Abdullah MZ et al (2013) Application of porous medium burner with micro cogeneration system. *Energy* 50:131–142
14. Karg R (1998) Air-free measurement of carbon monoxide emissions from gas ranges: analysis and suggested field procedure. *RJ Karg Associates*



15. Namkhat A, Jugjai S (2012) Prediction of total equivalence ratio for a self-aspirating burner. *J Res Appl Mech Eng* 1(2):31–36

## Chapter 24

# Analysis of the Lower Control Arm in a Front Suspension System Using Finite Element Analysis and Analysis of Variance (ANOVA) Method



**A. N. Ridzwan, A. R. A. Kadir, I. A. Azid, M. N. A. Hamid, T. A. A. Razak, and M. N. Ahmad**

**Abstract** In this paper, the existing lower control arm structural analysis and performance were investigated and analyzed by the implementation of reversed engineering method used in designing the three-dimensional model referring to the actual part. The initial design is modeled by using SolidWorks 2016 software and validated by using modal analysis method in Abaqus CAE. The natural frequencies can be compared with the load impact testing experiment to the actual part physically to determine the percentage deviation. After the model was validated, Abaqus CAE software used to analyze the structural strength-ability in a static condition. The result will be the main reference in creating the new design concept of the ASHIMORI lower control arm as the Abaqus CAE will be used for the finite element analysis process. The target safety factor of the all-new design must be lower than the actual concept which is defined between the different design and material. The main factor will be determined by using Analysis of Variances (ANOVA) method and the final design will be compared with the actual part focusing on the maximum stress value, performance and structural analysis in a static state.

---

A. N. Ridzwan (✉) · A. R. A. Kadir · I. A. Azid · M. N. A. Hamid · T. A. A. Razak · M. N. Ahmad

Engineering Section, Malaysian Spanish Institute Kulim Hi-Tech Park, Universiti Kuala Lumpur, 09000 Kulim, Kedah, Malaysia  
e-mail: [naqilah.ridzwan@s.unikl.edu.my](mailto:naqilah.ridzwan@s.unikl.edu.my)

A. R. A. Kadir  
e-mail: [ahmadrazlee@unikl.edu.my](mailto:ahmadrazlee@unikl.edu.my)

I. A. Azid  
e-mail: [ishak.abdulazid@unikl.edu.my](mailto:ishak.abdulazid@unikl.edu.my)

M. N. A. Hamid  
e-mail: [mnajib@unikl.edu.my](mailto:mnajib@unikl.edu.my)

T. A. A. Razak  
e-mail: [tajuladli@unikl.edu.my](mailto:tajuladli@unikl.edu.my)

M. N. Ahmad  
e-mail: [mohdnizam@unikl.edu.my](mailto:mohdnizam@unikl.edu.my)

**Keywords** Design · Lower control arm · Front suspension system · SolidWorks · Abaqus CAE · Automotive · ANOVA · Material performance

## 24.1 Introduction

Suspension system is one of the systems that includes shocks, linkages and springs, positioned at the lower front side of the car body that is connected to the chassis frame and wheels. The main function of the suspension system is to support the whole weight of the vehicle and instantly to control the ride quality, handling the abilities and the dynamics motion created. In the development of automobile industry, the suspension system components are very crucial in maintaining the driving efficiency and satisfaction as the suspension supports the structure body and absorbs all pressures between the body of the vehicle and road. The double-wishbone suspension and the Macpherson Strut system are the most prevalent types of front independent suspensions. The front side suspension component must maintain the wheel of the vehicle that aligns all over the road, restricting the body movement of the vehicle during steering and when moving over bumps, and providing a convenient and quiet ride. In this study, Macpherson strut system with lower control arm is considered. The previous research found that the lower control arm can function as a better shock absorber because of the position and load-bearing capacities. Lower control arms that are positioned on the left and right side are the most core components of a suspension. This part functions as the controller that allows the up and down motion of the wheel. The control arms are also assembled with other crucial parts in front suspension system such as steering knuckle, tie rod, coil spring and shock absorber. Lower side end of the spine is mounted to the top of the steering knuckle, and the lower end of the knuckle is connected to the ball joint in the lower control arm in MacPherson Strut systems. The top of the strut is attached to the frame by an upper strut frame. These systems are compact and optimal for smaller cars because the upper control arm is not included.

The relationship of the lower control arm that is positioned under suspension system requires a strong material as it undergoes a cyclic load, extreme driving condition and any irregularities that occurs on the road. Consideration of the material also depends on the weight ratio as the heavier the material, the higher the impact that will affect the structure of the lower control arm. The research found out that the stress analysis experienced by steel and aluminum alloy was about the same value that are 471 MPa and 470 MPa, respectively. At the end of the findings, conclude that the structural strength of the lower control arm can be manufactured by using both material as it was safe to be used [1]. Another research study was also carried out focusing on the materials selected, which were analyzed for the stress, deformation and the allowable stress for the safety. The selected materials were Gray Cast Iron, Stainless Steel 321, Aluminum Alloy, Mg Alloy AZ63T1 and Ti Alloy T1-6Al-4V. The result of the Aluminum and Magnesium accumulated higher stress than the allowable that automatically cannot be considered. Stainless steel has less

weight as 11.58% compared with other and 11.36% less stress. The material also has higher allowable strength than the structural steel. The comparative study of FEA and experimental result is about 4.58%. Stainless steel 321 is the best material that suited for the lower control arm purposes. Different from the research study implemented by Mohanraj and Manavalasundaram [2] stated that the selected material is depending on several characteristics that are availability, malleability, formability and mechanical properties.

To validate the 3D model created by using the selected software, the design model needs to be validated to ensure the originality concept design of the part compared with the actual part which was about 70% similar. Li et al. [3] stated that the natural frequencies and vibration mode shapes were obtained via measurement in LMS Test Lab. The frequency response functions were identified and computed by force and acceleration signals, and then mode shapes of this morphing wing structure were subsequently identified by PolyMAX modal parameter estimation method. FEM modal analysis was also implemented, and its numerical results convincingly presented the mode shape and natural frequency characteristics were in good agreement.

The calculation of load on the statics condition being analyzed by Singh [4] as considering the weight at the center of gravity on the study of Statics Structural Analysis of Suspension Arm By Using Finite Element Method. From the weight of the car, 0.39% was approximately supported by the front wheels and 0.61% by the rear wheels. The force analysis determined by the study of a New Design Optimization of Light Weight Front Lower Control Arm [5] was different from the other researcher as strength analysis was based on the suspension abusive load case that was evaluated from the PROTON model derived from the multibody dynamics (MBD) analysis of the suspension system. Total gross weight of the car is 1,500 kg and Kerb weight is 1,065 kg. In conducting the static analysis for the front weight distribution were assumed 40% for the rear part and the other support by the front weight.

The redesign suspension arms achieve an average weight saving of 27% with respect to the baseline steel arms. The natural frequency of composite material is higher than steel [6]. The other research stated that the base concept design was optimized based on standard suspension abusive load cases loading at FLCA hard point. The topology optimization is a method to optimize the design in design space with the constraint of loads and some boundary conditions. It is a stress-based optimization through load path on the geometry. This process was done in several iterations to get the optimum minimum of 20% weight reduction [5]. The linear weighing method used for the CA model under multiple loads can be expressed according to the specific formulation. The table below shows the six load cases used in the topology optimization of the CA [7].

In this paper, FEM was employed to investigate the high-stress region in order to know the exact part experiencing it as the static load's structural analysis was carried out in lower control arm in front suspension system. Then to get the actual result. When the vehicle passes on the road, it shows the high impact loads that will wear out the lower control arm as the critical part in the suspension system especially in extreme conditions, for example, potholes and bumpers.

There are three main objectives in this project.

1. To design the three-dimensional (3D) model and analyze the statics and dynamics structural analysis of the existing lower control arm.
2. To determine the main factors that affect the results of the structural performance and strength analysis of the new design by using ANOVA method.
3. To compare the existing analysis component design with the new design to improve the strength and function-ability of the product.

## **24.2 Methodology**

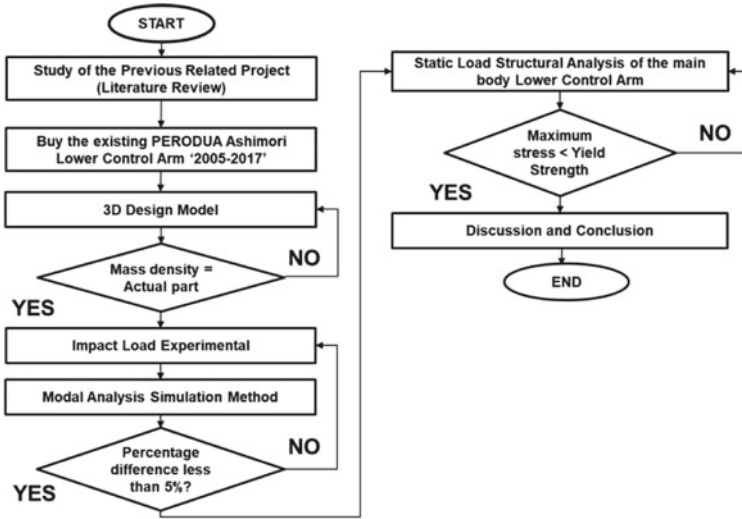
Five main processes were utilized in this research study. These processes were the design models of the existing lower control arm part: statics structural analysis, impact load testing experimental analysis, validation process by modal analysis and design modifications and determination of main factor by using ANOVA method. The last process was the statics structural analysis.

### ***24.2.1 Three-Dimensional Design Model***

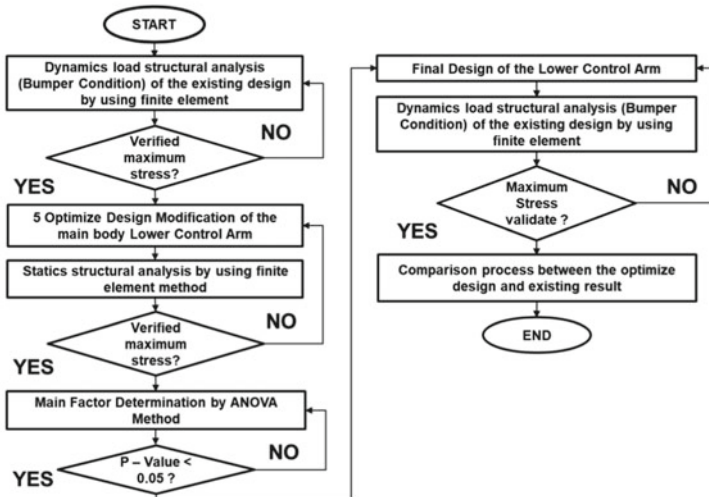
In this process, the reverse engineering method implemented as to get the initial concept design of the existing lower control arm as shown in Fig. 24.1 in which the obtained design of the model. SolidWorks 2016 software is used to design the three-dimensional model of the lower control arm. To prevent any significant changes to the external parts, the hard points of the lower control arm and withstand the same kinematics output, the general L-shape and parameter of the product remain to avoid any major changes that will affect the analysis result. After completing the 3D model of all the parts, the material for this main body lower control arm is established as Mild Steel specification. The mechanical properties of the material had fully inserted in the material library. The actual mass of the existing Ashimori Lower Control Arm is specified at 3 kg. In SolidWorks, the mass density of the three-dimensional design model is 3.14 kg. The design model is considered as 70% similar to the actual part (Fig. 24.2).

### ***24.2.2 Statics Structural Analysis of the Main Body Part***

The statics load structural analysis is the process to determine the loading applied to lower control arm, maximum value of stress and critical area that will experience the high impact load. The result from this section will be used in the simulation, and the failure of the part when the specified load is applied can also be identified. The analysis that will be carried out is based on the statics condition of the car. The statics



a) Phases 1



b) Phases 2

Fig. 24.1 Flowchart of the methodology for phase 1 and phase 2

load that will be applied was determined based on the Kerb weight of the vehicle. The load calculated specifically to the right-side wheel of the front suspension system is based on the parameter that is shown on the PERODUA MYVI specification and the position of the center of gravity (CG). The technical specification was listed on Table 24.1 that requires the load calculation (Fig. 24.3).

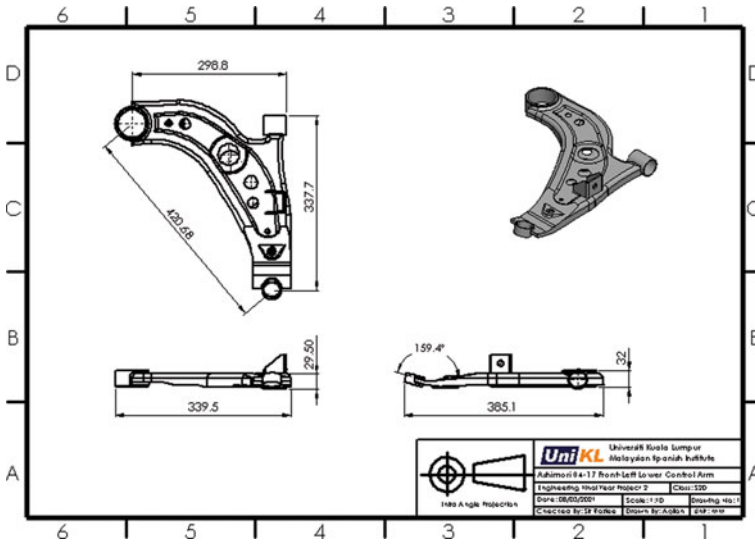
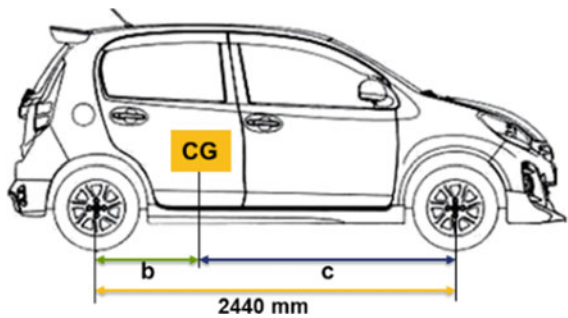


Fig. 24.2 Technical drawing of the 3D model

Table 24.1 The technical specification of PERODUA Myvi

Term	Details
Kerb weight	955 kg
Cargo volume	277 L
Front weight	60%
Rear weight	40%
Height	1,515 mm

Fig. 24.3 PERODUA MYVI specification. CG: Center of gravity of the car, b: Distance between the CG and rear wheel, c: Distance between the CG and front wheel



To determine the Kerb weight in Newton unit, the Kerb mass of the car needs to be multiplied with the standard gravitational force =  $9.81 \text{ m/s}^2$

$$G = m \times g = \text{Total weight (N)}$$

$$\begin{aligned}
 &= 955 \text{ kg } (9.81 \text{ m/s}^2) \\
 &= 9368.55 \text{ N}
 \end{aligned}
 \tag{24.1}$$

Solution:

Based on the vehicle parameter, the Kerb weight of the vehicle needs to be equally divided according to the position of the center of gravity (CG) stated. The distance between the CG to the front wheels is 2.5 m and the distance between the CG to the rear wheels is 0.725 m.

Static load (N) of front wheels

Load applied to the front wheels.

$$\begin{aligned}
 \text{GFA} &= G (b/b + c) \\
 &= 9368.55(0.725/2.5) \\
 &= 2716.88 \text{ N}
 \end{aligned}
 \tag{24.2}$$

Static load (N) of rear wheels

Load applied to the rear wheels.

$$\begin{aligned}
 \text{GRA} &= G (c/b + c) \\
 &= 9368.55(1.775/2.5) \\
 &= 6,651.70 \text{ N}
 \end{aligned}
 \tag{24.3}$$

The load supported by the front wheels needs to be divided into two in order to determine the one side of the load supported.

Static load (N) of a wheel from the front suspension

$$\begin{aligned}
 \text{GFAW} &= \text{GFA}/2 \\
 &= 2716.88/2 \\
 &= 1,358.44 \text{ N}
 \end{aligned}
 \tag{24.4}$$

The load supported by the rear wheels needs to be divided into two in order to determine the one side of the load supported.

Static load (N) of a wheel from the rear suspension.

To pressure is the parameter that will be applied in the finite element analysis that reflects the surface area of the part. The total surface area is 1,069.05 mm<sup>2</sup>

$$\begin{aligned}
 &\text{Pressure (MPa)} \\
 P &= \text{Load/Total Area} \\
 \text{Total Area} &= 1069.05 \text{ mm}^2
 \end{aligned}
 \tag{24.6}$$

The final pressure value will be used in defining the load in the finite element analysis.



$$P = \text{Load/Total Area} = 1358.44/1069.05 = 1.27 \text{ MPa} \quad (24.7)$$

The load that is supported by the right wheel is about 1358.44 N. This is the load that will be applied on the simulation analysis. The other parameter that can be used for the statics structural analysis is the value of the pressure. The pressure value calculated in this situation is about 1.27 MPa.

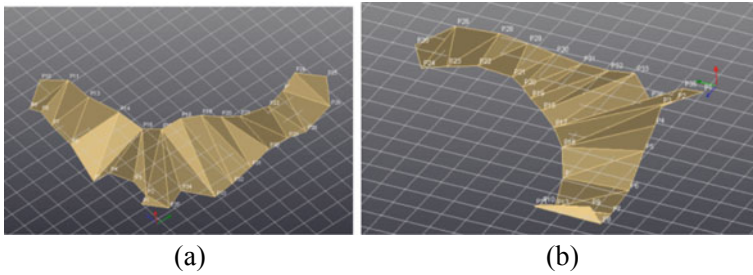
### 24.2.3 Load Impact Testing Experimental

The beginning of the experimental setup, the coordinate of the lower control arm in unit mm was identified to get the specified point that the impact load will be applied. The coordinate data was imported to the Test.lab Impact Testing Software to visualize the geometry of the part. After the geometry surface point is generated, the point was connected to each other to create the realistic and informative animated displays. This is the important process to avoid any changes that may affect the result of the natural frequency. The setup of the experiments starts by placing the lower control arm in hang-up position by using the supporting stand and the rope. The hang-up position will make the natural frequency become easier to detect. The accelerometer will be the connector of that part to the system. Figure 24.4 shows the hang-up position of the lower control arm.

Hit the marked point on the lower control starting from point 1 till point 35. Each point will be hit three times, to get the average result of the applied load. If the applied load is higher than the normal range, the data will automatically be deleted. The different modes were generated with different deflections, and the frequency will be analyzed. Then, the natural frequency result of the LMS Test.lab Impact Load Testing will be compared with the simulation result (Fig. 24.5).



Fig. 24.4 The hang-up position of lower control arm (a) and the top view (b)



**Fig. 24.5** The deflection mode 1 (a) and mode 3 (b)

### 24.2.4 Modal Analysis Simulation

To proceed with the statics structural analysis, the actual design concept model was validated first by comparing the natural frequency of the simulated lower control arm with the impact load testing experimental to the actual part. Abaqus CAE software is used to simulate the modal analysis to determine the value of the natural frequency. The 3D design model from the Solid Works is transferred to Abaqus via IGS file (Table 24.2).

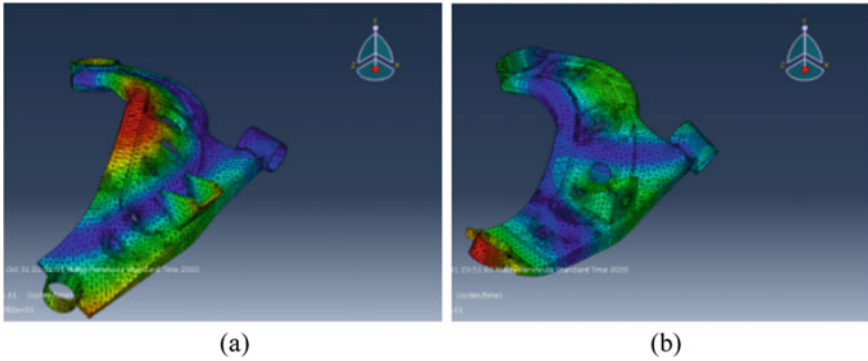
In creating the step in Abaqus CAE software, the procedure type will be Linear Perturbation, and frequency was selected because the purpose of the simulation process is to determine the natural frequency of the product. Throughout a truly nonlinear analysis, linear perturbation analyses can be conducted from time to time by adding the linear perturbation steps between the general response steps (Fig. 24.6).

Then the process continued with the simulation method, and the boundary condition of the part was set according to the specification below (Fig. 24.7 and Table 24.3).

The part that is applied with pressure is at the ball joint part. This is because the ball joint is the critical part that is connected to the steering knuckle part. The other front and rear bushings are fixed in terms of degrees of freedom meanwhile the rotational is not fixed (Fig. 24.8).

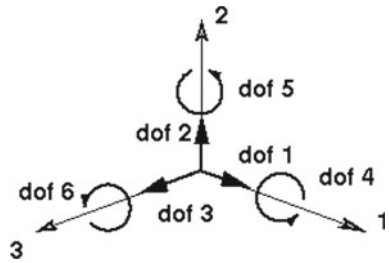
**Table 24.2** The mechanical properties of plain carbon steel

No	Mechanical properties	Value
1	Mass density (ton/mm <sup>2</sup> )	7.85 e-9
2	Young's modulus (N/mm <sup>2</sup> )	200,000
3	Poisson's ratio	0.29
4	Yield strength (MPa)	245
5	Plastic strain	0



**Fig. 24.6** The modal analysis result for mode 1 (a) and mode 2 (b)

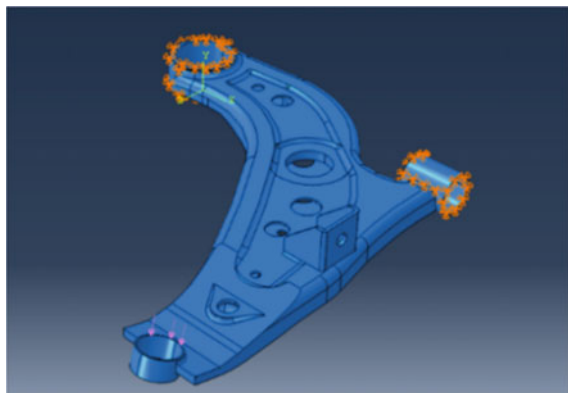
**Fig. 24.7** Boundary condition directional



**Table 24.3** Lower control arm boundary condition

Part fixed	U1	U2	U3	UR1	UR2	UR3
Front bushing, B		0	0		0	0
Rear bushing, A	0	0		0	0	











**Fig. 24.8** The boundary and loading condition



### 24.2.5 Design Modifications

The new design is being modified based on the high-stress region that is appointed based on the statics structural analysis resulted from the previous process. The modification was divided into two parts that were major and minor changes. Minor changes are only applicable at the appointed region that is about 15% differences from the actual meanwhile the major changes focusing about 50% changes. There are several design ideas from the other brands implemented in this new design as the changes are focusing on the shape as the base concept design of lower arm remains the same. The main factors determined in this part are material and design structure (Table 24.4).

**Table 24.4** The design modifications

Design	Top side	Back side
1 (Major)		
2 (Major)		
3 (Major)		
4 (Minor)		
5 (Minor)		

### 24.2.6 Determining Factor of Analysis by Using ANOVA Method

Based on the results of the analysis of all the new designs, the data was collected as the tabulated data and will be inserted by using ANOVA tools in Minitab 19 software. The data needs to pass all the assumptions for the two-way analysis, as the data was normally distributed and  $P$  value more than 0.05.

## 24.3 Result and Discussion

### 24.3.1 Modal Analysis with LMS Load Impact Testing Result

In this study, the part that is connected with the stabilizer bar, front bushing, rear bushing and ball joints were ignored to reduce any unnecessary complexity. The result is based on the first six modes shapes that are illustrated in table below (Fig. 24.9).

Based on the result, the modes can be classified that the result of the experimental and simulation modes are almost similar, for example, at the first mode is bending. The percentage deviation between the results is about 0.8578%. The data is still valid because the difference is still in range from 0.1 to 0.99%. Based on the geometry shape of the load impact testing experiment compared with the modal analysis in the Abaqus Software, the deflection shape of both the simulations are almost similar. However, the data of the natural frequency identified is specifically in detail shows the percentage difference between the result. The three-dimensional design model created in the SolidWorks software is verified and can be used in other simulation analysis.

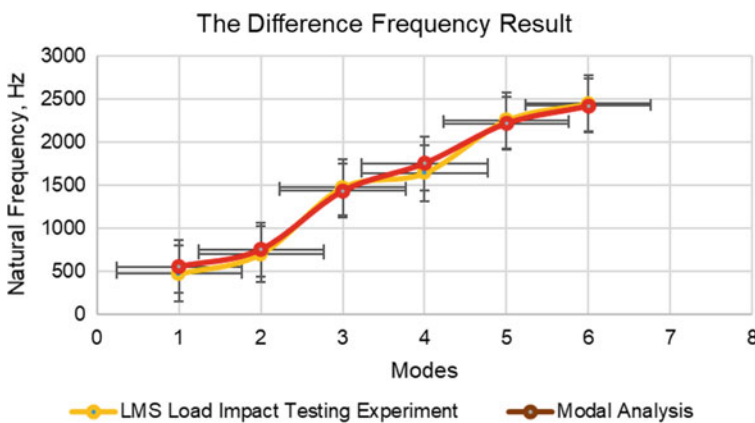
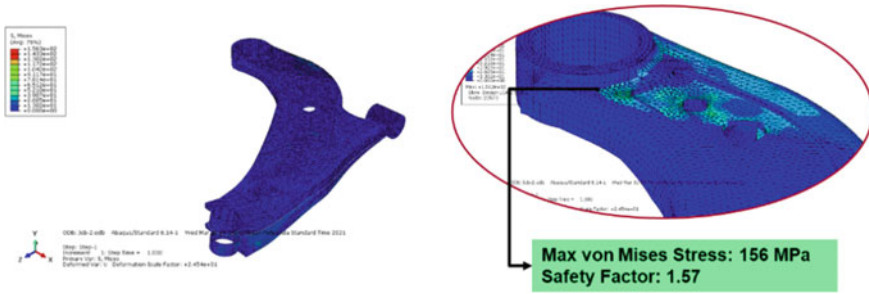


Fig. 24.9 The graph result for the comparison



**Fig. 24.10** The maximum von Misses stress

### 24.3.2 Statics Load Structural Analysis of Lower Control Arm

Based on the result shows, the value of the maximum Von-Mises stress is 156 MPa and the stress area is located at the rear bushing. The safety factor of this part is 1.57. The maximum stress is valid because the data is lower than the value of yield strength of the material (Fig. 24.10).

Referring to the stress–strain curve, the data is in range as it does not exceed the limit value of the yield strength as the elastic limit of the material. The part will return to its original shape when the load is applied. The value of the safety factor is also accepted as still in the good range that is one to five. The conclusion from this data is the value of the maximum stress experienced by the lower control arm when statics load applied is acceptable as the weight applied only regarding the Kerb mass of the car with no passengers and driver. The deformation result for the statics structural analysis is about 0.9 mm. This result defined that when the load is applied to the lower control arm. The deformation length is still in range and will return to the actual size of the lower control arm. The results also show that the deformation is still under control as the structure of the lower control arm is strong and will not cause any effect that will lead to the failure of the product.

### 24.3.3 Statics Structural Analysis Result of the New Modified Result

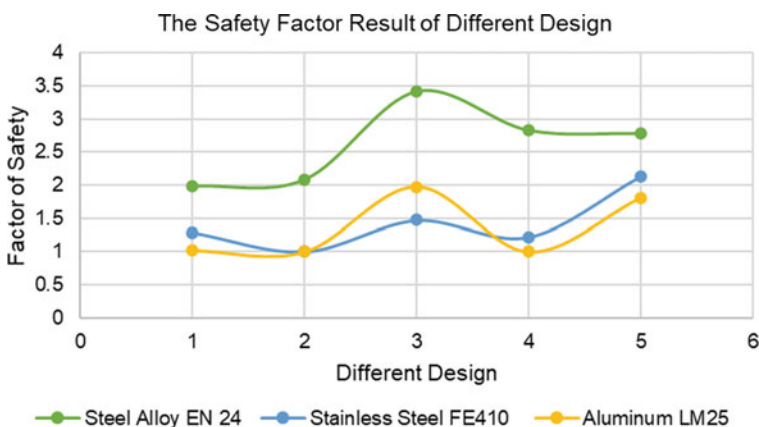
The five new design modifications have been analyzed onto the statics structural analysis by using Abaqus CAE software and the result of each design has been calculated to measure the strength–ability of the parts. Results from the analysis will show the structural design modification and the selected material performance when the load been applied toward the lower control arm. Based on Table 24.5, the maximum stress analysis from different designs and materials is shown. All the result data is then calculated with the yield strength of the material to get the value of the

**Table 24.5** The maximum stress result for different designs

Design	Type of material (MPa)		
	Steel alloy EN 24 (680 MPa)	Stainless steel FE410 (290 MPa)	Aluminum LM25 (235 MPa)
Design 1	343	224	230
Design 2	326	290	235
Design 3	199	198	119
Design 4	148	148	148
Design 5	245	136	131

factor of safety. The analysis will be evaluated based on the maximum stress value, factor of safety and stress region that accumulated from the load applied. Referring to the result of the analysis, the different designs, the major and minor changes result is almost the same. The percentage difference between the design is about 0.5%. This finding shows that the design modification main factor is the location of the changes, not the percentages different of it. The design with 50% changes different from the actual one also shows a similar value of the maximum stress of the minor changes. However, the design modification needs to be focused on the stress region part other than the target of creating the new design as it can save the cost and time to develop a new design.

The safety factor results shown in Fig. 24.11 indicate that the performance differences between the major and minor changes were smaller, the conclusion that can be concluded from the result is the minor 15% changes still acceptable, as the changes point is focusing on the hard point of the lower arm that also can change the lower control arm performance result. In terms of others, design 3 has the highest factor of safety even when it was analyzed by other materials. The compatible material



**Fig. 24.11** Safety factor result

**Factor Information**

Factor	Type	Levels	Values
Yield Strength (MPa)	Random	3	235, 290, 680
Design	Random	5	1, 2, 3, 4, 5

**Analysis of Variance for Factor of Safety**

Source	DF	SS	MS	F	P
Yield Strength (MPa)	2	12.9400	6.47001	21.78	0.001
Design	4	7.0101	1.75252	5.90	0.016
Yield Strength (MPa)*Design	8	2.3766	0.29707	20.81	0.000
Error	30	0.4282	0.01427		
Total	44	22.7549			

**Model Summary**

S	R-sq	R-sq(adj)
0.119471	98.12%	97.24%

**Fig. 24.22** ANOVA analysis

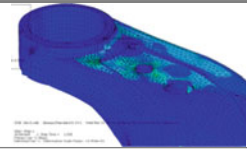
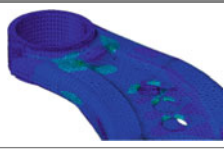
that can be used for the next product is Steel Alloy EN24 because of the material properties that tend to high allowable stress that can sustain the static load applied. In terms of weight reduction, design 3-EN24 is five percent lighter compared with the existing design as the added value that can be used as the other supporting point.

**24.3.4 Main Factor Analysis Result by using Analysis of Variance (ANOVA)**

The result from the ANOVA method shows that the new design modifications were basically high interact with the type of material than the different designs of the shape. The data analysis can be shown as Fig. 24.22.



### 24.3.5 Comparison of Final Design and Existing Final Design Project

Part view	Existing	Design 3-EN 24
Stress region of the top side part		
Maximum stress value (MPa)	156	199
Yield strength (MPa)	245	680
Factor of safety	1.57	3.42
Deformation (mm)	1.33	1.17
Dynamics maximum stress value	245	389

The comparison of the table above shows that the stress region accumulated by the new design is less than compared to the existing part. The stress is equally distributed to the other region instead of only focusing on the major position that needs to be improve from time to time. The blue region of Design 3-EN24 is less, green color on that part means the stress is distributed to the other parts. The objective of the modified design had been achieved as the new design shape idea has a higher safety factor compared with the existing one.

## 24.4 Conclusions

The main objective of this research is to analyze the maximum stress region area when the load is applied to the existing model of lower control arm by designing 70% accuracy of the three-dimensional design model to the actual part and transferred it for the finite element analysis in Abaqus CAE. The result analysis found has proven that the existing lower control arm tends to failure based on the safety of factor and suspected region that appointed at a specific region area. If more load is applied to that part, the fatigue life of the part will be short. The design needs to be modified and improved in several iterations to get the optimized design that is safe to use and longer fatigue life.

This research can be beneficial to the automotive industry and university in terms of knowledge transfer, experience and expertise to explore in lightweight material and manufacturing process which focusing on new casting process compared to current conventional stamping process so that the vehicle performance on par with other global Automotive Manufacturer in term of lightweight vehicle.

## References

1. Dahanu G, kattimani RS (2016) Comparison study of lower control arm with different material. *Int Res J Eng Technol (IRJET)* 3(10):702–708
2. Mohanraj R, Manavalasundaram VK (2016) *Int J Intell Adv Res Eng Comput* 1:6–9
3. Li J, Tan J, Dong J (2020) Lightweight design of front suspension upright of electric formula car based on topology optimization method. *World Elect Veh J* 11(1). <https://doi.org/10.3390/WEVJ11010015>
4. Singh, J (2015) Static Structural Analysis of Suspension Arm Using Finite Element Method. *Inter J Res Eng Technol* 04(07): 402–406.
5. Rahman MHA, Salleh MS, Abdullah A, Yahaya SH, Razak MSA, Kamal MRM, Marjom Z, Anuar L, Saad NAM (2018) A new design optimization of light weight front lower control arm. *J Adv Manuf Technol* 12(1):89–102
6. Taksande SP, Vanalkar AV (2015) Design, modeling and failure analysis of car front suspension lower arm. *Int J Sci Technol Eng* 2(01):235–249
7. Tang L, Wu J, Liu J, Jiang C, Shangguan WB (2014) Topology optimization and performance calculation for control arms of a suspension. *Adv Mech Eng* 2014. <https://doi.org/10.1155/2014/734568>

# Chapter 25

## Model of Effectiveness Earned Value Management in the Malaysian Manufacturing Sector



**Shahrizan Yusoff, Mohammad Hazim, Syed Ahmad Faiz, Sazali Said, and Huda Kassim**

**Abstract** Project management is the act of planning, organizing, motivating and controlling resources of time and cost to achieve specific goals known as the scope of the project. Earned value management (EVM) or earned value project/performance management (EVPM) is a project management technique that measures project progress and performance in an objective manner and provides an accurate forecast of any project performance problem. To practically demonstrate the effectiveness of EVM on manufacturing, a survey is created. The aim of this work is to show how effective EVM can be applied to the Malaysian manufacturing sector. The model is a more abstract way of schematizing a method, thus this approach may be extended to solve similar problems in other fields. The theory is a formalized model that is both generalizable and predictive and can thus be used prescriptively to other industries.

**Keywords** Project management · Earned value management (EVM) · Model of effectiveness EVM · Manufacturing project management

### 25.1 Introduction

This study describes the effectiveness earned value management system for the manufacturing sector. In Malaysia, the number of high-tech manufacturing projects is increasing rapidly and because manufacturing has a great impact on the country's

---

S. Yusoff (✉) · M. Hazim · S. A. Faiz · S. Said · H. Kassim  
Universiti Kuala Lumpur, Malaysian Spanish Institute, Kulim Hi-Tech Park, 09000 Kulim,  
Kedah, Malaysia  
e-mail: [mshahrizan@unikl.edu.my](mailto:mshahrizan@unikl.edu.my)

S. A. Faiz  
e-mail: [syedahmadfaiz@unikl.edu.my](mailto:syedahmadfaiz@unikl.edu.my)

S. Said  
e-mail: [msazali@unikl.edu.my](mailto:msazali@unikl.edu.my)

H. Kassim  
e-mail: [mhuda@unikl.edu.my](mailto:mhuda@unikl.edu.my)

economy, it is necessary for owners of companies, project managers, and contractors to effectively control and track the cost, time, and scope of their projects. The project performance can be assessed using different traditional methods and approaches daily.

This study discusses earned value management (EVM) as an important method for the assessment, tracking, and monitoring of project success and development. The project management methodology integrates cost, time, and scope of the project and allows project managers to predict potential project progress patterns. EVM uses three data sources including planned value (PV) or budgeted work scheduled, actual cost (AC) or actual expenditure and earned value (EV) of physical work performed; and compare these elements to assess the project performance (United States of America Department of Energy). EVM can provide a baseline for project performance measurement so that the project outcome can be determined and controlled.

## 25.2 Literature

This chapter will discuss the knowledge gained from the existing reviewed articles and journals. This chapter will cover the research of the previous experiments done by researchers around the world. Their topics and findings are closely related to this study. The summary, explanation and critical review of the research can be found in this chapter.

### 25.2.1 *Implementation EVM in a Project*

Based on the study by Morad et al. [1] entitled Use of Earned value management in the UAE industry, the paper provides an assessment of survey responses from project managers and cost engineers in the UAE construction industry. The results were assessed based on 53 responses. The analysis revealed that several companies are using EVM in their cost control systems. However, a significant portion of UAE's construction companies is not using EVM. Although many companies are not implementing EVM, the project showed that 87% of responses agreed on the necessity of EVM implementation as a cost control tool. Respondents were asked to state the level of usage of EVM in their organization. Figure 25.1 shows the usage percentages while Fig. 25.2 is showing the use of EVM for decision making.

Approximately half of EVM implementers are always using EVM in their projects. As for the use of EVM as a forecasting tool for cost at completion, the analysis shows that 76% use it often or always. On the other hand, 73% use it to forecast the project duration. 79% of the respondents often or always use the EVM index to measure performance.

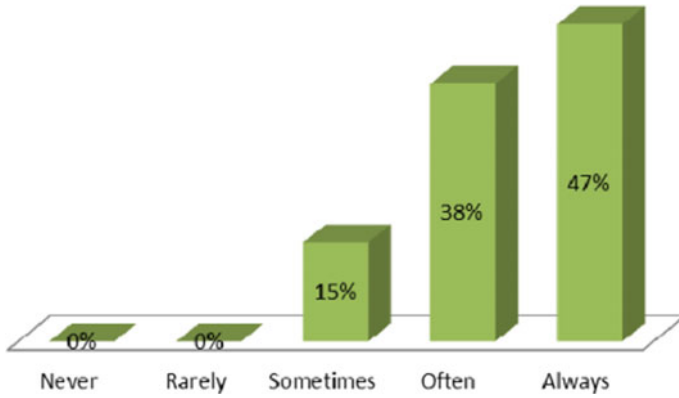


Fig. 25.1 Usage percentages of EVM

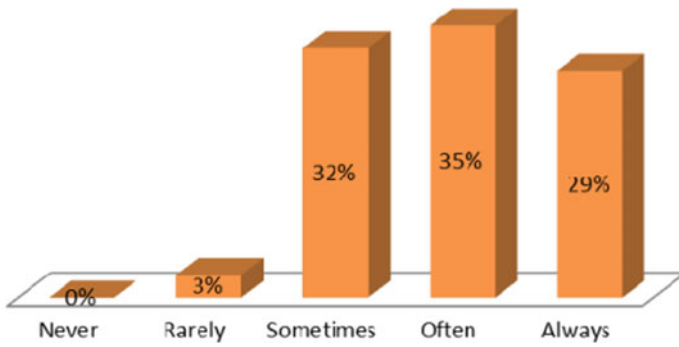


Fig. 25.2 Usage EVM for decision-making

Based on the study Picornell et al. [2] entitled Implementation of Earned Value Management in Unit-Price Payment Contracts, the findings indicate that EVM is not typically implemented by contractors when the payment agreement is based on unit-prices. In this payment approach, the owner pays the quantities executed according to the reagreed rate established in the contract for each unit or task; the income is received by the contractor from the owner. The EVM formulation can be directly applied to cost-reimbursable and lump-sum contracts, either by the owner or the contractor.

### **25.2.2 Problem Using Earn Value Management**

Based on the study by Kim et al. [3] entitled A model for Effective Implementation of Earned Value Management Methodology, a model is developed on the research effort the empirical studies mainly identified problems such as high cost, project manager lack of understanding, and government-led centralized EVM implementation and resulting lack of user participation was the problem affecting the EVM performance and participation.

Based on the study by Devanshu et al. [4], there are several factors that contributed to the problem of implementation EVM, i.e. lack of industry ownership, inadequate training, and an awkward technical jargon. A major factor was a failure in the early years to make the earned value process the responsibility of programme managers and contractors.

### **25.2.3 Benefit of Using EVM**

Based on a study by Gowan et al. [5], it is stated that the benefit of the technique is that the EVM system in manufacturing industry says the benefits on technique since the EVM monitors the physical completion of the project procedure. It has become an important part of project handling since it integrates three important project elements, i.e. the project cost, schedule, and time with project scopes, so that many studies and researches are done in this area.

Based on the study of study by Alvarado et al. [6], the cost benefits are more than the time benefit. The EVM contribution to achieve the cost objective is ranked 2nd while the EVM contribution to achieve the time objective was ranked 13th. Moreover, the benefits of the earned value management process exceed the costs that have not been adequately reported in the literature. Several studies report the costs but ignore the benefits. Others focus on the benefits but ignore the costs. The results show that the benefit using EVM for the system is the cost reduction for the project that can be less without applying this system.

## **25.3 Methodology**

Surveys, questionnaires and interviews are the common tools of research. In this phase, the research activity starts with a literature review survey by finding and collection of related journals and articles on EVM whether it applies to the industry. At the same time, the study of the best approach to use for the research, i.e. whether to apply a questionnaire or a case study or any other method to conclude this research, must be performed. The conceptual model will be created based on the finding of the literature review.

### 25.3.1 Design of Conceptual Model

The first variables are the factors that affect the EVM system. There were 8 indicators analysed based on the problem that exists in the EVM system as shown in Fig. 25.3.

1. Incorrect assessment
2. Misunderstanding
3. Bad image
4. Long time to train
5. Too many documents
6. Too many rules
7. A lot of costs
8. Weakening management power.



Fig. 25.3 Problem in EVM concept model

### 25.3.2 Conceptual Model of Effectiveness in EVM

The second variables of the model are the effectiveness of the EVM. The indicator was based on the successful factor that can bring the effectiveness of the EVM as shown in Fig. 25.4.

1. Communication from team members
2. Strong support from top management
3. Implementation training
4. Motivation from team member.

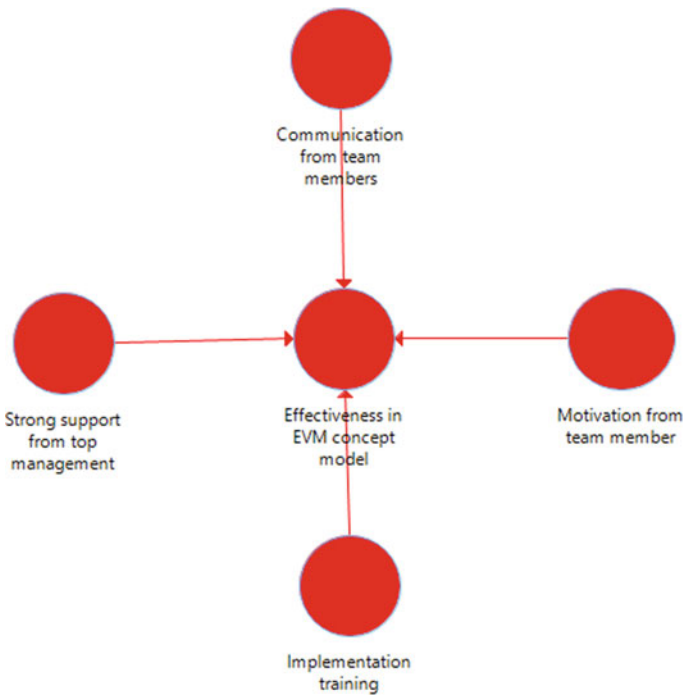


Fig. 25.4 Effectiveness in EVM concept model



### 25.3.3 Conceptual Model of Effect of Benefit in EVM

The third variables were the effect of effectiveness in EVM as shown in Fig. 25.5. The indicator is based on the benefit in the EVM system based on the following:

1. Offer early signal
2. Attain project costs
3. Provide reliable data
4. Useful for comparative analysis
5. Better communication among team members
6. Identify risk
7. Improving project
8. Achieve time objective.

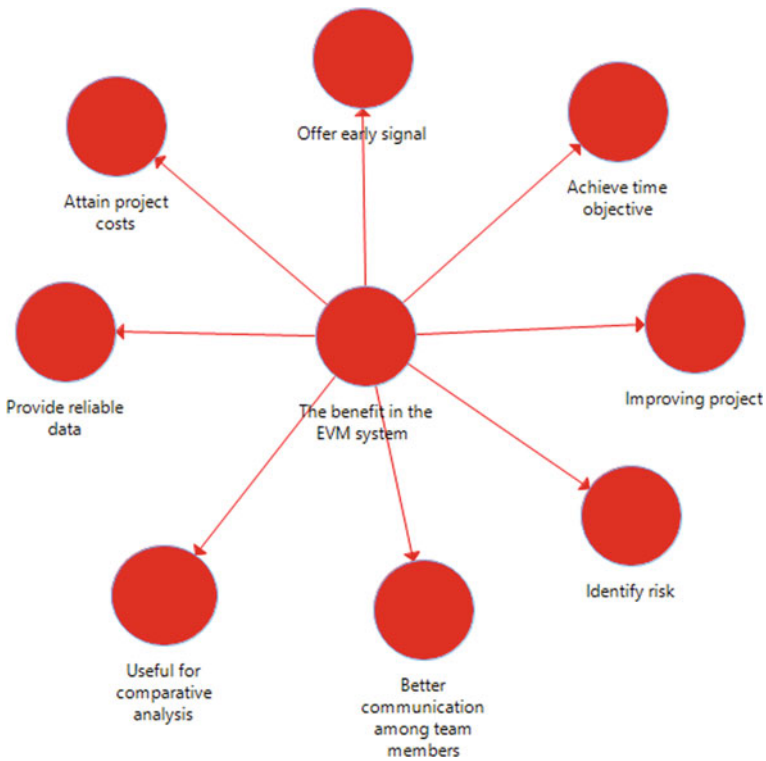


Fig. 25.5 Effect of benefit in EVM

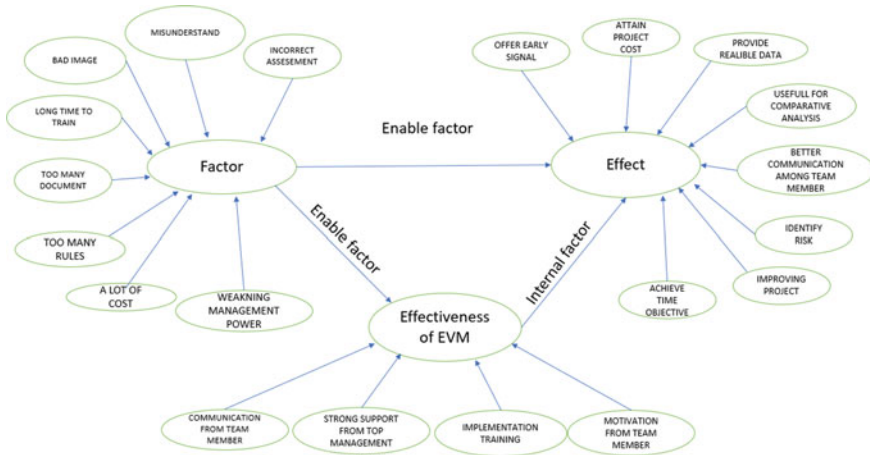


Fig. 25.6 Complete concept model

### 25.3.4 The Complete Conceptual Model

The complete conceptual model is as the diagram shown in Fig. 25.6.

## 25.4 Results and Discussion

A research model is a research strategy, whereas the theory or proposal is the product of the research. Quantitative research typically establishes a model based on which the researcher continues. The model is a strategy that is used to solve an issue. A model is a more abstract way of schematizing a method, so the approach may be extended to solve similar problems in other fields. The theory is a formalized model that is both generalizable and predictive and can thus be used prescriptively. The final model of the effectiveness of EVM is shown in Fig. 25.7.

In this model the problem implementation (prob), successful factor (suc), benefit (ben) (ben) are provided in partial least squares structural equation modelling (PLS) to produce the loading for the research.

### 25.4.1 Outer Loading Based on the Model

The outer measurement (indicator) loading is significant for verification of the reliability of a structure built to an estimated test of each variable on its corresponding indicator construct. The outer loading must be greater than 0.5 as shown in Table 25.1.

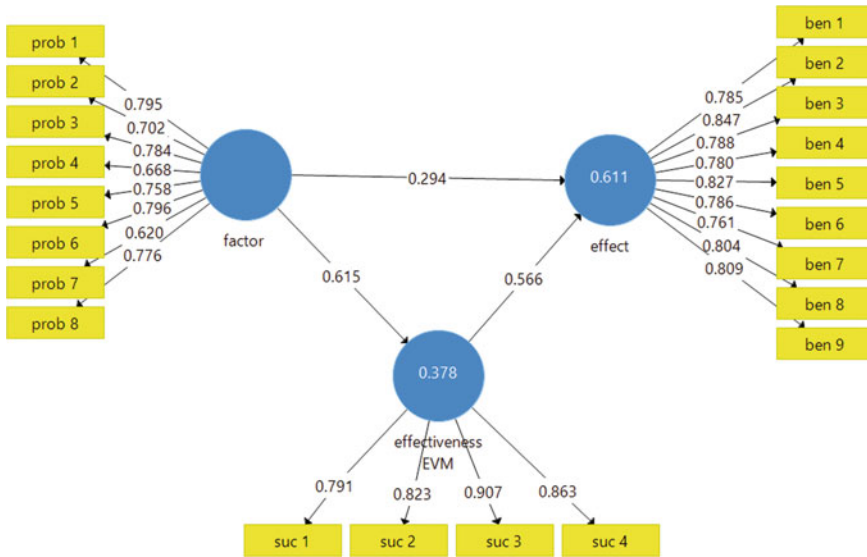


Fig. 25.7 PLS SEM result

Table 25.1 shows that every benefit (ben) was more than 0.5 and the majority has even the higher value of 0.8. The successful factor (suc) was also higher than 0.5 and some of them have a higher value of 0.9. Thus, the data can be considered as excellent. The prob also has values more than 0.5 but some of it has a value of less than 0.7, namely, for item prob 7 and prob 4 but the value was still higher than 0.5. The indicator shows that all have a value of more than 0.5 so all the indicators were deemed as valid. If the indicator is less than 0.5 the indicator must be removed and deleted from the model.

### 25.5 Conclusions

The EVM provides project managers with a very good insight into the state of projects and allows them to have a clear vision of the future project success. In this project, the EVM method as a powerful performance measurement and forecasting tool has been successfully applied and tested for the manufacturing industry, and very interesting results have been obtained for a long time. Based on the model, it shows that EVM consists of many problems agreed by most respondent. But through the problem, it can create the success factor and benefit for the project. As we can see EVM is rarely used in the industry, but it has a great benefit if applied to it especially in terms of cost and project management time.

**Table 25.1** The outer loading of EVM

	Effect	Effectiveness	Factor
ben 1	0.785		
ben 2	0.847		
ben 3	0.788		
ben 4	0.78		
ben 5	0.827		
ben 6	0.786		
ben 7	0.761		
ben 8	0.804		
ben 9	0.809		
suc 1		0.791	
suc 2		0.823	
suc 3		0.907	
suc 4		0.863	
prob 7			0.62
prob 4			0.668
prob 2			0.702
prob 5			0.758
prob 8			0.776
prob 3			0.784
prob 1			0.795
prob 6			0.796

## References

1. Morad M, El-Sayegh S (2016) Use of earned value management in the UAE construction industry. In: International conference on industrial engineering, management science and application (ICIMSA), pp 1–5 (2016)
2. Picornell M, Pellicer E, Torres-Machí C, Sutrisna M (2016) Implementation of earned value management in unit-price payment contracts. *J Manag Eng* 33:3
3. Kim EH, Wells WG, Duffey MR (2013) A model for effective implementation of earned value management methodology. *Int J Project Manag* 21(5):375–382
4. Devanshu V, Rajgor PM, Pitroda J (2018) A critical literature review on implementation of earned value management. *Int J Constr Res Civ Eng* 4(1):39–43
5. Gowan JA, Mathieu RG, Hey MB (2006) Earned value management in a data warehouse project. *Inf Manag Comput Secur* 14(1):37–50
6. Alvarado CM, Silverman RP, Wilson DS (2005) Assessing the performance of construction projects: implementing earned value management at the general services administration. *J Facil Manag* 3(1):92–105